Evaluating the stratospheric circulation and its variability in a Chemistry-Climate Model with reanalyses and observations of nitrous oxide

A thesis submitted for the partial fulfilment of the requirements for the academic degree of *Philosophiae Doctor* in Sciences at the University of Liège (College of Spatial Sciences) by

Daniele Minganti

Department of Astrophysics, Geophysics and Oceanography
UR SPHERES
University of Liège
Belgium
Academic Year 2021/2022

Jury Members:

Marilaure Grégoire	President	ULiège, Belgium
Guy Munhoven	Secretary	ULiège, Belgium
Emmanuel Mahieu	Promoter	ULiège, Belgium
Simon Chabrillat	Promoter	BIRA-IASB, Belgium
Marta Abalos		Universidad Complutense de Madrid, Spain
Xavier Fettweis		ULiège, Belgium

This work was partially supported by the Fonds de la Recherche Scientifique - FNRS under grant no. PDR.T.0040.16

Contents

1 Introduction **1**
- 1.1 The Earth's atmosphere . . . 1
  - 1.1.1 Equations of the static atmosphere . . . 4
  - 1.1.2 Atmospheric composition . . . 7
  - 1.1.3 Greenhouse gases . . . 8
    - 1.1.3.1 Radiation basics . . . 9
    - 1.1.3.2 The surface temperature of the Earth . . . 11
    - 1.1.3.3 The greenhouse effect . . . 12
  - 1.1.4 Nitrous oxide in the atmosphere . . . 17
- 1.2 The Stratosphere . . . 19
  - 1.2.1 Discovery of the stratosphere . . . 19
  - 1.2.2 Mean state of the stratosphere . . . 22
  - 1.2.3 Stratospheric zonal mean circulation . . . 23
  - 1.2.4 Waves interacting with the stratosphere . . . 25
    - 1.2.4.1 Gravity waves . . . 27
    - 1.2.4.2 Planetary waves . . . 28
    - 1.2.4.3 Equatorial waves . . . 29
  - 1.2.5 Variability of the Stratosphere . . . 30
    - 1.2.5.1 The Quasi Biennial Oscillation . . . 30
    - 1.2.5.2 The Polar Vortex . . . 32
  - 1.2.6 Stratospheric Ozone . . . 35
  - 1.2.7 Observing and modeling the stratosphere . . . 41

2 Overview of the Brewer-Dobson Circulation **45**
- 2.1 History of the BDC . . . 47
- 2.2 Residual Circulation . . . 48
- 2.3 Mixing and transport barriers . . . 51
- 2.4 Momentum and heat primitive equations in the conventional Eulerian mean in the stratosphere . . . 54
  - 2.4.1 The primitive equations . . . 54
  - 2.4.2 The beta-plane and the quasi-geostrophic approximations . . . 56
    - 2.4.2.1 The primitive equations on a beta-plane . . . 56
    - 2.4.2.2 The geostrophic balance . . . 57
    - 2.4.2.3 The quasi-geostrophic approximation . . . 57
  - 2.4.3 The primitive equations in the conventional eulerian mean . . . 58
- 2.5 Driving mechanisms of the BDC . . . 59

2.6 The age of air 64
2.7 Multi-annual changes in the BDC 65
2.7.1 modeled changes 65
2.7.2 Observed changes 69

3 Objectives of the thesis **73**

4 Observed and modeled datasets **75**
4.1 The Whole Atmosphere Community Climate Model 75
4.1.1 The Community Earth System Model 76
4.1.2 The Community Atmosphere Model 76
4.1.3 Extension of CAM to the Whole Atmosphere 78
4.1.4 WACCM simulations produced at BIRA-IASB 80
4.1.5 WACCM-REFC1 89
4.1.6 WACCM-REFD1 91
4.2 The Belgian Assimilation System of Chemical ObsErvations . 92
4.2.1 The BASCOE Chemistry-Transport Model Setup . . . 93
4.2.2 Input Meteorological Reanalyses 93
4.2.2.1 Generic Atmospheric Reanalysis 94
4.2.2.2 ERAI 97
4.2.2.3 ERA5 98
4.2.2.4 JRA55 98
4.2.2.5 MERRA 99
4.2.2.6 MERRA2 100
4.2.3 Preprocessing of the input reanalyses 100
4.3 Remote Sensing Measurements 101
4.3.1 Fourier Transform Spectrometer Basics 101
4.3.2 Ground-based measurements: Fourier Transform Infrared Data 103
4.3.3 The Atmospheric Chemistry Experiment - Fourier Transform Spectrometer 108
4.3.4 The Microwave Limb Sounder 110
4.4 The BASCOE Chemical Reanalysis 111
4.4.1 Description of the Chemical Reanalysis 112
4.4.2 The BASCOE Data Assimilation System 112
4.5 Other Considered Datasets 114
4.5.1 FTIR station: Paramaribo 114
4.5.2 BRAM3 115
4.6 Preliminary N_2O comparisons 116

5 Methods **120**
5.1 The Transformed Eulerian Mean Applied to Tracer Transport 120
5.2 Regression tools 123
5.2.1 Bootstrap Method 124
5.2.2 Multi Linear Regression 125
5.2.3 Dynamical Linear Modelling 126
5.2.4 DLM vs bootstrap 129
5.2.5 DLM vs MLR 132

6 Climatologies of N_2O and its TEM budget **136**
6.1 Climatological impact of the Brewer-Dobson circulation on the N_2O TEM budget in WACCM, a chemical reanalysis and a CTM driven by four dynamical reanalyses 136
6.2 Addition of the BASCOE CTM driven by ERA5 and WACCM-REFD1 simulations 160

7 Decadal changes of N_2O and impact of BDC **167**
7.1 N_2O rate of change as a diagnostic of the Brewer-Dobson Circulation in the stratosphere 167
7.2 Additional discussion 200
7.2.1 Impact of the seasonal cycle and regressors on the N_2O stratospheric columns 200
7.2.2 Hemispherical Differences of N_2O columns 203
7.2.3 Changes of ADV and MIX in the remaining datasets 205

8 Conclusions and Outlook **208**
8.1 Conclusions 208
8.1.1 Conclusions for Objective 1 208
8.1.2 Conclusions for Objective 2 209
8.1.3 General Conclusions 212
8.2 Outlook 212
8.2.1 Need of Improved Long-Term Observations of N_2O . . 213
8.2.2 Added Value of Modelling Studies 213
8.2.3 General Outlook 214

A List of Acronyms **216**

B List of Papers **220**

Acknowledgments

When I first arrived in Brussels to start my Ph.D., my life changed from many points of view, and I didn't know what I was heading into. I wanted an experience abroad, and a Ph.D. in a European capital was a perfect opportunity. After completing this journey, I can gladly say that I would do it again. However, none of it would have been possible without the help of many people, who spent a lot of time and energy to support me.

The completion of this thesis would not have been possible without my supervisor at BIRA-IASB: Simon Chabrillat. From the very first Skype interview to the last review of this thesis, he has constantly supported and encouraged me. His supervision and thorough reviews were essential for my work, and I learned a lot from our lively scientific discussions. Working together made me feel like a peer and boosted my curiosity towards new scientific achievements. It was a pleasure working with him during these years, and I am looking forward to the next tasks together.

Special thanks go to Emmanuel Mahieu, my promoter at the University of Liège. His expertise, comments and advice allowed me to expand my knowledge on fascinating subjects that I did not master well (in particular, the whole FTIR world). All the discussions we had (also together with Simon) stimulated me to look at my research from different perspectives and motivated me to investigate it in more detail.

Within my group at BIRA-IASB, many thanks go to our (retired) IT guru Yves Christophe. Always available for help, we sat together for many long hours of debugging sessions. In addition, thanks to his advice and expertise, I highly improved my programming skills. Many thanks also go to Quentin Errera, who always provided excellent expertise and helped on many scientific aspects I was unfamiliar with.

Although I didn't spend a lot of time at the University of Liège, I had the fortune to share my Ph.D. experience with Maxime Prignon. Now doing research in Sweden, I thank him for working together during these years and for the four enriching weeks we spent together in Grenoble for the ERCA school.

Within the course of my Ph.D. experience, I had the fortune to work with many excellent scientists, who were always available to share their knowledge, provide very constructive advice and start fruitful scientific discussions. I would like to thank Marta Abalos (University of Madrid, Spain), Doug Kinnison (National Center for Atmospheric Research, USA), Rolando Garcia (National Center for Atmospheric Research, USA), Justin Alsig (University of Stockholm, Sweden), Dan Smale (National Institute of Water and Atmo-

spheric research, New Zealand), Matthias Schneider (Karlsruhe Institute of Technology, Germany) and Nicholas Jones (University of Wollongong, Australia). I also would like to thank Mohamadou Diallo (Forschungszentrum Julich, Germany) for his thorough review of my first paper, which highly improved my skills in scientific writing.

I would like to thank all the colleagues at BIRA-IASB. In particular, special thanks go to the IT department, which was always available for help at my numerous demands. I also would like to warmly thank my fellow Ph.D. and postdoc friends who shared so many post-work beers with me: Ermioni Dimitropoulou, Miriam Cisneros, Shohei Aoki (now a junior professor in Tokyo), Justin Erwin, Sieglinde Callewaert, Catalina Poraicu and Lucie Lamort.

Special thanks also go to my Italian friends, who helped me through this long journey, always cheering me up with plenty of jokes. Thanks to Marco, Andrea, Mattian and Elena as well as to Valerio, Marco (Gotellini) and Daniele.

Sentiti ringraziamenti vanno anche ai miei genitori, che sono sempre stati presenti, dall'inizio degli studi della triennale fino alla fine e oltre. La mia partenza dall'Italia è stata difficile per tutti all'inizio, ma il vostro costante amore e aiuto (espresso, tra le altre cose, con innumerevoli chiamate Skype e i famosi 'pacchi') mi hanno permesso di terminare con successo questa sfida.

I would like to terminate my acknowledgments by expressing my gratitude to Hululain. You have always supported me during these years, in the good and (sometimes) bad moments. Your presence helped me a lot, encouraging me during the development and writing of this thesis - you were my right hand (literally for a period!). Thanks to you, I discovered that 'On est tous dans la même stratosphère'.

Grazie mille a tutti.

Summary

The circulation in the atmosphere is closely coupled with its composition through several feedback processes that affect radiative transfer, in the ultraviolet and the infrared, and thus climate. In the stratosphere (the layer between approximately 10 and 50 km above the surface), the Brewer-Dobson Circulation (BDC) transports air masses from the Tropics towards the polar latitudes. For the transport of long-lived trace gases (the tracers), the BDC is often separated into an advective component (the residual circulation) and a mixing component. Thus, the BDC plays a crucial role in determining the stratospheric distribution of these tracers, including, e.g., ozone, as well as the momentum and heat budgets in the stratosphere. Therefore, it is necessary to carefully evaluate the BDC changes that could arise from anthropogenic climate change and distinguish them from natural variability. Conversely, the distribution and variability of stratospheric tracers can be used to better understand the BDC and the causes of its time variations. Many studies have addressed this issue and concluded that climate models show an acceleration of the BDC, which is not confirmed by indirect measurements of the BDC obtained from tracer observations. This discrepancy calls for further research to better understand the BDC changes in the past decades, hence to better predict its future changes.

In this thesis, we study the BDC in the stratosphere and its changes through their impact on changes of a specific long-lived tracer: nitrous oxide (N_2O). N_2O is increasing continuously at the surface, and if the BDC were not changing interannually, then N_2O would be expected to increase in the stratosphere as well. We use observations from Fourier Transform Infrared Spectrometers (FTIR) at four stations in the southern and northern subtropics and mid-latitudes and space-borne observations from the Atmospheric Chemistry Experiment - Fourier Transport Spectrometer (ACE-FTS). We compare those observations with four simulations of the Belgian Assimilation System for Chemical ObsErvations Chemistry Transport Model (BASCOE CTM) driven by four modern reanalyses of atmospheric dynamics. These datasets are then used to evaluate the representation of the BDC in two versions of the Whole Atmosphere Community Climate Model (WACCM). In order to analyze the impact of the transport on the N_2O changes, we use the Transformed Eulerian Mean (TEM) diagnostic to separate the impact of the residual advection and mixing on the N_2O rates of change.

We first evaluate the climatologies of N_2O and its TEM budget according to the model simulations. Each BASCOE CTM simulation delivers a significantly different N_2O abundance above the Tropics. These differences reflect

the disagreements between the dynamical reanalyses that drive these simulations, showing the value of running multiple CTM simulations since no single reanalysis can be used to represent the "true" BDC. Regarding the climatological TEM budget analysis of the transport, the advection term agrees well among the datasets, but larger differences arise for the mixing term, especially in regions with strong horizontal gradients of tracer abundancies, e.g., the wintertime Antarctic. The WACCM model simulates a weaker mixing term over the Northern Hemisphere than the reanalyses. This underestimation could indicate that, in this climate model, the forcing by the breaking of planetary waves is too weak over the northern extratropics.

Once the climatologies of N_2O and its TEM budget have been characterized, we investigated their decadal changes in the stratosphere. Decadal trends of N_2O obtained from observations over the 2005-2018 period are different in each hemisphere: the FTIR instruments deliver increasing trends that are significantly larger at Lauder (latitude 45°S) than at Jungfraujoch (latitude 46°N); the ACE-FTS satellite instrument even finds increasing N_2O in the Southern Hemisphere and decreasing in the mid-lower stratosphere (pressure range 30 to 60 hPa) above the northern mid-latitudes (35°N to 65°N). However, the currently available N_2O observations suffer from instrument-related shortcomings: the N_2O retrieved from FTIR lacks sufficient vertical resolution, and the ACE-FTS measurements are affected by poor temporal and spatial sampling, which amplifies the trends in the mid-latitudes. On the other hand, model simulations provide valuable insights about the N_2O changes. In particular, sensitivity tests with the BASCOE CTM confirmed the role of a changing circulation in determining the hemispheric differences in the N_2O trends over the extratropical regions. Over the tropical regions, the TEM analysis shows that the stratospheric N_2O changes are caused mainly by the strengthening of the residual advection. Over the northern mid-latitudes, the N_2O trends simulated by WACCM are larger than those obtained with most reanalyses or with the ACE-FTS observations - hence weaker hemispheric differences are found by this climate model. This diversity indicates that climate change impacts the BDC differently in both hemispheres and that this difference is more pronounced in reality than in WACCM.

Résumé

La circulation et la composition de l'atmosphère sont étroitement couplés par des processus rétroactifs qui affectent le transfert radiatif, aussi bien dans l'ultraviolet que dans l'infrarouge, et donc le climat. Dans la stratosphère (la couche qui se situe approximativement entre 10 et 50 km au-dessus de la surface), la circulation de Brewer-Dobson (BDC) transporte les masses d'air des Tropiques vers les latitudes polaires. En ce qui concerne le transport des gaz en trace à longue durée de vie (les traceurs), elle est souvent séparée en un composant advectif (la circulation résiduelle) et un composant de mélange. La BDC joue donc un rôle crucial pour déterminer la distribution de ces traceurs, dont l'ozone, ainsi que les budgets de quantité de mouvement et de chaleur dans la stratosphère. Il est par conséquent nécessaire d'évaluer avec soin les changements de la BDC qui pourraient résulter du changement climatique anthropique et de les distinguer de la variabilité naturelle. Inversément, la distribution et la variabilité des traceurs stratosphériques peuvent être utilisées pour mieux comprendre la BDC et ses variations temporelles. De nombreuses études se sont intéressées à cette question et ont conclu que les modèles climatiques indiquent une accélération de la BDC, qui n'est pas confirmée par les mesures indirectes de la BDC obtenues à partir des observations de traceurs. Ce désaccord montre la nécessité de recherches plus approfondies visant à mieux comprendre les changements de la BDC des dernières décennies, et donc à mieux prévoir ses changements à venir.

Dans cette thèse nous étudions la BDC dans la stratosphère, et ses variations temporelles, à travers leur impact sur la distribution et les variations d'un traceur spécifique: l'oxyde nitreux (N_2O). Le N_2O augmente continuellement à la surface, et en l'absence de variations interannuelles de la BDC on s'attendrait à ce que le N_2O augmente simplement dans la stratosphère aussi. Nous utilisons des observations par spectromètres infrarouges à transformée de Fourier (FTIR) à quatre stations de mesure dans les latitudes sous-tropicales et moyennes des deux hémisphères, ainsi que des observations obtenues par l'instrument satellitaire ACE-FTS. Nous comparons ces observations avec quatre simulations par le modèle de chimie-transport BASCOE entrainé par quatre réanalyses modernes de la dynamique atmosphérique. Ces jeux de données sont alors utilisés pour évaluer la représentation de la BDC dans deux versions du modèle communautaire du climat atmosphérique WACCM. Pour analyser l'impact du transport sur les changements de N_2O, nous utilisons le diagnostic de la moyenne eulérienne transformée (TEM) afin de séparer l'impact de l'advection résiduelle et du mélange sur les taux de

variation du N_2O.

Nous évaluons d'abord les climatologies du N_2O et de son budget TEM selon les simulations des modèles. Chaque simulation du modèle BASCOE fournit une abondance significativement différente du N_2O au-dessus des Tropiques. Ces différences réflètent les désaccords entre les réanalyses dynamiques qui entrainent ces simulations, montrant l'utilité de notre approche multi-simulations puisqu'aucune de ces réanalyses ne peut être utilisée pour représenter la "vraie" BDC. En ce qui concerne l'analyse TEM climatologique du budget du transport résiduel, le terme d'advection est en bon accord entre les jeux de données mais de plus grandes différences apparaissent pour le terme de mélange, en particulier dans les régions avec de forts gradients horizontaux de l'abondance du traceur, par exemple l'Arctique en hiver. Par rapport aux réanalyses, le modèle WACCM simule un terme de mélange plus faible au-dessus de l'hémisphère Nord. Cela pourrait indiquer que dans ce modèle climatique, le forçage par dissipation des ondes planétaires est trop faible au-dessus des latitudes extratropicales de l'hémisphère Nord.

Après cette caractérisation des climatologies du N_2O et de son budget TEM, nous étudions leurs changements décénnaux dans la stratosphère. Les tendances décennales de N_2O déduites des observations sur la période 2005-2018 sont différentes dans chaque hémisphère: les instruments FTIR fournissent des tendances en hausse qui sont significativement plus grandes à Lauder (latitude 45°S) qu'à Jungfraujoch (latitude 46°N); l'instrument satellitaire ACE-FTS trouve même que le N_2O diminue dans la stratosphère moyenne-basse (entre les pressions 30 à 60 hPa) au-dessus des latitudes moyennes boréales (35°N à 65°N). Cependant les observations de N_2O actuellement disponibles souffrent de carences instrumentales: les colonnes de N_2O extraites des instruments FTIR manquent de résolution verticale, et l'échantillonage temporel et spatial de ACE-FTS est faible, ce qui amplifie les tendances aux latitudes moyennes. D'autre part les simulations des modèles fournissent un éclairage appréciable sur les changements de N_2O. Des test de sensibilité avec le modèle BASCOE confirment le rôle du changement de la circulation dans la détermination des différences de changement hémisphèriques au-dessus des règions extra-tropicales. Au-dessus des règions tropicales, l'analyse TEM indique que les changements de N_2O stratosphérique sont dûs principalement au renforcement de l'advection résiduelle. Au dessus des latitudes moyennes borèales, les tendances de N_2O simulèes par WACCM sont plus èlevèes que celles obtenues avec la plupart des rèanalyses ou par les observations ACE-FTS - et donc ce modèle de climat donne des diffèrences hémisphériques plus faibles. Ceci indique que le changement de climat a un effet diffèrent sur la BDC dans chacun des hémisphères, et que cette différence est plus prononcée dans la réalité que dans WACCM.

Sommario

La circolazione nell'atmosfera è strettamente legata alla sua composizione chimica attraverso numerosi processi retroattivi che influenzano il trasferimento radiativo nell'ultravioletto e nell'infrarosso, e di conseguenza il clima. Nella stratosfera (lo strato atmosferico all'incirca tra 10 e 50 kilometri al di sopra della superficie), la circolazione di Brewer-Dobson (BDC) trasporta masse d'aria dai Tropici verso le latitudini polari. Per il trasporto di gas in traccia a lunga vita (i traccianti), la BDC viene spesso separata in una componente avvettiva (la circolazione residua) e una di mescolamento. Pertanto la BDC, oltre ad avere un ruolo cruciale nel bilanciamento della quantità di moto e di calore in stratosfera, è fondamentale anche nel determinare la distribuzione di questi traccianti, tra i quali l'ozono. Di conseguenza è necessario valutare con attenzione i cambiamenti della BDC che potrebbero risultare da cambiamenti climatici antropici e distinguerli dai cambiamenti dovuti alla variabilità naturale. Viceversa, la distribuzione e la variabilità dei traccianti stratosferici possono essere usati per capire meglio la BDC e le cause delle sue variazioni temporali. Molti studi hanno affrontato questo argomento e concluso che i modelli climatici mostrano un'accelerazione della BDC, non confermata da misure indirette della BDC ottenute da osservazioni dei traccianti. Questa differenza mostra la necessità di ulteriori e più approfondite ricerche per capire meglio i cambiamenti della BDC nei decenni passati, e per predirne i cambiamenti futuri in modo migliore.

In questa tesi viene studiata la BDC nella stratosfera e i suoi cambiamenti temporali attraverso il loro impatto sulla distribuzione e sui cambiamenti di un tracciante specifico: l'ossido nitroso (N_2O). L'N_2O aumenta continuamente al suolo, e, in assenza di variazioni inter-annuali della BDC, esso aumenterebbe anche nella stratosfera. In questo studio vengono utilizzate osservazioni da spettrometri infrarossi a trasformata di Fourier (FTIR) acquisite da quattro stazioni di misura alle latitudini subtropicali e medie dei due emisferi, e misure satellitari ottenute dallo strumento ACE-FTS. Queste osservazioni vengono confrontate con quattro simulazioni del modello di trasporto e chimica BASCOE forzato da quattro rianalisi moderne della dinamica atmosferica. Questi set di dati sono poi utilizzati per valutare la rappresentazione della BDC in due versioni del modello climatico comunitario WACCM. Per analizzare l'impatto del trasporto sulle variazioni di N_2O, viene utilizzata la diagnostica della media euleriana trasformata (TEM) per separare l'impatto dell'avvezione residua e del mescolamento sui tassi di variazione di N_2O.

Per prima cosa le climatologie di N_2O e del suo bilancio TEM secondo

le simulazioni dei modelli saranno valutate. Ogni simulazione del modello BASCOE fornisce delle quantità significativamente differenti di N_2O al di sopra dei Tropici. Queste differenze riflettono il disaccordo tra le rianalisi dinamiche che guidano queste simulazioni, e mostrano l'utilità del nostro approccio con varie simulazioni, visto che nessuna di queste rianalisi da sola può essere utilizzata per rappresentare la "vera" BDC. Per quanto riguarda la climatologia dell'analisi TEM del bilancio del trasporto di N_2O, il termine di avvezione residua è in buon accordo tra i vari set di dati ma vi sono delle differenze più marcate per il termine di mescolamento, in particolare in regioni con forti gradienti orizzontali della quantità dei traccianti, per esempio nell'Antartico in inverno. Rispetto alle rianalisi, il modello WACCM simula un termine di mescolamento più piccolo al di sopra dell'emisfero Nord. Questa sottostima potrebbe indicare che, nel modello climatico, la forzante dovuta alla dissipazione delle onde planetarie è troppo debole al di sopra delle latitudini extra-tropicali dell'emisfero Nord.

Dopo la caratterizzazione delle climatologie di N_2O e del suo bilancio TEM, le loro variazioni decennali nella stratosfera vengono studiate. Le tendenze decennali di N_2O ottenute dalle osservazioni nel periodo 2005-2018 differiscono nei due emisferi: gli strumenti FTIR forniscono delle tendenze in aumento significativamente più grandi a Lauder (latitudine 45°S) che a Jungfraujoch (latitudine 45°N); le misure satellitari di ACE-FTS mostrano invece che l'N_2O diminuisce nella media-bassa stratosfera (tra le pressioni di 30 a 60 hPa) al di sopra delle medie latitudini boreali (da 35°N a 65°N). Tuttavia le osservazioni di N_2O attualmente disponibili soffrono di carenze strumentali: le colonne di N_2O ottenute dagli strumenti FTIR non presentano una buona risoluzione verticale, e il campionamento temporale e spaziale di ACE-FTS è carente, e amplifica le tendenze alle medie latitudini. D'altro lato le simulazioni dei modelli forniscono buoni risultati riguardo le variazioni di N_2O. Test di sensibilità con il modello BASCOE confermano il ruolo del cambiamento della circolazione stratosferica nel determinare le differenti variazioni emisferiche al di sopra delle regioni extra-tropicali. Al di sopra de Tropici, l'analisi TEM indica che i cambiamenti di N_2O stratosferico sono dovuti principalmente al rafforzamento dell'avvezione residua. Al di sopra delle medie latitudini boreali, le tendenze di N_2O simulate da WACCM sono più forti di quelle ottenute con la maggioranza delle rianalisi o dalle osservazioni di ACE-FTS - quindi questo modello climatico fornisce delle differenze emisferiche più piccole. Ciò indica che il cambiamento climatico ha un effetto differente sulla BDC nei due emisferi, e che questa differenza è più pronunciata nella realtà che in WACCM.

1 Introduction

The present Chapter introduces the most important mathematical, physical and chemical concepts that will be further addressed in this work. Section 1.1 gives a brief but essential overview of the structure of the atmosphere and its governing equations, which will physically lay the ground for the next Sections, together with a short description of the atmospheric composition that is relevant for this thesis. Section 1.2 focuses only on the stratosphere, from its discovery at the beginning of the 20th century to the current techniques to investigate it. Finally, Sect. 2 will provide a comprehensive description of the stratospheric Brewer-Dobson circulation that will drive the reader from the early findings in the late 1920s to the latest scientific production regarding possible man-driven long-term changes.

1.1 The Earth's atmosphere

The Earth's atmosphere (from Greek "atmos": vapor and "sphaira": ball, globe) is a mixture of gases that surrounds the planet and separates the solid Earth from space. The atmosphere is crucial for making life possible in several ways: it allows warm average surface temperatures, shields from most harmful ultraviolet (UV) radiation from the Sun, and drastically reduces temperature differences between night and day. The atmosphere also generates pressure on the Earth's surface that prevents liquid water from becoming water vapor and eventually escaping to outer space.

The atmosphere is divided into several vertical layers based on the temperature profile, which depends mostly on the atmospheric pressure and is determined in large part by the chemical composition. A schematics of this partition is shown in Fig. 1.1.

The lowermost layer, called the *troposphere*, is characterized by decreasing temperatures with increasing height. It accounts for around 85% of the mass of the atmosphere and the majority of the weather phenomena.

The troposphere extends from the surface to a region of minimum temperatures called the *tropopause*. The vertical location of the tropopause depends considerably on the latitude and the season, as it is largely dominated by the processes that happen in the layer underneath it (e.g., deep convection). At the Equator, the tropopause is located around 16 km, while it reaches 8 km at the Poles.

The vertical gradient of temperature in the troposphere is determined by the equilibrium between the radiative cooling and the heat transport (Holton, 2004). In the troposphere, the heat transport is induced by small-scale pro-

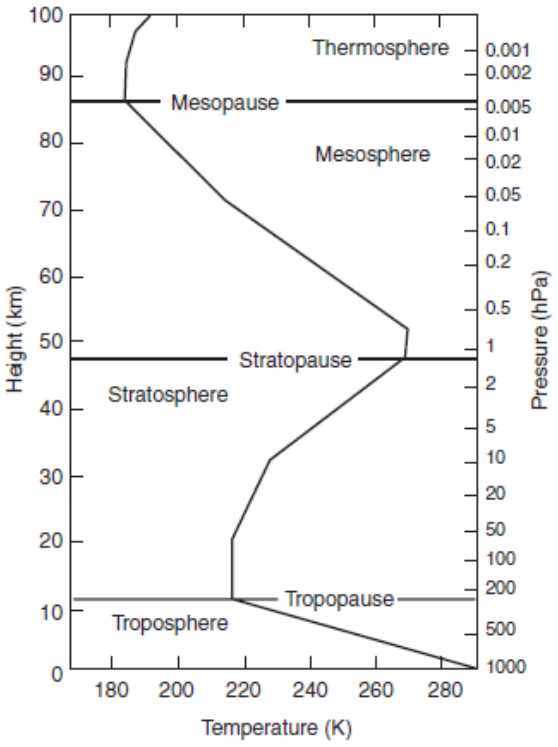

Figure 1.1: Mean temperature at midlatitudes, based on the US Standard Atmosphere. From Holton (2004).

cesses (e.g., transport of sensible and latent heat away from the surface) and large-scale phenomena (e.g., convection, eddies). The net result of these interactions is the negative temperature gradient with increasing altitude shown in Fig. 1.1, with a mean lapse rate of about 6 K km^{-1}. This thermal structure allows convective instability of air masses with air temperature decreasing with height more rapidly than the mentioned lapse rate. This instability does not happen everywhere in the troposphere because the rising air cools adiabatically (i.e., with no heat exchange, see Sect. 1.1.1) with decreasing pressure, but happens in the lowermost layers of the troposphere (Shepherd, 2003).

Above the tropopause, the temperature increases with height until around 50 km. This region is called *stratosphere*, and the boundary region with the layer above is called the *stratopause*. The stratosphere is characterized by large vertical stability because of the increasing temperature with height, which inhibits convection and makes the stratosphere stably stratified, contrarily to the troposphere. In the stratosphere, radiative cooling (i.e., caused by infrared radiation emitted towards space) is mainly balanced by radiative heating due to the absorption of solar UV radiation by ozone. We will not provide further description of the stratosphere in the present Section because, as the stratosphere is the main subject of the entire work, a more detailed description is provided in the next Sections.

The *mesosphere* resides above the stratopause and extends up to approximately 85 km above the surface. In this region, the temperature decreases with height because of the decreased absorption of UV solar radiation compared to the lower layers, and the increased radiative cooling. At the top of the mesosphere, the *mesopause*, temperatures are the coldest of the Earth's atmosphere, reaching values as low as 100 K, with very large seasonal variations.

Above the mesopause, the temperature increases again with height because of the absorption of solar UV radiation by O_2, O and N at very short wavelengths. This layer of increasing temperature is called *thermosphere*, and extends from 85-90 km to between 500 and 1000 km above the surface. In the thermosphere, the air density is so low that molecular diffusion separates the gaseous species depending on their molecular mass, so heavier compounds reside mostly in the lower thermosphere and lighter compounds (e.g., atomic hydrogen) in the upper thermosphere.

After this description of the vertical structure of the atmosphere, the Section is structured as follows. Section 1.1.1 defines some basic quantities and relationships that characterize the atmosphere. Section 1.1.2 is devoted to a general description of the atmospheric composition. Sections 1.1.3 and 1.1.4 describe the characteristics in the atmosphere of the greenhouse gases

in general and of nitrous oxide, specifically.

1.1.1 Equations of the static atmosphere

For atmospheric motions defined on weather and climatological length and time scales, the discrete molecular nature can be ignored, and the atmosphere can be considered as a continuous fluid medium. A "point" in the atmosphere is considered as a volume element that is very small compared to the atmospheric volume of air, but still contains a large number of molecules. The physical quantities that characterize the atmosphere (e.g., pressure, temperature, density) are thus assumed to have a unique value for each point of the atmosphere. The corresponding 3-D field variables (e.g., wind components, temperature) and their derivatives are assumed to be continuous functions of space and time. The fundamental laws of fluid dynamics and thermodynamics are then expressed in terms of partial differential equations.

Given the very large diversity of the atmospheric motions and their interactions, the atmospheric system is generally non-linear, and the complete set of partial differential equations governing the atmosphere is very complex (see e.g., Sect. 2.4), and no general solution exists. For an analytic exploration of the problem, several simplifications and approximations must be performed, depending on the phenomenon under investigation. This Section aims to provide a brief overview of the equations governing the atmosphere at hydrostatic equilibrium, i.e., in the absence of motions. For a more exhaustive treatment refer to e.g., Holton (2004) and Brasseur and Solomon (2005).

The thermodynamic state of the atmosphere is determined by the ideal gas law, which relates temperature, density, and pressure (respectively T, ρ and p) as follows

$$p = \rho R T, \tag{1.1}$$

where R is the gas constant for dry air ($R = 287$ J kg^{-1} K^{-1}). In the absence of atmospheric motion, the only forces acting on a generic air volume are the gravity force and the balancing force caused by the pressure gradient (Fig. 1.2). On each unit of area, the gravity exerts a downward force $\rho g dz$, where g is the gravity acceleration and z is the geometric height, which is counteracted by the net pressure force, given as the difference between the upward force across the lower surface of the air volume and the downward force across the upper surface, which is $-dp$.

The equilibrium condition can be thus written as

$$dp/dz = -\rho g, \tag{1.2}$$

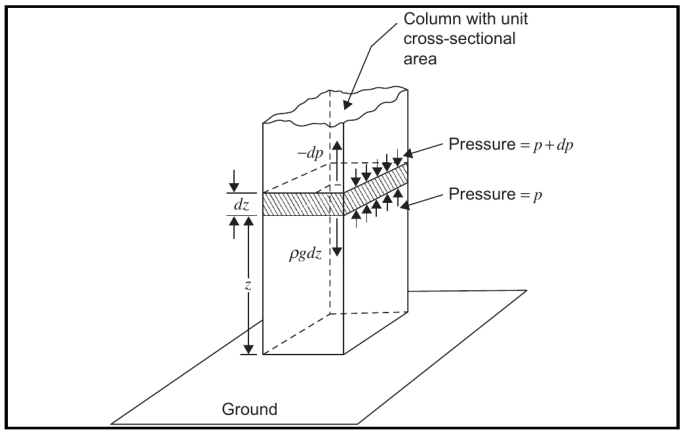

Figure 1.2: Balance of the forces for hydrostatic equilibrium. Small arrows show the upward and downward force exerted by the air pressure on the shaded block. From Holton (2004).

and takes the name of *hydrostatic balance*. This law provides a very good approximation for the vertical structure of the pressure of the real atmosphere and is used thoughout the whole work. The integral of Eq. 1.2 from a certain height z to the top of the atmosphere yields

$$p(z) = \int_z^\infty \rho g \, dz', \tag{1.3}$$

expressing that the pressure at any point is equal to the weight of the air column above that point.

The vertical component of the gravity force g can be generally expressed as the gradient of a potential ϕ: $d\phi/dz = g$, and ϕ takes the name of *geopotential*. If ϕ is zero at the surface, the geopotential at a certain height z is the work required to raise a mass of air to the height z from $z = 0$.

Given the definition of geopotential and the perfect gas law $\rho = p/RT$, we can express the hydrostatic balance as

$$gdz = d\phi = -(RT/p)dp = -RTd\ln p, \tag{1.4}$$

that states that variations of the geopotential with pressure depend only on temperature. Neglecting the decrease of g with z, the integration of Eq. 1.4 gives the *hypsometric equation*:

$$\phi(z_2) - \phi(z_1) = g_0(Z_2 - Z_1) = R \int_{p_2}^{p_1} T \, d\ln p. \tag{1.5}$$

The quantity $Z \equiv \phi(z)/g_0$ is the *geopotential height*, where $g_0 \equiv 9.80665$ m s^{-2} is the global average of the gravity at mean sea level. The hypsometric equation in terms of Z becomes

$$Z_T \equiv Z_2 - Z_1 = R/g_0 \int_{p_2}^{p_1} T \, d\ln p, \tag{1.6}$$

where Z_T is the thickness of the layers between the p_1 and p_2 pressure surfaces. We can then define the mean temperature of this layer as

$$\langle T \rangle = \int_{p_2}^{p_1} T \, d\ln p \left[\int_{p_2}^{p_1} d\ln p \right]^{-1} \tag{1.7}$$

together with a mean height of the layer $H \equiv R\langle T \rangle / g_0$, and, using Eq. 1.6, we have

$$Z_T = H \ln(p_1/p_2). \tag{1.8}$$

Thus, the thickness of a layer bounded by two isobaric surfaces is proportional to the mean temperature of the layer. It also follows that, for an isothermal atmosphere of temperature T, the geopotential height is proportional to the logarithm of the pressure normalized by the surface pressure p_0

$$Z = -H \ln(p/p_0). \tag{1.9}$$

As a consequence, the pressure decreases exponentially with geopotential height as

$$p(Z) = p(0)e^{-Z/H}. \tag{1.10}$$

Many atmospheric processes can be considered as *adiabatic*, i.e., do not involve any heat exchange between the considered air volume and the surrounding atmosphere. For an ideal gas that undergoes an adiabatic process, the first law of thermodynamics can be written as

$$c_p dT - \alpha dp = 0, \tag{1.11}$$

where $\alpha = 1/\rho$ is the specific volume and $c_p = 1004$ J K^{-1} kg^{-1} is the specific heat of dry air at constant pressure. Using Eq. 1.1, we can re-write Eq. 1.11 as

$$c_p d\ln T - R d\ln p = 0. \tag{1.12}$$

Integrating this equation from pressure p, with temperature T, to pressure p_s, with temperature θ, and taking the antilogarithm, we have

$$\theta = T(p_s/p)^{R/c_p}. \tag{1.13}$$

The temperature θ in Eq. 1.13 is called *potential temperature*, and is the temperature that a parcel of dry air at pressure p and temperature T would have if it were compressed adiabatically to p_s (usually taken as 1013.25 hPa). Unlike temperature, potential temperature is, by definition, conserved for adiabatic motions; hence θ is often preferred to T for describing the thermodynamic state of the atmosphere. For example, the sign of the vertical gradient of potential temperature is used to measure the static stability of the atmosphere. Considering an air parcel that is moved away from its initial position, we have three possibilities. For $\partial\theta/\partial z > 0$, it can be shown that the atmosphere is statically stable, i.e., the air parcel will oscillate about its initial position with frequency N (called buoyancy or Brunt-Väisälä frequency); if $\partial\theta/\partial z < 0$ the atmosphere is statically unstable, and the displacement will increase exponentially: the air parcel will develop instability (i.e., convection); if $\partial\theta/\partial z = 0$, the atmosphere is statically neutral, and the air parcel will not undergo any further displacement.

1.1.2 Atmospheric composition

Before describing the composition of the atmosphere, it is useful to define the chemical units that will be used in this work. We first start with the definition of *mole*. A mole is the basic unit of the amount of substance (e.g., electrons, atoms, molecules) in the International System of Units and is defined as $6.02214076 \times 10^{23}$ particles. We continue with the definition of *mixing ratio* (or *mole fraction*) C_X. The mixing ratio of a gas X is the number of moles of X per moles of air and is expressed in mol/mol. Since the number of particles in an ideal gas is proportional to the occupied volume, we can consider the volume of gas per volume of air, which is referred to as *volume mixing ratio* (vmr) and is expressed in parts per volume (ppv).

The atmosphere is composed by a large number of gases, the most abundant are the molecular nitrogen (N_2) at 78% of the total volume of air, molecular oxygen (O_2) at 20%, argon (Ar) at 0.9% and carbon dioxide (CO_2) at 0.03%. Together, these four gases account for 99.99% of the total volume of the air. The remaining 0.01% of air volume is composed of a multitude of gases that are called *trace gases* because of their very low abundances. Nonetheless, trace gases are extremely important because of their high reactivity and the consequent impacts on the atmospheric system (e.g., ozone). Since other constituents have very small abundances in the atmosphere, it

is convenient to express volume mixing ratios in parts per million by volume (ppmv=ppv$\times 10^{-6}$), parts per billion by volume (ppbv=ppv$\times 10^{-9}$), and parts per trillion by volume (pptv=ppv$\times 10^{-12}$).

The *number density* n_X of a gas X is defined as the number of molecules per unit volume of air and is expressed in molecules cm^{-3}. The integral of the number density along the vertical coordinate provides the *column abundancies*, which are expressed in molecules m^{-2} or cm^{-2}. If the vertical integral encompasses the whole atmosphere, we will refer to a *total column*, while, if the integral is limited between two fixed levels (e.g., in the stratosphere), to a *partial column*. For ozone, the column abundances are often expressed in Dobson units (DU). One DU corresponds to the height of an ozone column if the gas were at standard temperature and pressure and is equivalent to 2.687×10^{16} molecules cm^{-2}.

The composition of the atmosphere is well-known thanks to a large number of observations of the concentration of many important gases. The local surface sources of the atmospheric species are related to biological activity, volcanic eruptions and human activities. Some of the species emitted in the troposphere are destroyed there through biological, chemical or physical processes. Other species can be transported upwards, reaching the stratosphere, where they can undergo chemical interactions and long-range transport.

In the following, we shall focus on a few aspects of atmospheric chemistry relevant to the present work. Section 1.1.3 explains what the *greenhouse effect* is and gives an overview of the gases that cause it. Greenhouse gases play a major role in determining the thermal equilibrium of the atmosphere, and their increase causes climate change, which also affects the stratosphere. In addition, nitrous oxide itself is a greenhouse gas. Section 1.1.4 describes the most relevant chemical properties of nitrous oxide and highlights the importance of the chemical phenomena involving it. The interested reader is referred to the Brasseur and Solomon (2005) and Jacob (1999) for a more detailed treatment of atmospheric chemistry, and to Tuckett (2019) for a brief but effective and generic review of the current research concerning greenhouse gases.

1.1.3 Greenhouse gases

The most important characteristic of greenhouse gases is their interaction with infrared radiation and its consequences. For this reason, we shall first overview the basic concepts of radiation in the atmosphere in Sect. 1.1.3.1. Second, we will outline the role of greenhouse gases in maintaining the Earth's average temperature at the values currently measured in Sect. 1.1.3.2, and, last, we will describe the well-known greenhouse effect in Sect. 1.1.3.3.

1.1.3.1 Radiation basics

The primary heat source for the Earth system is solar energy, which is transmitted to the Earth by radiation and converted to heat. In order to balance this energy input, the surface of the Earth must emit radiation too, which can either be trapped in the atmosphere, releasing heat (warming the atmosphere), or travel directly towards space. Air masses also emit radiation, thereby cooling the atmosphere.

Radiation is energy transmitted by electromagnetic waves. A charged particle oscillating with frequency ν induces an electromagnetic field propagating at the speed of light $c = 3\times10^8$ m s^{-1}. The oscillating electromagnetic field is an electromagnetic wave with wavelength $\lambda = c/\nu$ that carries energy $E = h\nu = hc/\lambda$ (where h=6.626$\times10^{-34}$ J is the Planck constant) and induces oscillations on the charged particles that it encounters.

A typical object does not generally emit radiation at a single frequency, but over a range of frequencies hence over a range of wavelengths, defining the frequency and wavelength spectra. It is useful to define now the *radiation flux* Φ_λ, which measures the amount of radiation per unit surface that is received by a generic object at a certain wavelength λ, with units W m^{-2}.

An idealized object that can absorb or emit radiation at all wavelengths with 100% efficiency is called a *blackbody*. At the beginning of the 20th century, the German physicist Max Planck showed that the radiation flux Φ^b_λ emitted by a blackbody depends only on the wavelength λ and its temperature T

$$\Phi^b_\lambda = \frac{2\pi hc^2}{\lambda^5(exp(\frac{hc}{kT\lambda}) - 1)}, \tag{1.14}$$

where k=1.38$\times10^{-23}$J K^{-1} is the Boltzmann constant. The important properties of a blackbody are: 1) the total radiation flux (i.e., the integral of Φ_λ over all the wavelengths) is $\Phi_T = \sigma T^4$, where σ=5.67$\times10^{-8}$ is the Stefan-Boltzmann constant; 2) the emission of radiation peaks at a wavelength λ_{max} that is proportional to the inverse of the temperature: $\lambda_{max} \propto$1/T. The blackbody approximation can be extended to a generic object using Kirchhoff's law: if an object absorbs radiation at wavelength λ with an efficiency ε_λ, then it emits radiation of that wavelength at a fraction ε_λ of the corresponding blackbody emission at the same temperature. Thus, for any object, the emission spectrum is

$$\Phi_\lambda(T) = \varepsilon_\lambda(T)\Phi^b_\lambda(T). \tag{1.15}$$

Figure 1.3 shows the radiation spectra $\Phi_\lambda(T)$ for the Sun and the Earth. The solar radiation peaks in the visible range (VIS, 0.4$<\lambda<$0.7 μm) and is

maximum in the green ($\lambda = 0.5$ μm). A large part of the total solar radiation is at infra-red wavelengths (IR, λ >0.7 μm), and a small fraction is in the ultraviolet (UV, λ <0.4 μm).

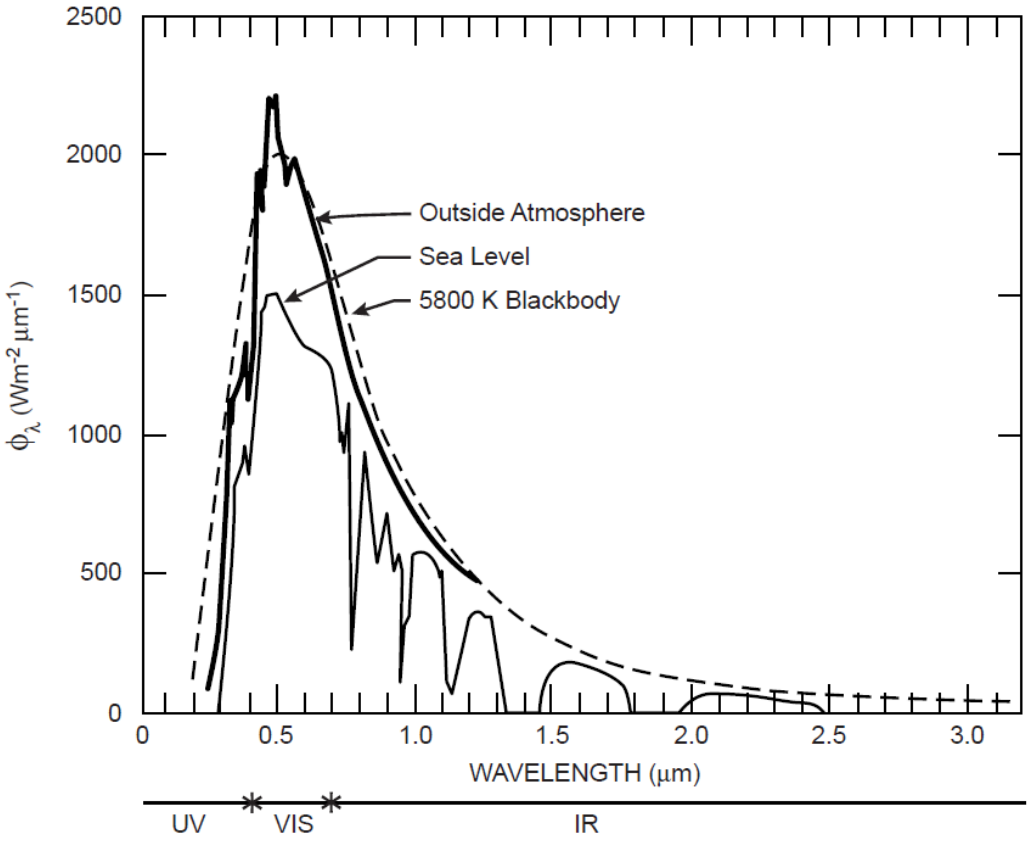

Figure 1.3: Solar radiation spectra measured from a satellite outside Earth (bold), at sea level (thin) and the spectrum of a blackbody at 5800 K (dashed). From Jacob (1999).

Note that the solar radiation at sea level is weaker than at the top of the atmosphere. This difference is the consequence of the absorption and scattering by clouds, other aerosols and atmospheric gases (e.g., oxygen and ozone in the UV and water vapor in the IR). Contrarily to the Sun, the Earth significantly emits only in the IR (5-20 μm) because our planet is not sufficiently hot to emit radiation at shorter wavelengths (recall that $\lambda_{max} \propto 1/T$). The Earth's radiation spectrum Φ^b_λ at the top of the atmosphere is shown in Fig. 1.4. Φ^b_λ moves away from the blackbody curve at, e.g., 320 K for several wavelength windows (e.g., around 15 μm). This is a crucial factor for the terrestrial heat balance, which means that the radiation emitted by

the Earth is absorbed by the atmosphere for those wavelength windows. In particular, the gases that are responsible for this absorption are highlighted in Fig. 1.4.

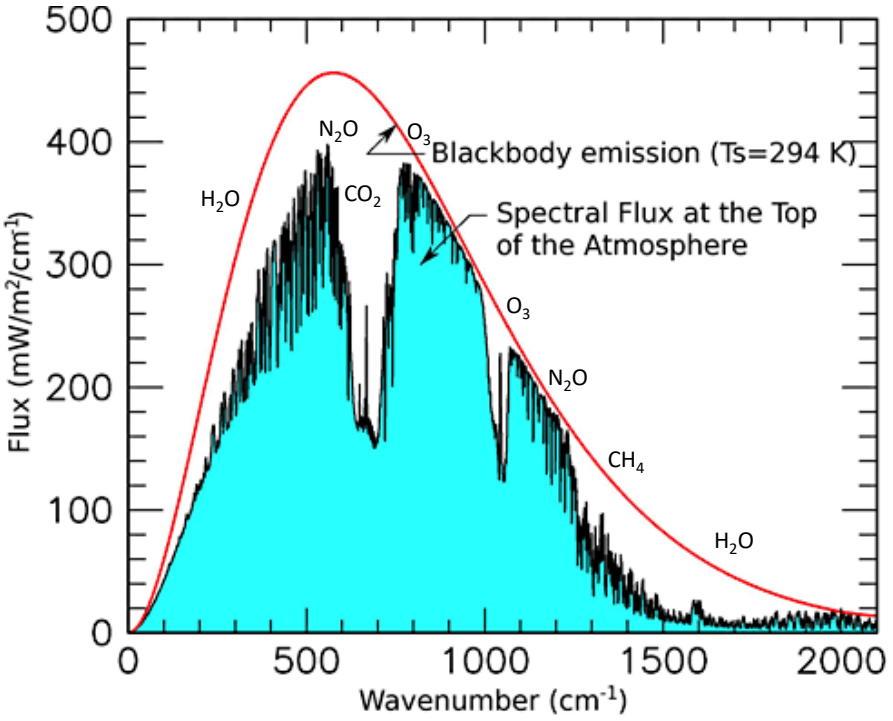

Figure 1.4: Outgoing spectral radiance at the top of Earth's atmosphere showing the absorption at specific frequencies and the principle absorber. The red curve shows the flux from a classic "blackbody" at 294°K. Adapted from `https://www.giss.nasa.gov/research/briefs/2010_schmidt_05/`.

1.1.3.2 The surface temperature of the Earth

In order to maintain the Earth system stable, there must be energy equilibrium between the incoming solar radiation and the radiation emitted by the Earth as displayed in Fig. 1.4. We can find the temperature corresponding to this equilibrium by equating the energy coming from the Sun and the energy emitted by the Earth.

The solar radiation flux outside the Earth (i.e., at the top of the atmosphere) has been measured as $F_s = 1368$ J s^{-1} m^{-2}, and is the solar constant of the Earth. Neglecting the absorption by the atmosphere, it can be shown that the mean solar flux per unit area reaching the Earth's surface

is $F_s(1-A)/4$, where A is the planetary albedo, i.e., the fraction of incoming radiation that is reflected to space (0.28 for the whole Earth).

While the absorption efficiency $\varepsilon_\lambda(T)$ of visible radiation for the Earth is around 0.7, it is close to the unity for IR radiation (Jacob, 1999). Thus, the radiation emitted from the Earth's surface in the IR window can be approximated by blackbody emission at temperature T_E, so that the equilibrium would result in

$$\frac{F_S(1-A)}{4} = \sigma T_E, \tag{1.16}$$

that can be rearranged to yield the effective temperature of the Earth's surface

$$T_E = \left[\frac{F_S(1-A)}{4\sigma}\right]^{1/4}. \tag{1.17}$$

Substituting numerical values, the average effective temperature of the Earth's surface is T_E =255 K. This value is considerably lower than the average observed value of T_E =290 K. The reason for this large difference is the presence of *greenhouse gases* (GHGs) in the Earth's atmosphere and is explained in the next Section 1.1.3.3.

1.1.3.3 The greenhouse effect

Before indicating the role of GHGs in maintaining the average Earth's surface temperature at around 290 K, it is necessary to provide some basic knowledge of the radiative properties of the atmospheric gases.

A gas molecule absorbs radiation of a particular wavelength only if that energy can change the energy level of the molecule. The molecule will thus change in either translational (not considered here), rotational, vibrational or electronic state. These transitions between states obey quantum mechanics rules and, albeit very interesting, will not be treated here. The energy associated with the electronic transition is generally in the UV and VIS range (λ <0.4 μm), while the energy required for vibrational transitions is smaller, in the near-IR (0.7< λ <20 μm). For rotational transitions, the required energy is even smaller and corresponds to wavelengths in the far-IR (λ <20 μm).

We will not cover the electronic transitions, as they are not relevant for the greenhouse effect, but we will briefly discuss vibrational and rotational transitions. Vibrational transitions can occur if the radiation interacts with a molecule that, by vibrating, can create an electric dipole moment. Rotational transitions can occur only for heteronuclear molecules and are often

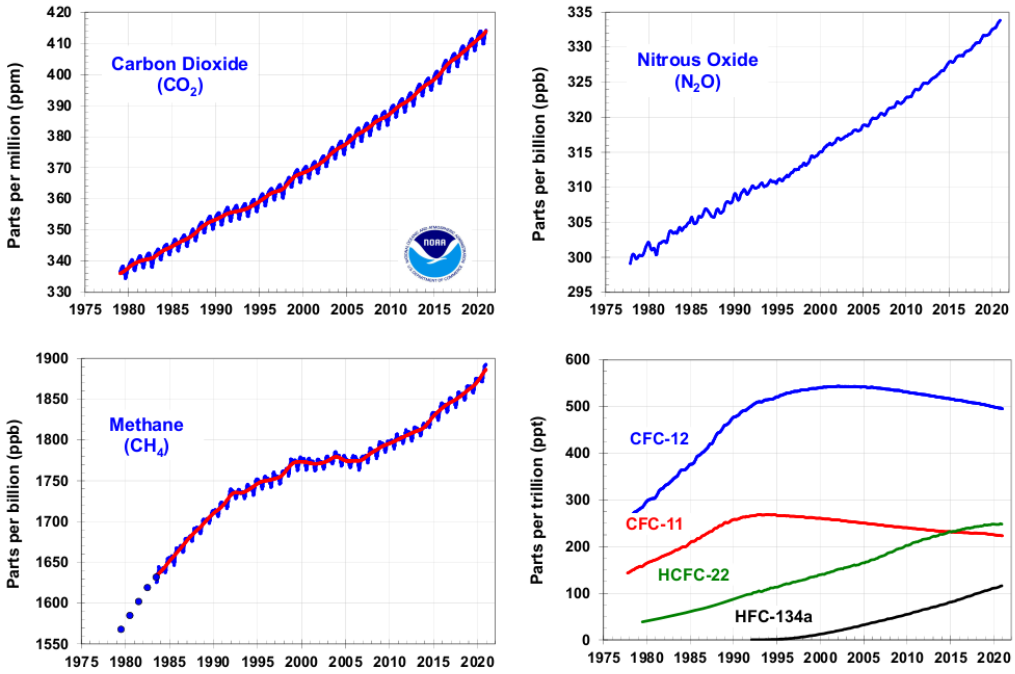

Figure 1.5: Global average abundances of the major, well-mixed long-lived GHG: CO_2, CH_4, N_2O and two chlorofluorocarbons (CFCs). Also shown are HCFC-22 ($CHClF_2$) and HFC-134a (CF_3CH_2F), two halogenated gases that have a smaller contribution to the greenhouse effect. From National Oceanix and Atmospheric Administration (NOAA, `https://gml.noaa.gov/aggi/aggi.html`).

combined with vibrational transitions, creating the so-called vibro-rotational transitions.

In general, molecules that can absorb in the IR window and obtain a charge asymmetry from roto-vibrational transitions are greenhouse gases. By Kirchhoff's law (Sect. 1.1.3.1), a body can re-emit only the radiation that it absorbs. When GHGs absorb the IR radiation emitted by the Earth's surface (Fig. 1.4) and undergo roto-vibrational transitions, they re-emit IR radiation back towards the Earth's atmosphere, thereby increasing its temperature. Thus, The IR absorption by atmospheric GHGs explains why the average surface temperature on Earth is 290 K and not the 255 K obtained only by radiative equilibrium in Sect. 1.1.3.2. This mechanism is often referred to as *primary greenhouse effect*. Examples of GHGs are carbon dioxide (CO_2), water vapor (H_2O), methane (CH_4), nitrous oxide (N_2O), molecular ozone (O_3), sulfur hexafluoride (SF_6) or cholofluorocarbons (CFCs). The main driver of the primary greenhouse effect is water vapor because it is the most abundant GHG in the atmosphere and has numerous IR absorption features. The next most abundant GHG is CO_2, which absorbs most at 15 μm, i.e., very close to the peak of Earth's blackbody curve, explaining why carbon dioxide has a large impact on the primary greenhouse effect.

If the concentrations of GHGs had remained constant in time, there would be no concern about the greenhouse effect as we know nowadays, as GHGs would just keep the average Earth's temperature at around 290 K through the primary greenhouse effect. Unfortunately, GHGs, notably CO_2, CH_4 and N_2O (as well as O_3 to a lesser extent) have increased during the last around 270 years, i.e., since the start of the Industrial Revolution (Fig. 1.5). Changes in concentrations of those GHGs, together with the appearance of man-made GHGs (e.g., CFCs), cause the so-called *secondary greenhouse effect* in this relatively short period, leading to the well-known temperature rise and to one of the major modern-day issues: the *global warming* (Houghton, 2005; Harvey, 2018). For example, CO_2 has increased from 280 ppmv to the current 400 in the past 270 years (43% increase). As a consequence of the secondary greenhouse effect on this short period, the average temperature of the planet has increased by about 0.8-1.1 K over the same period (Tuckett, 2019).

In the following, we describe a rough method to quantify and compare the radiative forcings of different GHGs; for a more precise treatment, see, e.g., Stocker et al. (2013). In order to quantify the climate impact of GHGs, it is necessary to consider several chemical and physical properties of a gas molecule. For example, the lifetime of a trace gas plays a major role: the longer the lifetime, the longer the GHG will remain in the atmosphere and will have a larger contribution in warming the atmosphere. It is helpful to summarize the major warming characteristics of GHGs into a dimension-

less number, the global warming potential (GWP). It measures the radiative forcing A_X (i.e., the change in the radiative flux caused by natural or anthropogenic factors) of a pulse emission of a GHG X over a certain time period t, relative to the time-integrated radiative forcing of a pulse emission of an equal mass of CO_2 (Tuckett, 2019)

$$GWP_X(t) = \frac{\int_0^t A_X(t)dt}{\int_0^t A_{CO_2}(t)dt}. \tag{1.18}$$

Since the GWP is calibrated to CO_2, its GWP value is 1. The GWP quantifies how important a molecule X is to global warming via the secondary greenhouse effect compared to a molecule of CO_2. A molecule with large GWP has strong IR absorption in windows where the primary GHGs such as CO_2 do not absorb, long lifetime, and is increasing rapidly due to anthropogenic activity (Table 1.1).

GHG	CO_2	O_3	CH_4	N_2O	SF_6	CF_2Cl_2
Lifetime (1) [years]	50-200	days-weeks	12	121	3200	100
GWP (1) [ ]	1	//	28	265	23500	10,200
Radiative efficiency (1) [W m^{-2} ppbv^{-1}]	1.37×10^{-5}	3.33×10^{-2}	3.63×10^{-4}	3.0×10^{-3}	0.57	0.32
Total radiative forcing (1,2) [W m^{-2}]	1.82	0.35	0.48	0.17	4.1×10^{-3}	0.17
Concentration (2018) [ppmv]	400	0.034	1.80	0.32	5.6×10^{-6}	0.0005
Change in oncentration (1748-2018) [ppmv]	120	0.009	1.08	0.05	5.6×10^{-6}	0.0005

Table 1.1: Six examples of secondary greenhouse gases and their contribution to global warming. (1) Data from the latest IPCC AR5 report published in 2013 (Stocker et al., 2013), although the data quoted are only accurate up to 2011. (2) Due to the change in concentration of long-lived GHG from the preindustrial era to the present time. Adapted from Tuckett (2019).

Another parameter that characterizes the IR absorption of a GHG is the radiative efficiency a_0, which measures the strength of the absorption of a GHG integrated over the IR window. It is usually expressed in W m^{-}2 ppbv^{-1}, and, if multiplied by the change in concentration of the GHG over a specific time, we obtain a rough estimation of the radiative forcing in W m^{-2} (Table 1.1).

From Table 1.1, the total radiative forcing for the majority of long-lived GHGs is 2.99 W m^{-2}, with CO_2 and CH_4 together contributing to more than 70% to the total radiative forcing (Table 1.1). H_2O does not significantly impact the secondary greenhouse effect, even though it is the most abundant GHG in the atmosphere and the main driver of the primary greenhouse effect. This is because water vapor is not a long-lived gas (its average lifetime is a few days), and because it is not well-mixed: its concentrations vary between 0-3% over the planet and have not changed significantly over the last centuries.

CO_2 is naturally emitted in the biosphere and in the oceans, but anthropogenic combustion-based processes have considerably altered its abundances, reaching approximately 419 ppmv in May 2021 (NOAA, `https://research.noaa.gov/article/ArtMID/587/ArticleID/2764/Coronavirus-response-barely-`
The prominent seasonality in Fig. 1.5 is due to the large seasonal cycle in the absorption of CO_2 by vegetation (decrease in spring and summer and increase in fall and winter) combined with the hemispheric asymmetry of landmasses.

Methane (CH_4) has increased by around 150% since preindustrial times, faster than CO_2, and is the second most important secondary GHG after carbon dioxide. Methane is naturally released through biological processes (e.g., swamps), but anthropogenic activities, such as growing rice, raising cattle and using natural gas, have taken the lead in producing this GHG.

O_3 and N_2O have smaller increase rates than CO_2 and CH_4 over the same period. Tropospheric ozone results mainly from the action of sunlight on carbon and nitrogen-containing molecules, which are mostly emitted by anthropogenic activities such as transport or industry. For this reason, the largest concentrations are found near urban areas and are an important contribution to smog. O_3 has the third highest total radiative forcing, even though in the stratosphere the forcing is negative (IR cooling) because the reduced density leads to emission prevailing over absorption. N_2O has the fourth total radiative forcing and will be discussed in detail in the next Section.

Dichloro-difluoromethane (CF_2Cl_2) is one of the most common CFCs. These anthropogenic compounds have increased from zero in preindustrial times to around 0.9 ppbv today, and are now decreasing thanks to the implementation of the Montreal Protocol (Velders et al., 2007). SF_6 is a long-lived gas that is used primarily as an electrical insulator, with currently very low concentrations, but with very high increase rates and lifetime (Table 1.1).

Considering their relative low GWP, one may wonder why there is great concern about CO_2 and CH_4, compared to other GHGs in Table 1.1. The reason is simply that, together with the GWP, the rate of increase of the gas plays a significant role in the secondary greenhouse effect. CO_2 and CH_4 are of great concern because they have been considerably increasing since the Industrial Revolution, while, e.g., SF_6 has a smaller secondary greenhouse effect because its concentrations are still very low, despite its large GWP value.

Despite some small changes in the values in Table 1.1 since 2018, the big picture does not change: CO_2 and CH_4 are responsible for 80-85% of the secondary greenhouse effect, hence the observed climate change, with the contribution from CO_2 three and a half times larger than that from CH_4.

The continuous increase of GHGs has raised concern in the scientific community and policymakers, which led to a number of international agreements in order to stabilize and reduce the emissions of such compounds. One of the most famous is probably the Kyoto Protocol adopted in 1997 and ratified in 2005. The Protocol sets targets for the reduction of GHGs emissions, which add up to an average 5% reduction compared to 1990 levels over the 2008-2012 period (United Nations Framework Convention on Climate Change , UNFCCC). In 2012, the Doha Amendment was adopted and entered into force at the end of 2020, setting up new commitments for the coming period and modifications of the Kyoto Protocol when needed `https://unfccc.int/process/the-kyoto-protocol/the-doha-amendment`. The most ambitious international treaty on climate change is probably the Paris agreement, which was signed in 2015 by more than 190 nations. The goal of the Paris agreement is to limit global warming below 2°C compared to preindustrial levels by achieving carbon neutrality by mid-century (`https://unfccc.int/sites/default/files/english_paris_agreement.pdf`).

1.1.4 Nitrous oxide in the atmosphere

Nitrous oxide (N_2O) is the fourth most important GHG on the planet (see Sect. 1.1.3.3), and also an ozone-depleting substance in the stratosphere (see Sect. 1.2.6). N_2O is produced in the troposphere through both natural and anthropogenic processes. Its abundancies increased continuously by more than 20% from 270 ppbv in 1750 to 331 ppbv in 2018, and, given its important role in the greenhouse effect, the anthropogenic N_2O emissions have been reported annually by the UNFCC (Tian et al., 2020).

The N_2O global budgets have been updated during the past years because of the uncertainties arising from both natural (role of the oceans) and anthropogenic sources (agriculture) (Syakila and Kroeze, 2011). The recent study of Tian et al. (2020) provided a global comprehensive N_2O budget that includes 18 sources and sinks (Fig. 1.6). Those sources and sinks can be categorized into six groups: 1) natural sources, including a very limited biogenic sink; 2) perturbed fluxes from natural ecosystems induced by changes in climate, CO_2 and land cover; 3) direct emissions from nitrogen additions in the agricultural sector; 4) other direct anthropogenic sources, such as fossil fuel and industry, waste and wastewater, and biomass burning; 5) indirect emissions from ecosystems that are downwind (downstream) from the initial release of reactive nitrogen into the environment; 6) atmospheric chemical sinks. Natural and anthropogenic emissions of N_2O are more prominent in the Northern Hemisphere, as a result of the more extensive land coverage. Among the different sources of N_2O, the current increase (see Fig. 1.5) is

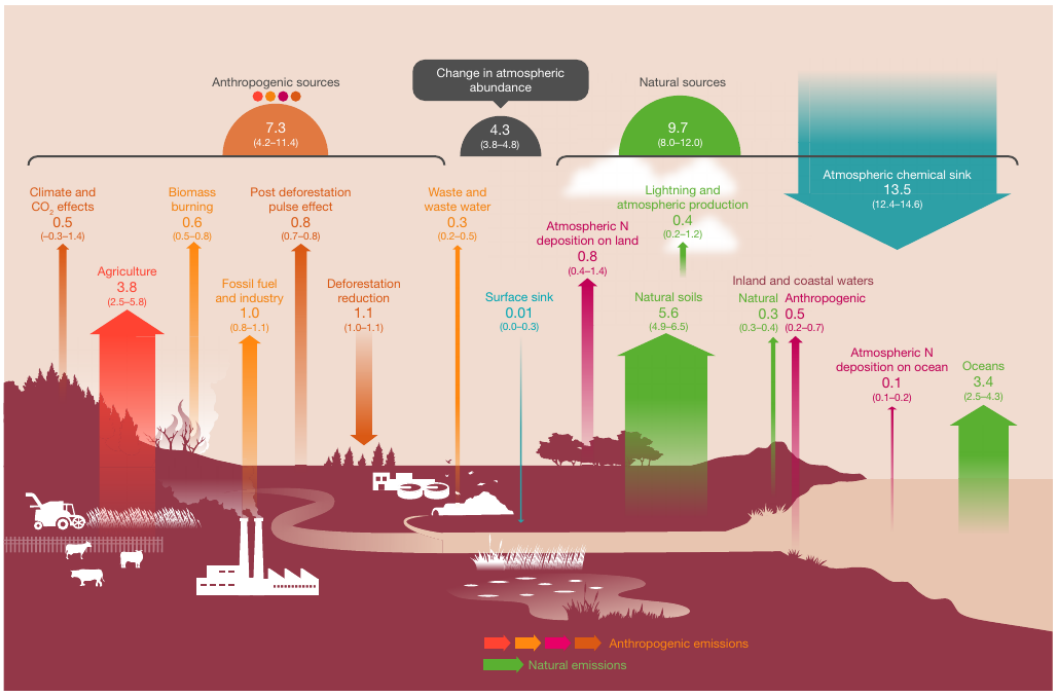

Figure 1.6: Global N_2O budget for the 2007-2016 period. The coloured arrows represent N_2O fluxes (in Tg N year^{-1}). Upward arrows indicate emissions, downward arrows indicate sinks. From Tian et al. (2020).

mainly due to the agricultural sector and is expected to increase in response to the growing world population (Tian et al., 2020).

N_2O does not have significant sinks at the surface (Fig. 1.6): its losses reside in the troposphere and especially in the stratosphere. N_2O reacts with the excited oxygen atom in the $O^1(D)$ state via two possible chemical reactions

$$N_2O + O^1(D) \longrightarrow 2\,NO \tag{1.19}$$

and

$$N_2O + O^1(D) \longrightarrow N_2 + O_2. \tag{1.20}$$

Reaction 1.19 is important also for the ozone budget, because the reaction of nitrous oxide with $O^1(D)$ yields two molecules of NO (Crutzen, 1970), which catalytically destroy ozone in the stratosphere (for more details, see Sect. 10.2.2 of Jacob, 1999). After the implementation of the Montreal Protocol, phasing out CFCs, N_2O became the single most important ozone-depleting compound and is expected to remain the largest contributor to the ozone depletion throughout the 21st century (Ravishankara et al., 2009).

In the stratosphere, N_2O is mainly destroyed by photolysis with UV radiation with typically $\lambda < 0.2$ μm

$$N_2O + h\,\nu \longrightarrow N_2 + O^1(D). \tag{1.21}$$

A production reaction of N_2O also takes place in the stratosphere

$$N_2 + O^1(D) + M \longrightarrow N_2O + M \tag{1.22}$$

but is extremely slow, thus not significant (Brasseur and Solomon, 2005).

The production and destruction processes described above make N_2O a so-called long-lived tracer, as its global estimated lifetime is 166±9 years (Prather et al., 2015), which is often approximated to 120 years (Brasseur and Solomon, 2005). Due to this very long lifetime, the distribution of N_2O in the stratosphere is primarily determined by transport, making it an excellent tracer to study transport processes in the stratosphere.

1.2 The Stratosphere

The present Section is devoted to the discussion of the stratosphere and its many peculiarities. Section 1.2.1 summarizes decades of active research in the past centuries regarding the discovery of the stratosphere. Section 1.2.2 reviews the mean wind and temperature structure of the stratosphere, and

Section 1.2.3 introduces the stratospheric circulation, which will be further developed in the following Sections. Section 1.2.4 gives an overview of the different tropospheric waves that drive the stratospheric circulation. Section 1.2.5 introduces those stratospheric features that are considered in the continuing of this work. Section 1.2.6 reviews the stratospheric ozone, together with the well-known *ozone hole* phenomenon. Lastly, Section 1.2.7 presents some methods of observing and modelling the stratosphere.

1.2.1 Discovery of the stratosphere

The stratosphere accounts for roughly 15% of the mass of the atmosphere, and we know nowadays how crucial it is in terms of dynamics, chemistry and transport for the whole Earth system. Nevertheless, its existence was unknown before the 20th century. Thanks to temperature and pressure measurements in the mountains, the well-known temperature decrease in the troposphere was already known before the 20th century. Those measurements yielded the simple rule that the temperature would decrease with height by about 0.7 K per 100 m, which would lead to absolute zero temperature at around 30 km. The scientific community was then very motivated to explore the upper atmosphere and reveal its actual temperature, but the efforts were limited mainly by the technological capabilities of that time, which unfortunately led also to casualties.

The first reliable balloon soundings of temperature and pressure were carried out at the end of the 19th century. One of the first sounding balloons, launched in November 1896 by the Frenchman Leon Teisserenc de Bort in Paris, reached around 14 km and measured constant temperature between 12 and 14 km, corresponding to the tropopause. At that time, it was believed that the measured temperature decrease in the troposphere extended to the whole atmosphere; therefore, the measured isothermal profile was considered an error and corrected (Hoinka, 1997).

In the following years, Teisserenc de Bort performed several more soundings and, in 1902, with a total of 236 soundings, he published his results (Teisserenc de Bort, 1902). He explicitly mentioned the existence of an "isothermal zone", and stated "[...] starting with an altitude that varies between 8 and 12 kilometers, according to the atmospheric condition, there begins a zone characterized by a very small rate of diminution of temperature, or even by a slight increase, with alternations of cooling and warming. We are not able to state precisely the thickness of this zone, but, according to the observations already made, it would seem to amount to at least several kilometers. This is a fact of which we were ignorant up to the present time, and it deserves to be taken into very serious consideration in the study of the

general circulation. I ought to add that these results are not in agreement with many previous conclusions that had been based upon very insufficient evidence [...]" (Hoinka, 1997). Teisserenc de Bort named this isothermal layer *the stratosphere* because of the absence of vertical motions (stratification), and, in contrast, he named the layer underneath *the troposphere*.

In the same period and independently from Teisserenc de Bort, the german scientist Richard Assmann published very similar results (Assmann, 1902). Using 6 balloon ascents made in Berlin, he declared that he obtained proof of an "upper atmosphere warm air current". He also doubted the results of Teisserenc de Bort, particularly the measurement techniques used by the French scientist, also stating that his measurement technique should be used instead. Most importantly, Assmann went a step further compared to Teisserenc de Bort. While the French scientist only mentioned an "isothermal layer", the precursor of the tropopause, Assmann proposed the existence of increasing temperatures and the existence of a warmer flow, which is the first identification of the stratosphere. Assmann also tried to discuss the causes of this "warm flow". Interestingly, he hypothesized the existence of a large-scale circulation, characterized by warm air rising above the tropical oceans and moving poleward, while maintaining its warmer temperature compared to the layers below (from the English translation of Assmann, 1902, `https://www.en.meteo.physik.uni-muenchen.de/~Thomas.Birner/papers/assmann.pdf`). This very primitive and simplified description resembles the pattern of the stratospheric circulation as we know it today (see Sect. 2). It is fascinating that a scientist from the beginning of the 20th century came up with such an evocative theory, even though Assmann himself declared it premature, and we currently know that convection is not the reason for the temperature structure in the stratosphere.

The decades following these discoveries thrived with scientific advances with respect to atmospheric dynamics. Experiments worldwide were carried out to understand whether the thermal inversion was a local or global phenomenon. Meteorologists of that time understood how important was the vertical structure in the atmosphere; hence, the use of balloon soundings was largely encouraged.

However, for the first 20 years of the 20th century, the atmosphere was still considered as composed of the troposphere and a nearly-isothermal layer above it, extending for several kilometers. This limited knowledge was the consequence of the very limited capability of the soundings at the time: at the beginning of the second decade of the 20th century, the balloons rarely reached 25 km.

Only at the beginning of the 1920s did Lindemann and Dobson (1923) report the existence of increasing temperatures in the stratosphere. Based

on meteor observations, they developed a theory to estimate the atmospheric density in the upper layers from the characteristics of the meteors at those layers. They stated that "Between 60 and 160 km [...] meteor observations [...] indicate densities very much greater than those calculated on the assumption of a uniform air temperature of 200K but consistent with a considerably higher temperature". The following decades were characterized by additional indirect determination of upper atmospheric temperatures (above the balloon limit) using acoustic measurements as well as observations of aurora emissions (Paneth, 1939).

Due to the invention of the V-2 rocket during World War II, sounding rockets became available to explore the upper atmosphere. Temperature profiles were calculated from the slope of the pressure-altitude curve and the ratio between the pressure exerted on the rocket and the ambient pressure (Best et al., 1947). These measurements provided a climatological temperature profile that is very close to the modern-day knowledge and revealed the existence of the stratopause and the mesosphere.

In the following decades, technological advancements and refined measurement methods improved the knowledge of the stratosphere. For example, by 1966, meteorological rockets could measure the temperature up to 130 km and provide valuable data to draw solid conclusions about the large-scale circulation in the stratosphere and mesosphere (Webb et al., 1966).

1.2.2 Mean state of the stratosphere

As mentioned in Sect. 1.1, the thermal equilibrium in the stratosphere is primarily maintained through a balance between the infrared radiative cooling and the heating caused by the absorption of UV radiation by ozone, resulting in temperatures that increase with height, and that reach a maximum around the stratopause.

The temperature in the stratosphere depends not only on the height but also on the latitude (Fig. 1.7 left panel). In the lower stratosphere, where the influence from tropospheric processes is strong, there is a minimum at the Equator and maxima at the summer Pole and in the mid-latitudes in the winter hemisphere (see Sect. 1.2.3). Above around 30 km, the temperature decreases uniformly from the summer to the winter pole.

The wind regimes in the stratosphere (Fig. 1.7 right panel) are directly determined by the temperature distribution trough the *thermal wind* equation

$$\frac{\partial u}{\partial z} = \frac{R}{H f_0} \frac{\partial T}{\partial y}, \tag{1.23}$$

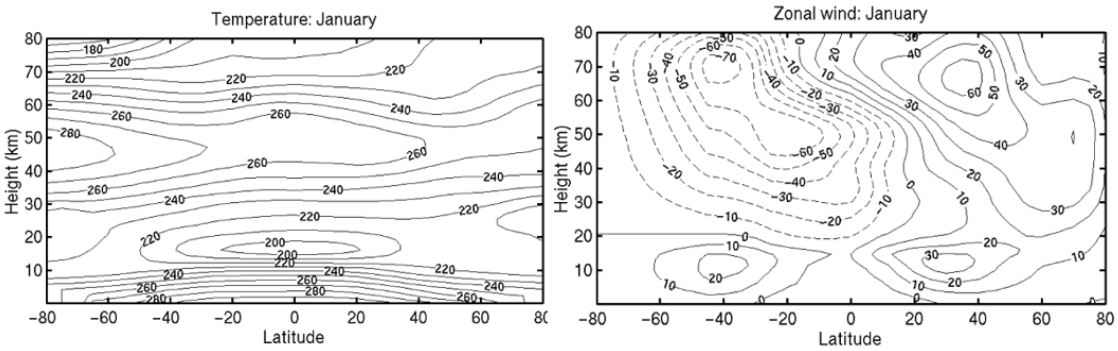

Figure 1.7: Observed monthly and zonally averaged temperature (K, left panel) and zonal wind (m s^{-1}, right panel) for January. From Holton (2004).

that relates the vertical gradient of the zonal wind with the meridional gradient of temperature. In Eq. 1.23, u is the zonal component of the wind, f_0 is the Coriolis parameter (associated to Earth's rotation, see Sect. 2.4.1), and y is the horizontal meridional coordinate (i.e., latitude in spherical coordinates). From the right panel of Fig. 1.7, we notice that, in the mid-upper stratosphere, the main zonal wind pattern is composed by eastward winds (i.e., $u > 0$, *westerlies*) in the winter hemisphere, and by westward winds (i.e., $u < 0$, *easterlies*) in the summer hemisphere. Those wind regimes are often called *jets* and peak in wind speed around 1 hPa (around 70 km, i.e., above the stratosphere). In the lower stratosphere, the wind regimes are characterized by two westerly jets in the subtropics with a larger wind speed in the winter hemisphere.

1.2.3 Stratospheric zonal mean circulation

The zonal wind regimes described in Sect. 1.2.2 are not the only wind patterns in the stratosphere. Meridional and vertical motions (the circulation) are crucial for the dynamical and thermal equilibrium of the stratosphere, and we will see that these motions actually drive the temperature and thus zonal wind depicted in Fig. 1.7. As for the troposphere, one could assume that the meridional and vertical wind regimes in the stratosphere are driven by diabatic heating (like, e.g., for the tropospheric Hadley cell, Holton, 2004). This assumption is incorrect, as the momentum and heat exchange with the troposphere itself must be considered. This Section briefly describes the circulation in the stratosphere and its physical causes.

In order to properly discuss the stratospheric circulation, we must first get back to the temperature structure of the stratosphere (Fig. 1.7) and understand what drives its meridional and vertical distribution. Figure 1.8

shows the temperature distribution in the stratosphere for an idealized model where only radiative processes are considered, i.e., all dynamical forcings from the troposphere are discarded.

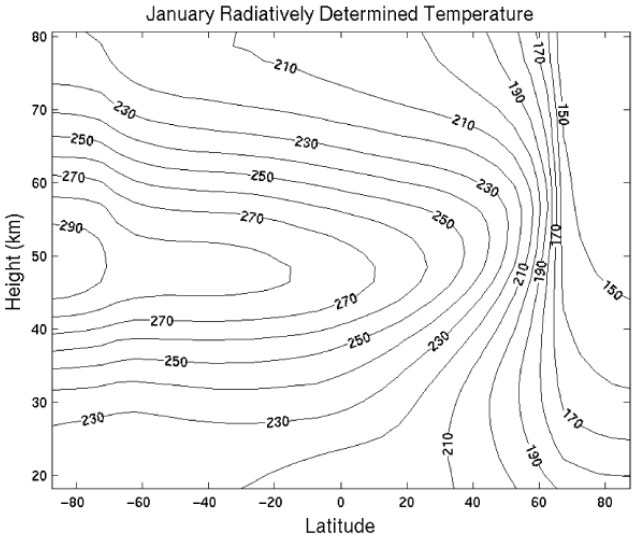

Figure 1.8: Radiatively determined zonal mean temperature of the middle atmosphere from a radiative model for January. From Holton (2004).

In the absence of forcing from below, the temperature in the stratosphere would relax to radiative equilibrium, which would simply follow the annual cycle of the solar heating. A comparison between the radiatively-determined (Fig. 1.8) and observed (Fig. 1.7 left panel) temperatures shows some striking differences. The temperature increase from winter to summer pole is present in both cases above 30 km, but the temperature difference between the two poles is much larger in the radiatively-determined state. In the tropical lower stratosphere, the radiatively-determined temperature is warmer by $\sim$20 K than the observed climatology. Also in the mesosphere, the sign of the pole-pole gradient is opposite between the two figures. In the radiative-determined thermal conditions, the circulation would consist entirely of a zonal flow determined by the thermal wind balance and not involve any meridional or vertical motions. The magnitude of the zonal flow would increase throughout the stratosphere and mesosphere (Fig. 1.9), while the observed zonal flow peaks around 60-70 km and decreases above (Fig. 1.7 right panel).

There must exist processes that determine the departures of the observed temperatures from the radiative equilibrium. Those processes are the impacts of tropospheric perturbances (*eddies*) with the stratosphere. In partic-

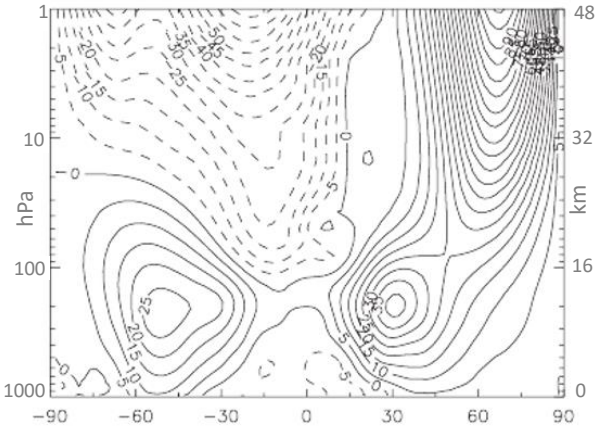

Figure 1.9: Zonal mean zonal wind for January for a model with no interaction between tropospheric disturbances and the stratosphere. Adapted from Geller et al. (2011).

ular, the eddies are tropospheric waves (see Sect. 1.2.4) that propagate and break into the stratosphere, with a consequent transfer of angular and heat momentum. These impacts ultimately are responsible for the generation of a stratospheric circulation on the meridional-vertical plane (the meridional circulation, which will be treated separately in Sect. 2), which in turn affects the temperatures and leads to the differences between Fig. 1.8, 1.9 and Fig. 1.7. Hence, the observed thermal structure (differences with respect to the thermal equilibrium) in the stratosphere is not the cause of the stratospheric meridional circulation but is the consequence of the propagation of waves from the troposphere into the stratosphere and mesosphere, their breaking driving the stratosphere away from its radiative equilibrium through the meridional circulation.

1.2.4 Waves interacting with the stratosphere

This Section gives a general overview of the waves that propagate from the troposphere into the stratosphere. For this reason, the simplest atmospheric waves, e.g., acoustic waves, are not treated here. The interested reader is referred to Holton (2004) or Andrews et al. (1987) for a much more detailed and mathematical analysis of atmospheric waves.

Waves are oscillations of field variables (wind, pressure, temperature) that can propagate in space and time. For simplicity, we will consider here linear sinusoidal waves whose period is independent from the amplitude of the wave (like the harmonic oscillator). We can generally express such a wave in the

form

$$\theta = \theta_0 \cos(\nu t - \alpha), \tag{1.24}$$

where θ_0 and α are constants, and ν is the *frequency* of the wave. The quantity $\phi(t) = \nu t - \alpha$ takes the name of *phase* of the wave. The phase of a wave generally depends simoultaneously on space and time. Thus, for a one-dimensional wave propagating in the x direction, the phase is $\phi(x,t) = kx - \nu t - \alpha$, where k is the *wavenumber* and is defined as $k = 2\pi/\lambda$, with λ denoting the *wavelength*.

The velocity at which the wave propagates is the *phase speed*, and is defined as $c \equiv \nu/k$ when the phase remains constant during the motion. This ratio is called the *dispersion relationship*, because the phase speed c generally varies with k (dispersive waves), and the wave components (i.e., the wave group) are dispersed along the motion. For dispersive waves, the speed of the ave wgroup is generally different from the average phase speed of the single wave components, thus we define the *group velocity*, i.e., the velocity at which the total disturbance (i.e., the energy) travels, which is defined as $c_g = \partial\nu/\partial k$.

For atmospheric waves, an exact treatment would be impossible because of the non-linearity of the system. The *perturbation method* provides a useful framework to address this issue by providing a qualitative analysis of the atmospheric waves. All field variables are divided in two parts: a mean state, usually independent of time and longitude, and a perturbation, defined as the deviation from the mean state. For example, let $A(x,t)$ be a generic variable that depends on longitude and time, we can define a mean state $\overline{A}$ and a perturbation (or disturbance) $A'(x,t)$ such that

$$A(x,t) = \overline{A} + A'(x,t). \tag{1.25}$$

The assumptions of the perturbation theory is that the mean state must satisfy the governing equations when the perturbations are set to zero, and the perturbations must be small enough that all products between them can be neglected $A'A' \approx 0$.

Furthermore, we have by definition that $|\overline{A}| > |A'(x,t)|$ and $\overline{A'(x,t)} = 0$. The perturbation method allows to have the governing equations in terms of pertubations, with the mean state as a coefficient, whose solutions are sinusoidal or exponential and allow us to have insights about the physical characterisitcs of the waves (propagating speed, vertical structure, conditions for breaking).

In the atmosphere, waves are balanced by a restoring force that defines their type. When the restoring force derives from the interaction with the

Earth's surface, e.g., sea-land contrast or topography, they take the name of forced modes. On the contrary, free modes are resonant oscillations produced by random forcing. In this Section, we will consider only forced modes. Some of those waves can propagate very high into the stratosphere and mesosphere, where they break and dissipate momentum.

In the following Sections, we limit to provide a general overview of the tropospheric waves that are the most relevant for driving the stratospheric circulation: *gravity waves* (Sect. 1.2.4.1), *planetary waves* (Sect. 1.2.4.2), and *equatorial waves* (Sect. 1.2.4.3). In particular, we shall focus on the propagation and breaking of those waves into the stratosphere, i.e., tropospheric sources are only shortly mentioned, and tropospheric motions are not addressed. Additional large-scale wave-like phenomena such as atmospheric thermal tides (Oberheide et al., 2015) are not treated here.

1.2.4.1 Gravity waves

Gravity waves have a relatively short horizontal wavelength (10-100 km) and are generated in the troposphere by air passing over mountainous regions (orographic gravity waves) or by other sources such as convection or fronts (non-orographic gravity waves). In a stably stratified atmosphere, this movement will cause a restoring force so that an air parcel displayed upwards will undergo buoyancy oscillations and return to its equilibrium position.

The propagation of gravity waves through the atmosphere depends first on its thermal structure. In the absence of dissipation, the amplitude of the gravity waves grows exponentially with altitude as the inverse square of the density because the group velocity is proportional to the buoyancy frequency N (Nappo, 2013). However, gravity waves cannot propagate indefinitely throughout the whole atmosphere because, at a certain level, their amplitude will have grown so large that they will become unstable and break, interacting with the surrounding atmosphere. In particular, for adiabatic waves, the criterion for gravity waves breaking can be estimated as $\partial\theta/\partial z = 0$ (when the condition for static stability is not valid). This condition allows to find the level where isentropic surfaces become vertical, and any increase in amplitude will become unstable (i.e., the so-called *critical level*, Holton and Alexander, 2000). Because of this condition, gravity wave breaking occurs mainly in the troposphere (where they are generated) and in the mesosphere, while in the stratosphere, where $\partial\theta/\partial z > 0$, the waves tend to continue their vertical motion (Nappo, 2013). Thus, the condition for the existence and propagation of gravity waves is that the atmosphere is stably stratified ($\partial\theta/\partial z > 0$).

The propagation of gravity waves also depends on the wind distribution. It can also be shown that, when the phase speed of the wave c is equal to the

zonal mean flow $\bar{u}$, the wave is absorbed by the mean wind flow, providing another way (equivalent to the previous, Holton and Alexander, 2000) to determine the critical level ($|\overline{u} - c| = 0$). This condition results from the absence of the requirement for stability in the dispersion relationship, and we refer to Nappo (2013) and Howard (1961) for its mathematical derivation.

The wave breaking produces a zonal wave drag that can be either eastward or westward. Gravity waves that propagate eastward relative to the zonal flow produce eastward forcing, while westward-propagating waves produce westward forcing. Within the stratosphere, gravity waves break and produce forcing primarily in the summer hemisphere and in the lower stratosphere, and they contribute to the equatorial quasi-biennial oscillation (Holton and Alexander, 2000). However, since the stratosphere allows the propagation of most gravity waves, the wave breaking occurs mainly in the mesosphere, which is dominated by eastward propagating waves in the summer and westward propagating waves in winter (Holton and Alexander, 2000; Brasseur and Solomon, 2005). This breaking causes eastward and westward forcing, thus the departure of the mesospheric temperatures from the radiative equilibrium discussed in Sect. 1.2.3.

For gravity waves with horizontal wavelengths larger than 300 km, the restoring force acting on the wave also includes the effect of the Earth's rotation, and the wave is called inertia-gravity wave (Holton, 2004).

The interested reader is referred to the exhaustive review of gravity waves theory and characteristics in Lindzen (1981) and Fritts and Alexander (2003).

1.2.4.2 Planetary waves

Planetary waves, or Rossby waves after C.G Rossby, who introduced them (Rossby, 1939), are large-scale waves that owe their existence to the isentropic gradient of potential vorticity (see 2.4.1 for the definition of potential vorticity), which results from meridional displacements of air masses (Holton, 2004). It can be shown that, unlike gravity waves, planetary waves propagate only westward with respect to the tropospheric mean flow.

The planetary waves that can propagate into the stratosphere are generated in the troposphere by flow over continental topography (e.g., Rockies or Himalayas), by land-ocean heat contrast, or by interactions between tropospheric disturbances (Holton and Alexander, 2000). Unlike gravity waves, the upward propagation critically depends on the season and the magnitude of the zonal flow. It can be shown that the upward propagation is possible only if the mean flow satisfies the condition $0 < \bar{u} < U_c$, (the Charney-Drazin criterion, Charney and Drazin, 1961). Hence, the vertical propagation of planetary waves can occur only in the presence of westerly wind regimes

that are weaker than U_c, the Rossby critical value, which depends on the horizontal wave scales (Holton, 2004). Thus, planetary waves can propagate vertically into the stratosphere primarily during winter, while the propagation is reduced during summer.

It can be shown that $U_c \approx 100$ m s^{-1} (Holton, 2004). Thus, since U_c is inversely proportional to the square of the wavenumber, only waves with the small zonal wavenumber 1 and 2 (i.e., very large-scale planetary waves) propagate significantly into the stratosphere of the winter hemisphere. The Charney-Drazin criterion thus explains both the observed inhibition of the propagation of planetary waves in the summer hemisphere and the predominance of vertically-propagating waves of zonal wavenumber 1 and 2 in the winter stratosphere (Holton and Alexander, 2000).

As for gravity waves, planetary waves can also break into the stratosphere. The wave breaking results in rapid, irreversible deformation of the material contours (e.g., potential vorticity) and eventually in a wave-induced zonal drag in the stratosphere (Holton and Alexander, 2000; Holton, 2004). It can be shown that planetary wave breaking occurs in the proximity of a critical surface, along which the phase speed of the wave is equal to the zonal mean flow $\bar{u} = c$ (similarly to the wave breaking of gravity waves). This condition is encountered when the approximation of linearity is not satisfied anymore in the governing equations, and the non-linear effects become important (Holton, 2004).

From mathematical analysis, several properties of the planetary waves breaking can be deduced. However, a rigorous treatment of the governing equation of planetary waves can be found in, e.g., Holton and Alexander (2000). Here, we only provide the physical meanings of this derivation because it will be used in the following Sections. It can be shown that the planetary waves activity generally tends to propagate upward and equatorward, and that the wave breaking occurs close to the critical surface in the equatorial region (Holton, 2004). Thus, the critical lines are characterized by a considerable convergence of the wave activity flux and are surrounded by regions in which non-linear processes dominate. Since planetary waves can propagate only westward with respect to the mean wind, their wave breaking is associated with a westward force on the stratospheric mean flow (Holton and Alexander, 2000).

1.2.4.3 Equatorial waves

Near the equator, where the Coriolis force is minimal and changes sign, exists a particular class of waves that are trapped near the Tropics: the equatorial waves (Matsuno, 1966), which are further cathegorized into Kelvin waves

(Canziani et al., 1994), and so-called Rossby-gravity waves. The latter tend to behave like gravity waves for large zonal wavelengths, and like a planetary (Rossby) wave for shorter zonal wavelengths (Matsuno, 1966).

Kelvin waves propagate eastward with an average phase speed of 50 m s^{-1}, and vertical wavelength of 6-10 km and zonal wavenumber 1-2. Rossby-gravity waves propagate westward (with average phase speed of -30 m s^{-1}) with vertical wavelengths of 4-8 km and zonal wavenumber 4 (Holton, 2004). Kelvin and Rossby-gravity waves are excited by oscillations in the large convective heating patterns in the equatorial troposphere, and they are a major source of disturbances for the equatorial stratosphere and mesosphere, through transport of momentum and energy (Holton, 2004).

1.2.5 Variability of the Stratosphere

This Section describes the stratospheric phenomena of major importance for the present work. In particular, Sections 1.2.5.1 and 1.2.5.2 give overviews of the quasi-biennial oscillation and the polar vortex, respectively. Additional sources of stratospheric variability, such as the sudden stratospheric warmings (Baldwin et al., 2021), or the Northern and Southern annular modes (Simpson et al., 2011), as well as tropospheric sources that impact the stratosphere, e.g., the El-Ninõ southern oscillation (Domeisen et al., 2019), are not addressed here.

1.2.5.1 The Quasi Biennial Oscillation

The quasi-biennial oscillation (QBO) consists of downward propagating easterly and westerly zonal wind regimes in the equatorial stratosphere, with a variable period from 24 to 30 months (see Fig. 1.10). Successive wind regimes appear above 30 km and propagate downward at the rate of 1 km $month^{-1}$ The downward propagation occurs with no loss of amplitude in the middle stratosphere but rapidly weakens below around 20 km. The oscillation is symmetric around the Equator with a maximum amplitude of 20-25 m s^{-1} and has a roughly Gaussian distribution in latitude with a half-width of around 12 degrees (Holton, 2004).

Because of the thermal wind balance (Eq. 1.23), the zone of westerly and easterly wind shear have warm and cold temperature anomalies, respectively (Holton, 2004). The temperature anomalies associated with the QBO result in radiative heating, and in a consequent secondary circulation in the meridional plane that balances it (Reed, 1965). Such circulation is characterized by anomalously large upwelling in the lower stratosphere during easterly phase QBO and by anomalously large downwelling in the middle-

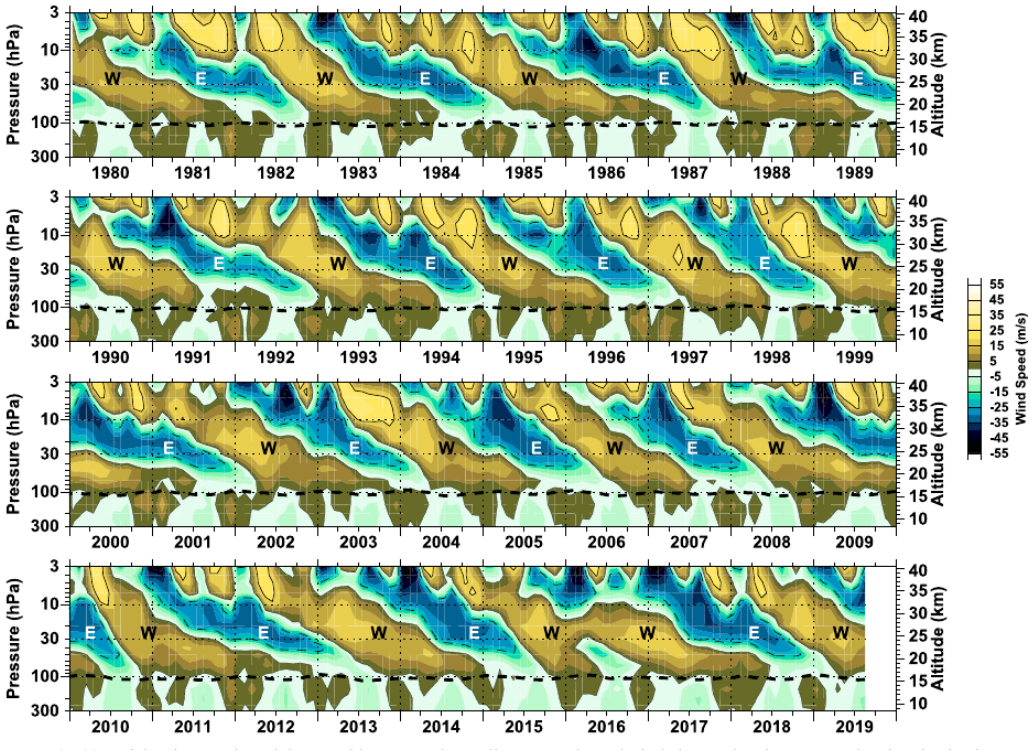

Figure 1.10: Pressure-time cross section of the monthly and zonally averaged zonal mean wind observed at the Equator showing the QBO. The dashed line shows the mean altitude of the tropopause. "W" stands for westerly phase QBO, and "E" for easterly phase QBO. From Baldwin et al. (2019).

upper stratosphere during westerly phase (Plumb and Bell, 1982; Baldwin et al., 2001).

The QBO also impacts the tropical stratospheric ozone: the westerly wind regimes produce positive ozone anomalies, while easterly winds result in negative ozone anomalies (Gray and Pyle, 1989). In addition, the velocity of the descent of the wind shear differs between the westerly and easterly phases of the QBO. On average, the easterly phase of the zonal winds, which occasionally stall at around 50 km, descends more slowly than the westerly phase (Pascoe et al., 2005). Besides the mentioned impacts in the Tropics, the QBO is now recognized to influence also the high latitudes. Notably, a crucial discovery was the study of Holton and Tan (1982), who showed that the westerly (easterly) QBO phase results in colder (warmer) polar regions and warmer (colder) mid-latitudes.

The QBO has been regularly observed for more than 50 years (Baldwin et al., 2001), but in 2016 an evident disruption of the typical pattern took place (Fig. 1.10): an easterly jet formed within the westerly phase QBO in the lower stratosphere, which was caused by waves transporting momentum from the Northern Hemisphere (Osprey et al., 2016; Newman et al., 2016).

The causes of the QBO were not understood at first after its official discovery in 1960 (Reed et al., 1961). The turning point was the work from Lindzen and Holton (1968), who stated that the accelerations responsible for the QBO were driven by the interaction of the zonal mean flow with gravity waves generated in the troposphere and propagating vertically and zonally. Further developments of the theory behind the QBO included the effect of planetary equatorial waves (Holton and Lindzen, 1972) and the combined effect of the latter type of wave with gravity waves (Dunkerton, 1997). The interested reader is referred to Baldwin et al. (2001) for an extensive review of the QBO and its impacts on circulation and chemical composition, as well as an analytical treatment of the driving dynamical mechanism and the numerical methods to model it.

1.2.5.2 The Polar Vortex

In the winter hemisphere, the zonal wind structure in the stratosphere is determined by the meridional gradient of temperature, which results in strong stratospheric westerly winds that peak at the mid-latitudes (40°to 60°) around 70 km of altitude (see Sect. 1.2.2). Those wind regimes are the edges of the so-called *polar vortex* and are in contrast with the easterly regime of the summer hemisphere (see Fig. 1.7). The polar vortices play a primary role in the dynamics and transport in the wintertime stratosphere and in the coupling between the troposphere and the stratosphere.

Stratospheric polar vortices form in fall, when the solar heating disappears over the polar regions, reach their maximum in mid-winter, and start to decay in late winter/early spring because of the return of the sunlight. This is depicted in Fig. 1.11, which shows the latitude-seasonal variations of the zonal winds at 10 hPa (around 30 km) for the ERA5 (European Centre for Medium-Range Weather Forecast reanalysis 5, Hersbach et al., 2020) reanalysis (see Sect. 1.2.7 for the definition of a reanalysis). In both hemispheres, easterly winds are found in the summer months, replaced by westerlies in fall that strengthen until midwinter. These westerlies weaken during spring and the easterly regime is restored in summer.

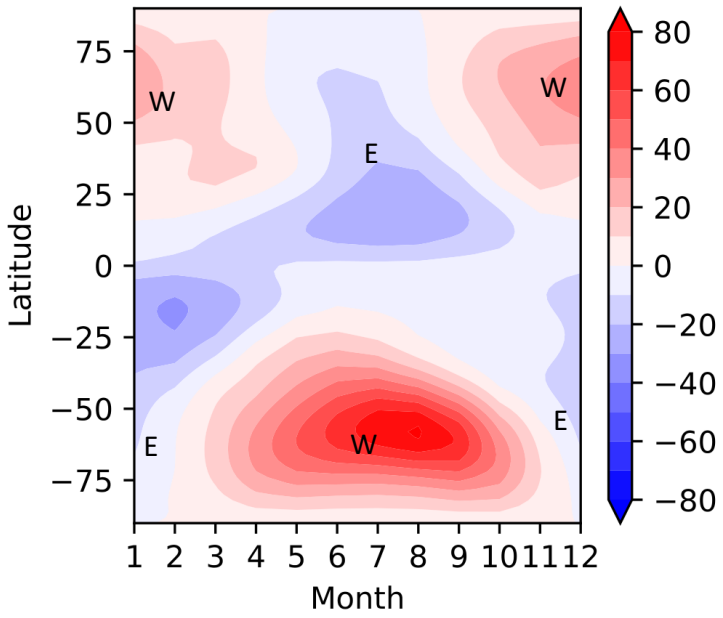

Figure 1.11: Seasonal cycle of the intensity of the zonal mean zonal wind at 10 hPa for the 2001-2018 period using the ERA5 reanalysis as a function of the latitude.

Significant hemispheric differences can be seen in Fig. 1.11 with respect to the strength and duration of the polar vortices. The Antarctic vortex is wider, stronger and lasts longer than its Arctic counterpart. These differences are caused by the hemispheric differences in tropospheric wave generation and propagation. The majority of the mountainous regions and the land-ocean contrast, which trigger large-scale planetary waves that disturb the stratospheric vortex (see Sect. 1.2.4), are in the Northern Hemisphere. Thus, the Antarctic polar vortex is less disturbed and closer to radiative equilibrium

conditions (Sect. 1.2.3). Those differences are crucial in understanding the ozone depletion over the Antarctic (see Sect. 1.2.6) and play an essential role in the budget of long-lived chemical tracers (see Sect. 6).

Significant inter-hemispheric differences also arise for interannual variability, with the Arctic vortex more variable than the Antarctic on inter-annual and intra-seasonal time scales (Waugh and Randel, 1999). The stronger wave activity in the Northern Hemisphere is responsible for the larger variability of the Arctic polar vortex, which presents its most potent manifestation in the sudden stratospheric warmings (SSW, Butler et al., 2017). During an SSW, the polar vortex becomes highly distorted and can also break down, with a consequent increase in polar temperatures and reversal of the zonal winds from westerly to easterly. Although the Antarctic polar vortex is much more stable than its Arctic counterpart, SSWs can also occur there, such as the events in 2002 (Newman and Nash, 2005), and 2019 (Yamazaki et al., 2020).

While zonal mean quantities usually give a good overview information about the general structure of the polar vortex, the examination in three dimensions is required to have further insights into the dynamical properties of the vortex. It is advantageous to use potential vorticity (PV, see Sect. 2.4.1) to investigate the structure of the polar vortex. PV is conserved for adiabatic and frictionless motions, and other dynamical quantities (e.g., wind and temperature) can be determined using the PV inversion (McIntyre and Norton, 2000).

Maps of PV provide useful information about the structure and evolution of the polar vortex (Fig. 1.12). On such maps, the polar vortex appears as a roughly circular, coherent region of large PV, surrounded by regions of steep PV gradients, which depict the strong westerly winds. The inter-hemispherical differences in the polar vortex appear clearly using PV maps, with the Antarctic polar vortex much more stable than the Arctic counterpart (Fig 1.12). PV also allows to highlight regions where wavebreaking (see Sect. 1.2.4) occurs as regions where the PV contours are not zonally symmetric, but elongated equatorward (McIntyre and Palmer, 1984).

1.2.6 Stratospheric Ozone

Section 1.1.3.3 described ozone as a tropospheric greenhouse gas, but we mentioned that its behaviour in the stratosphere is totally different. In the following, we will describe the role of ozone in the stratosphere and why it is essential for the Earth system. First, it is important to highlight that the stratosphere accounts for the majority of the total ozone in the atmosphere (around 90%) and that it resides approximately between 15 and 35 km above

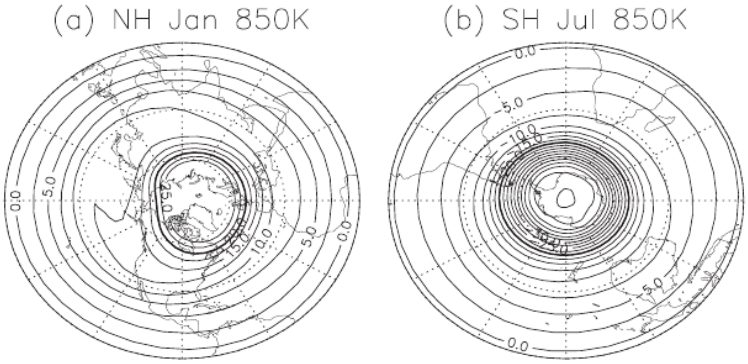

Figure 1.12: Maps of the climatological (1979-2008) PV on the 850 K isentropic surface (around 10 hPa) for (a) Northern Hemisphere in January and (b) Southern Hemisphere in July. From Waugh and Polvani (2010).

the surface, peaking around 22 km (Fahey and Hegglin, 2010).

After its discovery in 1839 by Schönbein (Rubin, 2001), ozone has been extensively studied in the following decades. It was found that ozone in the upper stratosphere absorbs solar UV radiation in the 200-300 nm wavelength range (Cornu, 1879; Hartley, 1880). Further key developments arrived in the 1930s, primarily thanks to technological improvements of the instruments, which led to the identification of the maximum of atmospheric ozone at approximately 22 km of altitude (Dobson, 1931; Götz et al., 1934).

The absorption of UV radiation by ozone is crucial both for the temperature structure of the stratosphere, as the increasing temperatures with height are a consequence of the warming due to UV absorption (see Sect. 1.2.2), and for shielding the surface from UV radiation, which is highly nocive for biological activities (van der Leun et al., 1998).

In the stratosphere, ozone is mainly formed by photolysis (i.e., the reaction in which a compound is broken down by electromagnetic energy) of molecular oxygen. This process requires very energetic UV radiation (λ <240 nm) (Chapman, 1930);, which is most intense in the tropical mid-upper stratosphere. O_2 photolysis braks the molecule into two oxygen atoms O by the absorption of UV radiation (Eq. 1.26). Then, the highly reactive oxygen atom combines with molecular oxygen in a three-body reaction to form ozone (Eq. 1.27). O_3 is photolysed into molecular and atomic oxygen (Eq. 1.28) after absorption of UV radiation, which can happen at longer wavelengths (λ <320 nm) than O_2 photolysis because the bonds in O_3 are weaker than in O_2. The oxygen atom can also react with ozone to form two

oxygen molecules (Eq. 1.29)

$$O_2 + h\,\nu \longrightarrow O + O, \tag{1.26}$$
$$O_2 + O + M \longrightarrow O_3 + M, \tag{1.27}$$
$$O_3 + h\,\nu \longrightarrow O_2 + O, \tag{1.28}$$
$$O_3 + O \longrightarrow 2\,O_2. \tag{1.29}$$

The Equations 1.26-1.29 form the so-called Chapman mechanism, which explains that the peak of the O_3 abundancies is located in the lower stratosphere, between 20 and 30 km of altitude. However, the Chapman mechanism alone would lead to approximately twice larger abundances of ozone in the stratosphere than observed (Bekki and Lefèvre, 2009). In the 1950s, several studies discovered that ozone destruction could be catalyzed by different chemical compounds in the atmosphere. Those species are the hydroxyl radical (OH, Bates and Nicolet, 1950) produced from water vapor, nitric oxide NO, which is produced by oxidation of N_2O (Eq. 1.19 in Sect. 1.1.4), chlorine and bromine monoxide, which are mainly produced from the photolysis of anthropogenic compounds (Cicerone et al., 1974; Wofsy et al., 1975). All the sources of those substances that catalytically destroy ozone (e.g., N_2O) are usually named ozone-depleting substances (ODS). Accounting for all these catalytic sinks allows models of atmospheric chemistry to explain the observed ozone profiles with a good degree of accuracy in the stratosphere (5-10%).

One would expect that the largest amount of stratospheric ozone would be in the Tropics, where is produced by photolysis. Satellite measurements show that this is not the case. Ozone is produced in the tropical mid-upper stratosphere at 25-35 km above the surface, then transported upward, poleward and downward by the stratospheric circulation (see Sect. 2) into the lower stratosphere, primarily during winter, in each hemisphere (Fig. 1.13). As a result, the highest ozone concentrations are found in the high latitudes, as already observed by Dobson et al. (1929).

In the 1970s, two potential threats to the ozone layer were pointed out, both coming from anthropogenic activities. Johnston (1971) noted that the nitrogen oxides emitted from supersonic flights could play a significant role in the catalytic ozone loss. The concern raised by this study took part in stopping the funding to the supersonic transport program. A few years later, another threat for ozone was discovered by Molina and Rowland (1974). They pointed out that the increasing concentrations of CFCs, in particular CFC-11 (CCl_3F) and CFC-12 (CCl_2F_2), would produce a major source of reactive chlorine in the stratosphere, which might lead to considerable ozone loss. These anthropogenic compounds have a lifetime long enough to reach the

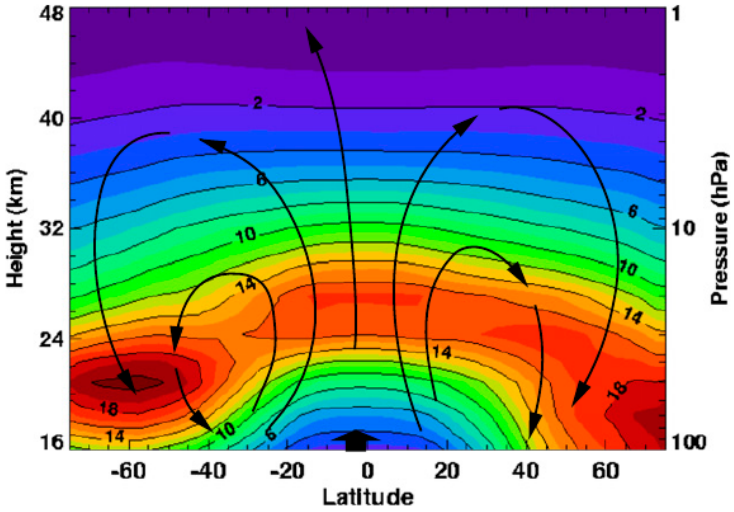

Figure 1.13: Latitude-vertical cross section of annual mean ozone density [DU], for the 1980-1989 period from satellite observations. Black arrows represent the transport by the stratospheric circulation. From Baldwin et al. (2019)

mid-upper stratosphere via the slow stratospheric circulation (see Table 1.1), where they are converted into reactive ClO and Cl radicals and catalytically destroy ozone.

In the 1980s, a strong and unexpected ozone decrease was measured in early spring above the Antarctic using ground-based (Farman et al., 1985) and satellite (Stolarski et al., 1986) observations. This phenomenon, which was later named *Antarctic ozone hole*, started in the 1970's and keeps occurring every year in late winter/early spring over the southern polar region (Fig. 1.14).

These ozone depletion episodes are maximum between 10 and 20 km and cannot be explained by the catalytic ozone loss cycles mentioned above. Several studies have then demonstrated that the Antarctic ozone hole is the result of the combination of particular chemical and meteorological conditions, which enhance the activation of chlorine and bromine, hence the catalytic ozone destruction from CFCs and other ODS.

The rapid and critical ozone destruction observed above the Antarctic requires very cold temperatures (T<195) so that the polar stratospheric clouds (PSCs, Steele et al., 1983; Tritscher et al., 2021) can be formed. In Sect. 1.2.5.2, we stated that the Antarctic polar vortex is much less disturbed than its Arctic counterpart; thus, very cold temperatures can be reached in this vortex during austral winter so that PSCs can develop and provide the con-

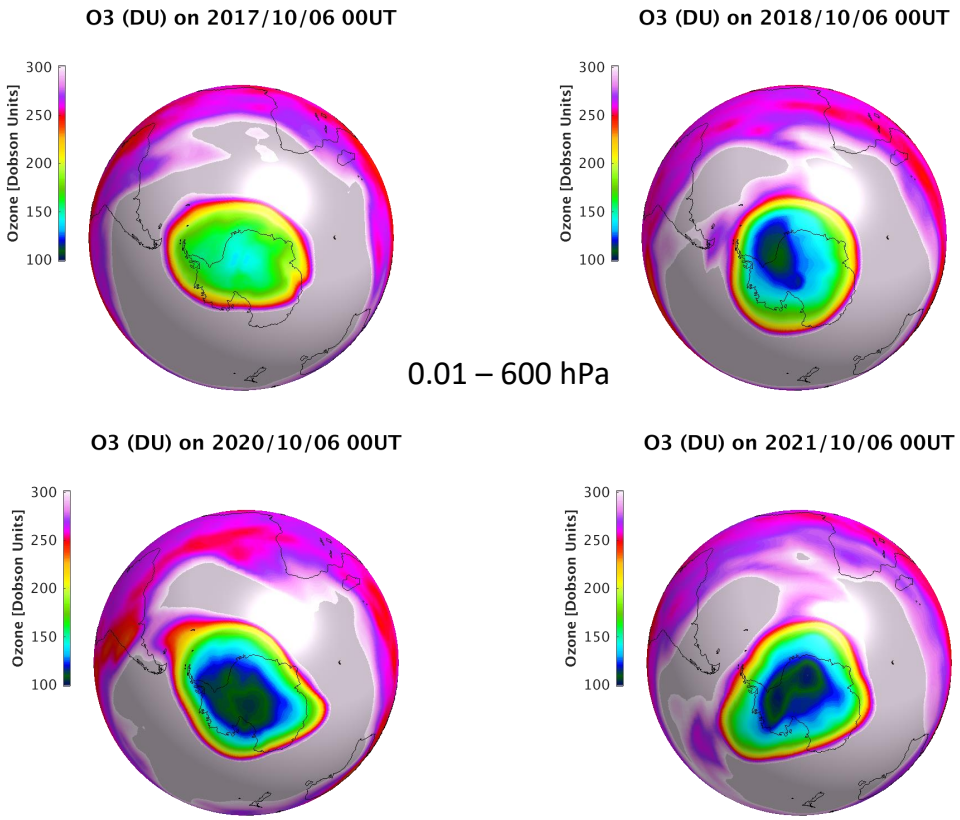

Figure 1.14: Partial (0.01-600 hPa) ozone density [DU] over the Antarctic pole on October 6 for 2017, 2018, 2020 and 2021 obtained from a near-real time analysis of the Microwave Limb Sounder on the Aura satellite.

ditions for the formation of the ozone hole (Toon et al., 1986). PSCs provide the surfaces for the heterogeneous reactions that activate the chlorine and bromine in the reservoirs HCl, $ClONO_2$, HBr, and $BrONO_2$. The released ClO and BrO radicals lead to catalytic ozone destruction when the sunlight returns over the Antarctic at the beginning of spring (Solomon et al., 1986). The Arctic, on the contrary, is characterized by higher temperatures and larger variability with respect to the Antarctic (see Sect. 1.2.5.2), which inhibit the PSC formation. However, in the 21st century, Arctic temperatures reached values cold enough to allow the formation of PSCs and consequent ozone depletion in late winter/early spring: 2010-2011 (Manney et al., 2011), 2015-2016 (Pommereau et al., 2018) and 2019-2020 (Inness et al., 2020).

The growing evidence of the catastrophic effects of increasing ODS on the ozone layer, the possible increase of solar UV radiation reaching the surface, and the consequent impacts on the biosphere and human life, resulted in intense international collaborations to mitigate and stop this effect. The Montreal Protocol, together with its amendments (latest in Kigali in 2016), has now been ratified by all the 197 United Nations members and succeeded in establishing mandatory limitations for developed and developing countries on the emission of ODS (WMO, 2018). The WMO coordinates a series of international ozone assessments of the impact of the Montreal Protocol on Substances that Deplete the Ozone Layer, signed in 1987. As a result of the Montreal Protocol and its amendments, the ODS concentrations have started to decrease in the late 1990s, and the ozone abundances have stopped declining and started increasing in the upper stratosphere (Solomon et al., 2016, and Fig. 1.15). A recent example of the success of the Montreal Protocol is the Arctic spring of 2020, when temperatures were very cold and a stable polar vortex led to an exceptional (for the Northern Hemisphere) ozone depletion (Inness et al., 2020). The successful implementation of the Montreal Protocol allowed avoiding an even much more severe ozone depletion, i.e., comparable to the ozone hole above the Antarctic (Wilka et al., 2021).

CCM simulations of the 21st century with a scenario following the Montreal Protocol scenario for ODS decrease (Fig. 1.15a)) and a medium IPCC scenario for GHG increase project by 2050 a recovery of the global ozone abundances to values similar to those at the beginning of the 1980s (Fig. 1.15c)). Over the Antarctic, where the ozone depletion is most severe, the recovery to pre-1980s values is expected with a delay of ten years compared to the global ozone (Langematz et al., 2018) (Fig. 1.15d)).

Despite the decline in ODS, large uncertainties remain about the future timing of the ozone recovery (Fang et al., 2019). In particular, some ODS are decreasing slower than expected (CCl_4) and uncontrolled emissions of other short-lived ODS (e.g., CH_2Cl_2) were also measured recently. In addition,

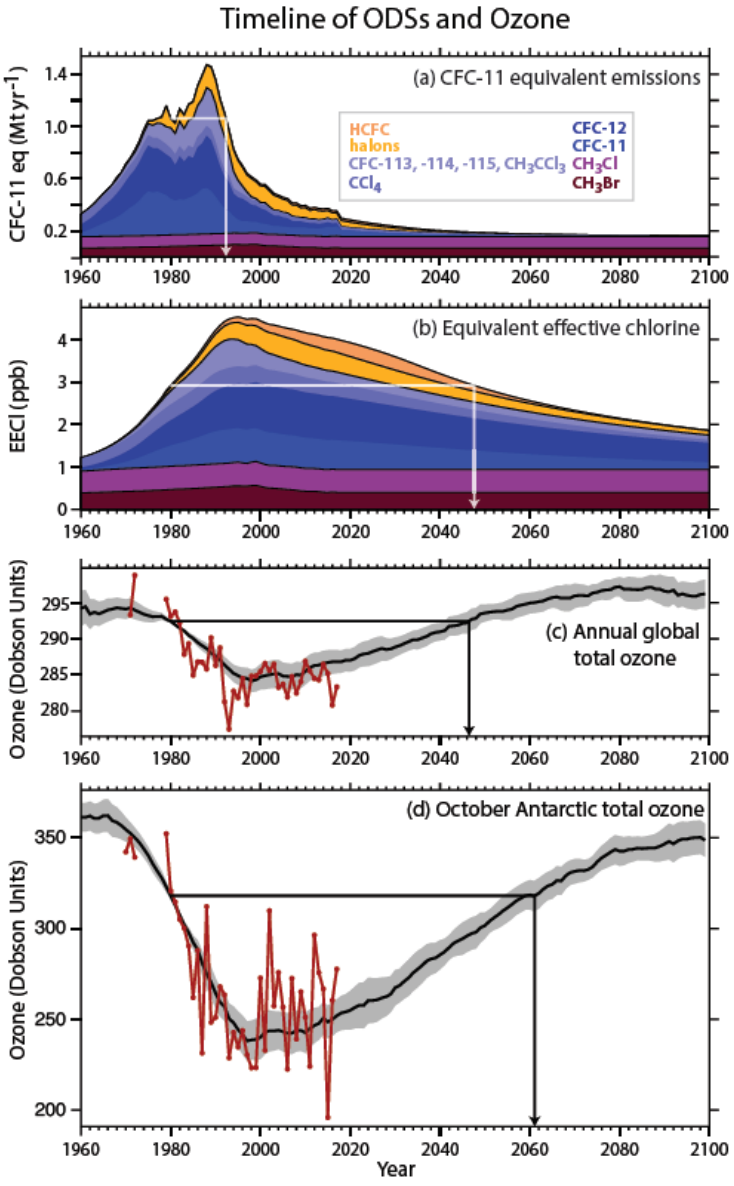

Figure 1.15: Time-series of: a) CFC-11-equivalent emissins, b) equivalent effective stratospheric chlorine (EESC), c) global total ozone, d) October Antarctic total ozone. From WMO, (2018).

changes in concentrations of greenhouse gases like N_2O and methane could also delay the projected ozone recovery (Fang et al., 2019).

1.2.7 Observing and modeling the stratosphere

This Section briefly describes some instruments and methods available to observe and model stratospheric composition and transport. Section 5 will provide a more detailed description of the specific datasets used in this work.

The stratosphere can be probed in several ways, depending on the target measurement (e.g., chemical compounds, wind, temperature), but here we limit ourselves to describing remote-sensing observations from space-borne or ground-based instruments. The remote sensing techniques acquire information from a distance using sensors that are sensitive to the atmospheric pressure and the abundance of absorbing gas and measure the radiation onboard of satellites or at the surface. Other remote-sensing instruments, e.g., from aircraft, are not considered here as they are not used in the present work. In the following, we will generally consider ground-based observations as a reference, when available.

Long-term observations of green-house gases (see Sect. 1.1.3) and ozone-depleting substances (see Sect. 1.2.6) from ground-based instruments are essential in understanding the changes of the atmosphere and their consequent impacts on the environment. We will use the Fourier transform infrared spectrometers (FTIR) that can record high-resolution solar spectra under clear-sky conditions to provide total or partial columnar measurements of atmospheric compounds (Prignon et al., 2019). FTIR measurements are well suited to target constituents that absorb in the IR part of the spectrum (e.g., nitrous oxide, chlorofluorocarbons, see the complete list in Table 1.2). Furthermore, FTIR observations are characterized by large signal-to-noise ratios, which allows the detection of chemically important trace gases at very low concentrations in the atmosphere. The data obtained from FTIR measurements can be used for testing numerical models and for calibrating/validating space-borne sensors of the atmosphere (Zander et al., 2008).

We will also use space-borne measurements from satellites to corroborate the ground-based measurements and to have a more comprehensive view of the studied phenomena. Space-borne measurements have indeed the great advantage to provide a global view of the atmosphere, as they can measure over oceans and regions challenging to access (Bron and Ciais, 2010). Satellites can measure using the *nadir* geometry, i.e., the line of sight intersects the Earth's surface, but this leads to difficulties in measuring below a certain level because of the larger atmospheric thickness close to the surface; on the other hand, nadir measurements usually have a fine horizontal res-

Required	Measured	Episodic
C_2H_6	CCl_3F (CFC-11)	SO_2
HCN	CH_3D	CH_3OH
CH_4	$CHClF_2$ (HCFC-22)	ClO
$ClONO_2$	CO_2	C_2H_2
CO	COF_2	CCl_4
HCl	H_2CO	CF_4
HF	H_2O	CH_3OH
HNO_3	CCl_2F_2 (CFC-12)	
N_2O	HDO	
O_3	N_2	
	NO	
	NO_2	
	O_2	
	OCS	
	SF_6	
	HCOOH	
	C_2H_4	
	NH_3	

Table 1.2: List of gases that are or might be measured by ground-based FTIR instruments. "Required" are those species that are required by the FTIR working group. "Measured" are those species that can be measured routinely at a typical FTIR measurement site. "Episodic" are gases that may be measured during episodic events or at some sites with unique optical configuration or just not routinely. Adapted from `https://www2.acom.ucar.edu/irwg`.

olution. Nadir instruments differ from *limb* sounders, as the latter directly measure the radiation that crosses the atmosphere limb but not the Earth's surface; limb instruments have a finer vertical resolution compared to nadir instruments but a much coarser horizontal resolution and they do not have sensitivity in the lower troposphere (Palmer, 2008).

The concentrations of relevant chemical compounds can be determined from space using three different techniques. Two are passive, i.e., measure radiation emitted from the Sun or the Earth, and one is active, i.e., the instrument emits radiation and measures the returning radiation. The first passive technique is called *emission spectroscopy*: the instrument measures in the microwave or thermal infrared window, where the radiation emitted by the atmosphere is essentially a function of the temperature and composition. The other passive technique is the *solar spectroscopy* and measures radiation with higher energy (near-IR, visible, UV) than the emission spectroscopy. In this window, the radiance emitted by the atmosphere or the surface is nearly zero, and the instrument measures the radiation emitted by the Sun or reflected by the surface or by atmospheric scattering. Last, with *active sensing* we refer to instruments that emit light in the atmosphere that is scattered back to the satellite either by reflection by the surface or by atmospheric scattering (Bron and Ciais, 2010).

The current knowledge of the stratosphere has been improved in the past decades also thanks to the extensive use of numerical models of the atmosphere. Numerical models have been mainly developed to improve our understanding of complex processes, and also allow to perform sensitivity tests and study the impact of a single forcing on the climate system. Modern-day climate models of the atmosphere can be separated into three large categories: General Circulation Models (GCMs), Chemistry-Climate Models (CCMs) and Chemistry-Transport Models (CTMs).

Atmospheric GCMs integrate the primitive equations governing the atmosphere to reconstruct the climate behavior. Those models can resolve large-scale motions but must include parameterizations for non-resolved processes (e.g., convection and gravity wave breaking, Brasseur and Solomon, 2005). GCMs are typically used to understand climate and project climate change. Some GCMs are used for Numerical Weather Prediction: these models are designed to run operationally at very high horizontal resolution and are often part of data assimilation systems (Sect. 4.2.2.1).

In the past decades, the advances in computing power allowed significant increases in the complexity of GCMs, notably by including submodels for interactive chemistry and radiation. Climate models that simulate atmospheric dynamics together with chemistry and radiation are called CCMs (Morgenstern et al., 2017) and can simulate radiative transfer, tropospheric and/or

stratospheric chemistry, dynamics and global climate. The model components (radiation, chemistry, dynamics) are strongly coupled: e.g., variations in ozone abundances can influence the temperature distribution through radiative heating, which can, in turn, change the wind regimes by thermal wind balance, thus modifying the transport that will influence the ozone distribution.

Before describing the last type of climate models (CTMs), it is necessary to introduce another dataset extensively used in stratospheric studies: the reanalyses. Reanalysis products merge dynamical atmospheric observations (e.g., surface pressure, wind and temperature) with a GCM using an assimilation scheme to provide the best reproduction of the past climate. Since they aim to cover long time scales, special care is given to time-varying biases between observations, and the resulting reanalysis provides a multivariate, consistent record of the global atmospheric state (Fujiwara et al., 2017). Reanalyses that assimilate only dynamical observations are called dynamical reanalyses, and they differ from chemical reanalyses because the latter assimilates observations of chemical composition. Chemical reanalyses can be used to evaluate CCMs or as a transfer tool to study differences between instruments (e.g., Gerber et al., 2010; Davis et al., 2016).

Lastly, CTMs simulate the formation, transport and destruction of chemical compounds in the atmosphere. CTMs cannot compute dynamics themselves; thus, they require external winds and temperature (typically from reanalyses) to calculate the distribution of chemical species at regular time intervals (e.g., every 6 hours). CTMs can be used to compare different reanalyses within the same transport framework and they are particularly useful to study atmospheric transport using real or idealized tracers (e.g., Chabrillat et al., 2018).

2 Overview of the Brewer-Dobson Circulation

Section 1.2.3 stated that the thermal structure of the stratosphere as a function of latitude and vertical is mainly determined by tropospheric eddies propagating vertically, which ultimately drive away the stratosphere from its radiative equilibrium. Those eddies transfer momentum into the stratosphere and cause the large-scale circulation on the vertical-meridional plane mentioned in Section 1.2.3: the so-called **Brewer-Dobson Circulation** or BDC. This Section is totally devoted to the BDC, from its discovery at the beginning of the past century to the latest discoveries with respect to its long-term changes, and with a focus on its prominent role in the determination of the 2-D thermal structure of the stratosphere.

The BDC is characterized by tropospheric air rising into the stratosphere in the Tropics, moving poleward and descending in the middle and high latitudes. The BDC determines not only the 2-D thermal structure of the stratosphere but also the lifetime of ODS and GHGs, the temperature of the tropical tropopause and plays a major role in the redistribution of chemical tracers such as ozone. For tracer transport studies, the BDC is often divided into a slow *residual mean meridional circulation* with a time-scale of several months or years (hereafter residual circulation), and a faster *isentropic mixing*, with time-scales ranging from days to few months (Birner and Bönisch, 2011; Butchart, 2014).

Figure 2.1 provides a useful schematics of the BDC structure in the stratosphere and mesosphere. In the stratosphere, the structure of the residual circulation is roughly composed of two cells (one per hemisphere), characterized by upwelling in the Tropics, followed by poleward drift and sinking at the middle and high latitudes. The residual circulation is responsible for the transport of ozone from the Tropics to the high latitudes (Solomon, 1999) and drives the 2-D thermal structure of the stratosphere (see Sect. 2.5). The isentropic mixing is also driven by wave-breaking and is prominent during winter in the middle latitudes (Plumb, 2002). The isentropic mixing is particularly important for tracer studies, as it tends to flatten out the tracer gradients created by the residual advection or by chemistry (Butchart, 2014).

This Section is structured as follows. Section 2.1 gives an overview of the key historical developments that led to the modern-day understanding of the BDC. Sections 2.2 and 2.3 describe the residual circulation and the isentropic mixing, respectively. Section 2.4 sets the mathematical background by providing the necessary approximations for the equations of momentum

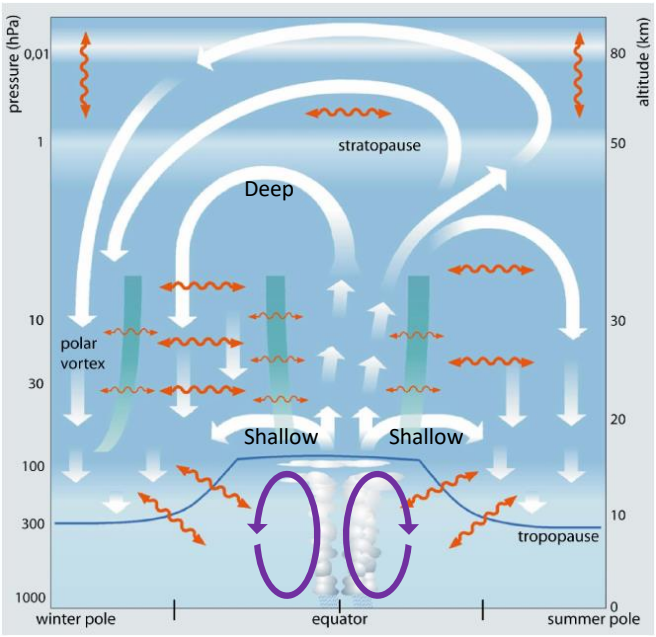

Figure 2.1: Schematic of the BDC as the combined effect of residual circulation (think white arrows) and mixing (wavy orange arrows). Thick green lines represent stratospheric transport barriers, see Sect. 2.3. Circular purple lines depict the tropical Hadley cells in the troposphere. Adapted from Bönisch et al. (2011).

and heat in the stratosphere. Section 2.5 gives an overview of the physical driving mechanism of the BDC, focusing on the wave-driven nature of the BDC and its consequences. Section 2.6 describes the age of air metric of the BDC that is further mentioned in this work. Finally, Section 2.7 presents the current status of the research in terms of observed and modeled long-term changes of the BDC.

2.1 History of the BDC

The initial speculation of the concept of a global stratospheric mass circulation originates from Dobson et al. (1929). They noted that "the only way in which we could reconcile the observed high ozone concentrations in the Arctic in spring and the low concentrations in the Tropics, with the hypothesis that the ozone is formed by the action of sunlight, would be to suppose *a general slow poleward drift in the highest atmosphere with a slow descent of air near the Pole*". Brewer (1949) deduced from water vapor observations that there must be a global meridional circulation in which air enters the stratosphere at the Equator, moves poleward and sinks into the troposphere. He also noted that he could not explain the momentum balance of the air in the presence of such poleward motion.

Further studies in the 1950s and 1960s found evidence of such a meridional circulation in the distribution patterns of radioactive isotopes from atmospheric testing of nuclear weapons (e.g., Sheppard, 1963). Starting with Newell (1963) this circulation has been referred to as the "Brewer-Dobson Circulation" in the literature. Alongside these studies using observed tracers, Murgatroyd and Singleton (1961) obtained the first estimate of a mean meridional circulation in the stratosphere and mesosphere using radiative heating rates. They found air rising slowly across the equatorial tropopause and sinking at the extratropical tropopause in both hemispheres, together with a flow towards the winter pole in the mesosphere. As Brewer (1949), they noted that the angular momentum was not balanced in their model, and they suggested that the eddy processes may be important in the momentum balance. At the same time, other studies suggested that transport due to eddies could explain the ozone distribution (Newell, 1963), or the heat budget balance (Sawyer, 1965), with no need for a mean meridional circulation. Vincent (1968) used an Eulerian-mean model accounting for the eddy contribution to investigate the stratospheric circulation in the Northern Hemisphere. Contrarily to the earlier works of Brewer and Dobson, he found a double-cell structure in each hemisphere: the already discovered air raising at the Equator and sinking at higher latitudes, together with an opposite flow in the extratropics characterized by upward motion in the polar region

and downward motion in the middle latitudes.

All these disagreements in the different descriptions of the circulation and the problem of the angular momentum conservation were solved independently by Boyd (1976), and Andrews and Mcintyre (1976); Andrews and McIntyre (1978a,b,c) using an innovative fluid dynamical interpretation. They argued that, instead of the Eulerian mean, it was more appropriate to use either a generalized Lagrangian mean or the so-called Transformed Eulerian Mean (TEM, see Sect. 2.2). Contrarily to the previous formulations, the TEM approach allows the poleward motion in the stratosphere while conserving the angular momentum. Dunkerton (1978) followed the Lagrangian approach to derive a dynamically consistent mean meridional circulation in the stratosphere and mesosphere, which now generally defines the basic concept of the BDC. Calculations of advective air trajectories confirmed the meridional circulation picture (Kida, 1983). The work of Andrews and Mcintyre (1976); Andrews and McIntyre (1978a,b,c) was crucial for the formulation of the "downward control principle" (Haynes and McIntyre, 1987), and in the understanding of the BDC as a wave-driven phenomenon (Haynes et al., 1991) and the so-called "gyroscopic pumping" (Holton et al., 1995, and Sect. 2.5).

2.2 Residual Circulation

This Section describes more in detail the stratospheric residual circulation, which transports air masses from the equatorial stratosphere to the high latitudes: once all oscillations in the meridional and vertical directions are considered, it is found that air rises in the Tropics (upwelling), moves poleward and sinks in the mid and high latitudes (downwelling). The residual circulation in the stratosphere is usually divided into two separate stratospheric branches: a deep branch (from 30 hPa upward) that encompasses the stratosphere and the mesosphere and is mostly driven by planetary waves breaking into the mid-upper stratosphere, and a shallow branch (usually located between 30 hPa and 70 hPa) associated with waves breaking in the subtropical lower stratosphere (Birner and Bönisch, 2011). An additional branch has been identified (but not depicted in Fig. 2.1): the transition branch, which is usually defined between 100 hPa and 70 hPa (Lin and Fu, 2013). The separation of the residual circulation in three branches is important mostly for trend analysis because the trends of the residual circulation are height-dependent and are sensitive to different forcings depending on the stratospheric region: e.g., ozone changes in the Southern Hemisphere or changes in the subtropical jets (Lin and Fu, 2013, see also Sect. 2.7). This Section gives an overview of the three branches of the residual circulation

and their main characteristics.

Figure 2.2 shows the streamfuction in the Transformed Eulerian Mean framework (see Sect. 2.5 for more details about this method). A generic stream function is integrated from the wind components:

$$u = \frac{\partial \psi}{\partial y}, v = -\frac{\partial \psi}{\partial x}. \tag{2.1}$$

Lines with constant ψ represent the trajectories that an air parcel follows within the two-dimensional flow. In Fig. 2.2, the stream function represents the path that the air masses follow in the stratosphere when transported by the residual circulation.

We start by considering the lowermost branch: the transition branch. Before reaching the stratosphere, tropospheric air must cross the equatorial tropopause. There, the transition from the troposphere to the stratosphere is not a sharp discontinuity and is usually referred to as the tropical tropopause layer (TTL, Fueglistaler et al., 2009). The TTL extends from the equatorial troposphere, from about 12-14 km, to the stratosphere, around 18 km, and is maintained by interactions between large- and small-scale circulation patterns, deep convection, clouds and radiation (Randel and Jensen, 2013). The transition branch crosses the TTL and, at 100 hPa, accounts for the transport away from the Tropics of half of the tropospheric air mass entering the tropical stratosphere, while the other half is divided by the stratospheric branches (Lin and Fu, 2013).

Among the stratospheric branches of the BDC, the shallow branch is the lowest: it extends from 70 hPa to 30 hPa and the extension of its trajectories is typically larger in the meridional direction than in the vertical (Birner and Bönisch, 2011). The shallow branch is mainly driven by synoptic-scale waves (i.e., planetary waves with zonal wavenumber 4 and larger). Those waves can break into the stratosphere regardless of the season; therefore, the shallow branch is a two-cell structure that is present throughout the year (Plumb, 2002; Konopka et al., 2015), with a marked minimum in the Southern Hemisphere in spring (between September and November, Fig. 2.2e)). Based on the results from Birner and Bönisch (2011), the shallow branch is tipically confined in the tropical stratosphere and lower mid-latitudinal stratosphere, i.e., it does not reach latitudes higher than 60°(Diallo et al., 2019).

The deep branch of the residual circulation extends from 30 hPa upwards. Contrarily to the shallow branch, the vertical extent of the deep branch is larger than its meridional extent (Birner and Bönisch, 2011). The air enters into the stratosphere very close to the Equator in the annual mean (within 5°), and the transported air mass is small compared to the shallow branch (Birner and Bönisch, 2011). The deep branch is driven mainly by

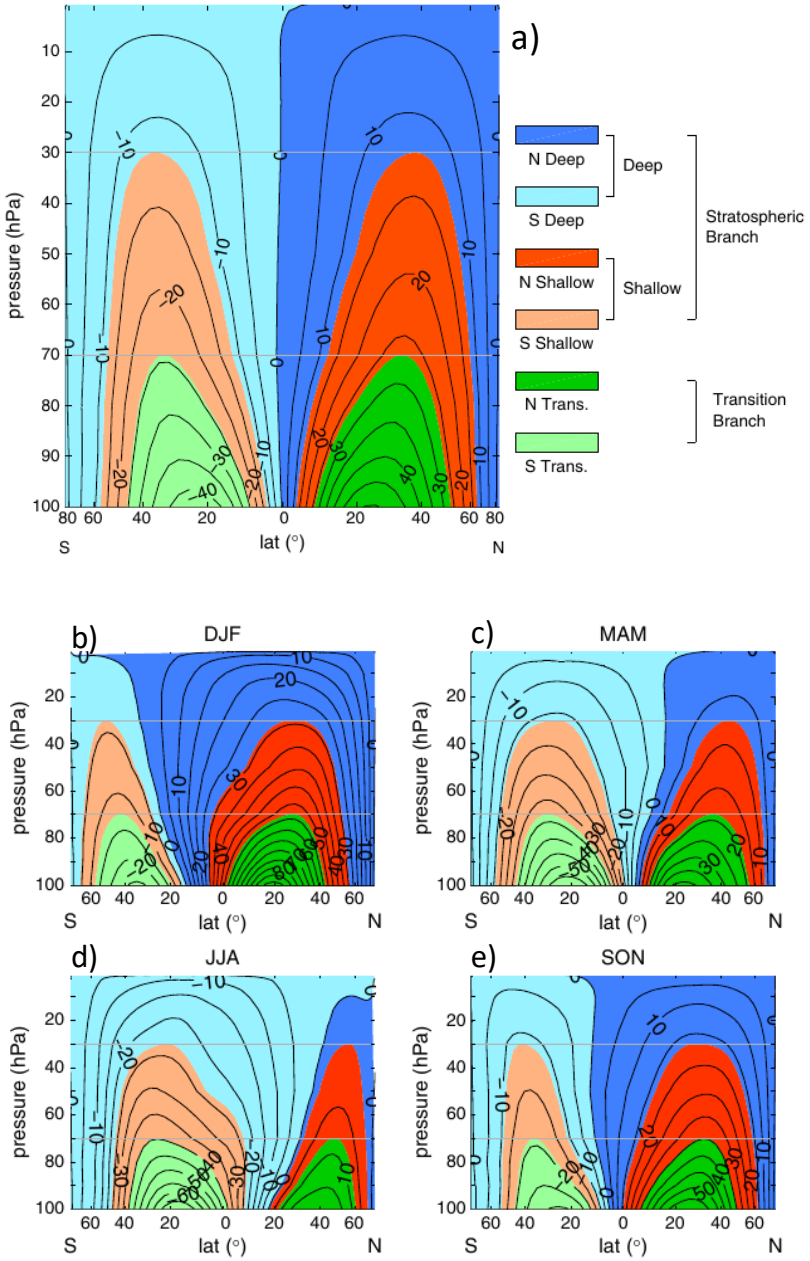

Figure 2.2: a): Climatology of annual mean Transformed Eulerian Mean stream function from the multi-model mean for 1980-2009 in units of 10^8 kg s^{-1}. Positive values for clockwise turning, and negative values for counter-clockwise turning. The branches of the residual circulation are represented by various colors. b), c), d) and e): as panel a) but for seasonal means, DJF, MAM, JJA and SON, respectively. Adapted from Lin and Fu (2013).

the breaking of planetary-scale Rossby waves (with zonal wavenumber 1-2), which break into the stratosphere mainly during winter (see Sect. 1.2.4.2). Hence, the deep branch is a single cell wintertime circulation that is quite reduced during summer (Fig. 2.2b) and d)).

2.3 Mixing and transport barriers

In addition to the residual circulation described above, the tropospheric waves also induce mixing, which is an additional transport mechanism in the stratosphere. By "mixing", we refer to the combined effect of the two-way transport by fluid motion and the molecular diffusion, which eventually makes this process irreversible (Shepherd, 2007). The mixing happens on material surfaces, which can be approximated with isentropic surfaces for adiabatic processes. As with most atmospheric processes, the wave motions associated with mixing in the stratosphere can be approximated as adiabatic. Thus, the mixing in the stratosphere is mainly quasi-horizontal and causes a net transport of tracers but not of mass.

We stated in Sect. 1.1.4 that N_2O is well-suited as a stratospheric tracer because of its long lifetime. In the following, we use this property of N_2O to support the present description of the mixing processes. The quasi-horizontal mixing in the stratosphere tends to flatten out the tracer gradients that are generated by the combination of the vertical motion (due to the residual circulation) and the faster chemical destruction at higher levels. This is evident for the N_2O abundances shown in Fig. 2.3. Above the Tropics and the winter pole, the tracer gradients bend upward and downward respectively due to the upwelling and downwelling, but the mixing acts to counteract this effect, and to maintain a quasi-horizontal distribution of the tracer.

In the stratosphere, the horizontal mixing results mainly from Rossby wave breaking, with the longest (planetary) waves breaking in the deep stratosphere and synoptic-scale waves breaking in the subtropical lower stratosphere (Shepherd, 2007). As mentioned in Sect. 1.2.4.2, planetary waves can break into the stratosphere primarily during winter; thus, the horizontal mixing mostly takes place during winter in the middle stratosphere. This wave breaking can occur over a large band of the mid-latitudes due to the large amplitude of planetary waves (Shepherd, 2007; Butchart, 2014). This wide latitude band of horizontal mixing that surrounds the wintertime polar vortex is called the *surf zone* (McIntyre and Palmer, 1984). In Fig. 2.3, the surf zone is clearly depicted by the quasi-horizontal isoplets of nitrous oxide concentrations in the wintertime middle latitudes. The map of the N_2O abundancies at 480K (around 20 km of altitude) for austral mid-winter also shows the surf zone above the southern mid-latitudes (Fig. 2.4), with

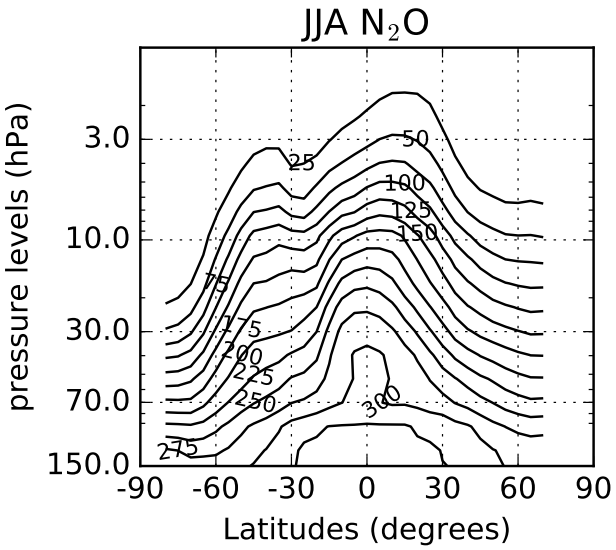

Figure 2.3: Latitude-pressure cross section of N_2O mixing ratio (ppmv) averaged in the June-July August (JJA) season measured from satellite by the Atmospheric Chemistry Experiment - Fourier Transform Spectrometer instrument (2004-2021 period). N_2O data are available upon signup at `https://databace.scisat.ca/l2signup.php`.

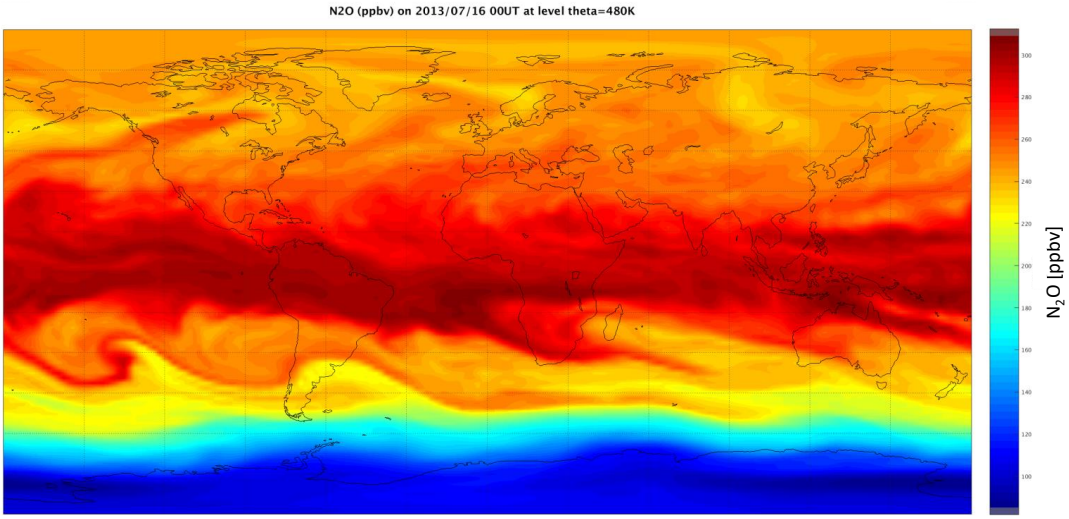

Figure 2.4: Latitude-longitude N_2O map on the 2013/07/16 at 480K simulated by the Integrated Forecast System (IFS, Huijnen et al., 2016).

nearly-constant N_2O abundancies around 250 ppbv. In addition, Figure 2.4 depicts the impact of large-scale planetary waves (wavenumber 1 and 2) on the stratospheric N_2O in the winter hemisphere, especially over the southern Pacific. On the other hand, the impact of gravity waves (see Sect. 1.2.4.1) on mixing is rather limited in the stratosphere because the Charney-Drazin criterion allows only propagation of planetary waves, while gravity waves have not reached as large amplitudes as in the mesosphere (Shepherd et al., 2000). However, gravity waves play a crucial role in driving the circulation and the vertical mixing of tracers in the mesosphere (Shepherd et al., 2000; Chabrillat et al., 2002).

The surf zone is bound above the subtropics and at the edge of the polar vortex by a strong latitudinal gradient of PV resulting in a sharp latitudinal gradient of chemical tracers (e.g., N_2O in Fig. 2.3 and 2.4). Those gradients indicate an inhibition of the horizontal mixing; therefore, they are called *mixing (transport) barriers* (Shepherd, 2003). The mixing barriers are a direct consequence of the latitudinal extent of the Rossby wave breaking and the wintertime surf zone, which are both determined by the fluid dynamics of the Rossby critical value (the U_c maximum zonal wind velocity introduced in Sect. 1.2.4.2). Thus, while the tracer abundancies are homogenized within the surf zone, sharp meridional gradients are created at its edges, i.e., where the Rossby wave breaking does not occur (Shepherd, 2007). Above the winter pole, the Rossby critical value is determined by the polar jet (see Sect. 1.2.5.2), while, on the equatorward edge of the surf zone, the mixing barrier is maintained by a relaxation to thermal equilibrium, which leads to strong PV gradients in the subtropics and thus to the formation of the subtropical edge of the surf zone (Polvani et al., 1995). In the summer hemisphere, a second mixing barrier takes place, but its cause is unclear (Butchart, 2014). While mixing within the surf zone occurs principally during winter as is driven by large-scale planetary waves, the mixing induced by synoptic-scale waves (Rossby waves smaller than planetary waves) occurs throughout the year in the subtropical lower stratosphere and in the proximity of the subtropical jets (Butchart, 2014).

Given the existence of the transport barriers, the stratosphere is often divided into four regions: the summer hemisphere, the Tropics, the surf zone and the wintertime polar vortex (Plumb, 2007). The summer hemisphere is rather quiescent, with weak mixing and residual circulation, even though the shallow branches of the BDC are present there throughout the year (see Sect. 2.2) Within the Tropics, the mixing is generally weak and the upwelling is strong, as depicted by the "tropical pipe" model (Plumb, 1996). However, mixing is not negligible within the Tropics because the mixing across the transport barriers can lead to important modification of the transport as-

sociated with the BDC (Neu and Plumb, 1999). In the winter hemisphere, mixing is very strong within the surf zone, where it dominates over the meridional component of the residual circulation (Plumb, 2002), while it is weak within the polar vortex, where the downwelling is dominant.

2.4 Momentum and heat primitive equations in the conventional Eulerian mean in the stratosphere

This Section provides the momentum and heat primitive equations derived using the conventional Eulerian mean framework. To that end, Section 2.4.1 first provides the primitive equations in spherical coordinates and defines the dynamical quantities used in their derivation. Secondly, Section 2.4.2 describes the geometrical simplifications and physical approximations necessary to focus on the large-scale dynamics. Lastly, Section 2.4.3 provides the definition of the conventional Eulerian mean and the primitive equations for the momentum and heat within this framework.

2.4.1 The primitive equations

For large-scale motions, the atmosphere is often considered as a shallow envelope of compressible fluid surrounding a rotating planet. The equations governing such gas are well-known, but their general form is very complicated. For this reason, several simplifications are made to those equations. In particular, the vertical motion is approximated by the hydrostatic equation, the Coriolis force associated with the horizontal component of Earth's rotation is neglected, and the distance r from any point of the atmosphere to the center of the Earth is replaced by the mean radius of the Earth a. The resulting set of equations takes the name of *primitive equations*.

In the following, we will not use the geometric height as a vertical coordinate, as the primitive equations read slighly simpler when the "log-pressure" coordinate is used

$$z \equiv -H \ln(p/p_s), \tag{2.2}$$

where H is the scale height and p_s is the surface pressure. In the rest of the thesis, we will assume log-pressure as vertical coordinate, if not otherwise stated. Using spherical coordinates in the horizontal, the primitive equations

take the form

$$\frac{Du}{Dt} - \left(f + \frac{u\tan\phi}{a}\right)v + \frac{\Phi_\lambda}{a\cos\phi} = X \tag{2.3}$$

$$\frac{Dv}{Dt} + \left(f + \frac{u\tan\phi}{a}\right)u + \frac{\Phi_\phi}{a} = Y \tag{2.4}$$

$$\Phi_z = H^{-1}R\theta e^{-\kappa z/H} \tag{2.5}$$

$$\frac{[u_\lambda + (v\cos\phi)_\phi]}{a\cos\phi} + \frac{(\rho_0 w)_z}{\rho_0} = 0 \tag{2.6}$$

$$\frac{D\theta}{Dt} = Q. \tag{2.7}$$

These equations express, respectively, zonal and meridional momentum balances, hydrostatic balance, mass continuity, and the relationship between the diabatic heating and the material derivative of the temperature.

In Eq. 2.7, ϕ denotes the geopotential defined in Sec. 1.1.1 and θ is the potential temperature defined is Eq. 1.13. λ and ϕ denote the longitude and latitude respectively, and the wind velocity componentes are

$$(u, v, w) = \left[(a\cos\phi)\frac{D\lambda}{Dt}, a\frac{D\phi}{Dt}, \frac{Dz}{Dt}\right],$$

where D/Dt is the material derivative, i.e., the time change following the fluid motion, and is expressed as

$$\frac{D}{Dt} = \frac{\partial}{\partial t} + \frac{u}{acos\phi}\frac{\partial}{\partial\lambda} + \frac{v}{a}\frac{\partial}{\partial\phi} + w\frac{\partial}{\partial z}. \tag{2.8}$$

The quantity $f = 2\Omega\sin\phi$ is the Coriolis parameter, that accounts for the Earth's rotation, $\Omega = 2\pi(\text{sidereal day})^{-1} = 7.292 \times 10^{-5}\text{s}^{-1}$ is the earth's rotation rate, and X and Y are horizontal components of the friction. $Q \equiv (J/c_p)e^{\kappa z/H}$ is the diabatic heating, where J is the diabatic heating rate per unit mass. The density is expressed as $\rho_0(z) \equiv \rho_s e^{-z/H}$, where $\rho_s \equiv p_s/RT$. The X and Y terms represent the horizontal components of the friction, or other generic mechanical forcings. Partial derivatives with respect to spatial coordinates are expressed by subscripts.

An additional important quantity is Ertel's potential vorticity P, defined as $P \equiv \rho^{-1}\omega_a\cdot\nabla\theta$, where $\omega_\mathbf{a}$ is the absolute vorticity (the curl of velocity). Under the approximations that led to Eqs. 2.7, we have

$$\rho_0 P \equiv \theta_z\left[f - \frac{(u\cos\phi)_\phi}{a\cos\phi} + \frac{v_\lambda}{a\cos\phi}\right] - \frac{\theta_\lambda v_z}{a\cos\phi} + \frac{\theta_\phi u_z}{a}. \tag{2.9}$$

A rather long and complicated calculation shows that

$$\frac{DP}{Dt} = (\rho_0 a \cos\phi)^{-1} \left[-\frac{\partial(X\cos\phi,\theta)}{\partial(\phi,z)} + \frac{\partial(Y,\theta)}{\partial(\lambda,z)} - \frac{\partial(Q,v)}{\partial(\lambda,z)} + \frac{\partial(Q,m)}{\partial(\phi,z)} \right], \tag{2.10}$$

where

$$\frac{\partial(\mathbf{A},\mathbf{B})}{\partial(x,y)} = \frac{\partial\mathbf{A}}{\partial x}\frac{\partial\mathbf{B}}{\partial y} - \frac{\partial\mathbf{A}}{\partial y}\frac{\partial\mathbf{B}}{\partial x}, \tag{2.11}$$

and $m = a\Omega\cos^2\phi + u\cos\phi$. Thus, if the friction and the diabatic heating both vanish, P is conserved during the motion.

2.4.2 The beta-plane and the quasi-geostrophic approximations

The primitive equations as expressed in Eq. 2.7 are still a quite complicated set of equations, despite the simplifications used in deriving them. In order to focus on large-scale and slow motions in the extratropics, it is useful to make further approximations that ultimately lead to the *quasi-geostrophic equations*.

2.4.2.1 The primitive equations on a beta-plane

It is useful to make a geometrical simplification to the Eqs. 2.7, by replacing the spherical coordinates (λ,ϕ) with eastward and northward cartesian coordinates (x,y), and restricting the flow domain to a certain area defined by the latitude ϕ_0. The resulting equations are

$$\frac{Du}{Dt} - fv + \Phi_x = X, \tag{2.12}$$

$$\frac{Dv}{Dt} + fu + \Phi_y = Y, \tag{2.13}$$

$$\Phi_z = H^{-1}R\theta e^{-\kappa z/H}, \tag{2.14}$$

$$u_x + v_y + {\rho_0}^{-1}(\rho_0 w)_z = 0, \tag{2.15}$$

$$\frac{D\theta}{Dt} = Q, \tag{2.16}$$

where

$$\frac{D}{Dt} = \frac{\partial}{\partial t} + u\frac{\partial}{\partial x} + v\frac{\partial}{\partial y} + w\frac{\partial}{\partial z}, \tag{2.17}$$

x and y are the eastward and northward distances from some origin (λ_0, ϕ_0), respectively, the subscripts x, y and z denote partial derivatives, and other symbols are as before, with the exception of f, which now is

$$f = f_0 + \beta y, \tag{2.18}$$

with $f_0 \equiv 2\Omega \sin\phi_0$ and $\beta \equiv 2\Omega a^{-1} \cos\phi_0$. The linear variation of f with y retains the most important dynamical effects of the variations of $2\Omega sin\phi$ with latitude. Equations 2.12-2.16 are called the "beta-plane" versions of the primitive equations.

2.4.2.2 The geostrophic balance

Having simplified the geometry, we can now better investigate the dynamical approximations. For large-scale, low frequency and extratropical flows the *geostrophical balance* is valid, i.e., the Coriolis term is balanced by the geopotential (pressure) gradients

$$-fv_g \approx -\frac{1}{\rho}\frac{\partial p}{\partial x} = \frac{\partial \Phi}{\partial x}, \tag{2.19}$$

$$fu_g \approx -\frac{1}{\rho}\frac{\partial p}{\partial y} = -\frac{\partial \Phi}{\partial y}, \tag{2.20}$$

where u_g and v_g are the longitudinal and meridional components of the geostrophic wind $\overline{\mathbf{u_g}} = (u_g, v_g, 0)$, respectively. From the hydrostatic balance (Eq. 1.2), we obtain the "thermal wind" relationship

$$\frac{\partial u_g}{\partial z} = -\frac{R}{Hf_0}\frac{\partial T}{\partial y}, \tag{2.21}$$

$$\frac{\partial v_g}{\partial z} = \frac{R}{Hf_0}\frac{\partial T}{\partial x}. \tag{2.22}$$

From the hydrostatic balance, we also have

$$\theta_e \equiv \theta - \theta_0(z) = HR^{-1}e^{\kappa z/H}\Phi_z \tag{2.23}$$

where $\theta_0(z)$ is a reference potential temperature.

2.4.2.3 The quasi-geostrophic approximation

The geostrophic balance is a strong approximation: it does not involve any time evolution D/Dt, non-conservative terms are neglected, and the Coriolis

effect does not depend on the meridional coordinate. In order to investigate the time evolution of the geostrophic flow, we define ageostrophic wind velocities, denoted by the subscript a

$$u_a \equiv u - u_g, \quad v_a \equiv v - v_g, \quad w_a \equiv w. \tag{2.24}$$

We define U as a typical order of magnitude of the geostrophic wind speed ($U \sim 10$ m s^{-1}), and L as the typical horizontal length ($L \sim 10^6$ m), so that d/dx and d/dy are $O(1/L)$. Having $|u_a| << |u_g|$ and $|v_a| << |v_g|$, it can be shown that the geostrophic balance is a valid approximation if the following conditions are satisfied

$$(a) \qquad Ro \equiv U/f_0 L << 1 \tag{2.25}$$

$$(b) \qquad \partial/\partial t << f_0 \tag{2.26}$$

$$(c) \qquad \beta L << f_0 \tag{2.27}$$

$$(d) \qquad |X|, |Y| << f_0 U. \tag{2.28}$$

Condition (a) states that the *Rossby number* Ro, which measures the ratio of the non-linear term to the Coriolis term, should be small. Similarly, condition (b) states that the ratio between the time derivative and the Coriolis term should be small. Condition (c) allows the use of f_0 instead of f, and condition (c) ensures that friction is small. Given those conditions, the Eqs. 2.12 to 2.16 can be written for the "quasi-geostrophic" flow as:

$$D_g u_g - f_0 v_a - \beta y v_g = X, \tag{2.29}$$

$$D_g v_g + f_0 u_a - \beta y u_g = Y, \tag{2.30}$$

$$u_a x + v_a y + \rho_0^{-1} (\rho w_a)_z = 0, \tag{2.31}$$

$$D_g \theta_e + w_a \theta_0 z = Q, \tag{2.32}$$

where

$$D_g \equiv \frac{\partial}{\partial t} + u_g \frac{\partial}{\partial x} + v_g \frac{\partial}{\partial y} \tag{2.33}$$

is the material time derivative following the geostrophic wind. We assume that the departures θ_e from the reference potential temperature θ_0 are small, so that $w_a \theta_z$ can be replaced by $w_a \theta_{0z}$ in Eq. 2.32. This is a good approximation in the stratosphere.

2.4.3 The primitive equations in the conventional eulerian mean

The majority of stratospheric motions can be regarded as a mean flow interacting with the disturbances produced by the interaction with the waves

(eddies). In general, this is a two-way interaction: the mean flow can modify the propagation of eddies, and eddies can change the mean flow itself through, typically, non-linear effects. For large-scale stratospheric motions, we consider a *zonal mean* flow, denoted by an overbar, which, for a generic variable A, is defined as

$$\overline{A}(y,z,t) = a_0^{-1} \int_0^{a_0} A(x,y,z,t)dx. \tag{2.34}$$

We thus define the departure from the zonal mean A' as

$$A'(x,y,z,t) \equiv A - \overline{A}. \tag{2.35}$$

The average in Eq. 2.34 is the Conventional Eulerian Mean (CEM), and is taken over all the longitudes x at fixed y, z and t. By definition, we have that $\overline{A}_x = 0$ and $\overline{A'} = 0$. We now replace each variable in Eqs. 2.29 to 2.32 by a zonal mean and a departure part (e.g., $u = \overline{u} + u'$) and we take the zonal mean. After some manipulations, we arrive at the following set of primitive equations for the quasi-geostrophic flow in the beta plane:

$$\overline{u}_t - f_0\overline{v}_a - \overline{X} = -(\overline{v'u'})_y, \tag{2.36}$$

$$\overline{\theta}_t + \overline{w}_a\overline{\theta}_{0z} - \overline{Q} = -(\overline{v'\theta'})_y, \tag{2.37}$$

$$\overline{u}_{ay} + \rho_0^{-1}(\rho_0\overline{w_a})_z = 0, \tag{2.38}$$

$$f_0\overline{u}_z + H^{-1}Re^{-\kappa z/H}\overline{\theta}_y = 0. \tag{2.39}$$

This set of equations can be solved provided appropriate boundary conditions and suitable expressions for $\overline{Q}$, $\overline{Y}$ and $\overline{X}$.

2.5 Driving mechanisms of the BDC

As mentioned in the previous Chapter, the thermal structure of the stratosphere is driven away from the radiative equilibrium because of the breaking of waves propagating from the troposphere, which ultimately results in the described BDC. This Section describes how the resulting eddies generate the required momentum to maintain such a circulation.

In Sect. 2.1, we pointed out that some early studies used the CEM framework (see Sect. 2.4.3) to study the meridional circulation. These studies showed that the CEM is not appropriate for the stratospheric circulation, as it cannot explain the resulting momentum budget. In the CEM approximation, if there is no meridional circulation (i.e., $v = w = 0$, dropping the a subscript

for clarity) the primitive equations for the quasi-geostrophic CEM flow in the beta plane (Eqs 2.36 and 2.37) become

$$\overline{u}_t = -(\overline{v'u'})_y + \overline{X}, \tag{2.40}$$

$$\overline{\theta}_t = -(\overline{v'\theta'})_y + \overline{Q}. \tag{2.41}$$

The eddies contributions $(\overline{v'u'})_y$ and $(\overline{v'\theta'})_y$ will tend to separately change $\overline{u}$ and $\overline{\theta}$, hence destroying the thermal wind and the geostrophic balance. Any departure from the geostrophic balance results in a pressure gradient $\nabla\overline{p}$, which induces a meridional circulation that will adjust $\overline{u}$ and $\overline{\theta}$ so that the thermal wind balance (Eqs. 2.21 and 2.22) remains valid. This compensation allows the zonal wind flow $\overline{u}$ to remain unchanged even in the presence of strong eddy momentum and heat fluxes (Holton, 2004). The CEM works well in the troposphere when describing the Hadley cell (see Fig. 2.1), but it is not satisfactory in the stratosphere because the cancellation between the eddies and the mean flux prevents the calculation of their interactions.

As stated in Sect. 2.1, a theoretical breakthrough was the formulation of the TEM framework by Andrews and Mcintyre (1976). In Eq. 2.37, if $\overline{w} \neq 0$, the adiabatic cooling $\overline{Q}$ tends to recover the thermal wind balance, leaving the diabatic heating $\overline{v'\theta'}_y$ as a small residual. Neglecting the diabatic heating is problematic since it is this forcing that actually allows an air parcel to rise to a higher equilibrium altitude by increasing its potential temperature. Thus, in order to explicitly account for diabatic processes, a *residual meridional circulation* is defined, which is defined as:

$$\overline{v}^* \equiv \overline{v} - \rho_0^{-1}(\rho_0\overline{v'\theta'}/\overline{\theta}_z)_z, \tag{2.42}$$

$$\overline{w}^* \equiv \overline{w} + (\overline{v'\theta'}/\overline{\theta}_z)_y. \tag{2.43}$$

This residual circulation represents that part of the mean circulation whose contribution to the mean flow (in particular to the temperature change Eq. 2.37) is not cancelled by the eddy flux. By replacing Eq. 2.42 and 2.43 in Eqs. 2.36-2.37, we can obtain the quasi-geostrophic primitive equations in the TEM framework:

$$\overline{u}_t - f_0\overline{v}^* - \overline{X} = {\rho_0}^{-1}\nabla\cdot\mathbf{F}, \tag{2.44}$$

$$f_0\overline{u}_z - H^{-1}R\overline{\theta}_y e^{-\kappa z/H} = 0, \tag{2.45}$$

$${\overline{v}^*}_y + \rho_0^{-1}(\rho_0\overline{w}^*)_z = 0, \tag{2.46}$$

$$\overline{\theta}_t + \overline{w}^*\overline{\theta}_z - \overline{Q} = 0. \tag{2.47}$$

The vector $\mathbf{F} = (0, F^{(y)}, F^z)$ is the *Eliassen-Palm flux* (EP) flux vector, and

its components are

$$F^{(y)} \equiv -\rho_0 \overline{v'u'}, \tag{2.48}$$

$$F^{(z)} \equiv \rho_0 f_0 \overline{v'\theta'}/\overline{\theta}_z. \tag{2.49}$$

The divergence of the EP flux is a measure of the dynamical forcing from resolved eddies (i.e., planetary waves) on the mean flow (Edmon Jr et al., 1980) and is defined as:

$$\nabla \cdot \mathbf{F} \equiv -(\rho_0 \overline{v'u'})_y + (\rho_0 f_0 \overline{v'\theta'}/\overline{\theta}_z)_z. \tag{2.50}$$

Using the TEM formulation, the eddy heat flux $\overline{v'u'}$ and momentum heat flux $\overline{v'\theta'}$ do not act separately on the mean zonal flow as for the CEM because of the divergence of the EP flux. Thus, the crucial role of the eddies is to generate a zonal force that acts on the mean zonal flow (Holton, 2004). Another advantage of the TEM with respect to the CEM is that the time-averaged residual circulation is proportional to the rate of the diabatic heating (Eq. 2.47). An air parcel that raises is diabatically heated, and a sinking parcel is diabatically cooled in order to maintain its potential temperature in equilibrium with the surrounding air. This circulation is often defined *diabatic circulation*.

We now use the TEM framework to explain how the zonal force exerted by eddies can cause the departure of the temperature from the radiative equilibrium (introduced in Sect. 1.2.3), and thus cause the meridional circulation. Equations 2.44 and 2.47 can be re-written as follows:

$$\overline{u}_t - f_0 \overline{v}^* = \rho_0^{-1} \nabla \cdot \mathbf{F} + \overline{X} \equiv \overline{G}, \tag{2.51}$$

$$\overline{\theta}_t + \overline{w}^* \overline{\theta}_z = \overline{Q} = -\alpha_{r\theta}(\overline{\theta} - \overline{\theta}_r) = -\alpha_r(\overline{T} - \overline{T}_r), \tag{2.52}$$

where $\overline{X}$ is the zonal force due to small-scale eddies (e.g., gravity waves), and $\overline{G}$ is the total zonal force. The diabatic heating rate $\overline{Q}$ is approximated as a relaxation term proportional to the departure of the mean temperature $\overline{T}$ from its radiative equilibrium state $\overline{T}_r$, where α_r is the Newtonian cooling rate (Eq. 2.52 right-hand side). We assume that $\overline{T}_r$ depends on height alone and that the vertical component of the residual circulation $\overline{w}^*$ and the total forcing $\overline{G}$ have a simple harmonic dependence on time with frequency σ: $\overline{w}^* = Re(\hat{w})e^{i\sigma t}$ and $\overline{G} = Re(\hat{G})e^{i\sigma t}$, respectively. The terms $\hat{w}$ and $\hat{G}$ are complex amplitudes that depend on latitude and height. Under these assumptions, we can combine Eqs. 2.51 to 2.46 to eliminate $\overline{v}^*$ and the resulting equation to Eq. 2.52 and 2.47 to eliminate $\overline{\theta}$. These combinations result in a differential equation that relates the vertical residual circulation

to the total zonal force $\overline{G}$:

$$\frac{\partial}{\partial z}\left(\frac{1}{\rho_0}\frac{\partial(\rho_0\hat{w})}{\partial z}\right)+\left(\frac{i\sigma}{i\sigma+\alpha_r}\right)\left(\frac{N^2}{f_0^2}\right)\frac{\partial^2\hat{w}}{\partial y^2}=\frac{1}{f_0}\frac{\partial}{\partial y}\left(\frac{\partial\hat{G}}{\partial z}\right) \tag{2.53}$$

Equation 2.53 is elliptic and implies that a local forcing applied in any region will produce a non-local response in the form of a circulation that tends to maintain the thermal wind balance between the zonal mean flow and the meridional temperature gradient (Holton, 2004).

Equation 2.53 is rather complicated; hence, we only try to give some insight about the dependance of the vertical residual velocity on the wave forcing, as a function of the coefficient $(i\sigma)/(i\sigma+\alpha_r)$. For high frequency variations ($\sigma >> \alpha_r$), the coefficient $(i\sigma)/(i\sigma+\alpha_r)$ tends to 1 and scale analysis indicates that the heating term $\overline{Q}$ in Eq. 2.52 can also be significant in driving the residual circulation. For low-frequency variations ($\sigma << \alpha_r$), a similar scale analysis shows that the response of the circulation to any increase of $\hat{G}$ in the vertical (Haynes, 2005). In the steady-state regime, i.e., when $\sigma/\alpha_r \to 0$, $\overline{u}_t = 0$, and Eq. 2.51 reduces to a simple balance between the Coriolis force and the zonal force

$$-f_0\overline{v}^* = \overline{G}. \tag{2.54}$$

We can now combine Eq. 2.54 with Eq. 2.46, and require the boundary condition at the top to be $\overline{w}^* \to 0$ for $z \to \infty$ in order to integrate the vertical component of the residual velocity:

$$\rho_0\overline{w}^* = -\frac{\partial}{\partial y}\left[\frac{1}{f_0}\int_z^\infty \rho_0\overline{G}dz'\right]. \tag{2.55}$$

From Eq. 2.55, the residual circulation across any level is controlled exclusively by the zonal force above that level. This principle is called "downward control", because it establishes the downward effect of the zonal drag (Haynes et al., 1991). We now finally have an expression that explicitly relates the residual circulation to the forcing due to eddies (recall that $\overline{G}$ accounts for both planetary and small-scale wave forcings). For unsteady state (i.e., $\sigma/\alpha_r \neq 0$), Eq. 2.55 accounts for around 84% of the residual circulation, and this percentage increases as σ approaches zero (Haynes et al., 1991). The downward control principle can be used for sufficiently long time averages and sufficiently large horizontal scales in the lower stratosphere, and a simple seasonal mean is sufficient for the steady-state assumption to be valid (Rosenlof and Holton, 1993).

We can now investigate further the dependence of the temperature distribution with the zonal forcing. To this end, we just substitute Eq. 2.55 in

Eq. 2.52 and, neglecting the time-dependance and considering temperature instead of potential temperature, we have

$$\overline{T} - \overline{T}_t = \frac{N^2 H}{\alpha_r \rho_0 R} \frac{\partial}{\partial y} \left[\frac{1}{f_0} \int_z^\infty \rho_0 \overline{G} dz' \right]. \tag{2.56}$$

Eq. 2.56 explicitly shows how the departure of the zonal and time-averaged temperature from its radiative equilibrium value depends on the eddy fluxes. Similar to the downward control principle, their departure of temperature from radiative equilibrium at a certain level depends on the meridional gradient of the eddy forcing above that level. In Eqs. 2.55 and 2.56, the Coriolis effect f_0 is at the denominator, thus these relationships are not valid at the Equator.

In light of these results, we can now have a more profound understanding of the 2-D thermal structure of the middle atmosphere (Figs. 1.7 left panel) and its departure from the radiative equilibrium (Fig. 1.8). In the stratosphere, the largest departures from thermal equilibrium are in the winter hemisphere, and, according to Eq. 2.56, the zonal forcing must be the strongest in this period and region. From Sect. 1.2.4, we know that the strongest forcing in the stratosphere is due primarily to planetary Rossby waves (the large-scale eddies contributing to $\overline{G}$), which can propagate and break into the stratosphere only when the flow is westerly (i.e., during winter). Thus, the thermal structure of the stratosphere in Fig. 1.7 is finally explained, with large departures from radiative equilibrium in the wintertime extratropics and smaller departures during summer.

We can now also explain the mechanism that drives the meridional circulation. The planetary Rossby waves exert a westward drag on the mean flow (because those waves can propagate only westward, see Sect. 1.2.4.2). To conserve momentum, the meridional component of the residual circulation $\overline{v}^*$ is poleward (Butchart, 2014). In the extratropical stratosphere, the eddies maintain the temperature above its radiative equilibrium value (Fig. 1.7); thus, there must be a process that acts to increase temperatures. Since $d\overline{v}^*/dy > 0$, from Eq. 2.46 the vertical residual transport must be downward (i.e., the downwelling $d\overline{w}^*/dz < 0$), thus increasing the temperatures at the high latitudes. By mass continuity, the vertical residual velocity must be upward in the Tropics (i.e., the upwelling), meaning that the temperature is lower than the thermal equilibrium. If we suppose an opposite flow, i.e., upwelling in extratropics and downwelling in the Tropics, it would require an eastward zonal force to balance the momentum, which is not possible for Rossby waves (Butchart, 2014).

The described mechanism is often called "extratropical pump" (Holton et al., 1995). Within the Tropics, the extratropical pump is not the only

factor that drives the upwelling because the local wave drag (within around 20°from the Equator) also contributes to a great part to the upwelling (Plumb and Eluszkiewicz, 1999; Kodera and Kuroda, 2002; Zhou et al., 2012).

We conclude this Section by pointing out that the different types of waves do not contribute separately to the zonal wave drag, but they can closely interact. We refer here to the small-scale gravity waves, whose contribution to the zonal force is $\overline{X}$ in the TEM framework, and to large-scale planetary Rossby waves, whose zonal force is approximated by the EP flux divergence $\nabla \cdot \mathbf{F}$. Modeling studies have demonstrated that there is a large degree of compensation between the forcings from gravity and planetary waves. In particular, when the gravity wave driving is changed, the force exerted by planetary waves changes in the opposite direction (Cohen et al., 2013; Sigmond and Shepherd, 2014; Cohen et al., 2014). Regarding the TEM analysis, we highlight that a recent study has extended it to 3-D, i.e., it is also possible to analyze longitudinal variations of the residual flow (Sato et al., 2021).

2.6 The age of air

The "age of air" (AoA) is a widely used transport diagnostic (Hall and Plumb, 1994) and is generally defined as the transit time for an air parcel to reach a particular location in the stratosphere starting from an initial location, usually taken as the tropical tropopause (Waugh and Hall, 2002).

Because of the mixing (see Sect. 2.3), the air parcels typically follow many transport pathways, each characterized by a different transit time. Hence, in general, we should not refer to a single age for a parcel, but rather to an "age spectrum" (Kida, 1983). The age spectrum is a probability function of all the possible transit times since an air parcel entered the stratosphere from the tropospheric entry point and is often used to quantify the effect of mixing (Li et al., 2012). The first momentum of the AoA, the mean AoA, is generally used to quantify the BDC, but that includes both the effect of the residual circulation and two-way mixing (Hall and Plumb, 1994; Waugh and Hall, 2002).

Figure 2.5 shows age spectra for the Tropics and for extratropics. In the Tropics, the distribution is mostly peaked and relatively close to zero, reflecting that the tropical tropopause is the entry point into the stratosphere (Hall and Plumb, 1994). The narrow transit time range is the result of weak recirculation (mixing) and of the strong residual circulation that plays a major role there (see also Fig. 2.1). In the extratropics, there are many more possible transit times, revealing that an air parcel can recirculate more than in the Tropics, which is the effect of two-way mixing, flattening the age spectrum.

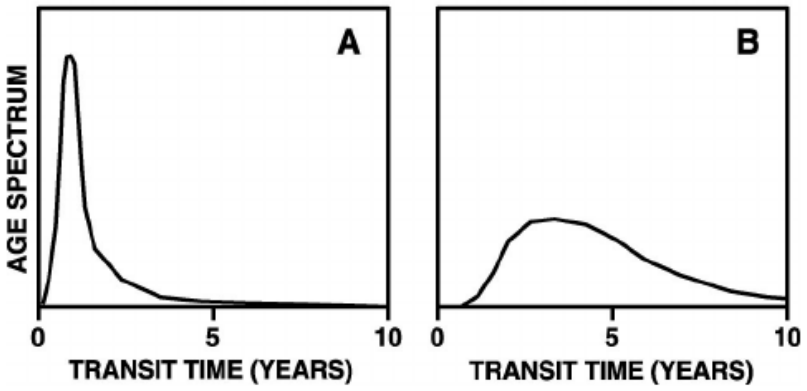

Figure 2.5: Typical age spectra in the Tropics (**A**), and extratropics (**B**). From Waugh and Hall (2002).

2.7 Multi-annual changes in the BDC

This Section discusses the possible changes in the BDC with respect to time (acceleration or deceleration) due to atmospheric anthropogenic-driven changes (e.g., increasing GHGs) and natural variability on time scales larger than a QBO period, i.e., at least one decade. This Section is separated into BDC changes as simulated by models (CCM and GCM, Sect. 2.7.1) and derived from observations of atmospheric tracers or temperature (Sect. 2.7.2). We include reanalyses-based studies in Sect. 2.7.2, as reanalyses should provide the most realistic representation of the atmospheric state.

2.7.1 modeled changes

One of the major challenges in studying the stratosphere is the BDC response to climate change. The increase of GHGs (see Sect. 1.1.3) could lead to two different consequences concerning changes of the BDC: a direct radiative effect due to radiative cooling of the stratosphere and an indirect effect due to the warming of the troposphere and consequent changes in the excitation and propagation of planetary and gravity waves (Kodama et al., 2007). It was found that the indirect effect from the warming troposphere is the primary driver of the modeled BDC changes compared to the direct radiative effect (Oberländer et al., 2013).

The physical mechanism behind the BDC changes in response to climate change is based on solid modeling results. The tropospheric warming expected from climate change leads to a strengthening of the upper flanks of the subtropical jets, which causes an increase of $\overline{u}$ and consequently of $\overline{u} - c$. Thus, the critical layers on the equatorward side of the jets, i.e., regions

where $\overline{u} - c = 0$, move upward, as larger phase velocities are required for the wave breaking condition, which leads to larger wave activity reaching the stratosphere (Shepherd and McLandress, 2011). Since the subtropics represent the most important region of wave breaking from driving the annual cycle of the BDC (Holton et al., 1995; Haynes, 2005, and Sect. 1.2.4.2), the circulation is there strengthened. The conclusion is that the increasing GHGs lead to an acceleration of the BDC.

More recently, Oberländer-Hayn et al. (2016) proposed a new interpretation of the conclusions of Shepherd and McLandress (2011) using several CCMs. Since the tropopause generally rises in response to increasing GHGs (Santer et al., 2003), Oberländer-Hayn et al. (2016) suggest that changes in the BDC could be mainly described by an upward shift of the stratospheric circulation (which includes the subtropical jets) and that an increase of the BDC strength would play a minor role. Such a mechanism is also corroborated by the results from Abalos et al. (2017) who used an artificial tracer to study transport in the lower stratosphere.

Studies of the impact of increasing GHGs on the BDC started as soon as the first climate models were sophisticated enough to account for such interactions. The first work investigating the response of the BDC to changing climate was the pioneer study of Rind et al. (1990). They doubled the CO_2 concentration in a short (3 years) GCM experiment with coarse horizontal resolution (8x10°latitude-longitude). They found a more intense residual circulation with the doubled CO_2 abundancies, which is consistent with more recent model results (e.g., Hardiman et al., 2014). They also argued that the faster residual circulation is driven by increased wave activity from the troposphere and noticed an increased removal of CFCs (see Sect. 1.1.3) and a decrease of ozone in the tropical lower stratosphere together with an increase in the mid-latitudes. An increase of mid-latitudes ozone was also found by Mahfouf et al. (1994) by doubling the CO_2 concentrations in a CCM, thus providing indirect evidence of a BDC acceleration.

A quantity that is often used to quantify the strength of the BDC is the net upward mass flux between turnaround latitudes (i.e., where the vertical residual circulation $\overline{w}^*$ changes sign) at 70 hPa (Rosenlof, 1995). The net upward mass flux $M(p)$ is defined as

$$M(p) = 2\pi a(\psi^*_{max} - \psi^*_{min}) \tag{2.57}$$

where ψ^* is the residual stream function that can be derived from the meridional component of the residual wind by integrating the following expression:

$$\overline{v}^* = -\frac{\partial \psi^*}{\partial x}, \tag{2.58}$$

Butchart and Scaife (2001) found a 3% increase of the strength of the BDC as quantified using the upward mass flux in a GCM during the first half of the twenty-first century in response to increasing GHG concentrations. Over the last decades, a large number of modeling studies has confirmed the increasing strength of the BDC in CCMs (e.g., Butchart et al., 2006; Garcia and Randel, 2008; Butchart et al., 2010; Hardiman et al., 2014, and Fig. 2.6). Furthermore, the BDC acceleration rates in response to increasing GHGs change with respect to height, with a lower trend at higher levels (e.g., Hardiman et al., 2014). In particular, Lin and Fu (2013) found that the magnitude of the BDC trends is stronger for the shallow and transition branches of the residual circulation compared to the deep branch.

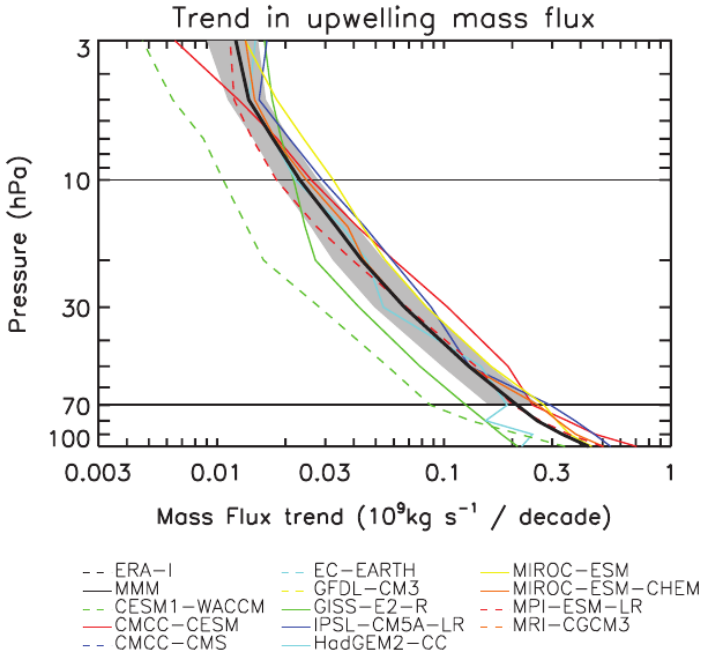

Figure 2.6: Trend in upward mass flux (2006-2099) for the models. The colored lines represent individual models (color code in the legend). Grey shading indicates inter-model standard error. The black line shows the multi-model mean. From Hardiman et al. (2014).

AoA studies provide additional support for increasing BDC strength. It was demonstrated that the upward mass flux M is proportional to the reciprocal of the AoA, i.e., decreasing AoA indicates strengthening of the BDC (Austin and Li, 2006). Modeling studies confirm this relationship and relate the decreasing stratospheric AoA to the increasing GHGs concentration (e.g.,

Oman et al., 2009; Deushi and Shibata, 2011; Li et al., 2018)

While the impact of GHGs on BDC trends has been widely examined, an increasing number of studies have investigated the impact of changes of ozone-depleting substances (ODS, see Sect. 1.2.6) on BDC trends. Austin and Li (2006) first noticed the absence of significant AoA trends when ozone was increasing and large AoA reduction when ozone depletion was occurring and suggested that the ODS could significatively impact the residual circulation trends. After these new and exciting results, a large number of studies continued investigating the impact of the ODS trends on BDC trends (e.g., Oman et al., 2009; Oberländer-Hayn et al., 2015; Garfinkel et al., 2017; Polvani et al., 2017). These studies have shown that, in many CCMs, increasing ODS are the main driver of the acceleration of the residual circulation in the summertime Southern Hemisphere over the last decades of the twenty-first century. Ozone depletion cools the springtime Antarctic lower stratosphere, and, as a consequence, the stratospheric polar vortex is strengthened, with a consequent delay of the polar vortex breakup (Orr et al., 2012; Previdi and Polvani, 2014). These changes also drive trends in the wave forcing, which feedback the BDC trends (Abalos et al., 2019).

The ban of ODS by the Montreal Protocol is expected to impact the BDC trends in the twenty-first century. Indeed, it was shown that the BDC trends in the coming decades will be largely reduced because of the phasing out of the ODS (Polvani et al., 2019). This reduction will tend to cancel out the increasing BDC trends due to increasing GHGs in the coming decades. However, the degree of cancellation between the contribution from decreasing ODS and increasing GHGs to the BDC trends is uncertain because it depends on the future distributions of these gases (Polvani et al., 2019).

In Sect. 2.3, we described the significant role for tracer transport of mixing processes together with the residual circulation. Studies that identify decreasing BDC trends often use mean AoA; hence, they cannot separate the effects of residual circulation and two-way mixing. For this reason, an increasing number of studies have investigated the effect of mixing on the total BDC trend, the latter often quantified as the total mean AoA trend. The decreasing AoA trend projected in the future has been attributed to both an acceleration of the residual circulation and a weakening of the mixing, each contributing to about half of the modeled decrease of mean AoA (Li et al., 2012; Garny et al., 2014; Ploeger et al., 2015a). Ploeger et al. (2015b) showed that, locally, mixing increases AoA at low latitudes and decreases AoA at higher latitudes and that the mixing is strongest below around 70 hPa. Recent modeling studies showed that the effect of mixing on the BDC trends are strongest in the lowermost stratosphere, while at higher levels they are related to changes in the residual circulation (Dietmüller et al.,

2017; Abalos et al., 2019). Mixing is also a major source of uncertainty when it comes to comparing BDC trends from CCMs. Inter-model differences in mixing are the primary cause of the spread in the AoA trends, with a minor effect of the residual circulation (Dietmüller et al., 2018).

2.7.2 Observed changes

While CCMs and GCMs simulate an acceleration of the BDC in the past decades, observational studies of BDC trends over few past decades seem to mostly disagree with modeling results. Engel et al. (2009) used baloon-borne measurements of SF_6 and CO_2 to estimate age of air in the northern mid-latitudes between 24 and 35 km from 1975 to 2005. They found a non-significant positive AoA trend, in contrast with the modeling studies mentioned in Sect. 2.7.1. Later on, the time series was extended up to 2016 with additional balloon-borne measurements (Engel et al., 2017). These AoA trends calculated over this extended time series are smaller than the previous estimate (Engel et al., 2009) and still not statistically significant.

Age of air trends were also obtained from space-borne measurements of sulphur hexafluoride by the Michelson Interferometer for Passive Atmospheric Sounding (MIPAS, Stiller et al., 2012; Haenel et al., 2015; Stiller et al., 2017), thus eliminating the problem of sparse data coverage highlighted for baloon-borne observations in Engel et al. (2009) and Engel et al. (2017). The AoA trends derived from satellite measurements reveal an inhomogeneous spatial distribution over both the meridional and vertical directions, in particular showing opposite signs of the AoA trends in the two hemispheres. Stiller et al. (2012) argued that their results are consistent with those from Engel et al. (2009) and with the increasing tropical upwelling detected by models, and Stiller et al. (2017) suggested that the inhomogeneous spatial pattern is caused by a southward shift of the stratospheric circulation as a consequence of a southward shift of the subtropical transport barriers. However, the interpretation of these results must take into account the short lifetime of the spacecraft used for the measurements, which flew only for the 2002-2012 period.

Together with SF_6 and CO_2, space-borne measurements of water vapor can be used to infer changes in the BDC (Hegglin et al., 2014). Over the 1986-2010 period, they found decreasing AoA derived from water vapor in the lower stratosphere and increasing AoA in the upper stratosphere, which is partly consistent with model results outlined in Sect. 2.7.1.

Ground-based FTIR measurements of hydrogen chloride also reveal possible changes in the BDC (Mahieu et al., 2014). Hydrogen chloride is expected to decrease throughout the stratosphere in response to the implementation of

the Montreal Protocol (see Sect. 1.2.6). However, around 2007, the measured hydrogen chloride concentrations increased significantly in the lower stratospheric Northern Hemisphere. Mahieu et al. (2014) attributes this anomaly to the slowdown of the BDC in the Northern Hemisphere over several years. More recently, Strahan et al. (2020) also used ground-based measurements of nitric acid and hydrogen chloride total columns from 1994 to 2018 combined with AoA calculations from a meteorological reanalysis to investigate lower stratospheric circulation changes. They found decreasing AoA (1 month per decade) in the Southern extratropical lower stratosphere compared to the Northern Hemisphere. This is in contrast with the modeling studies mentioned in Sect. 2.7.1, which simulate an AoA increase in the Southern Hemisphere due to the ODS decline.

The recent study from Strahan et al. (2020) has found that the BDC is characterized by a 5- to 7-years variability that is the result of the interaction between the BDC annual cycle and the QBO. As mentioned in Sect. 1.2.5.1, the interaction between the QBO and the BDC is not surprising: the QBO induces a secondary meridional circulation that was further investigated by Ploeger and Birner (2016) and that can explain tracer anomalies (Strahan et al., 2015, 2020).

Numerous studies have investigated BDC changes over short periods, typically less than 10 years after 2000 using space-borne tracer observations. Short-term BDC changes were reported using ozone (Nedoluha et al., 2015), hydrogen fluoride (HF, Harrison et al., 2016), chlorodifluoromethane ($CHClF_2$, Chirkov et al., 2016) and carbonyl sulphide (OCS, Glatthor et al., 2017). The mentioned studies over short-term BDC changes derived from observed tracers should thus be put into the perspective of the longer variability pointed out by Strahan et al. (2020).

As mentioned in Sect. 2.5, the residual circulation velocities are tightly related to temperature variations: a BDC acceleration would lead to a cooling of the tropical lower stratosphere and to warming of the polar latitudes. Based on this, Fu et al. (2015) analyzed the BDC changes during the period 1980-2009 using satellite measurements of lower stratospheric temperature. They found that the annual mean BDC has accelerated but the increase is statistically significant (at 90% confidence level) only in the Southern Hemisphere. More recently, Fu et al. (2019) have examined a longer record of temperature observations (1980-2018), which allowed the separation between ozone depletion (1980-1999) and ozone recovery (2000-2018) periods. They show that the BDC has accelerated for the 1980-1999 period, but decelerated for 2000-2018, with the changes mainly in the Southern Hemisphere, and argue that the effects of ozone recovery might play a role. They also found a global BDC acceleration over the last 40 years at the 90% confidence level.

Those temperature-based changes are in agreement with CCM and GCM simulations for ozone depletion and recovery periods and for GHG-induced changes over the past 40 years (see Sect. 2.7.1).

The derivation of AoA trends from observations could be flawed by a number of factors. Garcia et al. (2011) have assessed the issues in computing AoA trends from baloon-borne measurements of SF_6 and CO_2 concentrations. They found that sparse temporal and spatial sampling could be a major issue in computing AoA trends. Indeed, they computed AoA in a CCM with similar sampling as in the observations as a sensitivity test and found that AoA trends are roughly consistent with those reported by Engel et al. (2009). Note that the same CCM simulates a decreasing AoA as described in Sect. 2.7.1. Garcia et al. (2011) suggested that AoA trends obtained from observed tracers are ambiguous and that proper AoA calculations would require well-sampled and linearly increasing tracers, but such idealized tracers do not exist.

AoA trends derived from SF_6 observations are put into further doubt due to the existence of chemical sinks of SF_6 in the mesosphere, which were often not taken into account while deriving AoA from SF_6. The very recent paper of Loeffel et al. (2022) showed that AoA trends derived from SF_6 can actually change sign when the mesospheric sinks of SF_6 are taken into account. Furthermore, the AoA trends obtained from observed tracers are strongly sensitive to the choice of different methods and parameters applied to the tracer concentrations to derive AoA (Fritsch et al., 2020). It was indeed shown that these adjustable parameters lead to an uncertainty in the AoA trends that can be reduced by a factor of 2 (Fritsch et al., 2020). In addition, Hardiman et al. (2017) argued that, in order to have a significant BDC trend, a time series should be minimum of 30 years and showed that the dynamical variability of the BDC can mask possible trends on time scales shorter than 12 years.

In order to support climate model projections, meteorological reanalyses are often used to derive BDC trends. For example, Diallo et al. (2012) analyzed the European Centre for Medium-Range Weather Forecast reanalysis (ERA-Interim, Dee et al., 2011) for the 1989-2010 period and found significant negative AoA trends in the lower stratosphere (below 25 km) in the Southern Hemisphere equatorward of 40°. In the extratropical mid-stratosphere, marginally significant positive trends were detected above 25 km, which agrees with observational studies. The AoA trend becomes significant if a shorter period is considered and is consistent with the trends obtained from satellite data for the same period by Stiller et al. (2012). Those results with ERA-Interim were also confirmed by Monge-Sanz et al. (2013). However, calculations of upwelling mass flux at 70 hPa for the 1989-

2009 period with ERA-Interim yielded different results (Seviour et al., 2012), with statistically significant negative trends in the upwelling mass flux. Yet, this result was not considered reliable because it is inconsistent with the negative temperature trend in the same reanalysis, assuming a mainly adiabatic temperature response to changes in upwelling at 70 hPa.

More recent studies have compared the long-term AoA trends among modern reanalyses for the 1985-2015 period. Chabrillat et al. (2018) compared the mean AoA linear trends obtained from ERA-Interim, the Japanese 55-year Reanalysis (JRA-55 Kobayashi et al., 2015), Modern-Era Retrospective analysis for Research and Applications (MERRA, Rienecker et al., 2011) and its version 2 (MERRA-2 Gelaro et al., 2017), and the National Centers for Environmental Prediciton - Climate Forecast System Reanalyis (NCEP-CFSR Saha et al., 2010), and found large disagreements depending on the considered period and input reanalysis. The authors noted that no other reanalysis than ERA-Interim finds the dipole structure in the AoA trend that was found using MIPAS observations of SF_6 for the period 2002-2012 (Stiller et al., 2017). A reanalysis intercomparison was also performed by Ploeger et al. (2019), but limiting to ERA-Interim, JRA-55 and MERRA-2. While Chabrillat et al. (2018) analyzed only the mean AoA, they computed the whole time-dependent age spectrum. The mixing effect is very important when considering AoA trends (e.g., Ploeger et al., 2015a), and in particular Ploeger et al. (2019) found that the mixing can explain the mean AoA differences between ERA-Interim and MERRA-2. With regard to long-term trends, Ploeger et al. (2019) found decreasing AoA for the 1989-2015 period in the lower stratosphere, consistent with the modeling results outlined in Sect. 2.7.1, while in the upper levels the trends appear less robust. As for Chabrillat et al. (2018), the trends computed over shorter periods deliver different results depending on the considered reanalysis, with again only ERA-Interim showing the dipole structure as viewed from satellite observations. The main difference between these two studies is the type of CTM used to simulate the age. The CTM used in Chabrillat et al. (2018) is a kinematic model, i.e., it uses only surface pressure and horizontal winds from reanalyses as input. On the other hand, Ploeger et al. (2019) used a diabatic model, which calculates the transport from diabatic heating rates from the reanalyses. The largest trend differences between the studies occur for short-term (decadal) changes. For changes before 2000, the differences could be attributed to the missing representation of the Pinatubo eruption in the kinematic model (Chabrillat et al., 2018), but differences over other shorter periods are unclear to date (Ploeger et al., 2019).

3 Objectives of the thesis

The present thesis is part of a collaboration between the University of Liège and the Belgian Institute for Space Aeronomy (BIRA-IASB) through the research project ACCROSS (Atmospheric Composition and Circulation investigated with meteorological Reanalyses, Observational datasets and models for the Study of the Stratosphere and its changes). The main goal of the ACCROSS project is to improve our understanding of the circulation changes in the stratosphere during the past three decades through the use of observation and model simulation time series of selected long-lived tracers.

Within the ACCROSS project, another Ph.D. thesis was carried out by Maxime Prignon, which used the total inorganic fluorine in the stratosphere as a long-lived tracer. The first objective of that thesis was to evaluate the major source of total inorganic fluorine in the stratosphere using ground-based and satellite observations together with model simulations. The main goal was then to investigate long-term changes and the interannual variability of the BDC using satellite and FTIR observations and CTM simulations of total fluorine.

The present thesis is complementary to Maxime Prignon's work. Within the common aim set by the ACCROSS project, the present work uses a different long-lived tracer: nitrous oxide (N_2O), which, thanks to its relatively simple chemistry, allows me to focus more on the stratospheric dynamics, separating the impact of advection and mixing on its volume mixing ratio.

Before focusing on long-term changes, it is necessary to evaluate the performances of the models to simulate the mean N_2O abundances. To this end, we define **the first objective of the thesis** as:

- **Objective 1** - Evaluate the realism of the BDC in a CCM by investigating and evaluating the climatological abundances of N_2O and the impact of the BDC on those abundancies, and comparing them with CTM simulations and a chemical reanalysis.

This evaluation sets the ground for the **second and main objective of this thesis**.

- **Objective 2** - Evaluate the changing BDC in the same CCM by studying multi-decadal and decadal changes of N_2O in the stratosphere, comparing them with observations and CTM simulations, and calculating the impact of the BDC on those changes.

This investigation uses several CTM and CCM simulations as well as ground-based FTIR and satellite observations. Thanks to the model simulations, we

can further isolate the impact of the BDC on the N_2O changes, by separating the contribution from advection and mixing on those changes.

4 Observed and modeled datasets

The present Chapter describes the datasets employed in this thesis, together with those that were initially considered for inclusion, but ultimately discarded, and some preliminary comparisons of the N_2O products. Section 4.1 describes the CCM used in this thesis and its various configurations and versions. Section 4.2 illustrates the CTM used for comparison and the dynamical reanalyses that drive it. Section 4.3 provides an overview of the remote sensing measurements and Section 4.4 is devoted to the description of the chemical reanalysis. An overview of the model and reanalyses datasets is provided in Table 4.1. Section 4.5 examines the datasets that were initially considered for inclusion in this thesis, but ultimately discarded and the reasons for rejection. Lastly, Section 4.6 shows some preliminary comparisons of N_2O mixing ratios and columns among the datasets in order to set the ground for the following of this thesis.

Throughout the thesis (unless differently stated), we will refer to the CCM and the CTM simulations as "models" to distinguish them from the measurements obtained from the ground-based and satellite instruments and from the chemical reanalysis.

Dataset name	Reference	Dynamical Reanalysis	Chemical reanalysis of	Model grid	Top level
WACCM4	Marsh et al. (2013)	none	none	2.5°x1.9°, L66	$5.1x10^{-6}$ hPa
WACCM-CCMI	Garcia et al. (2017)	none	none	2.5°x1.9°, L66	$5.1x10^{-6}$ hPa
WACCM-REFD1	Gettelman et al. (2019)	none	none	1°x1°, L70	$5.1x10^{-6}$ hPa
CTM+ERAI	Chabrillat et al. (2018)	ERA-Interim (Dee et al., 2011)	none	2.5°x2°, L60	0.1 hPa
CTM+ERA5	Prignon et al. (2021)	ERA5 (Hersbach et al., 2020)	none	2.5°x2°, L87	0.01 hPa
CTM+JRA55	Chabrillat et al. (2018)	JRA-55 (Kobayashi et al., 2015)	none	2.5°x2°, L60	0.1 hPa
CTM+MERRA	Chabrillat et al. (2018)	MERRA (Rienecker et al., 2011)	none	2.5°x2°, L72	0.01 hPa
CTM+MERRA2	Chabrillat et al. (2018)	MERRA2 (Gelaro et al., 2017)	none	2.5°x2°, L72	0.01 hPa
BRAM2	Errera et al. (2019)	ERA-Interim (Dee et al., 2011)	MLS 190GHz (Livesey et al., 2015)	3.75°x2.5°, L37	0.1 hPa

Table 4.1: Overview of the model datasets and the chemical reanalysis used in this thesis.

4.1 The Whole Atmosphere Community Climate Model

The CCM used in this thesis is the Whole Atmosphere Community Climate Model (WACCM). WACCM is the extended version to the whole atmosphere of the Community Atmosphere Model (CAM, Neale et al., 2013), which is the atmospheric model of the Community Earth System Model (CESM, Hurrell et al., 2013), which is developed at the National Center of Atmospheric Research (NCAR) in Boulder, Colorado.

In the following, Section 4.1.1 provides a brief description of CESM and mentions its major components. Then, Section 4.1.2 describes the atmospheric model CAM in more detail, and Section 4.1.3 illustrates the WACCM

configuration, with a description of the differences with CAM, and its versions used here.

4.1.1 The Community Earth System Model

CESM is an Earth System Model (ESM), i.e., a global climate model that simulates an interacting atmosphere, ocean, land surface and sea ice (i.e., the physical climate system), together with the biogeochemical processes that can combine with the physical system (for example the carbon cycle, Flato, 2011). CESM uses CAM, or its whole atmosphere extension WACCM, as the atmospheric component. The model simulating the land surface is the Community Land Model, which accounts for all physical, chemical and biological processes that affect the climate (Lawrence et al., 2011). The sea ice component simulates the global ice cover, and has gained relevance in the past decades because of global warming and the consequent reduction of the ice cover (Holland et al., 2012). CESM uses the Community Ice Code as sea ice model (Hunke et al., 2010; Holland et al., 2012). The ocean component in CESM is the Parallel Ocean Program, which solves the primitive equations for ocean dynamics (Smith et al., 2010). The carbon cycle in CESM is implemented through a biogeochemical model that couples the atmosphere, the ocean and the land models (Lindsay et al., 2014). CESM also includes a coupled land ice model, which simulates the evolution of the ice cover over the land (e.g., Greenland or Antarctica, Rutt et al., 2009). All the fluxes from the different models interact through a central coupler (Craig et al., 2012).

4.1.2 The Community Atmosphere Model

In the past decades, NCAR has developed several versions of CAM with increasing complexity and interactive feedback processes. This Section describes version 4 of CAM (released in 2010), because it is used in both Chapters 6 and 7, while the description of version 6 of CAM (released in 2018) is devoted to Sect. 4.1.6. CAM4 is the sixth generation of the NCAR atmospheric models (earlier versions are: the Community Climate Model versions 0,1,2,3 and CAM3).

CAM is characterized by a finite volume (FV) dynamical core based on a flux-form semi-Lagrangian (FFSL) scheme (i.e., an Eulerian scheme) for the horizontal advection (Lin and Rood, 1996; Lin, 2004), while the vertical discretization is Lagrangian, with a terrain-following (hybrid sigma) coordinate system. The use of an Eulerian scheme for the horizontal discretization and a Lagrangian for the vertical is motivated by the fact that the governing

equations become 2-D instead of 3-D. The FV discretization is applied to a control volume that is bounded by two Lagrangian material surfaces, and that freely moves (floating, compressing or expanding) in the vertical according to the dynamics. Consequently, the Lagrangian surfaces will deform under the diabatic cooling or heating on a wide range of time scales depending on the atmospheric process. In order to reconcile the Lagrangian and the Eulerian frameworks, a conservative and accurate remapping from the first into the second is needed. In CAM, this conservative remapping algorithm uses the hydrostatic pressure as the mapping coordinate to reconstruct the mass, horizontal winds, tracers mixing ratios and energy, and, ultimately, it allows deriving the vertical velocity from mass conservation (Neale et al., 2010a).

In CAM, the default horizontal resolution is $0.9° \times 1.25°$latitude-longitude with 26 hybrid-sigma vertical levels from the surface to around 2 hPa (roughly 42 km of altitude). The deep convection scheme is based on the mass-flux scheme developed by Zhang and McFarlane (1995), and modified adding the convective momentum transport (Richter and Rasch, 2008) and a modified plume calculation (Raymond and Blyth, 1992). Regarding the shallow convection, i.e., the convective activity that is not resolved by the primary convection scheme, the energy and the total water equations are simplified and recursively solved, as described in Neale et al. (2010b). For the evaporation of the convective precipitation, CAM4 uses the scheme developed by Sundqvist (1988).

CAM4 uses a combination of dry and moist mixing ratios for tracer constituents, the former for the FV advective scheme and the latter for the convection scheme. The conversion bewteen "dry" and "wet" mixing ratios is described in Neale et al. (2010b). The processes involving non-convective clouds are parametrized following Rasch and Kristjánsson (1998) and Zhang et al. (2003). The cloud amount, with the relative optical properties, is a diagnostic approach based on Slingo (1987), and modified according to Hack et al. (1993); Kiehl et al. (1998); Rasch and Kristjánsson (1998), which can diagnose three types of clouds: low-level marine clouds, convective clouds and layered clouds (the latter form when relative humidity exceeds a pressure-depending threshold).

The parameterization of the shortwave radiation is based on Briegleb (1992) and Collins (2001), and the radiative transfer for longwave radiation is based on Ramanathan and Downey (1986). Both representations are described in Neale et al. (2010b). The vertical diffusion is parameterized in CAM4, computing molecular diffusivities through a turbulence parameterization, and updating the tendencies of the input variables (e.g., Boville and Bretherton, 2003). Furthermore, this parameterization accounts for the sep-

aration between the free atmosphere and the planetary boundary layer, with different values of the diffusivities for the two layers (Neale et al., 2010b). For CAM4, it is possible to have online chemistry that includes both tropospheric and stratospheric processes as well as aerosol models (CAM-Chem, Emmons et al., 2010; Lamarque et al., 2012).

4.1.3 Extension of CAM to the Whole Atmosphere

WACCM extends the parameterizations and physics of CAM to the whole atmosphere, and includes some adjustments and updates in the chemistry and physics in order to take into account the higher top. WACCM has 66 hybrid-sigma vertical levels (in its version 4) from the ground to around 140 km of altitude. The vertical resolution depends on the height: it is 3.5 km above 65 km, 1.75 km around 50 km, 1.1-1.4 km below 30 km, and 1.1 km in the troposphere, with a much larger vertical resolution in the planetary boundary layer. The standard horizontal resolution in WACCM is 1.9°x2.5°, with 96 longitude and 144 latitude points, which is coarser compared to CAM because of the much higher model top and finer vertical resolution. The time resolution is 1800 seconds (30 minutes) for the physical parameterizations, but can vary depending on the requirement for computation stability within the FV scheme.

WACCM is not able to internally generate the QBO (see Sect. 1.2.5.1). For this reason, the QBO is forced through a relaxation of the modeled winds to observed winds in the tropical stratosphere. The relaxation method can use observed fields that are fixed in time, with idealized east or west QBO phases or a repeating 28-month QBO, or can be time-varying using observed winds. Both relaxation methods are described in Matthes et al. (2010).

In the following, we will provide an overview of the major changes in WACCM version 4 compared to CAM4.

- The vertical diffusion of CAM is extended in WACCM to include the gravitational separation of constituents due to different molecular weights following Banks and Kockarts (2013).

- WACCM also includes a parameterization of vertically propagating gravity waves (see Sect. 1.2.4.1). The parameterization can separate between gravity waves originating from a flow passing over a mountainous region (orographic gravity waves, OGW), and generated from the atmospheric motion (non-orographic gravity waves, NOGW). The parameterization of the OGW is based on the subgrid standard deviation of the orography and follows McFarlane (1987). For NOGW, the waves

can be triggered by convective heat release (Beres et al., 2005), or excited by frontal system (Richter et al., 2010). For both processes, the waves are parametrized according to a trigger function that depends on the actual atmospheric state.

- With the WACCM default horizontal resolution, the mountain stress resolved by the model can account only for the major mountain ranges (e.g., the Rocky Mountains, Himalayas). The unresolved mountain stress is parametrized as the turbulence surface drag using the effective roughness length (Fiedler and Panofsky, 1972) and used to assess the height of the planetary boundary layer and non-local transport (Holtslag and Boville, 1993).

- The higher model top in WACCM requires a different handling of the radiation compared to CAM4. Above 65 km, the heating rates from parametrizations from the lower and upper atmosphere are merged together, as 65 km is near a local minimum for shortwave heating and longwave cooling. The new parametrizations of both shortwave and longwave radiations are described in Neale et al. (2010a).

- Version 4 of WACCM has a detailed neutral chemistry model for the middle atmosphere based on the Model for Ozone and Related Chemical Tracers, version 3 (MOZART3, Kinnison et al., 2007), which includes processes ranging from the troposphere to the thermosphere. This mechanism includes the O_x, NO_x, HO_x, ClO_x and BrO_x chemical families, together with CH_4 and its degradation products, for a total of 52 neutral species, one invariant (N_2), 127 gas-phase reactions, 48 neutral photolytic reactions and 17 heterogeneous reactions. The chemical rate constants for the gas-phase reactions are from the Jet Propulsion Laboratory publication 06-2 (JPL06-2, Sander et al., 2006). The heterogeneous reactions take place on different aerosol types, i.e., sulfate, nitric acid trihydrate and ice. WACCM includes also 6 ion constituents (O^+, $O_2{}^+$, N^+, $N_2{}^+$, NO^+ and electrons) for the ionosphere, with the reaction rate constants from Roble (1995). A comprehensive list of all the available species and reactions in version 4 of WACCM can be found in Neale et al. (2010a).

In the following, we describe the different WACCM versions used throughout this thesis. Section 4.1.4 describes the WACCM version that was downloaded at BIRA-IASB, and used for several sensitivity tests and two production runs. Section 4.1.5 continues with the description of an improved WACCM version, characterized by a better parametrization of the OGW. Section 4.1.6

concludes with the description of the latest CESM and WACCM versions, which have considerable improvements compared to their previous releases.

4.1.4 WACCM simulations produced at BIRA-IASB

CESM, hence WACCM, is a community model, i.e., it is publicly available for scientific use for the whole community. In October 2016, we downloaded the latest (at that time) public version of CESM (v1.2.2) at `https://svn-ccsm-models.cgd.ucar.edu/cesm1/release_tags/cesm1_2_2/`, which includes version 4 of WACCM (Marsh et al., 2013).

After the porting (i.e., installing) of CESM on the high-performance computer (HPC) at BIRA-IASB, we started some experiments in order to explore the tracer transport, in particular using the mean AoA. For this purpose, we used a particular configuration of WACCM, the specified-dynamics (SD) setup, which allows the dynamical variables of the model (e.g., horizontal winds and temperature) to be nudged towards external dynamical variables from reanalyses. Those external fields come from the Modern-Era Retrospective analysis for Research and Applications (MERRA, Rienecker et al., 2011), and are used to nudge the dynamical variables of the model as follows:

$$A_{sim} = A_{MERRA} \cdot \alpha + (1 - \alpha) A_{int}, \tag{4.1}$$

where A_{sim} is the variable simulated by the model, A_{MERRA} is the meteorological field from the MERRA reanalysis, A_{int} is the internally-generated variable in WACCM, and the α value is the nudging factor (default=0.1). This scheme is applied from the surface to 50 km of altitude, with fully interactive meteorological variables above 60 km and a linear transition in between (Kunz et al., 2011). The vertical transport is ultimately derived from the divergence of the A_{sim} horizontal winds within the model. The SD-WACCM configuration is very valuable, because it allows comparison with the free-running WACCM setup and thus the evaluation of its transport against a configuration where the meteorological variables are constrained to reanalyses.

We first ran some sensitivity tests to assess the ability of WACCM to simulate the observed mean AoA, both for the SD-WACCM and the free-running WACCM configurations. We first tested the impact of the QBO on the mean AoA in free-running WACCM by switching off the relaxation to the tropical stratospheric winds described in Sect. 4.1.3. We found that the lack of the QBO in WACCM leads to younger mean AoA throughout the stratosphere across the whole globe (Fig. 4.1). This large difference was not further investigated because the QBO is not the subject of this thesis, but

this sensitivity test allowed us to gain insights about the complexity of the model.

Concerning the SD-WACCM simulation, we found that nudging the meteorological fields towards reanalyses provides a more realistic representation of the stratospheric transport compared to the free-running configuration (Fig. 4.1). In order to further explore the impact of the nudging scheme on the simulated mean AoA, we performed some sensitivity tests varying the α parameter. Interestingly, we found that increasing α, i.e., forcing the model to be close to the reanalysis, delivers unrealistic results, specifically the mean AoA is underestimated by half in the extratropics when α is increased by a factor of 100 (Fig. 4.2). Indeed, for a newer version of WACCM, it was recently shown that the nudging scheme introduces errors in the tracer balance for the specified dynamics configuration (Davis et al., 2022).

We continued exploring the mean AoA in WACCM by implementing an idealized synthetic tracer that has no chemical sinks, but only a constant linear increase at the surface (Tracer Increasing Linearly at the Surface, TILS, Fig. 4.3). We implemented TILS because we aimed for a fair comparison with the synthetic tracer initially used in Chabrillat et al. (2018). Early experiments were promising, with the WACCM results similar to the CTM results (not shown). However, the initial location for the mean AoA computation in Chabrillat et al. (2018) changed during the review process from the surface to the tropical tropopause, which made the TILS tracer in WACCM not comparable anymore with the one in the CTM. We did not perform any production runs with the corrected TILS because of the computational cost of such experiments.

Within the framework of the ACCROSS project, we performed a multi-decadal (1985-2014) production run with a modified chemical scheme that is included in Prignon et al. (2019). In that study, WACCM is used for comparison with ground-based measurements of stratospheric columns of chlorodifluoromethane ($CHClF_2$, HCFC-22). Since HCFC-22 and the other hydrochlorofluorocarbons (HCFCs) and hydrofluorocarbons (HFCs) are not present in the default WACCM chemistry scheme, they were added along with their stratospheric reactions. We included the following chemical species: HF, HFC23 (CHF_3), HFC125 (CHF_2CF_3), HFC134a (CH_2FCF_3), HFC143a ($C_2H_3F_3$), HCFC141b ($C_2H_3Cl_2F$), HCFC142b (CH_3CClF_2), HA2402 ($C_2Br_2F_4$), HA1211 (CF_2ClBr), HA1301 ($CBrF_3$), CFC114 ($C_2Cl_2F_4$) and CFC115 (C_2ClF_5). We also introduced the new photolysis reactions (where $h = 6.626 \times 10^{-34}$JHz^{-1}

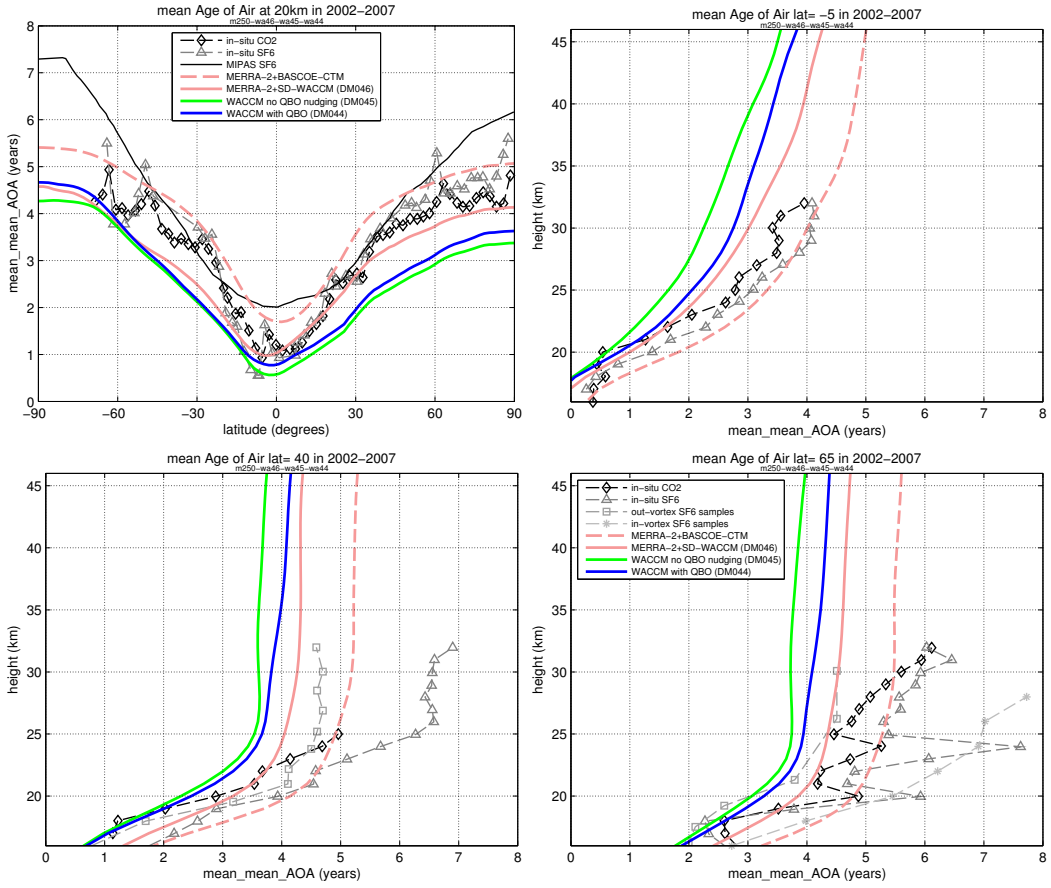

Figure 4.1: Mean AoA for the 2002-2007 period for free-running WACCM (blue), free-running WACCM with no QBO nudging (green), SD-WACCM (pink solid) and BASCOE CTM driven by MERRA (pink dashed). Upper left: values at 20 km; upper right: vertical profiles at 5°S; lower left: vertical profiles at 40°N; lower right: vertical profiles at 65°N. The black solid line represents AoA from the Michelson Interferometer for Passive Atmospheric Sounding (MIPAS) SF_6 observations in 2002-2007 (Kovács et al., 2017). The symbols represent in-situ observations collected during 1990's (Waugh and Hall, 2002).

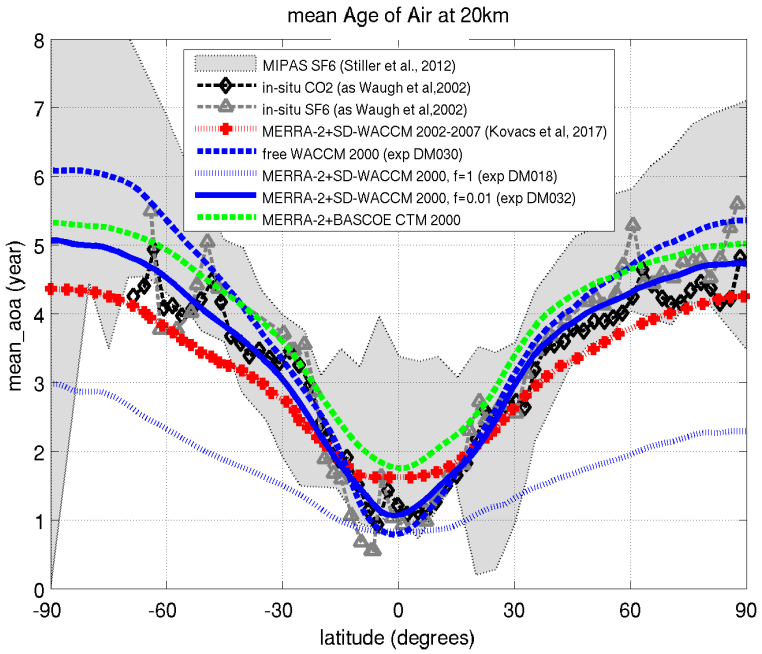

Figure 4.2: Mean AoA for year 2000 at 20 km. The grey envelope represents SF_6 data from Stiller et al. (2012); black and grey triangles denote respectively CO_2 and SF_6 data from (Waugh and Hall, 2002). The red crossed line indicates SD-WACCM simulation nudged to MERRA2 from Kovács et al. (2017). The dashed blue line is free-running WACCM with fixed year 2000. Dotted blue line is SD-WACCM with $\alpha = 1$, blue continuous line is SD-WACCM with $\alpha = 0.01$. The dashed green line is BASCOE CTM driven by MERRA2 for fixed year 2000.

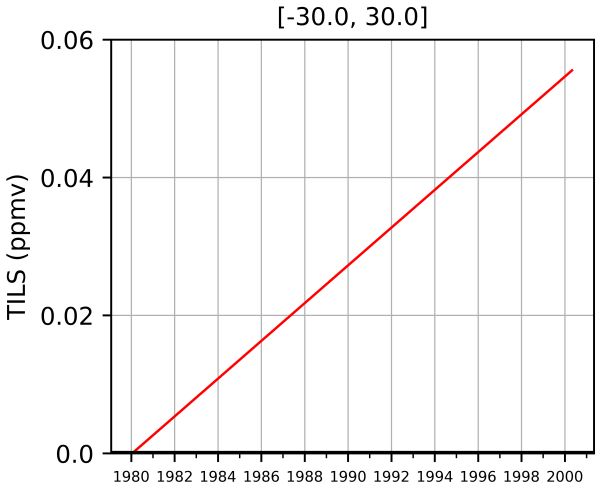

Figure 4.3: Concentration (ppmv) of TILS volume mixing ratio at the surface averaged between 30°S-30°N (1980-2000).

is the Planck constant and ν is the frequency of the incoming radiation):

$$
\begin{aligned}
&\mathrm{CFC114} + \mathrm{h}\nu \longrightarrow 2\,\mathrm{Cl} + 4\,\mathrm{HF}\\
&\mathrm{CFC115} + \mathrm{h}\nu \longrightarrow \mathrm{Cl} + 5\,\mathrm{HF}\\
&\mathrm{HFC23} + \mathrm{h}\nu \longrightarrow 3\,\mathrm{HF}\\
&\mathrm{HFC125} + \mathrm{h}\nu \longrightarrow 5\,\mathrm{HF}\\
&\mathrm{HFC134a} + \mathrm{h}\nu \longrightarrow 4\,\mathrm{HF}\\
&\mathrm{HFC143a} + \mathrm{h}\nu \longrightarrow 3\,\mathrm{HF}\\
&\mathrm{HCFC141b} + \mathrm{h}\nu \longrightarrow \mathrm{HF} + 2\,\mathrm{Cl}\\
&\mathrm{HCFC142b} + \mathrm{h}\nu \longrightarrow 2\,\mathrm{HF} + \mathrm{Cl}\\
&\mathrm{HA2402} + \mathrm{h}\nu \longrightarrow 4\,\mathrm{HF} + 2\,\mathrm{Br}\\
&\mathrm{HA1211} + \mathrm{h}\nu \longrightarrow \mathrm{Br} + \mathrm{Cl} + 2\,\mathrm{HF}\\
&\mathrm{HA1301} + \mathrm{h}\nu \longrightarrow \mathrm{Br} + 3\,\mathrm{HF}.
\end{aligned}
$$

We also added the following gas-phase reactions (with the reaction rates from

JPL-2015):

$$
\begin{aligned}
&\mathrm{CFC114} + \mathrm{O^1D} \longrightarrow 2\,\mathrm{Cl} + 4\,\mathrm{HF}\\
&\mathrm{CFC115} + \mathrm{O^1D} \longrightarrow \mathrm{Cl} + 5\,\mathrm{HF}\\
&\mathrm{HCFC\text{-}22} + \mathrm{Cl} \longrightarrow \mathrm{Cl} + 2\,\mathrm{HF} + \mathrm{HCl}\\
&\mathrm{HFC23} + \mathrm{O^1D} \longrightarrow 3\,\mathrm{HF}\\
&\mathrm{HFC23} + \mathrm{OH} \longrightarrow 3\,\mathrm{HF} + \mathrm{H_2O}\\
&\mathrm{HFC125} + \mathrm{O^1D} \longrightarrow 5\,\mathrm{HF}\\
&\mathrm{HFC125} + \mathrm{OH} \longrightarrow 5\,\mathrm{HF} + \mathrm{H_2O}\\
&\mathrm{HFC125} + \mathrm{Cl} \longrightarrow 5\,\mathrm{HF} + \mathrm{HCl}\\
&\mathrm{HFC134a} + \mathrm{O^1D} \longrightarrow 4\,\mathrm{HF}\\
&\mathrm{HFC134a} + \mathrm{OH} \longrightarrow 4\,\mathrm{HF} + \mathrm{H_2O}\\
&\mathrm{HFC134a} + \mathrm{Cl} \longrightarrow 4\,\mathrm{HF} + \mathrm{HCl}\\
&\mathrm{HFC143a} + \mathrm{O^1D} \longrightarrow 3\,\mathrm{HF}\\
&\mathrm{HFC143a} + \mathrm{OH} \longrightarrow 3\,\mathrm{HF} + \mathrm{H_2O}\\
&\mathrm{HFC143a} + \mathrm{Cl} \longrightarrow 4\,\mathrm{HF} + \mathrm{HCl}\\
&\mathrm{HCFC141b} + \mathrm{O^1D} \longrightarrow \mathrm{HF} + 2\,\mathrm{Cl}\\
&\mathrm{HCFC141b} + \mathrm{OH} \longrightarrow \mathrm{HF} + 2\,\mathrm{Cl} + \mathrm{H_2O}\\
&\mathrm{HCFC141b} + \mathrm{Cl} \longrightarrow \mathrm{HF} + 2\,\mathrm{Cl} + \mathrm{HCl}\\
&\mathrm{HCFC142b} + \mathrm{O^1D} \longrightarrow 2\,\mathrm{HF} + \mathrm{Cl}\\
&\mathrm{HCFC142b} + \mathrm{OH} \longrightarrow 2\,\mathrm{HF} + \mathrm{Cl} + \mathrm{H_2O}\\
&\mathrm{HCFC142b} + \mathrm{Cl} \longrightarrow 2\,\mathrm{HF} + \mathrm{Cl} + \mathrm{HCl}\\
&\mathrm{HA2402} + \mathrm{O^1D} \longrightarrow 4\,\mathrm{HF} + 2\,\mathrm{Br}\\
&\mathrm{O^1D} + \mathrm{N_2} \longrightarrow \mathrm{N_2O}.
\end{aligned}
$$

In addition to those new reactions, some existing reactions in the default

WACCM chemistry scheme were updated to yield HF as product:

$$\begin{aligned}
&\mathrm{CFC11} + \mathrm{h}\nu \longrightarrow 3\,\mathrm{Cl} + \mathrm{HF}\\
&\mathrm{CFC12} + \mathrm{h}\nu \longrightarrow 2\,\mathrm{Cl} + 2\,\mathrm{HF}\\
&\mathrm{CFC113} + \mathrm{h}\nu \longrightarrow 3\,\mathrm{Cl} + 3\,\mathrm{HF}\\
&\mathrm{HCFC\text{-}22} + \mathrm{h}\nu \longrightarrow \mathrm{Cl} + 2\,\mathrm{HF}\\
&\mathrm{O^1D} + \mathrm{CFC11} \longrightarrow 3\,\mathrm{Cl} + \mathrm{HF}\\
&\mathrm{O^1D} + \mathrm{CFC12} \longrightarrow 2\,\mathrm{Cl} + 2\,\mathrm{HF}\\
&\mathrm{O^1D} + \mathrm{CFC113} \longrightarrow 3\,\mathrm{Cl} + 3\,\mathrm{HF}\\
&\mathrm{O^1D} + \mathrm{HCFC\text{-}22} \longrightarrow \mathrm{Cl} + 2\,\mathrm{HF}\\
&\mathrm{HCFC\text{-}22} + \mathrm{OH} \longrightarrow \mathrm{Cl} + \mathrm{H_2O} + 2\,\mathrm{HF},
\end{aligned} \tag{4.2}$$

and we updated the reaction rates to JPL-2015 for the following reactions:

$$\begin{aligned}
&\mathrm{O^1D} + \mathrm{N_2O} \longrightarrow 2\,\mathrm{NO}\\
&\mathrm{O^1D} + \mathrm{N_2O} \longrightarrow \mathrm{N_2} + \mathrm{O_2}\\
&\mathrm{O^1D} + \mathrm{CH_4} \longrightarrow \mathrm{CH_3O_2} + \mathrm{OH}\\
&\mathrm{O^1D} + \mathrm{CH_4} \longrightarrow \mathrm{CH_2O} + \mathrm{H} + \mathrm{HO_2}\\
&\mathrm{O^1D} + \mathrm{CH_4} \longrightarrow \mathrm{CH_2O} + \mathrm{H_2}.
\end{aligned} \tag{4.3}$$

All the previous reactions are part of the updated chemical scheme that is also used in the CTM simulations in Prignon et al. (2019). The comparison between WACCM and the observations shows a large underestimation by around 30% of the HCFC-22 columns in WACCM compared both to satellite and ground-based measurements (Fig. 4.4). Conversely, the seasonal cycle simulated by WACCM agrees better with the observations, except during the boreal summer months, when the amplitude of the cycle is significantly larger compared to the observations (around 40%, Fig. 4.5).

After the mentioned experiment, we performed another multi-decadal (December 1984-December 2015) free-running production run in order to investigate the long-term changes in the BDC using N_2O as a tracer. This simulation is named WACCM4 and uses the default WACCM chemistry. WACCM4 is used as a sensitivity test for the impact of the parametrization of the OGW in Chapter 6.1 and its results are discussed there. The initial conditions for the long-lived chemical species were obtained from a chemical reanalysis that assimilated satellite observations for the year 2010, and which

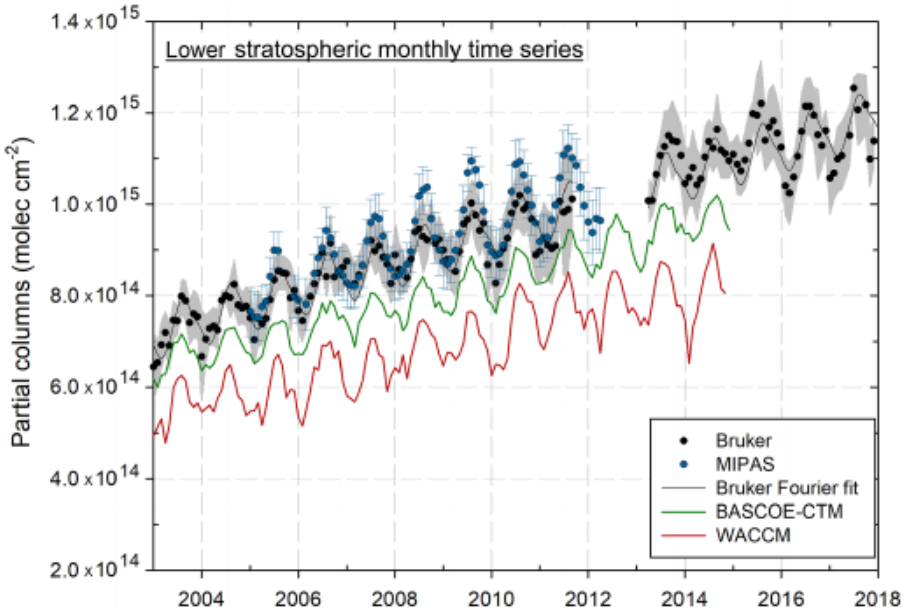

Figure 4.4: Time series of lower-stratospheric partial columns (11.21-30 km) above Jungfraujoch (MIPAS at 5°latitude around Jungfraujoch). The grey shaded area and the blue vertical bars depict the standard deviation around the FTIR and the MIPAS monthly means, respectively. A Fourier series fitted to the Bruker time series (black curve) is also represented. FTIR partial columns from the middle of 2011 to the middle of 2013 are not displayed because of the lower quality retrievals observed during this time period. From Prignon et al. (2019).

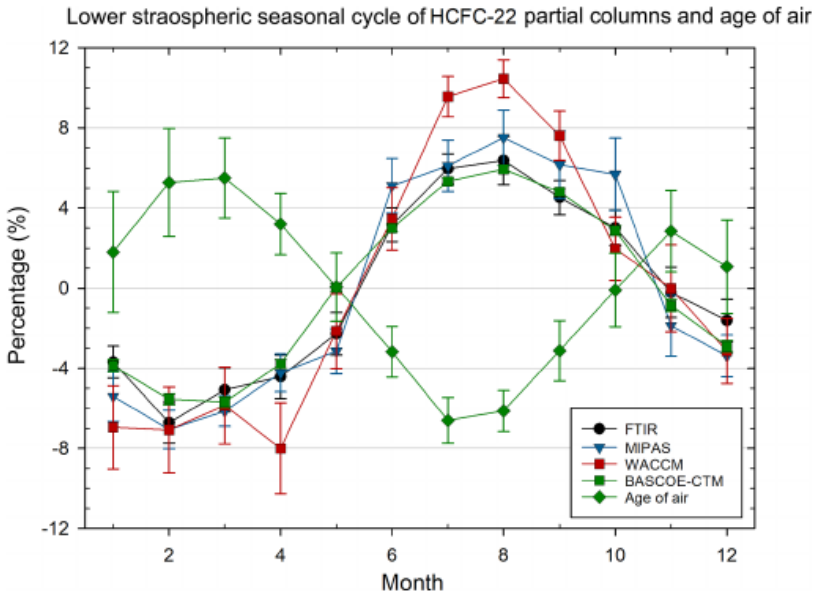

Figure 4.5: Seasonal cycle of HCFC-22 columns in the lower stratosphere (11.21-30 km) based on measurements and model outputs (2005-2012). MIPAS measurements are at a maximum distance of 500 km from the Jungfraujoch station. Vertical bars depict the 2σ standard error of the means. The AoA simulation is performed by BASCOE-CTM from the ERA-Interim reanalysis. The peak-to-peak amplitude of the age of air cycle is 0.37 years and the mean age of air is 2.96 years. From Prignon et al. (2019).

were scaled back to 1984. The lower boundary conditions of the long-lived chemical species are taken from the Coupled Model Intercomparison Project 6 (CMIP6, Eyring et al., 2016) recommendations (Meinshausen et al., 2017, and Fig. 4.6 for N_2O).

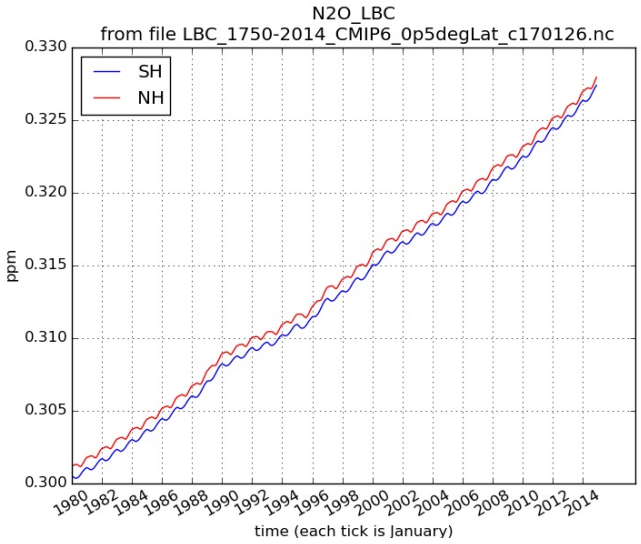

Figure 4.6: N_2O volume mixing ratio at the surface averaged for the Northern Hemisphere (NH, red) and Southern Hemisphere (SH, blue). As mentioned in Sect. 1.1.4, the abundancies in the NH are larger than the SH.

4.1.5 WACCM-REFC1

This Section describes the WACCM configuration that is used within the SPARC (Stratosphere-troposphere Processes And their Role in Climate) Chemistry-Climate Model Intercomparison phase 1 (CCMI-1, Morgenstern et al., 2017). The REFC1 experiments of CCMI-1 consist of free-running simulations of the recent past (1960-2010) using state-of-the-art historical forcings and observed sea surface temperatures (Morgenstern et al., 2017). For the WACCM model, its REFC1 experiments (WACCM-REFC1) were recently extended to the end of 2018. The WACCM version used in CCMI-1 is version 4, with the inclusion of important modifications regarding the heterogeneous chemistry and the gravity wave parameterization (Garcia et al., 2017). These modifications are motivated by the "cold-pole bias" that affected the previous WACCM version (e.g., the WACCM4 experiment described in the previous Section, Garcia et al., 2017). By cold pole bias, we refer to a substantial underestimation of the Antarctic polar stratospheric temperatures during winter and

spring in CCMs, which leads to an unrealistically large ozone depletion over the Antarctica (Eyring et al., 2006; Garcia et al., 2017). This cold bias is largely caused by a poor simulation of the stratospheric dynamics. As mentioned in Sect. 1.2.3, the temperature over the polar stratosphere is largely determined by the downwelling of the BDC, which results in adiabatic warming over that region. Thus, the cold bias results from an underestimation of the downwelling of the BDC over the Antarctic, which is caused by a lack in the wave forcing over that region and more generally over the Southern Hemisphere (SH). The forcing from resolved (planetary) waves cannot be modified, as is internally computed by the model. On the other hand, the driving due to gravity waves can be modified, as it is a sub-scale process and thus must be parametrized (see Sect. 4.1.3).

In the following, we describe the improvements in the heterogeneous chemistry and the gravity wave parameterization.

a) **Updated heterogeneous chemistry**

   Heterogeneous chemical processes are very important in the ozone budget over the Antarctic stratosphere. Their parameterization in WACCM-REFC1 has been updated by Solomon et al. (2015). Specifically, the new parameterization modifies the representation of the uptake of HNO_3 in the formation of nitric acid trihydrate and supercooled ternary solutions, as well as the threshold for the supersaturation of water to ice. These modifications result in a very good agreement with the space-borne measurements in terms of HNO_3 removal (Wegner et al., 2013). Since the updated chemistry scheme in WACCM-REFC1 is sensitive to temperature, the cold pole bias is thus properly addressed.

b) **Updated gravity waves parameterization** As mentioned in Sect. 4.1.3, the gravity waves can be triggered by orography (OGW) or by other tropospheric sources such as fronts and convection (NOGW). In WACCM-REFC1, only the parameterization of the OGW is updated.

   In the default WACCM version 4, the parameterization of the OGW assumes the same north-south and east-west orientations of the mountain ranges in the SH and Northern Hemisphere (NH), which in general is not true, as in the SH the major mountain ranges are oriented north-south. The parameterization in WACCM version 4 is then based just on the standard deviation of the subgrid-scale topography (with no reference to its orientation) and on the surface wind. Such parameterization underestimates the OGW stress in the SH.

   The new parameterization consists in doubling the magnitude of the orographic stress across the SH. Despite this relatively simple approach,

the modified gravity wave parameterization largely impacts the simulated climate in WACCM. The stronger forcing of the OGW results in a warmer polar lower stratosphere above the Antarctic stratosphere compared to WACCM4, with a consequently improved simulation of ozone. Furthermore, such change positively impacts the zonal wind in the SH, which becomes more similar to reanalyses, and does not negatively affect the mesopause or the dynamics in the NH. For a more detailed description of the new parameterization and its impacts on the climate simulated by WACCM, we refer to Garcia et al. (2017).

4.1.6 WACCM-REFD1

We also used one realization of the version 6 of WACCM (Gettelman et al., 2019), which is part of version 2 of CESM (Danabasoglu et al., 2020), which contributes to phase 6 of CMIP (CMIP6, Eyring et al., 2016). This Section does not provide details about the improvements of CESM2 compared to CESM1, but only the major differences between WACCM version 6 and WACCM version 4 (both WACCM4 and WACCM-REFC1).

The default horizontal resolution of WACCM6 is 0.9°x1.25°latitude-longitude, with 70 hybrid-sigma levels in the vertical from the ground to around 140 km of altitude, with a vertical resolution similar to WACCM version 4. The transition to WACCM6 involved a number of changes in the physical parameterizations. In the following, we give an overview of those changes. The primary change is the new subgrid turbulence scheme, which allows merging the different moist turbulence schemes of the previous version into a single one (Larson, 2017). The cloud microphysics scheme has changed and now follows Gettelman and Morrison (2015), and the radiation scheme has been updated to the Rapid Radiative Transfer Model for GCM (RRTMG, Iacono et al., 2008). Furthermore, the mixed-phase ice nucleation depends also on the aerosols, besides temperature (Wang et al., 2014; Shi et al., 2014). Aerosols are now treated using version 4 of the Modal Aerosol Model (Liu et al., 2016). The subgrid mountain drag parameterization now follows Beljaars et al. (2004). The orographic gravity wave parameterization has been improved since Garcia et al. (2017), and now accounts for the mountain orientation according to Scinocca and McFarlane (2000).

The default chemistry in WACCM6 comprises reactions from the troposphere to the lower thermosphere, and includes a total of 231 species and 583 chemical reactions, with reaction rates from JPL-2015. In particular, it includes an improved representation of the secondary organic aerosols (Tilmes et al., 2019), together with a new and more comprehensive treatment of stratospheric aerosol (Mills et al., 2016). In addition, WACCM6 can also

generate an internal QBO.

In this thesis, we use the REFD1 configuration of WACCM6, which is part of the support for the 2022 WMO (World Meteorological Organization) United Nations Environment Programme (UNEP) Scientific Assessment of Ozone depletion. In particular, it is part of a suite of hindcast simulations for the 1960-2018 period, which will be used to compare the models to observations. The REFD1 experiments aim to extend the early comparison done in the CCM Validation Activity (CCMVal-2, Eyring et al., 2008) to the current generation of CCMs (CCMI-2022). Since the goal of the REFD1 experiments is to be compared to observations, the forcings are based as much as possible on observations, and use the databases developed for CMIP6. The long-lived GHGs are specified through the CMIP6 recommendations (Meinshausen et al., 2017, 2020). The ODS mixing ratios follow the specifications of WMO (2018). The open biomass burning emissions are from the CMIP6 dataset (Van Marle et al., 2017) until 2015, and from the global fire emission database (`https://globalfiredata.org/pages/data/#emissions`). Anthropogenic emissions different from open biomass burning are from the database described in Hoesly et al. (2018) until 2014 and from Meinshausen et al. (2020) afterward. The sea surface temperatures and sea ice concentrations are taken from the UK Met Office Hadley Center (Rayner et al., 2003).

Although WACCM6 is able to produce the QBO internally, the REFD1 experiments include a nudged QBO towards observed winds to ensure a good synchronization of historical variability. The dataset containing the required tropical zonal winds is `https://drive.google.com/file/d/1YfCVADaaId5c5Euj9JTEUm8ZaQrSC` `view`. The time-varying solar flux is from the CMIP6 dataset of solar spectral irradiance (Matthes et al., 2017). The surface area density of stratospheric aerosols is specified according to the CMIP6 recommendations (Kovilakam et al., 2020).

4.2 The Belgian Assimilation System of Chemical ObsErvations

The Belgian Assimilation System of Chemical ObsErvations (BASCOE) is a data assimilation system developed at BIRA-IASB that can be either used as a CTM (e.g., Minganti et al., 2020) or as a data assimilation system (e.g., Skachko et al., 2016). Section 4.2.1 describes BASCOE in the CTM configuration and Section 4.2.2 gives an overview of the dynamical reanalyses that drive it. Section 4.2.3 illustrates the preprocessing required to properly feed the reanalyses to the BASCOE CTM.

4.2.1 The BASCOE Chemistry-Transport Model Setup

The BASCOE CTM is a kinematic transport model (Errera et al., 2008; Chabrillat et al., 2018), which simulates the stratospheric chemistry but cannot simulate the dynamics. Therefore, it takes as input the surface pressure and the horizontal winds from external datasets and computes the vertical component of the wind velocity internally through mass conservation. As WACCM, the BASCOE CTM uses an FFSL advection scheme, with a 2°x2.5°latitude-longitude grid. The time step of the model is 30 minutes, which is split into smaller intervals when necessary for stability reasons. Unlike WACCM, in the BASCOE CTM there is no convective process nor an explicit horizontal diffusion. More in general, no tropospheric process is taken into account in the BASCOE system. The default chemistry scheme in the BASCOE CTM includes 58 species interacting through 142 gas-phase, 9 heterogeneous and 52 photolytic reactions (Huijnen et al., 2016). Sulfate aerosols and PSCs are parameterized according to Daerden et al. (2007) and Errera et al. (2008), respectively.

The default chemistry scheme of BASCOE was modified by Prignon et al. (2019), through the addition of the total inorganic fluorine F_y and its sources (similarly to what was done for the inclusion of HF in WACCM4). The additional species are: HFC134a, HFC23, HFC125, HFC143a, HCFC141b, HCFC142b and HA2402. Those 7 new species require additional gas-phase (18) and photolysis (7) reactions. These new gas-phase and photolysis reactions are almost the same as what was implemented in WACCM4 (see Sect. 4.1.4). The WACCM4 updated chemistry scheme lacks the photolytic reaction of HA1211 and HA1301, but that does play any role for the HCFC-22 columns investigated in Prignon et al. (2019). The BASCOE CTM simulations use the same initial and boundary conditions as the WACCM4 simulation described in Sect. 4.1.4. The lower boundary conditions were extended to the end of 2018 using Meinshausen et al. (2020).

4.2.2 Input Meteorological Reanalyses

The BASCOE CTM takes in input the horizontal winds and surface pressure from meteorological reanalyses to drive its transport scheme. Section 4.2.2.1 gives an overview of how a generic reanalysis is produced and the different techniques to achieve it. A brief description of each reanalysis driving the BASCOE CTM is provided in Sections 4.2.2.2 to 4.2.2.6. For a more detailed description of the reanalyses driving the BASCOE CTM in this thesis, refer to Fujiwara et al. (2017) and references therein.

4.2.2.1 Generic Atmospheric Reanalysis

Reanalyses combine a global forecast model (e.g., a GCM) with some input observations and a data assimilation scheme, which produces the best estimate (analysis) of the past atmospheric state (see schematic in Fig. 4.7). The "re" in reanalysis arises from the fact that the assimilated input observations are previously evaluated in the context of operational forecasting. Reanalyses cover very long periods, and aim to reproduce a consistent state of the atmosphere, without spurious discontinuities or trends (Bengtsson and Shukla, 1988). Hence, reanalysis centers tend to use the same forecast model and data assimilation scheme for the whole period, and to carefully handle possible biases arising from changes in the input observations (Simmons et al., 2014). Compared to their assimilated observations, reanalyses have the major added value of being on a regular temporal and spatial grid. Reanalyses are used to understand a variety of atmospheric processes and variability (e.g., Patra et al., 2020), to validate CCMs (e.g., Eyring et al., 2010), and to identify climate change (e.g., Bellouin et al., 2020).

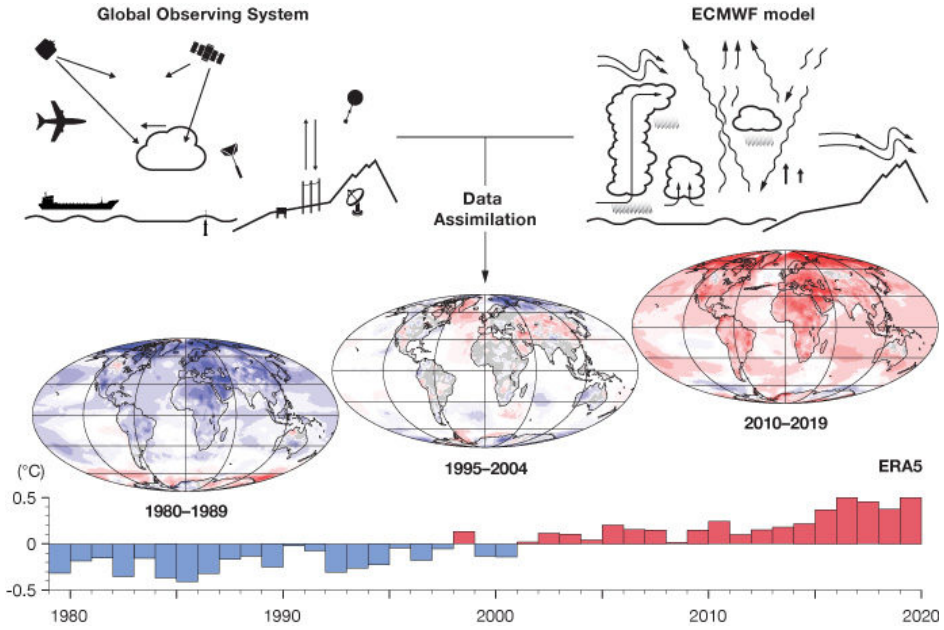

Figure 4.7: A schematic of the reanalysis process. From `https://www.ecmwf.int/en/about/media-centre/focus/2020/fact-sheet-reanalysis`.

Conceptually, the creation of a reanalysis is relatively simple. Starting from a previous generic analysis, the forecast model propagates the information forward in space and time. The data assimilation scheme then combines

the forecast and the input observations to provide consecutive analyses of the atmospheric state, then used for another forecast.

The data assimilation scheme is the key to the production of a reanalysis, as it combines the forecast with the observations. A generic data assimilation scheme takes as input the available observations and a background state (that can be a previous analysis or the model forecast), together with their respective uncertainties. Then, it minimizes the difference between the analysis and the true state of the atmosphere, to reduce the influence of the observational and backgrounds errors on the final analysis. This is achieved through statistics to represent the potential uncertainties, numerical techniques to convert between model and observational space (the "observation" operator), and ultimately minimize the resulting uncertainties. An observation operator converts the information from the background state space to the observation space by interpolating the model grid to the observation location and transforming model variables to observed quantities. This allows a direct comparison between the background state and the observations. For a more detailed treatment of the data assimilation techniques and methods, refer to, e.g., Kalnay (2003).

Among the different assimilation schemes, we can specify common quantities. The *assimilation increment* is defined as the adjustment applied to the background state after the assimilation of the observations (i.e., the difference between the background state and the analysis state). In contrast, the *observation increment* is the weight of a specific observation to a specific assimilation increment. The *assimilation window* is the period that contains observations that impact the analysis. The major differences between the assimilation methods used in current reanalyses mainly depend on the calculation and application of the assimilation increment within the assimilation window.

The data assimilation schemes used in the reanalyses that drive the BASCOE CTM considered in this thesis are the *variational* methods. Those methods minimize a cost function that tends to correct the differences between the observations and the background state, together with their uncertainties (Talagrand, 2010). Variational methods can be implemented to derive optimal estimates at discrete times (i.e., the *3D-Var*), or find optimal state trajectories within a finite time window (i.e., the *4D-Var*).

The 3D-Var scheme applies the assimilation increment only at discrete times. On the other hand, the observation increments within the assimilation window can be either treated as measured at the analysis time, or weighted by the measurement time (i.e., with a stronger impact of observations closer to the analysis time). Many 3D-Var methods estimate the observation increments at the observation time rather than at the analysis

time (the 3D-FGAT, i.e., "first guess at appropriate time", Lawless, 2010).

The 4D-Var technique differs from the 3D-Var and 3D-FGAT because it relates the observations and the forecast trajectories within the entire assimilation window instead of at discrete times (Park and Županski, 2003). Therefore, 4D-Var exploits the available observations in a more exhaustive way than 3D-Var or 3D-FGAT, resulting in better analysis (Talagrand, 2010). However, running the full 4D-Var technique is computationally very expensive. Hence, the 4D-Var is usually simplified through the "incremental 4D-Var" approach (Courtier et al., 1994). This is an iterative method where the model state at the beginning of the assimilation window is adjusted to derive a better fit between the observation and the forecast trajectory. Within this process, the information is propagated backward and forward in time, which significantly enhances the resulting analysis but requires double the computational resources as the model must be run twice. To overcome this issue, the 4D-Var is usually run within two nested loops. In order to gain computational efficiency, the inner loop has lower resolution and simplified physics, and computes the assimilation increments. Upon the convergence of the inner loop, the outer loop, with full resolution and physics, uses the assimilation increments calculated by the inner loop to derive the final analysis.

Reanalysis systems assimilate data from a large number of observational sources. These sources are divided into two groups: conventional data (e.g., surface records, radiosonde profiles, aircraft data) and satellite data. The data availability largely depends on space and time: conventional data are very sparse, and satellite data are often inhomogeneous over time as their sensors deteriorate and break down. These sources of changes and inconsistencies have significant impacts on the quality of the reanalyses. We do not address the large variety of assimilated observations here, but we refer to Chapter 2 of the recently released SPARC Report (`https://www.sparc-climate.org/wp-content/uploads/sites/5/2021/07/02_SRIP_Report_Ch02_EarlyOnlineRelease-1.pdf`) for further details.

In this thesis, we use five meteorological reanalyses: the European Centre for Medium-Range Weather Forecast (ECMWF) Interim reanalysis (ERA-Interim, hefeafter ERAI, Dee et al., 2011), and the ECMWF fifth reanalysis (ERA5, Hersbach et al., 2020), the Japanese 55-year Reanalysis (JRA-55, hefeafter JRA55, Kobayashi et al., 2015), the Modern-Era Retrospective analysis for Research and Applications version 1 (MERRA, Rienecker et al., 2011) and version 2 (MERRA2, Gelaro et al., 2017). Table 4.2 summarizes some of the principal differences among the reanalyses. Chapter 6 does not include ERA5 as the corresponding BASCOE CTM run was yet done at the time of the study, and Chapter 7 does not include MERRA, in order to focus

only on the most recent reanalyses.

The following Sections 4.2.2.2 to 4.2.2.6 briefly describe each reanalysis, in particular those parametrizations of the forecast model that are relevant for stratospheric transport studies. For a more detailed description of the different forecast models, we refer to the respective references or to Chapter 2 of the recently released SPARC Report (`https://www.sparc-climate.org/wp-content/uploads/sites/5/2021/07/02_SRIP_Report_Ch02_EarlyOnlineRelease-1.pdf`).

Reanalysis	Reference	Orig. horiz grid	Top Level	Assim. scheme
ERAI	Dee et al. (2011)	∼79 km	0.1 hPa (L60)	incremental 4D-Var
ERA5	Hersbach et al. (2020)	∼31 km	0.01 hPa (L87)	incremental 4D-Var
JRA55	Kobayashi et al. (2015)	∼55 km	0.1 hPa (L60)	incremental 4D-Var
MERRA2	Gelaro et al. (2017)	0.5°x0.625°lat,lon	0.01 hPa (L72)	3-D-FGAT
MERRA	Rienecker et al. (2011)	0.5°x0.666°lat,lon	0.01 hPa (L72)	3-D-FGAT

Table 4.2: Overview of the five reanalyses used to drive the BASCOE CTM in this thesis.

4.2.2.2 ERAI

The ERAI reanalysis uses the incremental 4D-Var as data assimilation scheme and covers the period from 1979 to August 2019. The forecast model used to produce ERAI is IFS, developed at the ECMWF, which couples the atmospheric model with the land and ocean models. The IFS model has changed substantially since its first release in 1985, and the history of those changes is documented in `https://www.ecmwf.int/en/publications/ifs-documentation`. ERAI is based on the IFS release Cy31r2 (Cycle 31r2), introduced in 2007. The radiative transfer is parameterized using an updated version of the scheme developed by Fouquart et al. (1980) for the shortwave radiation, and a revised version of Mlawer et al. (1997) described in Dee et al. (2011) for the longwave radiation. The gravity wave drag is parametrized using the scheme developed by Lott and Miller (1997) for subgrid orographic waves, while the orographic source follows Miller et al. (1989) and Baines and Palmer (1990) and the NOGW drag is represented only as a Rayleigh friction above the stratopause (Dee et al., 2011). The horizontal diffusion is represented with an implicit linear fourth-order diffusion scheme in spectral space. The vertical diffusion under stable conditions is based on Beljaars (1995), and for unstable conditions on the eddy-diffusivity scheme by Köhler et al. (2011).

4.2.2.3 ERA5

The ERA5 reanalysis covers the period from 1979 to the present, with a recent preliminary version that extends back to 1950. As ERAI, ERA5 is built on IFS, but uses the more recent release Cy41r2, which was introduced in 2016. Regarding the radiation parameterization, both shortwave and longwave radiative transfer follow Iacono et al. (2008) with hourly calculations. The parameterization of subgrid OGW drag is similar to ERAI, with increased wave activity (Hersbach et al., 2020), and NOGW drag is now included using the method developed by Scinocca (2003) with an additional latitudinal dependence of the NOGW flux. The parameterization of the horizontal diffusion is the same as ERAI, while the vertical diffusion is a modified version (Poli et al., 2016; Hersbach et al., 2020).

The assimilation scheme in ERA5 is an improved version of the incremental 4D-Var implemented in ERAI. It employs an ensemble of 10 forecast members (all using the same assimilation scheme). One member is the control simulation, and the other 9 members are at lower resolution, each with different random perturbations added to the observations and to the model tendencies. The ensemble method results in more robust estimates of the analysis uncertainties and the background error covariances (Hersbach et al., 2020).

The ERA5 reanalysis exhibits a cold bias in the lower stratosphere for the 2000-2006 period. This is due to inappropriate error covariances specified prior to 2006. Hence, a new reanalysis was produced for that period, named ERA5.1, where the cold bias is solved (Simmons et al., 2020). In this thesis, we use ERA5.1 between 2000 and 2006 to drive the BASCOE CTM and ERA5 for the rest of the considered period.

4.2.2.4 JRA55

JRA55 uses the incremental 4D-Var technique as assimilation scheme and extends from 1958 to the present. The forecast model used for JRA55 is the spectral resolution Japan Meteorological Agency (JMA) global spectral model (GSM), released in 2009. Details about the different model versions can be found at `http://www.jma.go.jp/jma/jma-eng/jma-center/nwp/nwp-top.htm`.

The radiation scheme is based on Briegleb (1992) and updated according to Freidenreich and Ramaswamy (1999) for the absorption of ozone, O_2 and CO_2 for the shortwave radiation, and on Murai et al. (2005) for the longwave radiation. These schemes are applied to the whole model grid, with hourly frequency for the shortwave radiation and three-hourly for the longwave.

The parametrization of OGW drag is based on their wavelength, separating the longwave component (wavelength larger than 100 km) and the short wave component (wavelength around 10 km) (Iwasaki et al., 1989a,b). According to this parametrization, long waves can propagate upward and dissipate into the stratosphere, exerting drag (Palmer et al., 1986), while short waves are trapped in the troposphere. Differently from the other reanalyses and WACCM, JRA55 does not include a parametrization for the NOGW.

For the horizontal diffusion parameterization, JRA55 implements an implicit linear fourth-order diffusion scheme in spectral space as done for ERAI and ERA5. The vertical diffusion is based on the scheme developed by Mellor and Yamada (1974).

4.2.2.5 MERRA

MERRA is based on version 5.2.0 of the Goddard Earth Observing System (GEOS) global model (Rienecker et al., 2008), and encompasses the period from 1979 to February 2016. The radiative transfer is parametrized using Chou and Suarez (1999) for the shortwave part of the spectrum, and according to Chou et al. (2001) for the longwave part. In MERRA, the parametrization of the OGW drag follows McFarlane (1987) and for the NOGW follows Garcia and Boville (1994). The horizontal diffusion in MERRA is solved using an explicit second-order horizontal divergence damping that is included in the dynamical core (Rienecker et al., 2011). The vertical diffusion under stable conditions is based on the scheme from Louis (1982), and under unstable conditions on Lock et al. (2000).

MERRA uses the 3D-FGAT assimilation method, but generates two analysis products: "ANA" (analysis state) and "ASM" (assimilated state). The ANA product is analog to any other 3D-FGAT analysis. However, the ASM implements a 6h "corrector" forecast centered at the analysis time, together with an incremental analysis update, to apply the assimilation increment gradually at each model time step rather than only at the analysis time (Bloom et al., 1996). In general, the ANA products represent the closest correspondence to the assimilated observations, while the ASM products provide a more complete and consistent set of variables and tendencies with smaller imbalances compared to the plain 3D-FGAT analysis (Fujiwara et al., 2017). Thus, the ASM analyses are preferred for transport studies (Chabrillat et al., 2018). For MERRA, we had to use the ANA products, because the ASM products are defined only on the constant pressure levels, that are incompatible with the preprocessing of the BASCOE CTM.

4.2.2.6 MERRA2

MERRA2 is produced using version 5.12.4 of the GEOS atmospheric model (Rienecker et al., 2008; Molod et al., 2015) and covers the period from 1980 to present. The radiation scheme in MERRA2 is parametrized as in MERRA, and the parameterization of gravity waves drag is similar to MERRA, with updates described in Molod et al. (2015). In MERRA2, the horizontal diffusion is parametrized similarly to MERRA (Gelaro et al., 2017). Also, the vertical diffusion is similar to MERRA, with improvements in the representation of the fluxes across the surface (Helfand and Schubert, 1995) and in the turbulent mixing in the lowermost troposphere (Gelaro et al., 2017).

MERRA2 uses the same "predictor-corrector" 3D-FGAT method as MERRA as assimilation scheme. Differently from its previous version, we could use the ASM product for driving the BASCOE CTM.

4.2.3 Preprocessing of the input reanalyses

In Chapters 6 and 7, the BASCOE CTM is used as a transfer tool to perform a fair comparison between the reanalyses, in particular of their representation of the stratospheric transport. It requires in input the surface pressure and the zonal wind u staggered in longitude and the meridional wind v staggered in latitude (i.e., defined on an Arakawa-C grid). The BASCOE CTM uses a common horizontal grid of 2°x2.5°longitude-latitude for all the reanalyses, but keeps the original vertical grid of each reanalysis (or a subset in the case of ERA5). Given these constraints, it is important to carefully preprocess the dynamical fields from the original high-resolution variables in the horizontal to the format required by the CTM.

Because of the respective assimilation method, reanalysis systems are prone to have dynamical mass imbalances that can negatively affect stratospheric transport. It is then crucial to properly handle these imbalances in order to simulate the transport correctly. To this end, the BASCOE CTM uses a preprocessor that allows to filter out dynamical imbalances explicitly (Segers et al., 2002). This preprocessor uses the vorticity and divergence as spherical harmonics to evaluate the horizontal winds on a regular grid. At the same time, it corrects for possible imbalances of the pressure tendencies by comparing them to the divergence and vorticity. This results in consistent pressure and horizontal wind fields even in the presence of artificial pressure gradients.

For ERAI and ERA5, the ECMWF directly provides the vorticity and divergence in spherical harmonics. However, for the other reanalyses (JRA55, MERRA and MERRA2), the horizontal winds are available only on a con-

stant pressure grid. Therefore, a preliminary step is needed to derive the spherical harmonics of vorticity and divergence for these reanalyses. For all reanalyses, the spherical harmonics are truncated at wavenumber 47 to avoid aliasing on the coarser horizontal grid (Chabrillat et al., 2018).

4.3 Remote Sensing Measurements

In this thesis, we use measurements of N_2O volume mixing ratios obtained from remote sensing instruments. Remote sensing is the technique of observing and analyzing objects from a distance without direct contact. Remote observations use sensors onboard satellites, aircraft, or on the surface that detect and record the radiation coming from the Sun (passive sensors) or emitted by the instrument (active sensors). This thesis uses remote measurements from passive sensors on the ground (ground-based) and on satellites (space-borne) that record the IR and microwave radiation emitted by the Sun.

Section 4.3.1 provides an overview of the technique that allows obtaining measurements of volume mixing ratios from observations of IR radiation. Section 4.3.2 describes the remote ground-based measurements. Sections 4.3.3 and 4.3.4 describe the satellite measurements obtained from measurements of IR and microwave radiation, respectively.

4.3.1 Fourier Transform Spectrometer Basics

As mentioned in Sect. 1.1.3.3, some atmospheric molecules interact with the IR radiation through absorption. A Fourier Transform Spectrometer (FTS) measures the radiation in the IR spectral region and is based on a Michelson interferometer, which divides the incoming solar radiance into two beams through a beamsplitter (Giacomo, 1987). One beam is reflected by a fixed mirror, and the other interacts with a moving mirror resulting in an optical path difference. Both beams reach the beamsplitter again and recombine, with constructive or destructive interference depending on their wavelength and optical path difference. The resulting beam is sent to the detector that measures its intensity and the optical path difference. The measured intensity is ultimately converted into a spectrum by a Fourier Transformation (Bracewell, 1986).

The FTS measures the intensity of the solar radiation and requires constant solar radiances, which implies that measurements can be obtained only under clear sky conditions. The time needed to record one spectrum varies between one and ten minutes, with longer windows for high sun measurements, and depends on the required quality. The IR absorption spectra mea-

sured by FTS contain information for more than 25 atmospheric molecules, many of them notably crucial for the greenhouse effect and ozone depletion (see Sects. 1.1.3.3 and 1.2.6). In particular, a generic high-resolution FTS IR spectrum contains a large number of roto-vibrational absorption lines of several relevant gases (e.g., CO_2, N_2O, see Sect. 1.1.3.3). Hence, the FTS technique is very powerful and extremely useful in understanding the time evolution of GHGs and ODS. Furthermore, a generic high-resolution spectrum provides information on the vertical distribution of the absorbing molecule thanks to the pressure broadening (i.e., the absorption lines broaden with increasing pressure).

The atmospheric distribution of an absorbing molecule as measured by the FTS results from its interactions with the solar radiation. Thus, the abundancies of the atmospheric constituents must be retrieved by inverting the relationship between the distribution of a molecule and its absorption spectra (the so-called "inverse problem"). Conceptually, the absorption spectrum and the tracer distribution are related by:

$$\overrightarrow{y} = \overrightarrow{F}(\overrightarrow{x}, \overrightarrow{p}_{atmos}, \overrightarrow{p}_{exp}), \tag{4.4}$$

where $\overrightarrow{y}$ represents the absorption spectrum, $\overrightarrow{x}$ the tracer distribution, $\overrightarrow{p}_{atmos}$ a set of parameters describing the atmospheric state and $\overrightarrow{p}_{exp}$ the parameters describing the measurement. The function $\overrightarrow{F}$ is a forward function that simulates the radiative transfer and the characteristics of the instrument. Any change of the absorption spectrum for changes of the tracer distribution is evaluated by the derivative $\partial\overrightarrow{y}/\partial\overrightarrow{x}$, that determines the matrix $\mathbf{K}$ (the Jacobian matrix of $\mathbf{F}$ with respect to $\overrightarrow{x}$):

$$\partial\overrightarrow{y} = \mathbf{K}\partial\overrightarrow{x}. \tag{4.5}$$

The inversion of $\mathbf{K}$ would yield the $\overrightarrow{x}$ state. Unfortunately, the inverse problem usually is under-determined, i.e., the columns of $\mathbf{K}$ are not linearly independent and there can be many solutions for a given measurement. These incoveniences are usually due to technical difficulties or to the noise of the measurements. Consequently, the inversion mechanism must include some additional constraints to converge, e.g., on the vertical resolution, and use a climatological distribution of the target molecule as prior information (the "a-priori" state). Then, an optimal estimation method combines the measurement and the a-priori distribution of the gas to provide its most probable measured distribution. The general solution of the problem, which is generally non-linear, is given iteratively by:

$$\overrightarrow{x}_{i+1} = \overrightarrow{x}_a + \mathbf{S}_a\mathbf{K}_i^T(\mathbf{K}_i\mathbf{S}_a\mathbf{K}_i^T + \mathbf{S}_\epsilon)^{-1}[\overrightarrow{y} - \overrightarrow{F}(\overrightarrow{x}) + \mathbf{K}_i(\overrightarrow{x}_i - \overrightarrow{x}_a)]. \tag{4.6}$$

In Eq. 4.6, $\overrightarrow{x}_a$ is the a-priori distribution, $\mathbf{S}_a$ the a-priori covariance matrix and $\mathbf{S}_\epsilon$ is the measurement noise covariance. A very important componenent of the retrieved solution is the *averaging kernel matrix* (AVK) $\mathbf{A}$, defined as:

$$\mathbf{A} = (\mathbf{K}^T\mathbf{S}_\epsilon^{-1}\mathbf{K} + \mathbf{S}_a^{-1})^{-1}\mathbf{K}^T\mathbf{S}_\epsilon)^{-1}\mathbf{K}. \tag{4.7}$$

The averaging kernel matrix describes the smoothing of the actual vertical distributions of the gas by the measurement process. The trace of the $\mathbf{A}$ matrix quantifies the amount of information that directly comes from the measurement, and can be interpreted as the *degrees of freedom* of the measurement.

The retrieved profile of the gas is affected by a total error, which can be separated into three contributions: the smoothing error, the forward model error and the retrieval noise. The smoothing error identifies the uncertainties due to the limited vertical resolution of the retrieval. The forward model error quantifies the errors in the parameters $\overrightarrow{p}_{atmos}$ and $\overrightarrow{p}_{exp}$ of the forward model, and the retrieval noise is the measurement noise and is predominantly random. For a more detailed description of the Fourier transform IR spectroscopy and inverse problems, the interested reader is referred to Schneider et al. (2013) and Rodgers (2000).

4.3.2 Ground-based measurements: Fourier Transform Infrared Data

This Section provides an overview of the ground-based FTIR measurements of N_2O volume mixing ratio used in Chapter 7. All the FTIR measurements described in this Section are part of the Network for the Detection of Atmospheric Composition Change (NDACC, De Mazière et al., 2018, `http://www.ndaccdemo.org/`). NDACC is currently composed of more than 70 research stations around the globe and more than 160 active instruments, and started operations in January 1991 under the name of Network for Detection of Stratospheric Change. The major objectives of NDACC are to establish long-term databases for detecting changes in the atmospheric composition, to determine feedbacks between composition, climate and air quality, and to validate observations from other platforms (e.g., satellites).

In this thesis, we use observations from four NDACC stations (see Table 4.3) that represent the mid-latitudes and subtropics in the SH and NH: Lauder (45°S, 169°E; New Zealand), Wollongong (34°S, 150°E; Australia), Izãna (28°N, 16°E; Spain) and Jungfraujoch (46°N, 7°E; Switzerland). FTIR measurements are obtained through an FTS using the same technique as described in the previous Section.

For ground-based FTIR measurements, the averaging kernel matrix **A** is very important, as it objectively and quantitatively describes the vertical resolution of the retrieved quantity through its eigenvectors and associated eigenvalues. The shape of the eigenvectors of **A** specifies the region where the instrument is most sensitive (e.g., troposphere, stratosphere). The eigenvalues associated with those eigenvectors measure the contribution of the measured state to the retrieved state: when the eigenvectors have eigenvalues close to one (or one), the retrieved state comes mainly from the observation; when the eigenvalues approach zero, the relative measurement is just replicating the a-priori state.

Figure 4.8 shows the first three eigenvectors and associated eigenvalues for the four FTIR stations for N_2O. At all the stations, the shape of the first eigenvector (blue line) corresponds to the tropospheric N_2O column, thus is not useful for our purposes. The second eigenvector (orange line) characterizes the stratosphere and yields a very significant amount of information from the measurement at all stations (between 91 and 97 %), and becomes larger (smaller) than 0.25 (-0.25) above around 12 km (except for Wollongong). This is the reason we chose 12 km as the bottom for the stratospheric columns in Chapter 7. The third eigenvector (green line) also identifies the stratosphere and provides independent measurements at Lauder and Wollongong, where respectively 93 and 94 % of the state comes from the measurements, but not at Izãna (71% contribution from the measurement) and Jungfraujoch, where the measurement contributes only at 32%. We chose the upper limit of the stratospheric column at 40 km, because the three eigenvectors tend to zero above that altitude.

As introduced in Sect. 4.3.1, the trace of **A** yields the degrees of freedom of the signal (DOFS). The DOFS provide the number of independent pieces of information obtained from a measurement, which ultimately are the number of atmospheric layers that can be resolved. Figure 4.9 shows the stratospheric DOFS for N_2O between 12 and 40 km as a function of time. For Lauder and Wollongong, it is possible to separate two stratospheric layers, but this is not possible for Izãna and Jungfraujoch, where only one stratospheric layer can be resolved. Because of this, and to maintain consistency in the comparison, we consider only one stratospheric layer (12-40 km) at all stations when computing N_2O stratospheric columns in Chapter 7.

Given the limitations in terms of sensitivity and vertical resolution of the FTIR measurements, one must apply extreme care when comparing them with model output or satellite measurements. The first step for a proper comparison is to vertically re-grid the datasets with the finer vertical resolution to the retrieval grid of the FTIR. To that end, we use a method similar to what is described in Langerock et al. (2015). This method implements

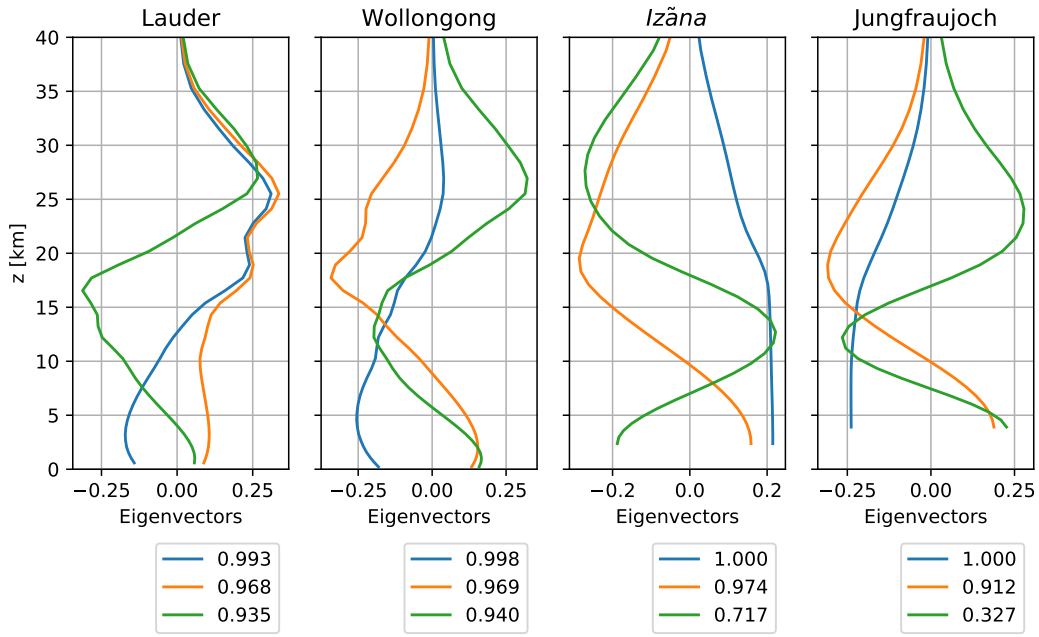

Figure 4.8: Three first eigenvectors and eigenvalues of the mean AVK matrix for the FTIR instruments at the four considered stations (left to right: Lauder, Wollongong, Izãna, Jungfraujoch).

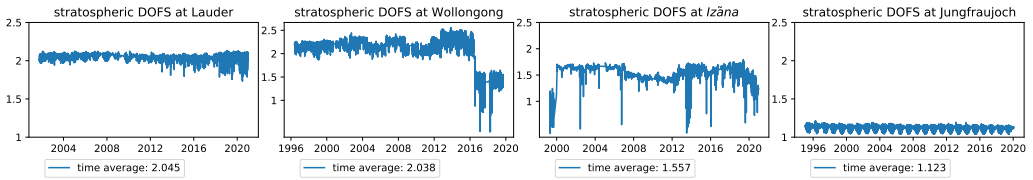

Figure 4.9: Time-dependent stratospheric (averaged between 12 and 40 km) DOFS and their time mean for the FTIR instruments at the four considered stations (left to right: Lauder, Wollongong, Izãna, Jungfraujoch).

a mass-conservative vertical regridding, to properly convert from a typical vertical grid of models and satellites (usually hybrid pressure or pressure) to the altitude grid of the FTIR instruments. After the vertical regridding, the AVKs of the FTIR must be applied to the other datasets in order to account for the limited FTIR vertical sensitivity. Such process smooths the profiles from the models or the satellite as follows:

$$x_s = x_a + A(x_m - x_a), \tag{4.8}$$

where x_m is the profile from the model or satellite, x_a is the a-priori profile of the target compound, A is the AVK matrix defined in Sect. 4.3.1, and x_s is the resulting smoothed profile. This procedure ensures that the smoothed profile x_s from the higher resolution dataset is under the same observational conditions as the FTIR measurement (usually a much lower vertical resolution).

In the following, we will provide more details about the instruments at the stations considered during this thesis (see Table 4.3): Lauder, Wollongong, Izãna and Jungfraujoch.

Station name	Reference	Location (lat, lon)	Altitude (abs)	Year Range
Lauder	Zhou et al. (2019)	45.4°S, 169.68°E	370 m	2001-2020
Wollongong	Griffith et al. (2012)	34.45°S, 150.88°E	30 m	1996-2019
Izãna	García et al. (2021)	28.30°N, 16.48°E	2367 m	1999-2020
Jungfrajouch	Zander et al. (2008)	46.55°N, 7.98°E	3580 m	1995-2020

Table 4.3: Overview of the NDACC FTIR stations considered in this thesis.

- **Lauder**

  The Lauder research station was established in 1961 for photometric observations and aurora emissions and maintained by the National Institute of Water and Atmosphere (Smale et al., 2019). The site was chosen because it is relatively free from clouds and not affected by air and light pollution, making it a very good site for clear-sky FTIR observations.

  In this thesis, we use N_2O volume mixing ratio data from 2001 to the present, because earlier measurements include only total columns of N_2O. Measurements are taken using a Bruker (Bruker Optics) IFS 120HR spectrometer starting in October 2001. In May 2017, a new Bruker 125HR was installed to replace the older Bruker 120HR, with an overlap period from November 2017 to April 2018. From 2001, profile measurements include CO, N_2O, HNO_3, CH_4, C_2H_6, O_3, HCl, HF, and HCN.

The algorithm used for the retrieval is the SFIT4 version 0.9.4.4 (`https://wiki.ucar.edu/display/sfit4/Infrared+Working+Group+Retrieval+Code%2C+SFIT`), which is an update of SFIT 2 (Pougatchev et al., 1995). The SFIT4 code uses a forward model ($\overrightarrow{F}$ in Eq. 4.4) to simulate the measured spectrum for a given atmospheric state and instrument parameters (respectively $\overrightarrow{p}_{atmos}$ and $\overrightarrow{p}_{exp}$ in Eq. 4.4). The code then uses the optimal estimation technique (Rodgers, 2000) to vary the mixing ratio of the target gas in each atmospheric layer to achieve the fit. The a-priori profiles come from simulations of the WACCM model version 6, and daily pressure and temperature profiles from the National Centers for Environmental Prediction (NCEP). For more details, refer to Smale et al. (2019) and references therein.

- **Wollongong**

  The research station at Wollongong is managed by the University of Wollongong and is located close to emission sources of CO due to forest fires (Paton-Walsh et al., 2005; De Laat et al., 2010). We use N_2O volume mixing ratios data starting in May 1996 measured by a Bomem DA-8 spectrometer, which was replaced by a Bruker 125HR in April 2008 after running simultaneously for some months.

  The vertical profiles of the measured gases (that include H_2O, C_2H_6, CH_4,CO, HCl, HCN,N_2O and O_3) are retrieved using the SFIT4 algorithm version 0.9.4.4. The a-priori data come from WACCM version 6 simulations, except for H_2O that uses NCEP data, and CO that are based on aircraft data. Further information can be found in Griffith et al. (2012) and in the NDACC web page `http://www.ndaccdemo.org/`.

- **Izãna**

  The Izãna research station is located on the top of the Izãna mountain on the Tenerife island (Spain), thus far from large pollution sources. These two factors (high elevation and clear air) make the Izãna station optimal for measurements that require clean and dry air conditions.

  We use N_2O volume mixing ratio data from February 1999 measured by a Bruker IFS 120M spectrometer, which was replaced by a Bruker 125HR in January 2005. Other measured gases include C_2H_6, CH_4, $ClONO_2$, CO, HCl, HCN, HF, NO_3 and O_3.

  Differently from the retrievals at the other stations, the algorithm used to retrieve the mentioned gases is PROFFIT (PRO-File FIT, Hase et al., 2004). The a-priori profiles for the retrieved gases are taken from

simulations of WACCM6, and the daily temperature and pressure profiles from NCEP. Additional information can be found in García et al. (2021).

- **Jungfraujoch** The International Scientific Station of Jungfraujoch is managed, for NDACC, by the University of Liège. Located in a mountainous region, the station offers excellent observational conditions, thanks to its high altitude and its position far from major pollution sources.

  Regular FTIR measurements at Jungfraujoch started in 1984 and continue nowadays, making the FTIR dataset at Jungfraujoch the oldest among the NDACC stations across the world. In this thesis, we use measurements of N_2O volume mixing ratio by a Bruker IFS 120HR that started in 1990.

  Here also, the SFIT4 (v0.9.4.4) was used to retrieve the target gases. The a-priori profiles are taken from WACCM6 simulations, and water vapor, pressure and temperature from NCEP data. For a more detailed description, refer to, e.g., Zander et al. (2008).

4.3.3 The Atmospheric Chemistry Experiment - Fourier Transform Spectrometer

In addition to ground-based observations, we use the measurements obtained from the Atmospheric Chemistry Experiment (ACE) using an infrared Fourier Transform Spectrometer (FTS) onboard the SCISAT satellite. The current list of ACE-FTS tracers includes 44 atmospheric compounds: H_2O, O_3, N_2O, NO, NO_2, HNO_3, N_2O_5, H_2O_2, HO_2NO_2, O_2, N_2, SO_2, HCl, HF, ClO, $ClONO_2$, CFC11, CFC12, CFC113, COF_2, $COCl_2$, COClF, CF_4, SF_6, CH_3Cl, CCl_4, HCFC-22, HCFC141b, HCFC142b, HFC134a, HFC23, CO, CH_4, CH_3OH, H_2CO, HCOOH, C_2H_2, C_2H_6, OCS, HCN, $CH_3C(O)CH_3$, CH_3CN, $CH_3C(O)OONO_2$. ACE-FTS was launched in orbit in August 2003, and collected the first data for scientific use in February 2004. The whole ACE mission was designed to last two years, but the instruments continue to provide reliable observations to date, without noticeable degradation in its performance. Besides the FTS, ACE carries another instrument for the detection of atmospheric tracers, the spectrophotometer MAESTRO (Measurement of Aerosol Extinction in the Stratosphere and Troposphere Retrieved by Occultation, McElroy et al., 2007).

ACE-FTS is a spectrometer achieving a spectral resolution of 0.02 cm^{-1}, which covers at once the 750 to 4500 cm^{-1} spectral range in solar occultation to determine the vertical profiles of volume mixing ratios of atmospheric

constituents and temperature. In the solar occultation technique, the radiation is measured by looking directly at the Sun at a series of tangent heights. Hence, ACE-FTS measures the absorption spectra in the limb geometry only during sunrise and sunset. The orbital period of ACE allows around 30 occultations per day (15 sunrises and 15 sunsets). The vertical resolution is quite fine: about 3 km from 5 km of altitude (or above the cloud top) up to 150 km (Bernath, 2017).

Since ACE-FTS works in solar occultation, the temporal sampling is limited to sunsets and sunrises and, therefore, very irregular. For example, in 2019, ACE-FTS measured more than 250 N_2O profiles per day before December the 9th, but zero profiles after December the 13th, with a decreasing number of profiles per day in between. The orbit of the SCISAT satellite has an inclination of 74°, which was chosen to provide a combination of a large number of measurements, global coverage and extension to high latitudes. Because of this orbit inclination, the spatial sampling is much poorer in tropical regions compared to the extratropics. From its launch to March 2021, ACE-FTS measured around 7000 N_2O profiles within the 20°S-20°N latitude band, while it recorded around N_2O 37700 profiles southward of 50°S and more than 40000 northward of 50°N. Consequently, trends averaged over a specific latitudinal band are implicitly weighted toward the higher latitudes, because the number of profiles is larger than tropical regions (Kolonjari et al., 2018).

Measurements from ACE-FTS have undergone several improvements during the last decade, with the release of several ACE-FTS versions. The latest major development is version 4 (ACE-FTS v4), which implements an improved accuracy of the retrieved quantities and a better treatment of the errors compared to previous versions (Boone et al., 2020). In this thesis, we use an updated version of ACE-FTS v4, which was released in July 2020: v4.1 (Bernath et al., 2021). The most significant update of ACE-FTS v4.1 compared to its earlier version is the improved retrievals at lower altitudes, including the effect of clouds and aerosols. This improvement had a major impact on the tropospheric molecules, but did not substantially change the retrieved trends (Bernath et al., 2021). However, v4 and v4.1 of ACE-FTS represent considerable improvements compared to previous versions (e.g., v3.5, Sheese et al., 2017) in terms of trends (Bernath et al., 2021).

The profiles measured by ACE-FTS cannot be used without a previous data screening. In particular, before scientific use, a two-stage procedure must be applied to detect unphysical outliers, with a method that evaluates the probability density function of the mixing ratios against a determined statistical error. Therefore, the procedure does not depend on the considered species (Sheese et al., 2015). The ACE-FTS profiles are then vertically re-

gridded to a constant altitude vertical grid using a mass-conservative scheme (Bader et al., 2017). For trend analysis, profiles are monthly averaged on latitude bins with 5°spacing from pole to pole.

When comparing N_2O trends from model simulations with those obtained from ACE-FTS measurements, the model datasets are first re-sampled in time and space as ACE-FTS. This procedure is important because of the limited spatial and temporal sampling of ACE-FTS discussed before. The resampling consists of a linear interpolation of the model values to the ACE-FTS time and to the profile geolocation. The re-sampled model datasets are then monthly averaged as done with ACE-FTS.

4.3.4 The Microwave Limb Sounder

The Microwave Limb Sounder (MLS) instrument (Waters et al., 2006) is onboard of National Aeronautic Space Agency (NASA)'s Aura satellite. MLS measures vertical profiles of a number of atmospheric compounds: OH, HO_2, H_2O, O_3, HCl, ClO, HOCl, BrO, HNO_3, N_2O, CO, HCN, CH_3CN, volcanic SO_2, together with cloud ice, temperature and geopotential height.

MLS was launched in July 2004 and is still operational to date (Schoeberl et al., 2006). The instrument scans the atmosphere vertically in the limb geometry, from the surface to around 95 km every ∼26 seconds, providing around 3500 profiles measured daily, both at day- and night-time. Since the Aura orbit is near-polar sun-synchronous, MLS provides data from 82°S to 82°N for each orbit (Livesey et al., 2021).

MLS measures atmospheric constituents by observing microwave (millimeter and submillimeter wavelengths) thermal emission. This technique benefits from reliable measurements, even in the presence of aerosols, cirrus or PSC that can negatively impact measurements taken at shorter wavelengths (IR or VIS), and allows measuring temperature, pressure and cloud ice. The use of microwave emission allows measuring at all times, i.e., both day and night, providing daily global coverage. MLS can also resolve the microwave emission at all altitudes, separating the contribution from very weak lines from the strong ones nearby (Waters et al., 2006).

In this thesis, we consider the version 4 of MLS (MLS v4, Livesey et al., 2015). For MLS v4, the standard N_2O product is retrieved from the 190 GHz radiometer, instead of the 640 GHz as in the previous MLS versions. This is because the N_2O profiles from the 640 GHz instrument had started to deteriorate in June 2013 (e.g., increased radiance noise) and continued to show severe degradation in quality with time. Because of this, the 640 GHz N_2O product was turned off on August, 6 2013, and data later than June 2013 are not recommended for scientific use (Livesey et al., 2015). The 190 GHz

product is characterized by a slightly worse quality than the 640 GHz. Compared to independent observations, the bias of the 190 GHz instrument in the lowermost stratosphere (around 100 hPa) is larger than 30%, with smaller biases above (5-10% at 68 hPa), and less than 5% in the mid-stratosphere (Livesey et al., 2015).

The N_2O MLS product obtained from the 190 GHz radiometer suffers from a negative drift that is more pronounced in the lower stratosphere, reaching 15% difference compared to other satellite measurements (Livesey et al., 2021). The drift is in contrast with the expected N_2O increase in the stratosphere as a consequence of the global increase at the surface (see Sect. 1.1.4). The drift was reduced in the recently released version 5 of MLS, but is still statistically significant, and the MLS team recommends using caution when examining long-term trends of N_2O (Livesey et al., 2021).

4.4 The BASCOE Chemical Reanalysis

This Section describes the chemical reanalysis used in Chapter 6. Before describing its characteristics, it is important to highlight the added value of a chemical reanalysis compared to regular observations of atmospheric composition and its possible applications. Besides evaluating relevant stratospheric processes (e.g., the evolution of the polar vortex, Braathen, 2016), chemical reanalyses have additional purposes. They are used to evaluate simulations of climate models (e.g., Davis et al., 2016), whose outputs are usually delivered as zonal and monthly means. These outputs are difficult to compare with the observations, which are characterized by irregular and/or sparse spatial and temporal samplings (Toohey and von Clarmann, 2013). Chemical reanalyses can also be used as a transfer tool to study differences between instruments (similarly to the BASCOE CTM as a transfer tool for dynamical reanalyses) (Errera et al., 2008). In addition, chemical reanalyses provide a consistent set of interactive species that allow addressing scientific questions. Finally, chemical reanalyses can provide reliable boundary conditions (Müller et al., 2018), or initial conditions for periods where good observations are not available, as done for the studies in Chapters 6 and 7. Chemical reanalyses can focus on tropospheric composition (e.g., the Copernicus Atmospheric Monitoring Service reanalysis; Inness et al., 2019), or in the stratosphere, where the assimilation of observations of ozone is also a major topic of research (Viscardy et al., 2010). Section 4.4.1 describes the main characteristics of the BASCOE chemical reanalysis, with a focus on the N_2O product, and Section 4.4.2 the BASCOE analysis system.

4.4.1 Description of the Chemical Reanalysis

The chemical reanalysis used in this thesis assimilates observations from MLS v4 (see Sect. 4.3.4) using the BASCOE data assimilation system to perform the analysis and the dynamical fields from ERAI to drive the dynamics of BASCOE (Errera et al., 2019). The resulting chemical reanalysis is named BASCOE Reanalysis of Aura MLS version 2 (BRAM2), and covers the period from August 2004 to August 2019. In BRAM2, only a subset of the species measured by MLS is assimilated, focusing on the atmospheric gases well suited for assimilation and use in scientific studies: ozone, H_2O, N_2O, HNO_3, HCl, ClO, CH_3Cl, and CO.

Before the assimilation into the BASCOE system, each MLS profile is strictly checked to follow the species-dependent recommendations of Livesey et al. (2015) in terms of vertical validity range, estimated precision, quality convergence and status. For N_2O, only the 190 GHz product (valid in the 68-0.46 hPa pressure range) is assimilated in BRAM2, to ensure consistency across the whole period without switching between the 190 and 640 GHz products in 2013. The drift of the N_2O product derived from the 190GHz radiometer in MLS v4 negatively impacts BRAM2; hence, it is not used in Chapter 7, but is included in Chapter 6 because the climatologies of N_2O mixing ratios are not affected by the drift. Because of this drift, a new BRAM version (BRAM3, not published) was created to address the issue by assimilating the N_2O product from the 640 GHz radiometer. The comparison between BRAM2 and BRAM3 for N_2O is discussed in Sect. 4.5.2. The interested reader is referred to Errera et al. (2019) for a thorough evaluation of BRAM2 against a variety of observational datasets.

4.4.2 The BASCOE Data Assimilation System

BRAM2 is produced by the assimilation of MLS v4 observations through the BASCOE data assimilation system (Errera et al., 2008)). As already mentioned, BRAM2 is dynamically driven by ERAI, with a lower resolution than the CTM setup: 3.75°x2.5°latitude-longitude in the horizontal, and 37 vertical levels from the surface to 0.1 hPa, which are a subset of the ERAI vertical levels. The vertical resolution is altitude-dependent, ranging from 1-1.5 km in the troposphere and mid-lower stratosphere to 5 km in the upper stratosphere. The dynamical fields from ERAI are preprocessed as done for the CTM (see Sect. 4.2.3). The chemistry scheme is the default BASCOE scheme (Errera et al., 2019), i.e., it does not include the update described in Sect. 4.2.1.

The data assimilation in BASCOE can be performed using either 4D-Var

(Errera and Ménard, 2012) or the Ensemble Kalman filter (EnKF, Skachko et al., 2016). Differently from the variational methods (see Sect. 4.2.2.1), in the EnKF the analyses benefit from an ensemble of forecasts that define the probability distribution of a set of background states (prior distribution), which is combined with the observations and associated uncertainties to provide a posterior probability distribution of analysis states (Evensen, 2009). This posterior distribution is determined using a Kalman filter (Kalman, 1960). For the production of BRAM2, the EnKF technique was used to perform the data analysis because it is more adaptable to the HPC than the 4D-Var.

In order to reduce the production time, BRAM2 was run using four streams (i.e., four time periods) in parallel (2004-2008, 2008-2012, 2012-2016, 2016-2019) with one month overlap. Initial conditions were taken from a 20-years BASCOE CTM run that used lower boundary conditions from Meinshausen et al. (2017). The N_2O observations from MLS v4 undergo a background quality check before the assimilation, i.e., the BASCOE system discards any observation whose difference with the mean ensemble state is 5 times larger than the combined error of the observation and the background state (Skachko et al., 2016). The averaging kernels of MLS v4 are not applied in the production of BRAM2 because their use is not implemented in the BASCOE EnKF.

In BRAM2, the EnKF is implemented as follows (see also Fig. 4.10):

1. at time $t = 0$, 20 ensemble members are generated based on a 20% Gaussian perturbation on a given model state.

2. The BASCOE CTM simulates the model state of each ensemble member to the next time step.

3. The system perturbates each ensemble member if an MLS observation is available at the current time (Skachko et al., 2014).

4. The ensemble mean and variance are saved.

5. If MLS observations are available, the analysis for each ensemble member is computed.

6. Steps 2 to 5 are repeated until the end.

For a more comprehensive description of the technical details on the production of BRAM2, refer to Skachko et al. (2016) for the BASCOE setup and to Errera et al. (2019) for a more quantitative description.

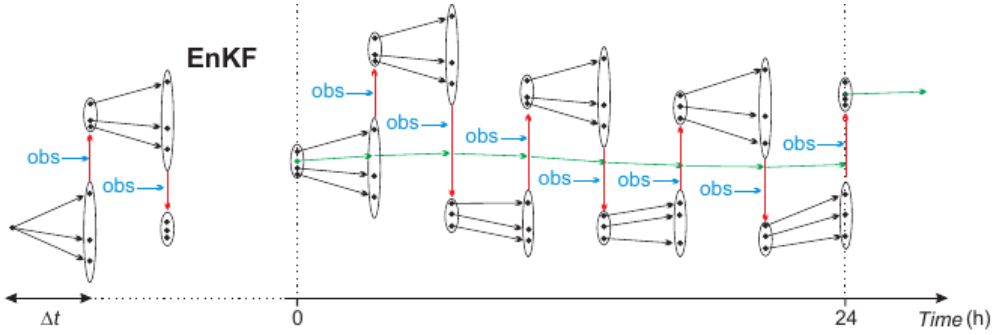

Figure 4.10: Schematics of the practical implementation of the EnKF assimilation method in BASCOE. Black dots represent the model state, and the observational information is in blue. The black arrows depict the model integration over one time step, and vertical red arrows represent the model state optimization. The green dot represents the analysis at 0h used as the initial condition for the 24h forecast (green lines). For clarity, the number of EnKF ensemble members is limited to three. From Skachko et al. (2016).

4.5 Other Considered Datasets

This Section briefly discusses the two datasets that were initially considered for inclusion in the present work but eventually discarded and the reasons for their exclusion. These datasets are the NDACC FTIR station at Paramaribo (Sect. 4.5.1), and the new version of the chemical reanalysis from MLS: BRAM3 (Sect. 4.5.2).

4.5.1 FTIR station: Paramaribo

When considering the possible FTIR stations to include in this thesis, we also investigated N_2O measurements from the station at Paramaribo, Suriname (5.8°N, 55.2°W, Petersen et al., 2008). The inclusion of this tropical station could be complementary to the stations at the subtropics and mid-latitudes in the two hemispheres, and could provide insights into the impact of possible changes in the upwelling on the tropical N_2O stratospheric columns.

Unfortunately, we had to discard the N_2O product at Paramaribo because of several, and occasionally long, periods of no data. Figure 4.11 shows stratospheric N_2O columns between 15 and 40 km and clearly illustrates this issue, for example during the whole years 2008 and 2013. In addition, the year 2009 has only one N_2O measurement and the year 2011 have less than 10 days of measurements. In general, the temporal sampling of the N_2O data at Paramaribo is insufficient for trend analysis, especially before 2016,

and the associated errors are very large in several cases. The same choice of discarding the N_2O data obtained at the Paramaribo station was made by Barret et al. (2021) because of the poor temporal sampling.

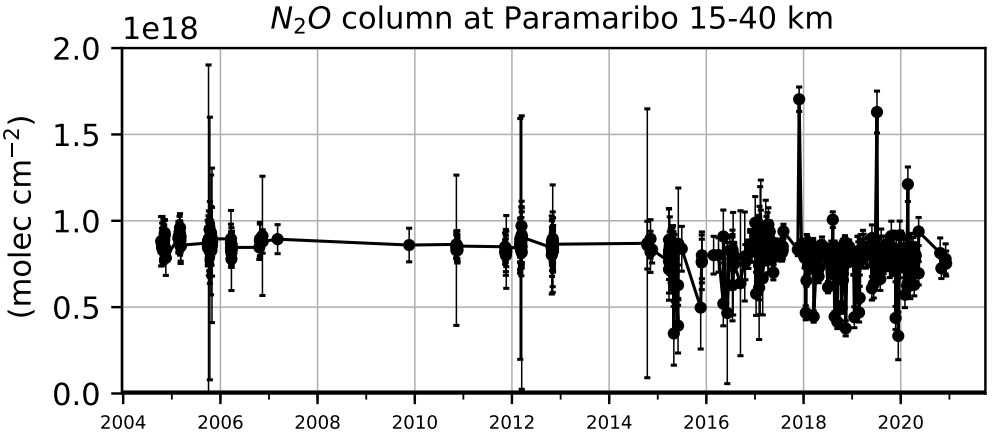

Figure 4.11: N_2O stratospheric column at Paramaribo, 15-40 km. Error bars are shown every 5 points.

4.5.2 BRAM3

As mentioned in Sect. 4.3.4, the N_2O abundancies obtained from BRAM2 suffer from the negative drift of the N_2O product measured from the 190 GHz spectrometer in MLS v4. Because of this drift, a new version of BRAM was produced (BRAM3, not published) that assimilates the N_2O product from the 640 GHz radiometer. BRAM3 differs from BRAM2 also because it is driven by the ERA5 dynamical fields and uses an updated chemistry mechanism. In addition, BRAM3 also has finer horizontal and vertical resolutions compared to BRAM2. Figure 4.12 shows the mean relative bias for N_2O of BRAM3 and BRAM2 with respect to ACE-FTS v3.6, and indicates that the drift in BRAM2 starts around 2010 and becomes severe after 2013.

Because of the deterioration of the instrument, the 640 GHz N_2O product from MLS ceased to be delivered in August 2013, providing only 9 years of measurements (August 2004-June 2013). Thus, BRAM3 assimilates MLS N_2O only for that period (becoming a normal CTM run afterward), and is not suitable for studies of long-term, or even decadal, changes. Furthermore, there is no substantial difference between the N_2O abundancies at 32 hPa between BRAM3 and BRAM2, and the N_2O mixing ratios in BRAM3 are low-biased compared to ACE-FTS at 100 hPa (Fig. 4.12). For those reasons, BRAM3 is not included in either Chapter 6 nor Chapter 7.

We notice that it is possible to artificially correct the drift of the 190 GHz N_2O product using the rate of increase of the 640 GHz N_2O product for the common period (Stolarski et al., 2018). However, this assumes that the rate of increase of N_2O computed from the 640 GHz product remains the same until the end of the 190 GHz data record. Even though the two products are very similar over the common period, we do not use this approach because we find that such assumption would hinder the possible short-term variability, and force the N_2O trends to be artificial.

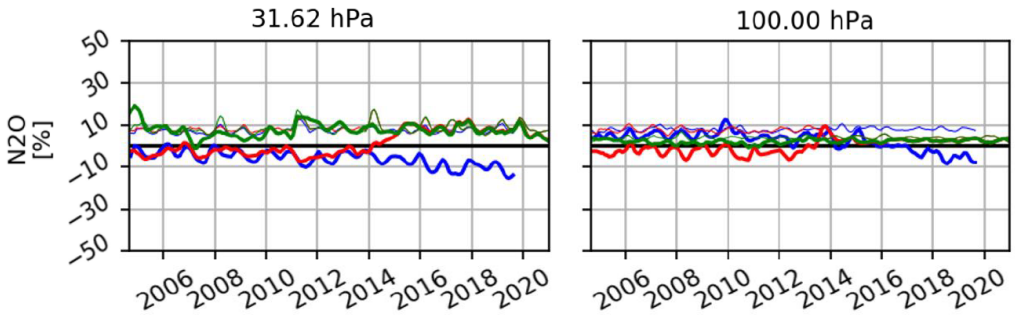

Figure 4.12: Mean relative bias for N_2O with respect to ACE-FTS v3.6 of BRAM3, BRAM2 and the BRAM3 control run of the BASCOE CTM, averaged in the northern mid-latitudes (30°-60°N) for 31,62 hPa (left panel) and 100 hPa (right panel). The color code is: **BRAM2**, **BRAM3**, **CTRL**, **Observations**. Thick lines are the mean bias; thin lines are the standard deviations. The period is September 2004 to December 2020. N_2O in BRAM3 is not assimilated after July 2013, i.e., after that it becomes a normal CTM run. Courtesy of Quentin Errera.

4.6 Preliminary N_2O comparisons

This Section shows some preliminary comparisons of N_2O mixing ratios and stratospheric columns between the previously described datasets. We first reproduce Fig. 7f of Froidevaux et al. (2019) that shows the average seasonal cycle of the N_2O abundancies in the mid-stratosphere at 46 hPa over the Antarctic (Fig. 4.13, left panel). The BASCOE CTM experiments consistently simulate larger N_2O abundancies compared to BRAM2 throughout the year, especially from June to January (reaching a 30% difference). MERRA2 is the only exception, underestimating the N_2O abundancies only by more than 10 % between January and July. The large difference between the seasonal cycles in MERRA2 and the other reanalyses will be further inves-

tigated in Chapter 6. Interestingly, the WACCM simulations agree better with BRAM2 than the BASCOE CTM simulations. A similar peculiarity was already pointed out by Froidevaux et al. (2019), who showed a better agreement between the N_2O abundancies simulated from the free-running WACCM configuration and measured from MLS, compared to those simulated by SD-WACCM.

The right panel of Fig. 4.13 shows the same N_2O abundancies as its left panel but above the tropical region. The N_2O abundancies largely depend on the dataset, with the largest differences between the WACCM simulations and the CTM simulations driven by the MERRA reanalyses. In particular, compared to the Antarctic, the performances of the WACCM model worsen over the Tropics, where the N_2O abundancies are overestimated compared to BRAM2 (reaching 7% difference). Such differences in the N_2O abundancies are further investigated in Chapter 6.

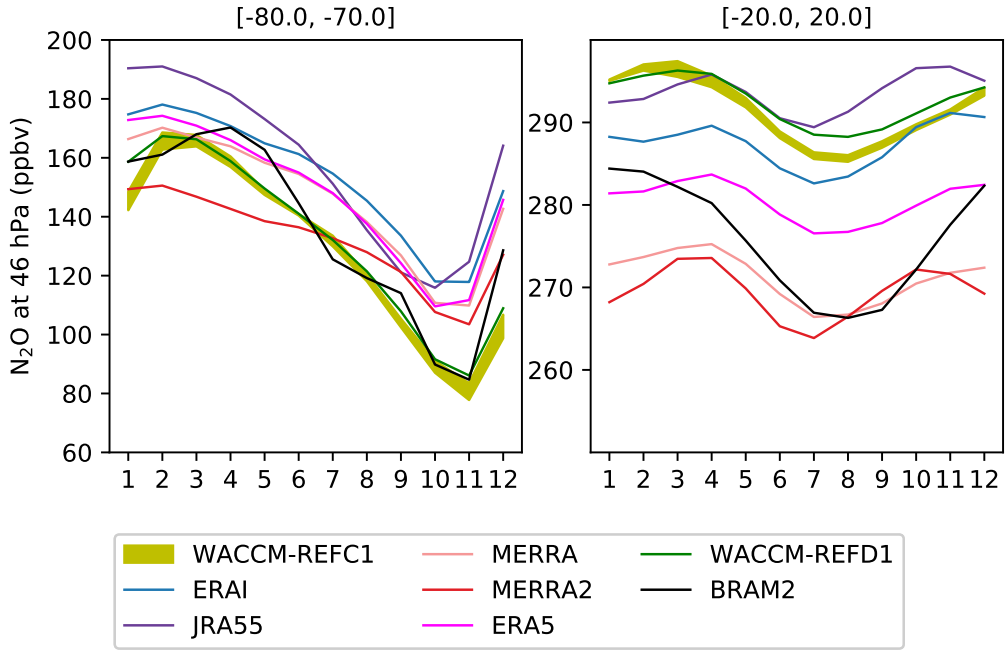

Figure 4.13: Average seasonal cycle of the N_2O volume mixing ratio at 46 hPa for 70°-80°S (left panel) and for 20°S-20°N (right panel). The color code is in the legend. The left panel is a reproduction of Fig.7 panel (f) of Froidevaux et al. (2019). Note that the vertical range differs between the panels.

Figure 4.14 shows the near-global average (80°S to 80°N) of the N_2O abundancies at the lowest level for the WACCM-REFC1 and WACCM-REFD1

simulations and the BASCOE CTM experiments driven by ERAI, ERA5, JRA55 and MERRA2. The BASCOE CTM driven by MERRA is not shown because not included in the study of long-term and decadal N_2O changes (Chapter 7). As expected, the N_2O increase at the surface is mostly linear across the 35 years of data for all the considered datasets, with a weak seasonality that is dampened by the near-global average. The linearity of the N_2O increase at the surface confirms that N_2O is a very suitable tracer for studies of stratospheric transport, because any N_2O change in the stratosphere that is not an increase is due to the effect of transport. This property of N_2O in the stratosphere is extensively used in Chapter 7.

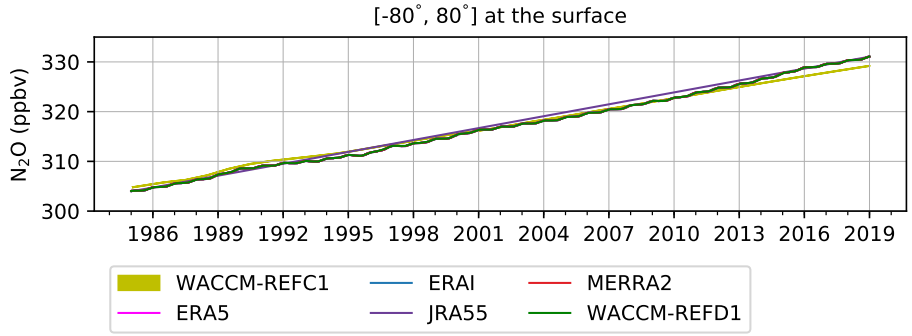

Figure 4.14: Near-global (80°S-80°N) N_2O abundancies at the lowest level for the WACCM-REFC1 and WACCM-REFD1 simulations, and the BASCOE CTM driven by ERAI, ERA5, JRA55 and MERRA2. The WACCM-REFC1 line is the mean of the three ensemble members.

Figure 4.15 shows the vertical profiles of the mean N_2O volume mixing ratio obtained from measurements and CTM and CCM model datasets, averaged for 2005-2018. We chose this period because it is the longest common period for all datasets: it is limited by the start of the ACE-FTS measurements at the end of 2004, and the end of the WACCM runs in December 2018. The mean N_2O mixing ratios are calculated as the N_2O partial columns divided by the density of the air for each layer. This comparison reveals a very good agreement between the FTIR measurements, the CTM simulations and ACE-FTS measurements at all the stations. The only exception is the BASCOE simulation driven by MERRA2, which yields consistently smaller mean volume mixing ratios than the other datasets (around 10% difference). This difference will be addressed more in detail in Chapter 7. The WACCCM simulations are in excellent agreement with the FTIR measurements at all stations, always within the uncertainty ranges.

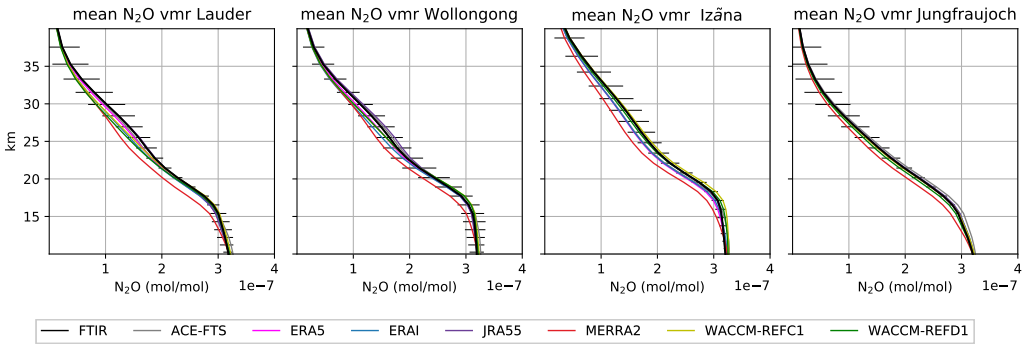

Figure 4.15: Vertical profiles of N_2O mean volume mixing ratios over the 2005-2018 period for the BASCOE CTM driven by ERA5, ERAI, JRA55, MERRA2, the WACCM-REFC1 and REFD1 simulations, and the ACE-FTS and FTIR observations. The color code is shown in the legend. From left to right: Lauder, Wollongong, Izãna , Jungfraujoch. Error bars represent the provided error for each instrument.

5 Methods

This Chapter focuses on the relevant methodologies used in this thesis. Section 5.1 describes the TEM framework (already introduced in Sect. 2.5) applied to tracer transport. Section 5.2 provides an overview of the regression tool that is used in the present study to derive trends. In addition, we compare the trends obtained using this tool with those obtained from other regression tools used in companion studies.

5.1 The Transformed Eulerian Mean Applied to Tracer Transport

In Sect. 2.5, we introduced the TEM diagnostic and described its advantages with respect to the CEM framework. This Section describes the TEM diagnostic applied to the study of the transport of stratospheric tracers, which is extensively investigated in Chapters 6 and 7.

We start by considering a generic tracer with mixing ratio χ in the stratosphere (e.g., N_2O, CH_4, O_3). The abundances of χ are conserved following the motion; hence, they satisfy the continuity equation:

$$D\chi/Dt = S, \tag{5.1}$$

where S is the sum of the chemical sources and losses, and D/Dt is the material derivative defined in Eq. 2.8. Generally, the S term does not include only the chemical sources and sinks but also the contribution of unresolved small-scale diffusion. However, for the stratospheric tracers that we consider, the effect of such diffusion is negligible compared to the resolved transport terms using the same notations as in Chapter 2. We can expand and rewrite Eq. 5.1 in the flux form in Cartesian coordinates as:

$$(\rho_0\chi)_t + (\rho_0 u\chi)_x + (\rho_0 v\chi)_y + (\rho_0 w\chi)_z = \rho_0 S, \tag{5.2}$$

and, applying the CEM conditions (Eqs. 2.34 and Eq. 2.35) and using Eq. 2.54, we have the CEM mean equation of transport of the tracer χ:

$$\overline{\chi}_t + \overline{v}\overline{\chi}_y + \overline{w}\overline{\chi}_z = -\overline{S} - \rho_0^{-1}\nabla\cdot(\rho_0\overline{\mathbf{u}'\chi'}). \tag{5.3}$$

As for the CEM momentum equations the shortcoming of the cancellation between the eddy fluxes and the mean circulation also holds for the CEM equation of tracer transport. As mentioned in Sect. 2.5, the absence of eddies would imply a stratosphere close to its radiative equilibrium, with near-zero meridional transport. In that case (with $\overline{v} \sim \overline{w} \sim \overline{\mathbf{u}'\chi'} \sim 0$), if $\overline{S}$ is small, $\overline{\chi}_t$

must also be small by Eq. 5.3. As a consequence, the eddies and advective terms in Eq. 5.3 would just cancel each other, with no meridional transport.

To overcome the eddy-flow cancellation, we apply the TEM framework to the CEM tracer transport equation (Eq. 5.3) to obtain the TEM tracer transport equation:

$$\overline{\chi}_t + \overline{v}^*\overline{\chi}_y + \overline{w}^*\overline{\chi}_z = \overline{S} + \rho_0^{-1}\nabla \cdot \mathbf{M},$$

where the local rate of change of $\overline{\chi}_t$ can be isolated as:

$$\overline{\chi}_t = -\overline{v}^*\overline{\chi}_y - \overline{w}^*\overline{\chi}_z + \rho_0^{-1}\nabla \cdot \mathbf{M} + \overline{S}. \tag{5.4}$$

This formulation highlights that the TEM framework provides the instantaneous "budget" of the rate of change of the tracer $\overline{\chi}_t$. This budget is computed as the sum of the rates of change due to the impact of transport ($-\overline{v}^*\overline{\chi}_y - \overline{w}^*\overline{\chi}_z + \rho_0^{-1}\nabla \cdot \mathbf{M}$) and of the chemistry ($\overline{S}$). By definition, all terms in Eq. 5.4 have the units of a dimensionless volume mixing ratio (i.e., mol/mol, which can also be written in ppmv=10^{-6} mol/mol or ppbv=10^{-9} mol/mol) divided by units of time (e.g., days, years).

In Eq. 5.4, the terms containing the residual circulation velocities ($\overline{v}^*\overline{\chi}_y$ and $\overline{w}^*\overline{\chi}_z$) represent the impact of the residual advection on the tracer. Those terms are associated with the advection due to the upwelling and downwelling of the BDC (e.g., Abalos et al., 2013). The $\mathbf{M} = (0, M^{(y)}, M^{(z)})$ vector is the eddy flux vector that is defined as:

$$M^{(y)} \equiv -e^{-z/H}(\overline{v'\chi'} - \overline{v'\theta'}\overline{\chi}_z/\overline{\theta}_z) \tag{5.5}$$

$$M^{(z)} \equiv -e^{-z/H}(\overline{w'\chi'} - \overline{v'\theta'}\overline{\chi}_y/\overline{\theta}_z). \tag{5.6}$$

The divergence of the eddy flux vector represents the effects of the resolved diffusive processes on the mixing ratios of χ, mainly through the meridional and vertical eddy fluxes of the tracer concentrations, respectively $\overline{v'\chi'}$ and $\overline{w'\chi'}$. However, the eddy flux vector does not contain only the effects of the eddies (the mixing) but also advective processes that are not resolved by the advection from residual circulation terms (Andrews et al., 1987; Holton, 2004).

When applied to real tracers meshed on a grid with a finite resolution, the residual of the budget $\overline{\epsilon}$ needs to be included in Eq. 5.4:

$$\overline{\chi}_t = -\overline{v}^*\overline{\chi}_y - \overline{w}^*\overline{\chi}_z + \overline{S} + \rho_0^{-1}\nabla \cdot M + \overline{\epsilon}. \tag{5.7}$$

The residual is defined as the difference between the actual rate of change of χ on the left-hand side of Eq. 5.4 and the sum of the transport and

chemistry terms on the right-hand side of Eq. 5.4. It measures how well the TEM framework approximates the rate of change of $\overline{\chi}$ in a specific region of the stratosphere. When the residual is large (mainly because of unresolved processes), the TEM framework does not correctly approximate the rate of change of $\overline{\chi}$. A more detailed description of the possible causes of a large residual is discussed in subsection 2.4 of Sect. 6.1.

Equation 5.7 can be arranged to separate the impact of the meridional and vertical transports due to the residual advection and the mixing:

$$\overline{\chi}_t = A_y + M_y + A_z + M_z + \overline{S} + \bar{\epsilon}, \tag{5.8}$$

where

$$A_y = -\overline{v}^* \overline{\chi}_y, \tag{5.9}$$
$$M_y = e^{z/H} \cos\phi^{-1} (M^{(y)} \cos\phi)_y, \tag{5.10}$$
$$A_z = -\overline{w}^* \overline{\chi}_z, \tag{5.11}$$
$$M_z = e^{z/H} (M^{(z)})_z. \tag{5.12}$$

Here, A_y represents the impact from the meridional residual advection, M_y is the impact from the horizontal transport from eddy mixing, A_z is the effect of the vertical residual advection (upwelling and downwelling) and M_z represents the impact from vertical eddy mixing. The total effects of the residual advection and mixing are respectively $ADV = A_y + A_z$ and $MIX = M_y + M_z$. Such namings are used in Sects. 6.1 and 7.1.

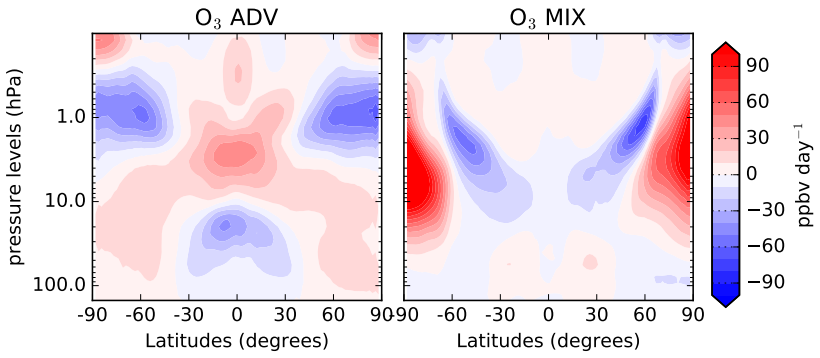

Figure 5.1: Annual means of the advection (ADV, left panel) and mixing (MIX, right panel) terms of the O_3 TEM budget. The data are from an SD-WACCM-REFC1 run nudged to MERRA for the 2005-2014 period. Note that the ozone TEM budget is not complete as the chemistry term $\overline{S}$ could not be computed.

For illustration purposes, Fig. 5.1 shows the mean advection and mixing terms (respectively ADV and MIX) of the TEM budget of ozone in an SD-WACCM experiment driven by MERRA. As mentioned in Sect. 1.2.6, ozone is produced in the tropical lower stratosphere. The tropical upwelling of the BDC transports ozone from that region (between 30 and 100 hPa) to the upper stratosphere above 10 hPa. The meridional advection transports ozone poleward into the extratropics, where it sinks over the polar regions in the mid-stratosphere (below 10 hPa).

The mixing contribution generally has opposite signs compared to the residual advection term because it tends to flatten out the tracer gradients created by the residual advection. Mixing has a significant impact on ozone over the mid-latitudes due to the surf zones (where the planetary wave breaking is large, see Sect. 2.3). In addition, the mixing contribution is also large inside the polar vortices, where it tends to increase the ozone abundancies. This large contribution over the polar regions is due to eddy transport from the ozone-rich mid-latitudes and tends to counteract the ozone removal by the chemistry in spring and summer (see Sect. 1.2.6) and by the transport of ozone-poor air from the layers above in winter.

In this thesis, we extensively use the TEM framework to study the stratospheric transport of N_2O. Chapter 6 investigates the climatoglogies of the main transport terms of the N_2O TEM budget (A_z and M_y). Based on that work, Chapter 7 studies the decadal changes of the advection and mixing terms of the N_2O TEM budget (ADV and MIX).

5.2 Regression tools

Regression tools are numerical models used to explain empirically the time variations of an arbitrary quantity (here the N_2O volume mixing ratios) and extract its linear trend (rate of change) over a specified period. This Section begins with an overview of two widely used regression tools, which are also employed in companion studies: the bootstrap (Sect. 5.2.1) and the Multiple Linear Regression (MLR, Sect. 5.2.2) tools. Section 5.2.3 thoroughly describes the regression tool used in this thesis, the Dynamic Linear Modelling tool (DLM). Section 5.2.4 and Section 5.2.5 evaluate the DLM performances through a qualitative comparison with the bootstrap and the MLR methods, respectively. The main characteristics of the three regression tools are summarized in Table 5.1.

Name	Reference	Linear trend	Seasonal cycle	Autocorr	Proxies	Uncertainty
DLM	Laine et al. (2014)	time-dependent	time-dependent	online	Yes	time-dependent
MLR	Vigouroux et al. (2015)	fixed in time	fixed in time	offline	Yes	fixed in time
Bootstrap	Friedrich et al. (2020)	time-dependent	fixed in time	offline	No	time-dependent

Table 5.1: Main characteristics of the DLM, MLR and bootstrap regression tools.

5.2.1 Bootstrap Method

The bootstrap technique allows to robustly evaluate data that are not regularly distributed with a constant time interval. It relies on the concept that the distribution of the random effects in the data is best represented by the residual between an empirical model fit and the data.

An empirical model function $F(t, a, b)$ is fitted to the data (t_i, M_i) to determine an estimate of the parameters that minimise $\sum_{m=1}^{M}(M_i - F(t_i, a_i, b_i))^2$ using a simple linear least squares method (Gardiner et al., 2008). In the previous expression, t is the time in years, b the parameters of the seasonal variability, a the linear trend and M_i represent some data time series.

After determining the initial fit, the residuals $R_{i,0} = M_i - F(t_i, a_0, b_0)$ are used to approximate the distribution associated with the random effects in the data, and are randomly redistributed to other points in the time series in order to generate a new dataset $M_i^{'}$. The empirical model is then refitted to this "perturbed" data, and this procedure is repeated a large number of times, generating large matrices that contain the parameters of interest (trend and seasonal contribution in this case).

Since each matrix row contains one sample of the distribution of a parameter, we can approximate the rows of the matrices as discrete distributions of that parameter. Thus, the 2.5 and 97.5 percentiles of these empirical distributions provide a 95% confidence interval associated with the given parameter.

A disadvantage of the standard bootstrap sampling is that it does not account for autocorrelation in the data, i.e., the residuals are generally correlated and do not reflect purely random variations, thereby underestimating the uncertainties in the parameters (Gardiner et al., 2008). To overcome this issue, an autoregressive "wild" bootstrap method was developed, where the residuals are generated through an auto-regressive process, with an associated parameter (for more details, see Friedrich et al., 2020).

For a stratospheric time series, the generic model F for fitting the data y_t is a simple linear trend model, that can be formulated as a function of time

t (with units of months) as follows:

$$y_t = \alpha + \beta t + \sum_{j=i}^{S} a_j \cos(2j\pi t/12) + b_j \sin(2j\pi t/12). \tag{5.13}$$

In Eq. 5.13, the long-term trend is $\alpha + \beta t$, where α is the intercept and β is the slope of the trend. The β term can be either fixed in time (classic bootstrap) or time-dependent, i.e., a non-parametric trend fitted to the data locally along the model run (Friedrich et al., 2020). The seasonal effects are modeled using the Fourier terms: $\sum_{j=i}^{S} a_j \cos(2j\pi t) + b_j \sin(2j\pi t)$, with $S = 3$ to capture the semi-annual and quarterly periodicity of the data (Prignon et al., 2021). The coefficients a_j and b_j of the seasonal cycle do not depend on time. The last parameter u_t is a stochastic error term that accounts for autocorrelation. By construction, the bootstrap method does not include any additional representation of atmospheric variability (e.g., the QBO).

5.2.2 Multi Linear Regression

A limitation of the bootstrap method is that it can account only for the seasonal cycle and the linear trend, with all the remaining natural variability regarded as noise. The MLR tool can account for this natural variability through the use of explanatory variables (proxies) that allow isolating the effects of, e.g., the QBO, the solar cycle, or the El-Niño Southern Oscillation (ENSO) (Vigouroux et al., 2015). The MLR has been extensively used as a standard tool for investigating long-term trends and variability in atmospheric time series (e.g., for studies of stratospheric ozone, Chipperfield et al., 2017; Shangguan et al., 2019).

Given an atmospheric time series y_t at time t, a generic MLR can be expressed as:

$$y_t = A_0 + A_1 \cdot t + S(t) + Q(t) + \epsilon(t), \tag{5.14}$$

where A_0 is the baseline value (the intercept) and A_1 is the long-term trend, which is fixed in time. The term $S(t)$ represents the seasonal term as $S(t) = S_1 \cdot \cos(2\pi t/12) + S_2 \cdot \sin(2\pi t/12) + S_3 \cdot \cos(4\pi t) + S_4 \cdot \sin(4\pi t)$, where the coefficients S_i describe the seasonal cycle and are also fixed in time. The term $Q(t)$ describes the variations due to the QBO as $Q(t) = Q10(t) \cdot A_{Q10} + Q30(t) \cdot A_{Q30}$, where the proxies $Q10(t)$ and $Q30(t)$ are generally the observed zonal winds above Singapore at 10 and 30 hPa (available at `http://www.geo.fu-berlin.de/en/met/ag/strat/produkte/qbo/index.html`), and A_{Q10} and A_{Q30} are the coefficients associated with those

proxies. A generic MLR model can include additional proxies, e.g., the solar cycle, the ENSO or the volcanic forcing, to capture and isolate the natural variability on the fitted trends. The uncertainties $\epsilon(t)$ are corrected for the autocorrelation after the regression is complete, i.e., the autocorrelation does not change along the model run according to the data (Santer et al., 2000).

5.2.3 Dynamical Linear Modelling

In the present study we use the DLM tool to investigate stratospheric time-series. "Dynamical" means that the trend and the coefficients of the seasonal cycle and proxies can evolve in time, contrary to the MLR and the classical bootstrap. This Section aims to give a general description of the DLM applied to stratospheric time series. For a more comprehensive review of the DLM analysis, refer to Durbin and Koopman (2012). For an atmospheric-based application, Laine et al. (2014) provides a detailed description of the DLM applied to stratospheric ozone.

The DLM is based on the Bayesian inference (Box and Tiao, 2011). Given some unknown parameters θ and some data d, the Bayes' theorem asserts:

$$P(\theta|d) \propto P(d|\theta)P(\theta), \tag{5.15}$$

where $P(\theta|d)$ is the distribution of the posterior probability of the model parameters, $P(\theta)$ is the probability distribution of the prior knowledge about those parameters, and $P(d|\theta)$ is the likelihood of getting the data as a function of different values of the parameters given the assumptions on them. Given the likelihood and the prior distributions, the DLM uses the Markov chain Monte Carlo (MCMC) method to draw samples from the posterior probability distribution of the model parameters (Gamerman and Lopes, 2006). After obtaining the sample from the posterior distribution, the sampled parameters are used to simulate N realizations of the new state using the Kalman simulation smoother (Petris et al., 2009). From Eq. 5.15, the computation of $P(\theta|d)$ requires the specification of the likelihood $P(d|\theta)$ and the probability $P(\theta)$, together with the definition of the unknown parameters θ.

In order to specify the likelihood $P(d|\theta)$, we need to set up a linear model in the state space to fit the data. Within the DLM, the data can be modeled as the sum of one or several proxies (e.g., QBO, ENSO, solar cycle), a seasonal cycle with annual and semi-annual components, a linear background trend, and an autoregressive process. Thus, a generic time series y_t at time t can

be modeled as follows:

$$
\begin{aligned}
y_t = &\beta_{1,t} z_{1,t} + \beta_{2,t} z_{2,t} ... + \beta_{n,t} z_{n,t} \\
&+ \beta^{12}_{1,t} \sin(2\pi t/12) + \beta^{12}_{2,t} \cos(2\pi t/12) \\
&+ \beta^{6}_{1,t} \sin(2\pi t/6) + \beta^{6}_{2,t} \cos(2\pi t/6) \\
&+ \mu_t \\
&+ z^{AR}_t \\
&+ \epsilon_t.
\end{aligned}
\tag{5.16}
$$

In Eq. 5.16, the forcing from the regressor variables is composed by the time series corresponding to each regressor $z_{1,t}, ..., z_{n,t}$ and their coefficients $\beta_{i,t}$. Those coefficients can be time-dependent and are expressed as $\beta_{i,t} = \beta_{i,t-1} + w_t$, where $w_t \sim \mathcal{N}(0, \sigma_z)$ is assumed to be a Gaussian error with zero mean and σ_z standard deviation. The parameter σ_z controls the time dependency of the amplitudes of the proxies $\beta_{i,t}$: if $\sigma_z = 0$ their amplitudes are constant in time, and the DLM incorporates proxies in a time-independent manner as in the case of the MLR. In general, σ_z can be left as a free parameter, so the data can determine which regressor amplitudes are preferred. This feature is useful when a regressor has seasonal variations or when using merged satellite data. In the present study, we set $\sigma_z = 0$ as done in previous studies using stratospheric tracers (e.g., Laine et al., 2014; Ball et al., 2018).

The seasonal cycle is modeled through the 6- and 12-months components, with amplitudes $\beta^k_{1,t}$ that depend on time and are defined as $\beta^k_{1,t} = \beta^k_{1,t-1} + w_t$, where $w_t \sim \mathcal{N}(0, \sigma_{\text{seas}})$. The degree at which the amplitudes of the seasonal cycles can evolve with time is governed by σ_{seas}: setting $\sigma_{\text{seas}} = 0$ corresponds to constant amplitudes of the seasonal cycle, while $\sigma_{\text{seas}} > 0$ allows for the evolution of the amplitudes of the seasonal cycle over time. In our calculations, we keep $\sigma_{\text{seas}} \neq 0$, i.e., as a free parameter to be fit alongside the model run, allowing for the modulation of the seasonal amplitude if this is preferred by the data. For monthly data, the 6- and 12-months seasonal components are respectively described by $k = 2$ and $k = 1$ in Eq. 5.16.

The background linear trend is modeled by μ_t, which is defined as:

$$\mu_t = \mu_{t-1} + \alpha_{t-1} \tag{5.17}$$

$$\alpha_t = \alpha_{t-1} + \mathcal{N}(0, \sigma_{\text{trend}}). \tag{5.18}$$

In Eq. 5.17, μ_t is the background linear fit and α_t is the change of the fit from t to $t + 1$ (i.e., it approximates the slope of the fit). Thus, the background fit μ_t is governed by a locally linear model with slope α_t that is allowed to vary with time. The rate at which the slope can evolve in time

is controlled entirely by the parameter σ_{trend}: larger values of σ_{trend} will lead to non-linear background evolution, i.e., α_t can significantly change between adjacent time steps and the resulting trend will strongly fluctuate, while the limit $\sigma_{\text{trend}} \to 0$ recovers a linear trend with a constant slope (as in MLR). In our experiments, we keep σ_{trend} as a free parameter to be fitted with the rest of the model. In this way, the DLM can "decide" (within reasonable prior constraints) how smooth the background trend can be.

The autoregressive processes (ARn) enter the DLM via the z_t^{AR} term in Eq. 5.16. In our calculations, we use a first-order autoregressive model (AR1) to allow autocorrelation. The AR1 component can be written as $z_t^{AR1} = \rho z_{t-1}^{AR1} + \mathcal{N}(0, \sigma_{\text{AR1}})$, where ρ is the time-dependent autoregression coefficient and is fitted throughout the model run together with σ_{AR1}.

Once the model is set up, we need to specify the prior distribution of the parameters $P(\theta)$ and the state at time $t = 0$ in order to perform Bayesian inference. The parameters θ that need to be determined are: σ_{trend}, σ_{seas}, σ_{z}, σ_{AR1} and ρ_{AR1}. All the other terms (μ, βs, ...) are obtained from those parameters; hence the σs and the ρ_{AR1} parameters are called "hyper-parameters". The σ_{trend}, σ_{seas}, σ_{z}, and σ_{AR1} hyper-parameters are defined using half-normal positive prior distributions (i.e., the priors $P(\theta)$):

$$\sigma_{\text{trend}} \sim \text{HalfNormal}(0, \sigma_{\text{trend}}^{\text{prior}}) \tag{5.19}$$

$$\sigma_{\text{seas}} \sim \text{HalfNormal}(0, \sigma_{\text{seas}}^{\text{prior}}) \tag{5.20}$$

$$\sigma_{\text{z}} \sim \text{HalfNormal}(0, \sigma_{\text{z}}^{\text{prior}}) \tag{5.21}$$

$$\sigma_{\text{AR1}} \sim \text{HalfNormal}(0, \sigma_{\text{AR1}}^{\text{prior}}), \tag{5.22}$$

where the widths of the priors are $\sigma_{\text{trend}}^{\text{prior}}$, $\sigma_{\text{seas}}^{\text{prior}}$, $\sigma_{\text{z}}^{\text{prior}}$ and $\sigma_{\text{AR1}}^{\text{prior}}$, and can be specified by the user at $t = 0$. Among those prior widths, it is important to carefully set $\sigma_{\text{trend}}^{\text{prior}}$. If it is set to be large and there is non-modeled variance in the data, the model tends to make σ_{trend} even larger and have a strongly fluctuating trend, which tends to balance the residual and the variance that is not modeled. Therefore, the user needs to be careful in constraining the initial value of $\sigma_{\text{trend}}^{\text{prior}}$ to be small enough to keep a reasonably smooth background trend, but large enough to follow the data if allowed.

For the initial state at $t = 0$, we refer to the amplitudes of the regressors coefficients $\beta_{i,t}$, of the seasonal cycle $\beta_{i,t}^k$, and the trend μ_t. For these quantities, a zero-mean Gaussian distribution with standard deviation S, initially specified by the user, is chosen.

The DLM source code is written in Python and freely available for download at `https://github.com/justinalsing/dlmmc` (Alsing, 2019). This code was also used in studies of changes in stratospheric ozone in Ball et al. (2017) and Ball et al. (2018).

As proxies, we used the 30 cm radio flux as a proxy of the solar UV variability (de Wit et al., 2014), an index for the ENSO (Wolter and Timlin, 2011) from the NOAA (`http://www.esrl.noaa.gov/psd/enso/mei/`), and two indices for the QBO at 30 and 50 hPa from the Freie Universität Berlin (`http://www.geo.fu-berlin.de/en/met/ag/strat/produkte/qbo/index.html`). All proxy variables are normalized to have zero mean and range from -0.5 to 0.5, so they are all on the same scale.

In this thesis, we fed the DLM with monthly data, running N=3000 iterations where the first 1000 were considered as a warmup and discarded. We set the widths of the priors for the hyper-parameters as follows: $\sigma^{\text{prior}}_{\text{trend}}$ =10^{-4}, $\sigma^{\text{prior}}_{\text{seas}} = 0.01$, $\sigma^{\text{prior}}_{\text{AR1}} = 0.5$, $S = 10$. Those values derive from several sensitivity tests performed by the model developers, which led to robust values for a wide range of cases (Justin Alsing, personal communication). However, the value of $\sigma^{\text{prior}}_{\text{trend}}$ generally depends on the period and on the variability of the considered quantity. Therefore, we performed four senstitvity tests running the same DLM model on the N_2O abundances obtained from the BASCOE CTM experiment driven by ERA5 using different initial values of $\sigma^{\text{prior}}_{\text{trend}}$: 10^{-2}, 10^{-3}, 10^{-4}, 10^{-5}. We compare the N_2O fits obtained from those experiments in Fig. 5.2 above the northern and southern mid-latitudes (45°N and S) at 50 hPa. The different values of $\sigma^{\text{prior}}_{\text{trend}}$ do not significantly impact the N_2O linear fits obtained from the DLM, both in the NH and in the SH. Given the results of these sensitivity tests, we use $\sigma^{\text{prior}}_{\text{trend}} = 0.0001$ in all the DLM runs described in this thesis.

It is important to explicitly highlight how the background trend, i.e., the rate of change of the background fit in time, is computed from the DLM output. The DLM provides a distribution of the N fit samples with dimensions $[\mu]$=[nsamples,ntime,nspace]. The background trend is computed from this distribution as the difference (delta) between the end and start dates of the considered period and has dimensions [trend]=[nsamples,nspace]. The uncertainties associated with this trend are computed as the percentage of the delta values that are positive or negative. This percentage can be interpreted as the posterior probability that the overall change in the fit is positive (or negative) between the considered dates. Such a method does not require any assumption on the shape of the distribution of the deltas, i.e., it is not assumed gaussian nor even symmetrical. In this thesis, we show three values of the posterior probability of positive or negative change: 80, 90 and 95 %.

5.2.4 DLM vs bootstrap

This Section highlights the major differences between the DLM and the bootstrap described in Sect. 5.2.1 and used by Prignon et al. (2021), and com-

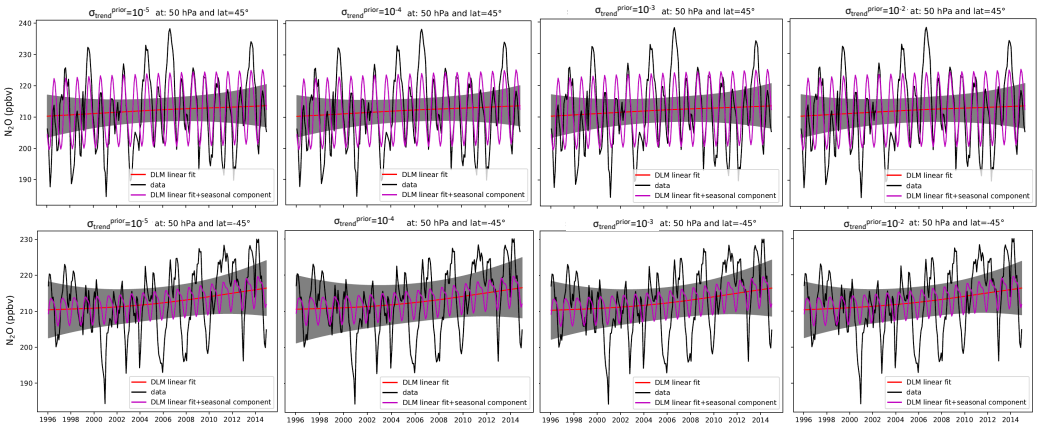

Figure 5.2: N_2O abundancies obtained from the BASCOE CTM simulation driven by ERA5 at 50 hPa. The upper panels show the N_2O abundances above 45°N and the lower panels above 45°S. The black line represents the model output, the red line the linear fit obtained from the DLM model, the purple line the sum of the linear fit and the seasonal component both obtained from the DLM. From left to right $\sigma_{\text{trend}}^{\text{prior}}$ is: 10^{-5}, 10^{-4}, 10^{-3}, 10^{-2}.

pares the trends obtained from these two regression tools. As mentioned in the previous Sections, the background trend in the DLM is modeled by a time-dependent dynamical term, while in the bootstrap it can be either modeled using a linear fit with slope and intercept fixed in time or through a non-parametric fit that evolves in time. In addition, the model used within the DLM implements a time-varying seasonal cycle and three proxies, while the bootstrap can model only a seasonal cycle fixed in time and does not include proxies.

Keeping in mind these major differences between the tools, we compare the outputs of the DLM with those from the bootstrap method with the slope and intercept fixed in time, which are shown in Figs. 6 and 7 of Prignon et al. (2021). Figure 5.3 shows the F_y abundances above the southern subtropics in the middle stratosphere simulated by the BASCOE CTM driven by ERAI, together with its fits obtained with the bootstrap (with 1 sigma uncertainty) and with the DLM (the uncertainties for the DLM are omitted for clarity). We consider this particular stratospheric region because the differences between the DLM and bootstrap in the recovered fits of the F_y abundances are the largest.

The F_y abundances simulated by the BASCOE CTM increase during the '90s until the mid-2000s, then stabilise throughout the first two decades of the 21st century because of the implementation of the Montreal Protocol. In

order to investigate its short-term variability, the bootstrap was run on the F_y abundances for the 2004-2011 period and delivered a significant negative trend over that period (Prignon et al., 2021). The DLM model, which is run for the period 1990-2019, instead delivers a near-zero trend over the same period, which is derived from the nearly horizontal linear fit.

From this simple comparison, we conclude that the choice of the analyzed period is crucial when setting up the run for a given regression tool, as it can deliver opposite trends. For the bootstrap method, this is especially important when it is used with the linear trend fixed in time. The best practice would be to run the regression tools for the longest possible period, in order to capture and model any natural variability present in the data. However, for time-independent trends, this would mask any change in the slope of the retrieved trend (as for the F_y fits from the bootstrap). Thus, when possible, a regression tool should be run with time-dependent trends, in order to identify the possible variations due to natural variability.

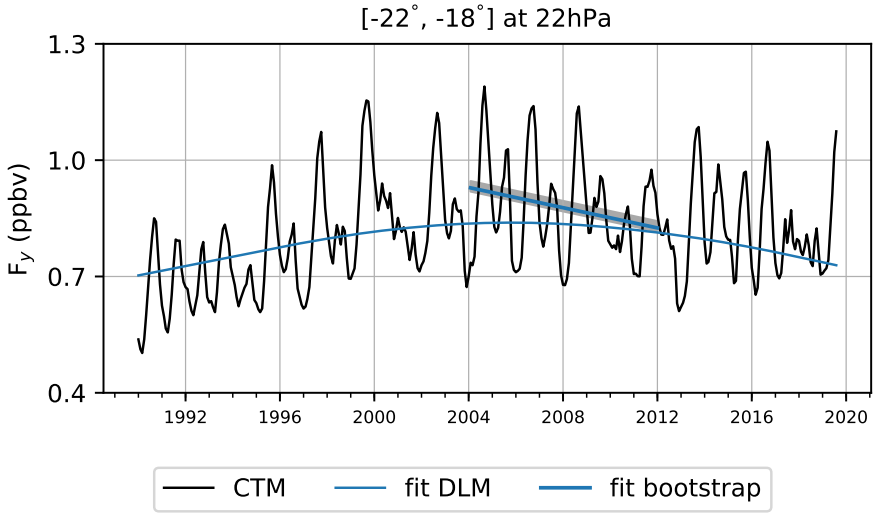

Figure 5.3: Time series of the total inorganic fluorine F_y mixing ratio [ppbv] at 22 hPa averaged between 22°and 18°S from the BASCOE CTM run driven by ERAI. The black line is the CTM output, the light blue straight line is the F_y fit obtained from the bootstrap tool only for the 2004-2011 period, and the blue is the F_y fit obtained from the DLM tool.

5.2.5 DLM vs MLR

This Section briefly reviews the main differences between the DLM and MLR tools and compares the trends obtained from them. To that end, we compute

the long-term and decadal trends of mean AoA with the DLM from the BASCOE CTM simulations driven by the ERAI, JRA55, MERRA, MERRA2 and NCEP-CFSR reanalyses. We compare those trends with the trends obtained with a standard MLR from the same datasets (Fig. 12 in Chabrillat et al., 2018, replicated in Fig. 5.4). In order to perform a fair comparison between the two regression tools, the DLM model includes the same QBO regressors as the MLR model, and all other regressors (ENSO, solar cycle, ...) are not considered. In Chabrillat et al. (2018), the MLR model was run over three different periods based on a known improvement in the quality of the satellite data that was assimilated into the reanalyses, but in general the behaviour of the data is unknown in advance.

Figure 5.5 shows the background trends of the mean AoA obtained with the DLM, defined as stated at the end of Sect. 5.2.3, for the various BASCOE CTM simulations. Each panel of Fig. 5.5 should be compared with the corresponding panel of Fig. 5.4, which shows the trends of the mean AoA for the same dataset but derived from the MLR (i.e., the A_1 term in Eq. 5.14). The trends computed using the DLM agree remarkably well with those from the MLR for the various periods across all the reanalyses. However, the uncertainties differ between the two regression tools, with the DLM typically delivering smaller regions where the retrieved trend is statistically significant (e.g., the MERRA simulation over the 1989-2015 period). Those differences in the significance of the trends are caused by their fundamentally different definitions and implementations between the two tools (see Sects. 5.2.2 and 5.2.3). The time-dependence results in more severe constraints for the significance of the trends derived with the DLM, compared to the time-independent trends obtained with the MLR.

Figure 5.5 does not provide the additional time-dependent information that the DLM can supply. In order to briefly analyze the impact of the time-dependence, the left panel of Fig. 5.6 shows the mean AoA at 70 hPa above 30°N obtained from the BASCOE CTM driven by ERAI, together with its background fit and the sum of this fit and the seasonal cycle component. We chose this particular stratospheric region because it shows well the impact of the time-dependence that the DLM is able to catch. The fits obtained from the DLM, both the linear and the linear plus seasonal, follow the evolution of the data, with increasing mean AoA until the early 2000s and near-constant mean AoA afterward. When an MLR model is used for the whole period, the recovered (time-independent) trend hides the different slopes, and it does not completely recover the actual tendency of the data over the considered period. The right panel of Fig. 5.6 shows the seasonal cycle component of the recovered fit of the mean AoA (i.e., the sum of the $\beta^k_{1,t}\cos(...)$ and $\beta^k_{1,t}\sin(...)$ terms in Eq. 5.16) for the same region. The seasonal component largely

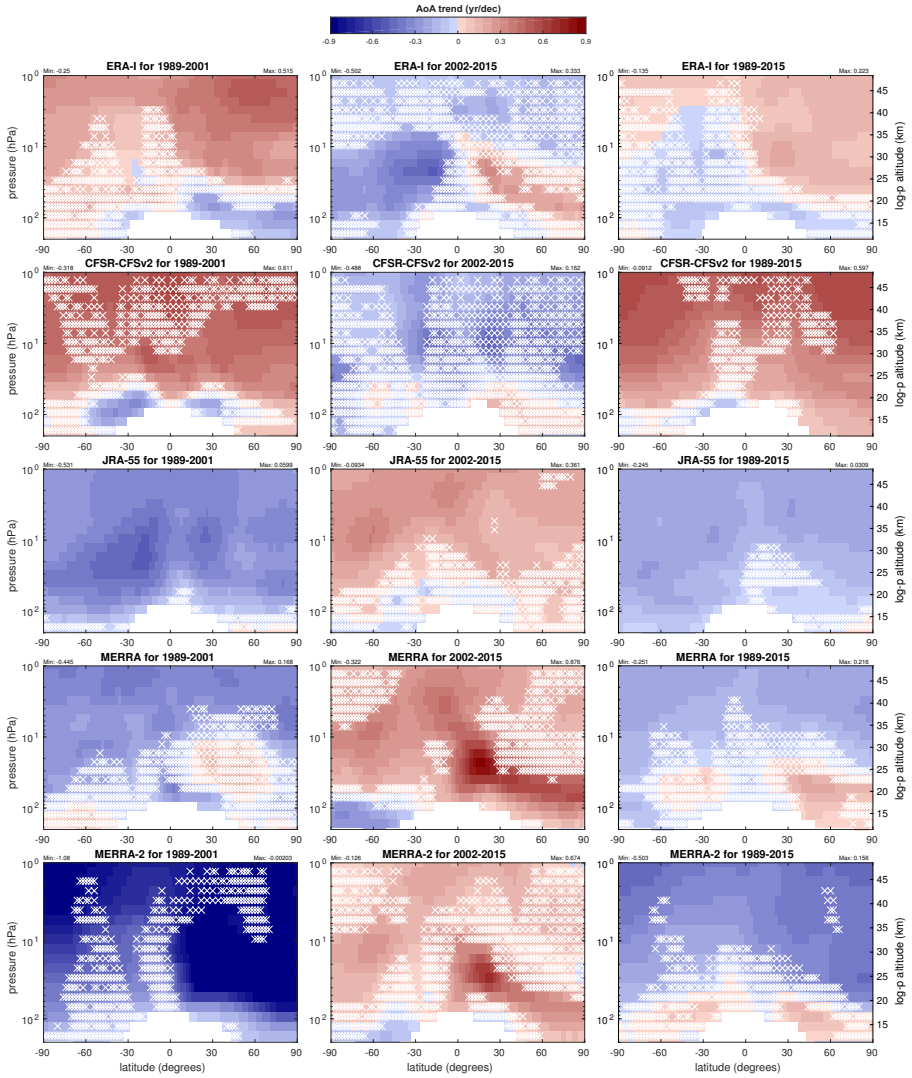

Figure 5.4: Latitude-pressure distributions of the mean AoA trends (in years per decade) over 1989-2001 (left column), 2002-2015 (middle column) and 1989-2015 (right column) from the BASCOE CTM driven by the five reanalyses (from top to bottom: ERA-I, CFSR, JRA-55, MERRA, MERRA-2). White crosses indicate grid points where the sign of the trend is not significant; i.e., its absolute value is smaller than the uncertainty delivered by the regression analysis at the 95% confidence level. The color scale is the same as in Haenel et al. (2015, Figs. 6 and 10) with darker blues indicating more negative trends and darker reds more positive trends. From Chabrillat et al. (2018).

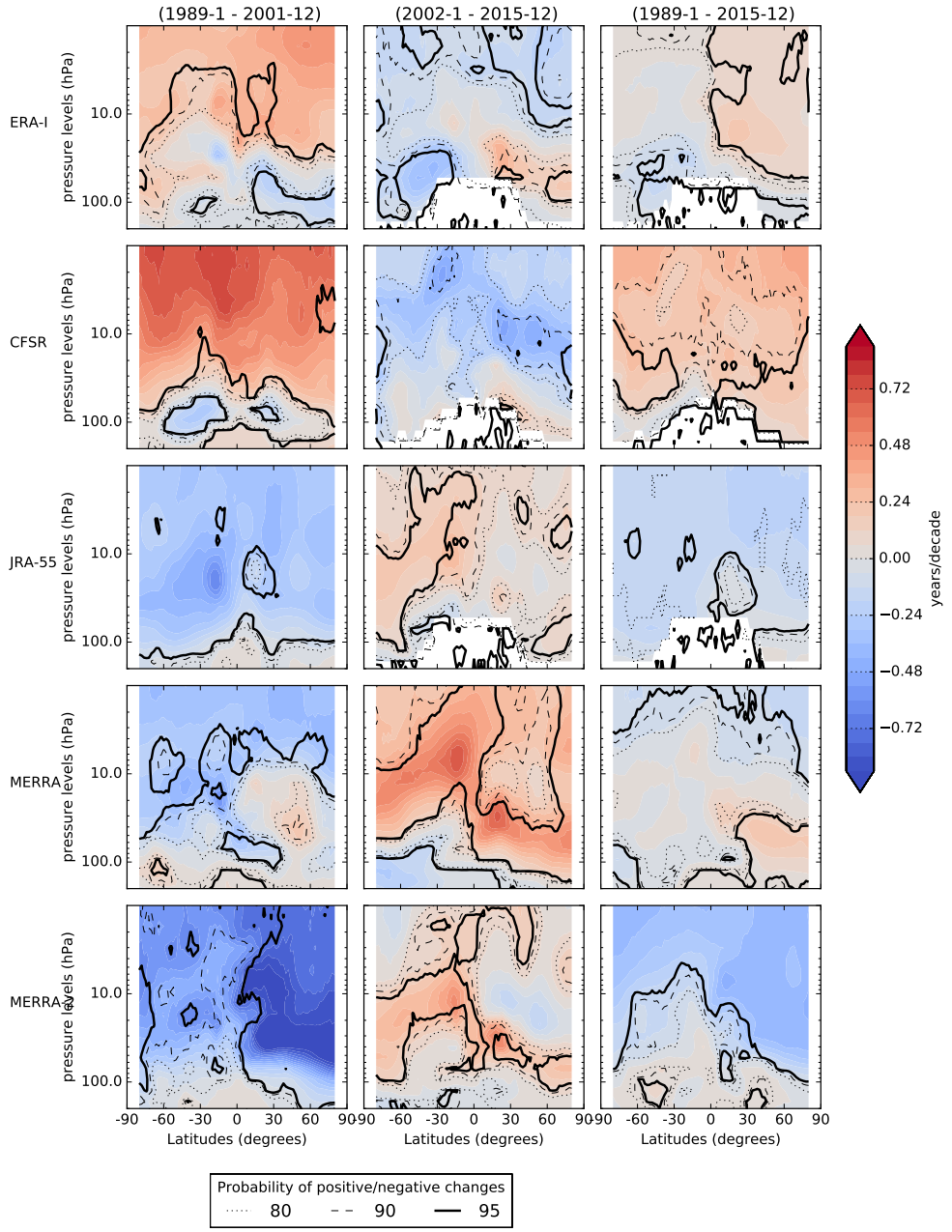

Figure 5.5: Reproduction of Fig.12 of Chabrillat et al. (2018) using the DLM instead of the MLR.

depends on time, with values twice larger before the 2000s than afterward. This modulation plays an important role in determining the uncertainties on the fit obtained from the DLM and contributes to the differences with the uncertainties obtained with the MLR.

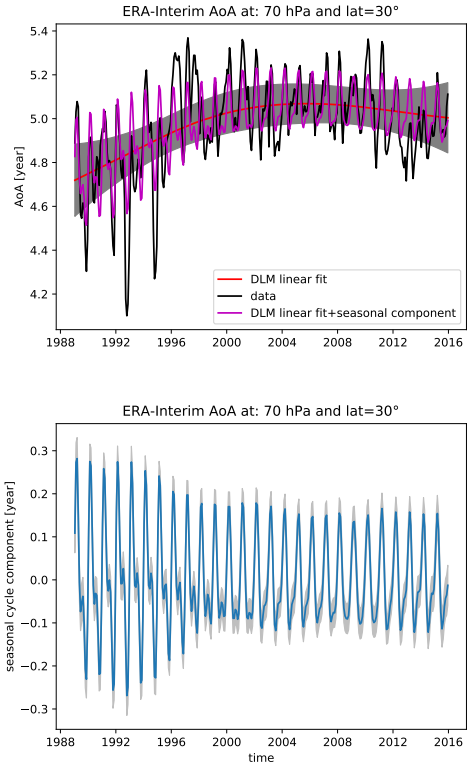

Figure 5.6: Mean AoA obtained from the BASCOE CTM run driven by ERAI at 70 hPa and 30°N. Left panel: the black line represents the CTM output, the red line its time-dependent linear fit from the DLM, and the purple line the sum of the linear fit and the contribution from the seasonal cycle. Right panel: time-dependent contribution of the seasonal cycle to the recovered fit of mean AoA obtained with the DLM.

6 Climatologies of N_2O and its TEM budget

This Chapter studies the climatologies of the N_2O TEM budget and the N_2O volume mixing ratios themselves. Section 6.1 represents the main part of the Chapter, with Sect. 6.2 sexpanding the comparison with two recent datasets not included in Sect. 6.1: the BASCOE CTM driven by ERA5 and the WACCM-REFD1 model.

6.1 Climatological impact of the Brewer-Dobson circulation on the N_2O TEM budget in WACCM, a chemical reanalysis and a CTM driven by four dynamical reanalyses

This Section investigates the climatologies of the N_2O mixing ratios and the two main contributions to its TEM budget (A_z and M_y) over the 2005-2014 period. We compare four BASCOE CTM simulations driven by ERAI, JRA55, MERRA and MERRA2 with the BRAM2 chemical reanalysis and two versions of the WACCM model: WACCM4 and WACCM-REFC1. The Section is re-printed from a paper published in 2020 in the peer-reviewed journal Atmospheric Chemistry and Physics:

Minganti, D., Chabrillat, S., Christophe, Y., Errera, Q., Abalos, M., Prignon, M., Kinnison, D. E., and Mahieu, E.: Climatological impact of the Brewer-Dobson circulation on the N_2O budget in WACCM, a chemical reanalysis and a CTM driven by four dynamical reanalyses, Atmos. Chem. Phys., 20, 12609-201312631, `https://doi.org/10.5194/acp-20-12609-2020`, 2020.

Atmos. Chem. Phys., 20, 12609–12631, 2020
https://doi.org/10.5194/acp-20-12609-2020

Atmospheric Chemistry and Physics
Open Access
EGU

Climatological impact of the Brewer–Dobson circulation on the N_2O budget in WACCM, a chemical reanalysis and a CTM driven by four dynamical reanalyses

Daniele Minganti[1], Simon Chabrillat[1], Yves Christophe[1], Quentin Errera[1], Marta Abalos[2], Maxime Prignon[3], Douglas E. Kinnison[4], and Emmanuel Mahieu[3]

[1]Royal Belgian Institute for Space Aeronomy, BIRA-IASB, 1180 Brussels, Belgium
[2]Earth Physics and Astrophysics Department, Universidad Complutense de Madrid, 28040 Madrid, Spain
[3]Institute of Astrophysics and Geophysics, University of Liège, 4000 Liège, Belgium
[4]National Center for Atmospheric Research, Boulder, 80301 CO, USA

Correspondence: Daniele Minganti (daniele.minganti@aeronomie.be)

Received: 19 March 2020 – Discussion started: 16 April 2020
Revised: 7 August 2020 – Accepted: 23 September 2020 – Published: 3 November 2020

Abstract. The Brewer–Dobson circulation (BDC) is a stratospheric circulation characterized by upwelling of tropospheric air in the tropics, poleward flow in the stratosphere, and downwelling at mid and high latitudes, with important implications for chemical tracer distributions, stratospheric heat and momentum budgets, and mass exchange with the troposphere. As the photochemical losses of nitrous oxide (N_2O) are well known, model differences in its rate of change are due to transport processes that can be separated into the mean residual advection and the isentropic mixing terms in the transformed Eulerian mean (TEM) framework. Here, the climatological impact of the stratospheric BDC on the long-lived tracer N_2O is evaluated through a comparison of its TEM budget in the Whole Atmosphere Community Climate Model (WACCM), in a chemical reanalysis of the Aura Microwave Limb Sounder version 2 (BRAM2) and in a chemistry transport model (CTM) driven by four modern reanalyses: the European Centre for Medium-Range Weather Forecasts Interim reanalysis (ERA-Interim; Dee et al., 2011), the Japanese 55-year Reanalysis (JRA-55; Kobayashi et al., 2015), and the Modern-Era Retrospective analysis for Research and Applications version 1 (MERRA; Rienecker et al., 2011) and version 2 (MERRA-2; Gelaro et al., 2017). The effects of stratospheric transport on the N_2O rate of change, as depicted in this study, have not been compared before across this variety of datasets and have never been investigated in a modern chemical reanalysis. We focus on the seasonal means and climatological annual cycles of the two main contributions to the N_2O TEM budget: the vertical residual advection and the horizontal mixing terms.

The N_2O mixing ratio in the CTM experiments has a spread of approximately $\sim 20\,\%$ in the middle stratosphere, reflecting the large diversity in the mean age of air obtained with the same CTM experiments in a previous study. In all datasets, the TEM budget is closed well; the agreement between the vertical advection terms is qualitatively very good in the Northern Hemisphere, and it is good in the Southern Hemisphere except above the Antarctic region. The datasets do not agree as well with respect to the horizontal mixing term, especially in the Northern Hemisphere where horizontal mixing has a smaller contribution in WACCM than in the reanalyses. WACCM is investigated through three model realizations and a sensitivity test using the previous version of the gravity wave parameterization. The internal variability of the horizontal mixing in WACCM is large in the polar regions and is comparable to the differences between the dynamical reanalyses. The sensitivity test has a relatively small impact on the horizontal mixing term, but it significantly changes the vertical advection term and produces a less realistic N_2O annual cycle above the Antarctic. In this region, all reanalyses show a large wintertime N_2O decrease, which is mainly due to horizontal mixing. This is not seen with WACCM, where the horizontal mixing term barely contributes to the TEM budget. While we must use caution in the interpretation

of the differences in this region (where the reanalyses show large residuals of the TEM budget), they could be due to the fact that the polar jet is stronger and is not tilted equatorward in WACCM compared with the reanalyses.

We also compare the interannual variability in the horizontal mixing and the vertical advection terms between the different datasets. As expected, the horizontal mixing term presents a large variability during austral fall and boreal winter in the polar regions. In the tropics, the interannual variability of the vertical advection term is much smaller in WACCM and JRA-55 than in the other experiments. The large residual in the reanalyses and the disagreement between WACCM and the reanalyses in the Antarctic region highlight the need for further investigations on the modeling of transport in this region of the stratosphere.

1 Introduction

The Brewer–Dobson circulation (BDC; Dobson et al., 1929; Brewer, 1949; Dobson, 1956) in the stratosphere is characterized by upwelling of tropospheric air to the stratosphere in the tropics, followed by poleward transport in the stratosphere and extra-tropical downwelling. For tracer-transport purposes the BDC is often divided into an advective component, the residual mean meridional circulation (hereafter residual circulation) and a quasi-horizontal two-way mixing, which causes net transport of tracers but not of mass (Butchart, 2014).

The BDC is driven by tropospheric waves breaking into the stratosphere (Charney and Drazin, 1961), which transfer angular momentum and force the stratosphere away from its radiative equilibrium. This is balanced by a poleward displacement of air masses, which implies tropical upwelling and extra-tropical downwelling (Holton, 2004). The residual circulation can be further separated into three branches: the transition branch, the shallow branch and the deep branch (Lin and Fu, 2013). The transition branch encompasses the upper part of the transition layer between the troposphere and the stratosphere (the tropical tropopause layer; Fueglistaler et al., 2009); the shallow branch is a year-round, lower stratospheric, two-cell system driven by breaking of synoptic-scale waves; and the deep branch is driven by Rossby and gravity waves breaking in the middle and high parts of the stratosphere during winter (Plumb, 2002; Birner and Bönisch, 2011). The contributions of different wave types to driving the BDC branches has been quantified using the downward control principle, which states that the poleward mass flux across an isentropic surface is controlled by the Rossby or gravity waves breaking above that level (Haynes et al., 1991; Rosenlof and Holton, 1993), and using eddy heat flux calculations as an estimate of the wave activity from the troposphere (e.g., Newman and Nash, 2000).

The quasi-horizontal two-way mixing is generated by two-way transport due to the adiabatic motion of Rossby waves. In the stratosphere this motion is ultimately combined with molecular diffusion which makes the total process irreversible (Shepherd, 2007). The two-way mixing is stronger in a specific latitudinal region of the winter stratosphere, the "surf zone" (McIntyre and Palmer, 1983), and in the subtropical lower stratosphere all year round (e.g., Fig.1 of Bönisch et al., 2011). The mixing process homogenizes the tracer concentration in the surf zone and creates sharp tracer and potential vorticity (PV) gradients on its edges (in the subtropics and at the polar vortex edge), indicating an inhibition of mixing. For this reason, the subtropics and the polar vortex edge are often called transport barriers (Shepherd, 2007).

The BDC plays a major role in controlling the spatial and temporal distributions of chemical tracers, such as ozone, water vapor, aerosols and greenhouse gases, as well as in coupling stratospheric processes with the climate system (Riese et al., 2012; Butchart, 2014; Tweedy et al., 2017). The natural variability of the atmosphere largely influences the BDC (Hardiman et al., 2017). All three branches of the BDC are affected by changes in sea surface temperatures and the El Niño–Southern Oscillation (Yang et al., 2014; Diallo et al., 2019) as well as the phase of the quasi-biennial oscillation (QBO, Diallo et al., 2018) and the Arctic oscillation (Salby and Callaghan, 2005).

Modeling studies have predicted an acceleration of the BDC over the last few decades and the 21st century due to the increase in well-mixed greenhouse gases (Butchart et al., 2010; Hardiman et al., 2014; Palmeiro et al., 2014) and ozone-depleting substances (Polvani et al., 2018), but these results cannot be evaluated easily because the BDC cannot be observed directly (Butchart, 2014). Observational studies over short periods (typically 2003–2012) show significant evidence of a changing BDC in the boreal lower stratosphere (Schoeberl et al., 2008; Stiller et al., 2012; Hegglin et al., 2014; Mahieu et al., 2014; Haenel et al., 2015), but balloon-borne observations of SF_6 and CO_2 in the northern midlatitudes show a nonsignificant trend of the deep branch of the BDC over the past few decades (Engel et al., 2009, 2017). This difficulty in deriving observational trends in the BDC can be partly attributed to the spatial and temporal sparseness of the observations as well as its large dynamical variability and the uncertainty of trends derived from nonlinearly increasing tracers (Garcia et al., 2011; Hardiman et al., 2017; Fritsch et al., 2020). Before investigating multidecadal changes of the BDC, it is important to perform an accurate evaluation of its climatological state and interannual variability, which is the aim of this paper.

In this study, we use N_2O as a tracer to study the BDC. N_2O is continuously emitted in the troposphere (with larger abundances in the Northern Hemisphere, NH) and transported into the stratosphere where it is destroyed by photodissociation and, to a lesser extent, by reaction with $O(^1D)$. The estimated lifetime of N_2O is approximately 120 years,

which makes it an excellent long-lived tracer for transport studies in the middle atmosphere (Brasseur and Solomon, 2006; Seinfeld and Pandis, 2016).

We use the transformed Eulerian mean (TEM, Andrews et al., 1987) analysis to separate the local rates of change of N_2O due to transport and chemistry (Randel et al., 1994). The transport term can be further separated into the contribution of isentropic mixing and residual advection, as done previously for O_3 and CO (Abalos et al., 2013). The isentropic mixing and the residual advection can be additionally separated in their horizontal and vertical contributions. In the tropical lower stratosphere, the distinction between vertical and horizontal transport is important, as they impact the seasonality of N_2O differently in the northern and southern tropics (Tweedy et al., 2017). We choose to focus our study on the horizontal mixing and vertical advection, because their magnitudes are larger than the vertical mixing and the meridional residual advection in most of the stratosphere.

Chemistry climate models (CCMs) include the full representation of dynamical, radiative and chemical processes in the atmosphere as well as their interactions. In particular, they combine the feedbacks of the chemical tracers on the heat budget and dynamics, which ultimately affects tracer transport. We use version 4 of the Whole Atmosphere Community Climate Model (WACCM; Garcia et al., 2017) to simulate the N_2O TEM budget in the stratosphere for the 2005–2014 period. WACCM has been widely used for studies of tracers' transport in the stratosphere and upper troposphere based on the TEM analysis (e.g., Abalos et al., 2017). WACCM simulations of the climatological N_2O over the 2005–2014 period have also been evaluated favorably with satellite observations in the stratosphere (Froidevaux et al., 2019).

In order to assess their representation of the atmospheric processes, CCMs are often compared to reanalyses (e.g., Gerber et al., 2010). Reanalysis products merge dynamical atmospheric observations (e.g., surface pressure, wind and temperature) with a global forecast model using an assimilation scheme to offer the best reproduction of the past climate. They provide a multivariate, consistent record of the global atmospheric state. Reanalyses are made using different assimilation methods and forecast models (Cameron et al., 2019), and they are often compared among each other and with CCMs (Rao et al., 2015). The SPARC (Stratosphere-troposphere Processes And their Role in Climate) Reanalysis Intercomparison Project (S-RIP) coordinates the intercomparison of all major global atmospheric reanalyses and provides reports to document these results (Fujiwara et al., 2017; Long et al., 2017).

Meteorological fields from reanalyses are often used to drive chemistry transport models (CTMs) in order to study the BDC through a common diagnostic, namely the age of air (AoA; Waugh and Hall, 2002), and simulate realistic distributions of chemical tracers (Monge-Sanz et al., 2012; Ménard et al., 2020). Thanks to their simplicity, CTMs are useful to compare different reanalyses within the same transport framework, thereby contributing to the study of the BDC in S-RIP (chapter 5 of the S-RIP report; see Fig. 1 in Fujiwara et al., 2017). CTMs may use either sigma-pressure levels with a kinematic transport scheme and vertical velocities simply derived from mass conservation or isentropic levels with a diabatic transport scheme (Chipperfield, 2006). Recent intercomparisons showed that the AoA depends to a large extent on the input reanalysis, both using the kinematic approach (Chabrillat et al., 2018) and the diabatic approach (Ploeger et al., 2019).

Here, we use the same CTM as for the kinematic AoA study, i.e., the Belgian Assimilation System of Chemical ObsErvation (BASCOE) CTM. Observations of another long-lived stratospheric tracer, HCFC-22, were recently interpreted with WACCM and BASCOE CTM simulations, showing the interest of this model intercomparison (Prignon et al., 2019). In order to contribute further to the S-RIP BDC activity, four different dynamical reanalyses are used here to drive the BASCOE CTM simulations, compute the N_2O TEM budget and compare its components with the results derived from WACCM, namely the European Centre for Medium-Range Weather Forecasts Interim reanalysis (ERA-Interim; Dee et al., 2011), the Japanese 55-year Reanalysis (JRA-55; Kobayashi et al., 2015), and the Modern-Era Retrospective analysis for Research and Applications version 1 (MERRA; Rienecker et al., 2011) and version 2 (MERRA-2; Gelaro et al., 2017).

While dynamical reanalyses do not assimilate observations of chemical compounds, chemical reanalyses achieve this step and can be used to evaluate CCMs or study differences between instruments using the reanalysis as a transfer tool (Errera et al., 2008; Lahoz and Errera, 2010; Davis et al., 2016). To our knowledge, chemical reanalyses driven by meteorological fields from modern dynamical reanalyses have not been used to study tracer transport in the stratosphere using the TEM framework. WACCM and the CTM experiments are compared with a chemical reanalysis of the Aura Microwave Limb Sounder (MLS) using the BASCOE data assimilation system (DAS) driven by the ERA-Interim reanalysis (BRAM2; Errera et al., 2019).

To summarize, in this study we analyze the representation of the BDC in WACCM through an analysis of the TEM budget of N_2O, and we evaluate the simulation of this budget through comparisons with the BASCOE CTM (driven by four dynamical reanalyses) and the BRAM2 chemical reanalysis. In Sect. 2, we describe the datasets used in the study and the TEM analysis of N_2O. In Sect. 3, we analyze the seasonal mean patterns of the TEM N_2O budget in each dataset and their differences. Sections 4 and 5 investigate the mean annual cycle and the variability of the N_2O TEM budget terms, respectively, with a focus on the differences between the datasets. Section 6 concludes the study with a summary of our findings and directions for possible future research.

Table 1. Overview of the datasets used in this study.

Dataset name	Reference	Dynamical reanalysis	Chemical reanalysis	Model grid	Top level
WACCM4	Marsh et al. (2013)	None	None	$2.5° \times 1.9°$, L66	5.1×10^{-6} hPa
WACCM-CCMI	Garcia et al. (2017)	None	None	$2.5° \times 1.9°$, L66	5.1×10^{-6} hPa
ERAI	Chabrillat et al. (2018)	ERA-Interim (Dee et al., 2011)	None	$2.5° \times 2°$, L60	0.1 hPa
JRA-55	Chabrillat et al. (2018)	JRA-55 (Kobayashi et al., 2015)	None	$2.5° \times 2°$, L60	0.1 hPa
MERRA	Chabrillat et al. (2018)	MERRA (Rienecker et al., 2011)	None	$2.5° \times 2°$, L72	0.01 hPa
MERRA-2	Chabrillat et al. (2018)	MERRA-2 (Gelaro et al., 2017)	None	$2.5° \times 2°$, L72	0.01 hPa
BRAM2	Errera et al. (2019)	ERA-Interim (Dee et al., 2011)	MLS (Livesey et al., 2015)	$3.75° \times 2.5°$, L37	0.1 hPa

2 Data and method

This work uses seven datasets that were generated by WACCM, the BASCOE CTM and the BASCOE DAS. Table 1 provides an overview of these datasets and their main differences, and the next three subsections provide details about the models and systems that generated them.

2.1 WACCM

WACCM (Garcia et al., 2017) is the atmospheric component of the Community Earth System Model version 1.2.2 (Hurrell et al., 2013), which has been developed by the U.S. National Center for Atmospheric Research. It is the extended (whole atmosphere) version of the Community Atmosphere Model version 4 (CAM4; Neale et al., 2013).

We ran one realization of the public version of WACCM (hereafter WACCM4; Marsh et al., 2013) with a similar setup (e.g., lower boundary conditions) to the CTM experiments; the source code of WACCM4 is available for download at https://svn-ccsm-models.cgd.ucar.edu/cesm1/release_tags/cesm1_2_2/, last access: 28 October 2020. In this study we also use three realizations of the REF-C1 simulation used in the SPARC Chemistry-Climate Model Initiative (CCMI; Morgenstern et al., 2017). The CCMI experiments, hereafter WACCM-CCMI, differ from WACCM4 with respect to the modified gravity wave parameterization and the updated heterogenous chemistry (Garcia et al., 2017). The inclusion of WACCM4 allows us to carry out a sensitivity test regarding the impact of the modified gravity wave parameterization on the simulation of the N_2O transport (see Sect. 4 for detailed analysis). We use 3-D daily mean output over the 2005–2014 period to allow a fair comparison with the BRAM2 dataset (see Sect. 2.3 for detailed analysis). WACCM has a longitude–latitude grid of $2.5° \times 1.9°$ and 66 vertical levels ranging from the surface to an altitude of about 140 km. The vertical coordinate is hybrid-pressure, i.e., terrain-following below 100 hPa and purely isobaric above this level. The vertical resolution depends on the height: it is approximately 3.5 km above 65 km, 1.75 km around the stratopause (50 km), 1.1–1.4 km in the lower stratosphere (below 30 km) and 1.1 km in the troposphere. The time step for the physics in the model is 30 min.

The physics of WACCM is the same as CAM4, and the dynamical core is a finite volume with a horizontal discretization based on a conservative flux-form semi-Lagrangian (FFSL) scheme (Lin, 2004). The gravity wave parameterization accounts for momentum and heat deposition separating orographic and non-orographic sources. The orographic waves are modified according to Garcia et al. (2017), whereas non-orographic waves are parameterized depending on the convection and the frontogenesis occurrence in the model (Richter et al., 2010).

In this study, the WACCM versions considered are not able to internally generate the quasi-biennial oscillation (QBO; see, e.g., Baldwin et al., 2001). Thus, the QBO is nudged by a relaxation of stratospheric winds to observations in the tropics (Matthes et al., 2010). The solar forcing uses the Lean et al. (2005) approach.

WACCM includes a detailed coupled chemistry module for the middle atmosphere based on the Model for Ozone and Related Chemical Tracers, version 3 (MOZART-3; Kinnison et al., 2007; Marsh et al., 2013). The species included within this mechanism are contained within the O_x, NO_x, HO_x, ClO_x and BrO_x chemical families, along with CH_4 and its degradation products. In addition, 20 primary nonmethane hydrocarbons and related oxygenated organic compounds are represented along with their surface emission. There are a total of 183 species and 472 chemical reactions; this includes 17 heterogeneous reactions on multiple aerosol types, i.e., sulfate, nitric acid trihydrate and ice. In WACCM-CCMI the heterogeneous chemistry is updated by Solomon et al. (2015).

2.2 BASCOE CTM

The BASCOE data assimilation system (Errera et al., 2019) is built on a chemistry transport model, which consists in a kinematic transport module with the FFSL advection scheme (Lin and Rood, 1996) and an explicit solver for stratospheric chemistry, comprising 65 species and 243 reactions (Prignon et al., 2019). Chabrillat et al. (2018) explain in detail the preprocessing procedure that allows the BASCOE CTM to be driven by arbitrary reanalysis datasets as well as the setup of model transport. As usual for kinematic transport modules, the FFSL scheme only needs the surface pressure and

horizontal wind fields from reanalyses as input, because it is set on a coarser grid than the input reanalyses, and relies on mass continuity to derive vertical mass fluxes corresponding to its own grid. Similar to Chabrillat et al. (2018), the model is driven by four different reanalysis datasets on a common, low-resolution, latitude–longitude grid ($2.5° \times 2°$), but it retains their native vertical grids. In this way, we avoid any vertical regridding, and the intercomparison explicitly accounts for the different vertical resolutions.

The four input reanalyses, the European Centre for Medium-Range Weather Forecasts Interim reanalysis (ERA-Interim, hereafter ERAI; Dee et al., 2011), the Japanese 55-year Reanalysis (JRA-55; Kobayashi et al., 2015), and the Modern-Era Retrospective analysis for Research and Applications (MERRA; Rienecker et al., 2011) and its version 2 (MERRA-2; Gelaro et al., 2017), are part of the SPARC Reanalysis Intercomparison Project (S-RIP), which is a coordinated intercomparison of all major global atmospheric reanalyses, and they are described in Fujiwara et al. (2017). ERAI and JRA-55 have 60 levels up to 0.1 hPa while MERRA and MERRA-2 have 72 levels up to 0.01 hPa. The CTM time step is set to 30 min. As for the WACCM experiment, we used the daily mean outputs from the BASCOE CTM over the 2005–2014 period.

2.3 BASCOE reanalysis

BRAM2 is the BASCOE reanalysis of Aura MLS, version 2, which covers the period from August 2004 to August 2019 (Errera et al., 2019). For BRAM2, BASCOE is driven by dynamical fields from ERA-Interim, with a $3.75° \times 2.5°$ (longitude $\times$ latitude) horizontal resolution. The vertical grid is represented by 37 hybrid-pressure levels which are a subset of the ERA-Interim 60 levels.

In BRAM2, N_2O profiles from the MLS version 4 standard product have been assimilated within the 0.46–68 hPa pressure ranges (Livesey et al., 2015). This dataset is retrieved from the MLS 190 GHz radiometer instead of the 640 GHz radiometer in an earlier MLS version. The 640 GHz radiometer, which provided a slightly better quality retrieval down to 100 hPa, ceased to be delivered after August 2013 because of instrumental degradation in the band used for that retrieval. To avoid any artificial discontinuity due to switching from one product to the other in August 2013, BRAM2 has assimilated the 190 GHz N_2O during the whole reanalysis period.

BRAM2 N_2O has been validated between 3 and 68 hPa against several instruments with a general agreement within 15 % depending on the instrument and the atmospheric region (the middle stratosphere or the polar vortex; see Errera et al., 2019). It is not recommended to use the BRAM2 N_2O reanalysis outside of this pressure range. BRAM2 N_2O is also affected by a small drift of around -4 % between 2005 and 2015 (see also Froidevaux et al., 2019).

2.4 TEM diagnostics

For atmospheric tracers, the TEM analysis (Andrews et al., 1987) allows for the separation of the local change in a tracer with the volume mixing ratio χ in terms of transport and chemistry (Eq. 1).

$$\overline{\chi}_t = -\overline{v}^*\overline{\chi}_y - \overline{w}^*\overline{\chi}_z + e^{z/H}\nabla\cdot M + \overline{S}, \tag{1}$$

where χ is the volume mixing ratio of N_2O, and $\boldsymbol{M}$ is the eddy flux vector, which is defined as

$$M^{(y)} \equiv -e^{-z/H}\left(\overline{v'\chi'} - \overline{v'\theta'}\,\overline{\chi}_z/\overline{\theta}_z\right), \tag{2a}$$

$$M^{(z)} \equiv -e^{-z/H}\left(\overline{w'\chi'} + \overline{v'\theta'}\,\overline{\chi}_y/\overline{\theta}_z\right). \tag{2b}$$

$\overline{v}^*$ and $\overline{w}^*$ are the meridional and vertical components of the residual mean meridional circulation, respectively, and they are defined as

$$\overline{v}^* \equiv \overline{v} - e^{z/H}\left(e^{-z/H}\overline{v'\theta'}/\overline{\theta}_z\right)_z, \tag{3a}$$

$$\overline{w}^* \equiv \overline{w} + (a\cos\phi)^{-1}\left(\cos\phi\,\overline{v'\theta'}/\overline{\theta}_z\right)_\phi. \tag{3b}$$

Here, $\overline{v}$, $\overline{w}$ and $\overline{\theta}$ are the Eulerian zonal-mean meridional and vertical velocities and the potential temperature, respectively; ϕ is the latitude; and S is the net rate of change due to chemistry, i.e., $\overline{S} = \overline{P} - \overline{L}$, where $\overline{P}$ and $\overline{L}$ are the respective zonal-mean chemical production and loss rates. Overbar quantities represent zonal-mean fields, primed quantities represent the departures from the zonal mean and subscripts denote derivatives. Meridional derivatives are evaluated in spherical coordinates and vertical derivatives with respect to log-pressure altitude $z \equiv -H\log_e(p/p_s)$, with $p_s = 10^5$ Pa and $H = 7$ km.

Hence, transport is separated into advection due to the residual circulation (first two terms on the right-hand side, RHS, of Eq. 1) and irreversible quasi-horizontal isentropic eddy mixing, $e^{z/H}\nabla\cdot\boldsymbol{M}$.

In order to better understand the role of each term in the tracer balance, it is useful to separate the components of the vector $\boldsymbol{M}$ and rearrange the terms of Eq. (1) as follows:

$$\overline{\chi}_t = A_y + M_y + A_z + M_z + \left(\overline{P} - \overline{L}\right) + \overline{\epsilon}, \tag{4}$$

where

$$A_y = -\overline{v}^*\overline{\chi}_y, \tag{5a}$$

$$M_y = e^{z/H}\cos\phi^{-1}\left(M^{(y)}\cos\phi\right)_y, \tag{5b}$$

$$A_z = -\overline{w}^*\overline{\chi}_z, \tag{5c}$$

$$M_z = e^{z/H}\left(M^{(z)}\right)_z. \tag{5d}$$

Here, A_y represents the meridional residual advection, M_y represents the horizontal transport due to eddy mixing, A_z

represents the vertical residual advection and M_z represents the vertical eddy mixing (all expressed in ppbv d^{-1}). It is important to note that the total mixing term ($M_y + M_z$) includes not only the effects of irreversible mixing but also some effects of the advective transport that are not resolved by the residual advection (Andrews et al., 1987; Holton, 2004).

Before any TEM calculation, all of the input fields are interpolated to constant pressure levels from the hybrid-sigma coefficients, which retain the same vertical resolution as the original vertical grid of each dataset (Table 1). Each derivative is computed using a centered differences method.

In addition to the physical TEM terms (Eq. 1), it is necessary to include an additional term on the RHS of Eq. (4): the residual term ϵ. It is the difference between the actual rate of change of χ (LHS of Eq. 4) and the sum of all of the transport and chemical terms of the TEM budget. This nonzero residual has several causes (Abalos et al., 2017). The TEM calculations for WACCM rely on the diagnostic variable w, which is not used to advect the tracers, because the model is based on a finite volume dynamical core (Lin, 2004). Furthermore, an implicit numerical diffusion is added to the transport scheme in WACCM in order to balance the small-scale noise without altering the large-scale features. This numerical diffusion is not included in the TEM budget and is larger in regions with large small-scale features, i.e., regions where gradients are stronger (Conley et al., 2012). All TEM calculations are done using daily mean data, even though WACCM and BASCOE both run with a much smaller time step of 30 min. The daily mean fields are interpolated from their native hybrid-sigma levels to constant pressure levels prior to the TEM analysis, leading to numerical errors in the lower stratosphere. The BASCOE datasets have a coarser horizontal resolution than their input reanalyses (especially BRAM2; see Table 1). This affects the accuracy of the vertical and horizontal derivatives, with possible implications for the residual. The possible causes of the residual in the five reanalysis datasets are discussed in more detail in Sect. 3. For WACCM-CCMI, the TEM budget is computed for each realization, allowing for the examination of both the ensemble mean (e.g., for seasonal means) or the model envelope (e.g., for line plots). In order to validate our N_2O TEM budget, we reproduced the findings reported in Tweedy et al. (2017, Fig. 7) with WACCM-CCMI in the tropical lower stratosphere, and we noticed similar results (not shown).

In order to interpret the TEM analysis of the N_2O budget, we also compute the Eliassen–Palm flux divergence (EPFD). The Eliassen–Palm flux is a 2-D vector defined as $\boldsymbol{F} \equiv (F^{(\phi)}, F^{(z)})$ (Andrews et al., 1987), with its meridional and vertical components, respectively, given by

$$F^{(\phi)} \equiv e^{-z/H} a \cos\phi \left(\overline{u}_z \overline{v'\theta'}/\overline{\theta}_z - \overline{v'u'} \right) \tag{6a}$$

$$F^{(z)} \equiv e^{-z/H} a \cos\phi \left\{ \left[f - (acos\phi)^{-1} (\overline{u}\cos\phi)_\phi \right] \overline{v'\theta'}/\overline{\theta}_z - \overline{w'u'} \right\}. \tag{6b}$$

The EPFD reflects the magnitude of the eddy processes and provides a direct measure of the dynamical forcing of the zonal-mean state by the resolved eddies (Edmon et al., 1980).

The four dynamical reanalyses used in this study provide overall consistent temperature and winds in the stratosphere, but they can lead to a different representation of large-scale transport (e.g., Chabrillat et al., 2018) due to the biases in the temperature and wind fields (Kawatani et al., 2016; Tao et al., 2019). Note that the TEM quantities are not directly constrained by observations, especially the upwelling velocity $\overline{w}^*$, that can vary considerably in the dynamical reanalyses, as it is a small residual quantity (Abalos et al., 2015).

In the rest of the paper, we will assume that the BRAM2 product provides the best available approximation of the TEM budget for N_2O – at least where the residual is smaller than the vertical advection and horizontal mixing terms. This assumption relies on the combination in BRAM2 of dynamical constraints from ERA-Interim and chemical constraints from MLS (Errera et al., 2019).

Figures 1 and 2 show the N_2O TEM budget terms at 15 hPa for all of the datasets for the boreal winter (December–January–February, DJF, mean) and summer (June–July–August, JJA, mean), respectively. The 15 hPa level (around 30 km altitude) was chosen because large differences can be found between WACCM-CCMI, BRAM2 and the CTM runs at this level and because the dynamical reanalyses are not constrained as well by meteorological observations at higher levels (Manney et al., 2003). Figures 1 and 2 aim to show how the dynamical and chemical terms of the budget balance each other to recover the tendency $\overline{\chi}_t$ at different latitudes. A discussion on the differences between the datasets and their possible physical causes is given in the next sections.

The vertical advection term A_z shows how the upwelling contributes to increasing the N_2O abundances in the tropics and summertime midlatitudes and how polar downwelling contributes to decreasing the N_2O abundances in the winter hemisphere. The horizontal transport out of the tropics due to eddies, as represented by M_y, reduces the N_2O abundance in the tropical latitudes of the wintertime hemisphere and increases the N_2O mixing ratio at high latitudes in the winter hemisphere. The other terms of the TEM budget are weaker than A_z and M_y: the meridional advection term A_y tends to increase the N_2O abundance in the winter subtropics and extra-tropics; the vertical transport term due to eddy mixing, M_z, decreases the N_2O mixing ratio over the northern polar latitudes; and the chemistry term $P - L$ shows that N_2O

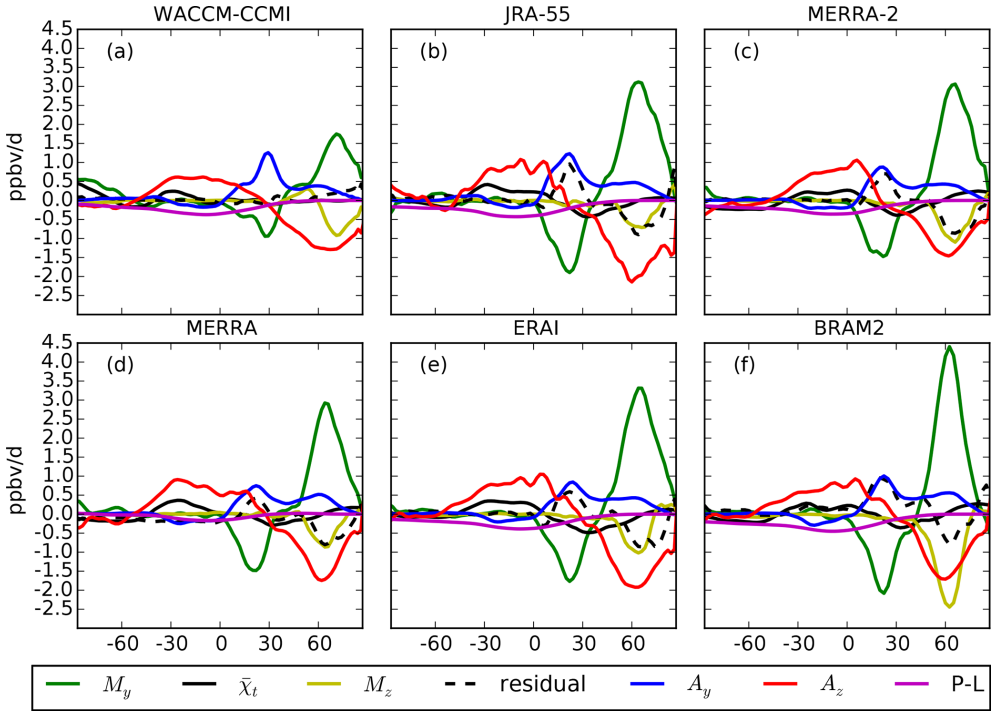

Figure 1. Latitudinal profiles of the N_2O TEM budget terms at 15 hPa averaged in DJF (2005–2014) with WACCM-CCMI **(a)**, JRA-55 **(b)**, MERRA-2 **(c)**, MERRA **(d)**, ERAI **(e)** and BRAM2 **(f)**. The color code is shown in the legend. Units are in parts per billion by volume per day (ppbv d^{-1}).

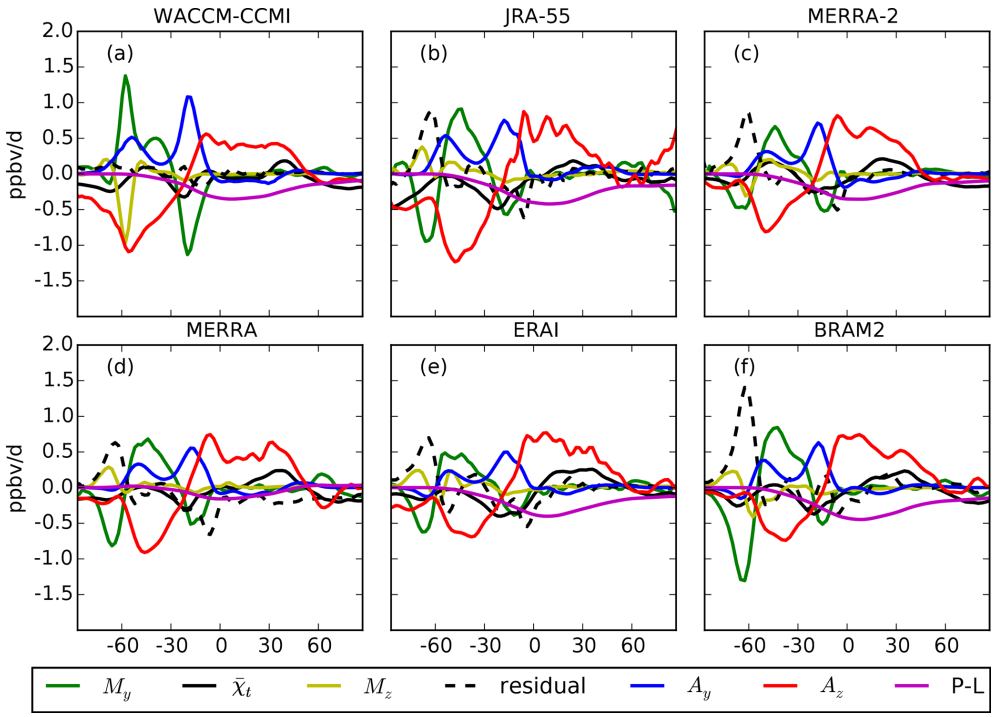

Figure 2. Same as for Fig. 1 but for JJA.

destruction by photodissociation and $O(^1D)$ oxidation contributes to the budget in the tropics and also in the summertime hemisphere. All budget terms are weaker in the summer hemisphere than in the winter hemisphere. Over the southern polar winter latitudes, the reanalyses deliver negative M_y that are balanced by large positive residuals, which implies a less robust TEM balance (Fig. 2). This is not the case with WACCM, where M_y tends to increase the N_2O abundance in the polar vortex. Such differences between the datasets are highlighted and discussed in the next sections.

3 Latitude–pressure cross sections

Figures 3 and 4 show the DJF and JJA means of three contributions to the N_2O TEM budget, respectively, namely the horizontal mixing M_y, the vertical advection A_z and the residual terms ϵ, for WACCM-CCMI, JRA-55, MERRA-2 and BRAM2. For those datasets, the remaining terms of the TEM budget (A_y, M_z and $P - L$) for DJF and JJA are shown in Supplement Figs. S1 and S2, respectively. The full N_2O TEM budgets obtained with MERRA and ERAI for DJF and JJA are shown in Figs. S3 and S4, respectively. In the case of WACCM-CCMI, the seasonal means were computed separately for each realization, and we verified that the ensemble means show the same features as the individual realizations. Large differences arise in the dynamical terms of the TEM budget between summer and winter for both hemispheres in the extra-tropics. The strong seasonality of the deep branch of the BDC and of the transport barriers are the causes of these differences, as for the seasonal variations of the age of air spectrum (Li et al., 2012).

We also reproduced the results of Randel et al. (1994, Fig. 8) for the WACCM-CCMI multi-model mean and the reanalysis mean in DJF (Figs. S5 and S5, respectively). The WACCM-CCMI and the reanalysis means agree with the Community Climate Model version 2 of the early 1990s with regard to the general pattern of the TEM terms, although both deliver stronger contributions, especially the reanalyses mean.

We first compare the contribution of A_z across the datasets in Figs. 3 and 4. The tropical upwelling increases the abundance of N_2O mostly in the mid–high stratosphere (between 1 and 15 hPa) with the maximum contribution in the summer tropics, whereas the downwelling decreases it mostly in the wintertime extra-tropics in the middle and low stratosphere (between 5 and 100 hPa). This reflects the path followed by the deep branch of the BDC (Birner and Bönisch, 2011). During boreal winter, these features are very similar across all datasets (Fig. 3), but noticeable differences appear during the austral winter (Fig. 4): the tropical upwelling has a larger secondary maximum in the southern tropics with JRA-55 and MERRA-2 than with the other datasets, and the extra-tropical downwelling extends to the South Pole in WACCM-CCMI and JRA-55 whereas it is mostly confined to the midlatitudinal surf zone in the other reanalyses. In the lower stratosphere, A_z shows the contribution of the residual advection by the shallow branch of the BDC to the N_2O abundances in the winter and summer hemispheres. The two-cell structure, consisting of upwelling of N_2O in the subtropics and downwelling in the extra-tropics, consistently agrees across all datasets. The meridional residual advection term A_y contributes to the poleward transport of air masses in the middle stratosphere, mostly during the winter, and its contribution to the N_2O TEM budget is weaker than A_z. A_y agrees well among the datasets in boreal winter (Figs. S1, S3), while during austral winter WACCM-CCMI overestimates it by around 30° S compared with the reanalyses (Figs. S2, S4).

We move now to the mixing contributions to the N_2O budget. The horizontal mixing is the predominant contribution to the poleward tracer transport in the middle and lower stratosphere (Abalos et al., 2013), as it flattens the tracer gradients generated by the residual advection. In the N_2O TEM budget during boreal winter, M_y mostly balances the extra-tropical downwelling and part of the tropical upwelling (Figs. S3, S4). The surf zone is characterized by strong horizontal mixing, depicted here as large positive M_y contributions, and delimited by transport barriers which appear as intense gradients of M_y in the winter hemispheres (panels b, e, h and k in Figs. 3 and 4). In the wintertime NH, the patterns of M_y are similar in all datasets (Fig. 3), but the effect of horizontal eddy mixing on N_2O is stronger in the reanalyses than in WACCM-CCMI. In Sect. 4, we quantitatively analyze the differences in the mid-stratospheric M_y between datasets. The residual terms in the reanalyses (Fig. 3c, f, i, l) are largest in the middle stratosphere at the latitudes of the transport barriers, and their signs are opposite to M_y.

In the austral winter, over the Antarctic polar cap and below 30 hPa, M_y agrees remarkably well in all datasets (Fig. 4). Closer to the vortex edge and above 30 hPa, the wintertime decrease in N_2O is mainly due to downwelling in WACCM-CCMI, whereas the reanalyses, especially BRAM2, show that the horizontal mixing plays a major role (Fig. 4). The impact of horizontal mixing on N_2O inside the wintertime polar vortex is not negligible (e.g., de la Cámara et al., 2013; Abalos et al., 2016a), as Rossby wave breaking occurs there as well as in the surf zone. In contrast to the reanalyses, in WACCM-CCMI the M_y contribution is close to zero in the Antarctic vortex and maximum along the vortex edge (Fig. 4). This disagreement can be related to differences in the zonal wind: it is overestimated in WACCM above 30 km at subpolar latitudes compared with MERRA (Garcia et al., 2017), and the polar jet is not tilted equatorward as in the reanalyses (see black thin lines in Figs. 4 and 3 of Roscoe et al., 2012). However, the differences in M_y and A_z above the Antarctic in winter should be put into perspective with the relatively large residual terms that point to incomplete TEM budgets in the reanalyses (Figs. 4 and S4 right columns). Near the Antarctic polar vortex, the assumptions of the TEM analysis (such as small amplitude waves)

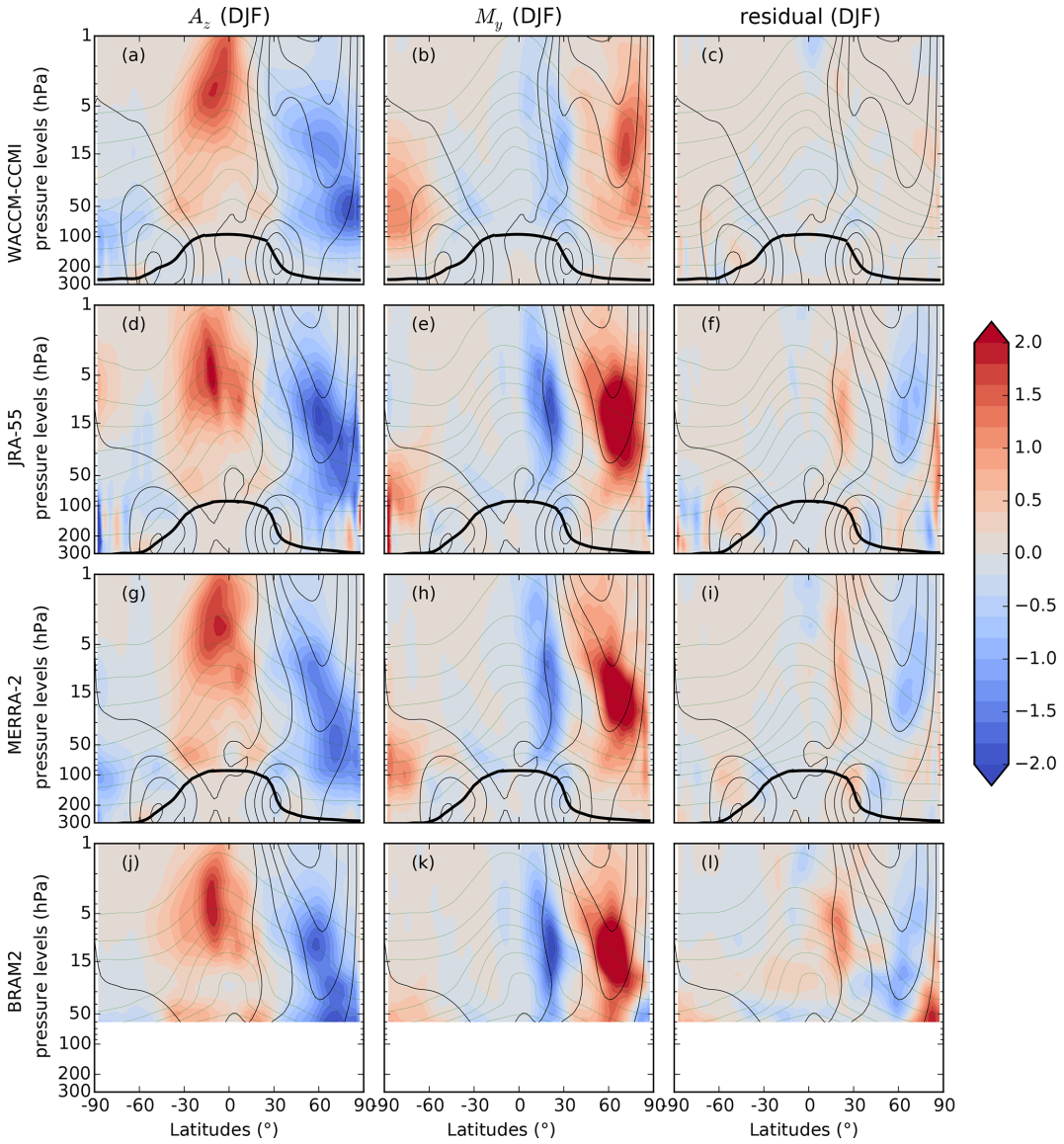

Figure 3. Climatological (2005–2014) latitude–pressure cross sections of three N_2O TEM budget terms averaged in DJF (ppbv d^{-1}) for the horizontal mixing term **(a, d, g, j)**, the vertical residual advection term **(b, e, h, k)** and the residual term **(c, f, i, l)**. The datasets are, from top to bottom, WACCM-CCMI, JRA-55, MERRA-2 and BRAM2. The residual term for WACCM-CCMI is from a single realization of the model. The thin black lines show the zonal-mean zonal wind (from 0 to 40 m s^{-1} every 10 m s^{-1}), the black thick line represents the dynamical tropopause for the considered season and the green thin lines show the climatological mixing ratio of N_2O (from 20 to 300 ppbv with 40 ppbv spacing).

are less valid, leading to larger errors in the evaluation of the mean transport and eddy fluxes (Miyazaki and Iwasaki, 2005).

As the relative importance of the residual is considerable above the Antarctic in the reanalyses (Fig. 4), it is necessary to better understand its physical meaning. Dietmüller et al. (2017) applied the TEM continuity equation to the age of air in CCM simulations. Computing the "resolved aging by mixing" (i.e., the AoA counterpart of $M_y + M_z$) as the time integral of the local mixing tendency along the residual circulation trajectories and the "total aging by mixing" as the difference between the mean AoA (mAoA) and the residual circulation transit time, they defined the "aging by mixing on unresolved scales" (i.e., by diffusion) as the difference between the latter and the former. This "aging by diffusion", which can be related by construction to our residual term, arises around 60° S from the gradients due to the polar vortex edge. Even though we use a real tracer (N_2O), we find a qualitative agreement with this analysis based on AoA: our residual term is larger in regions characterized by strong gradients

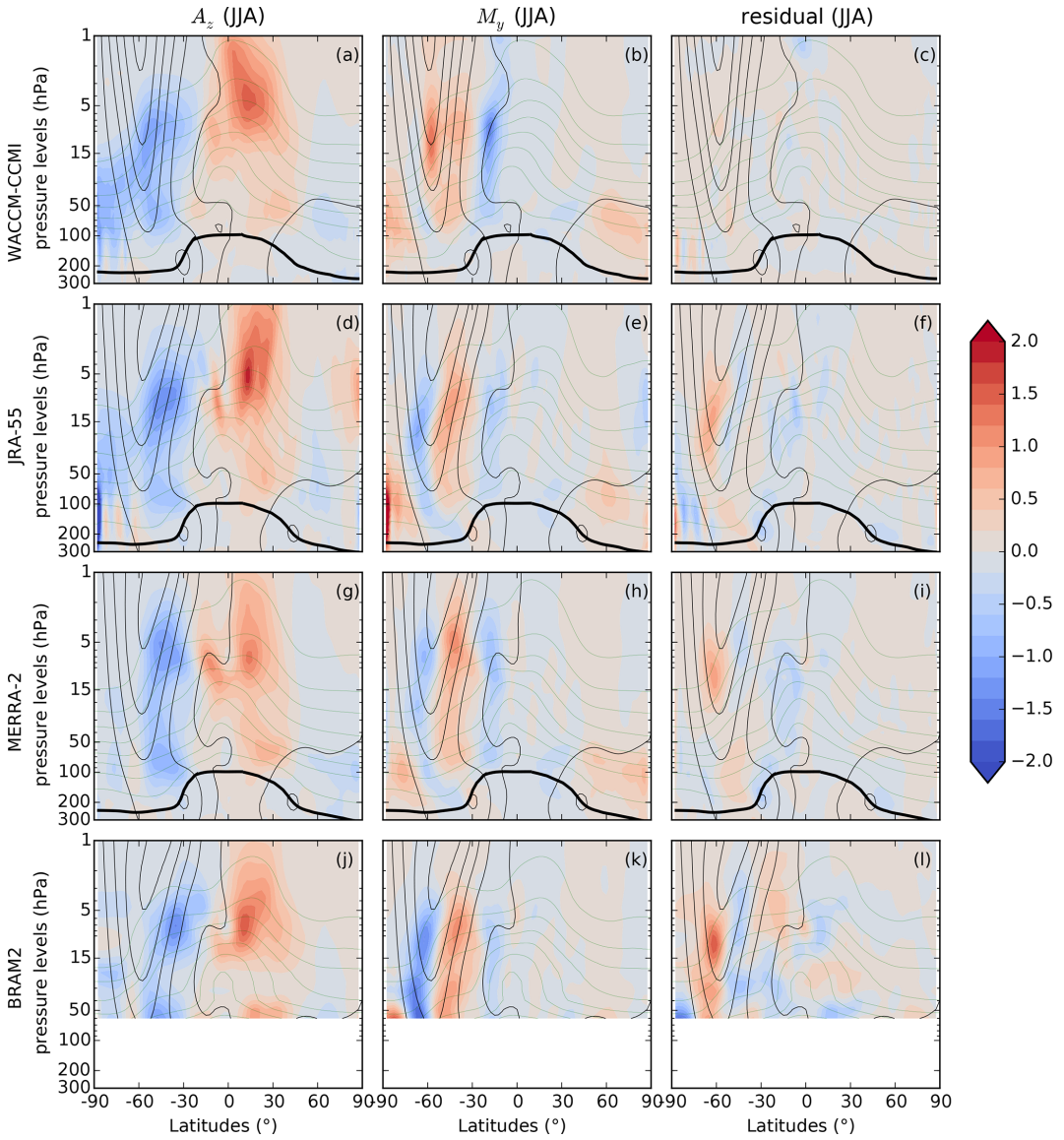

Figure 4. Same as Fig. 3 but for JJA and with a different color scale. The thin black contours show the zonal-mean zonal wind (from 0 to 100 $m s^{-1}$ every 20 $m s^{-1}$).

such as the Antarctic vortex edge and larger with dynamics constrained to a reanalysis than with a free-running CCM (see EMAC results in Fig. 1d by Dietmüller et al., 2017). Thus, we interpret the residual as the sum of mixing at unresolved scales and numerical errors (Abalos et al., 2017).

In the summertime lower stratosphere, we note a stronger contribution of M_y to the N_2O abundances above the subtropical jets in both hemispheres and for all datasets compared with higher levels in summer (panels b, e, h and k in Figs. 3 and 4). This behavior is consistent with calculations of the effective diffusivity and age spectra (Haynes and Shuckburgh, 2000; Ploeger and Birner, 2016). It is due to transient Rossby waves that cannot travel further up into the stratosphere owing to the presence of critical lines, i.e., where the phase velocity of the wave matches the background wind velocity, generally leading to wave breaking (Abalos et al., 2016b). In particular, above the northern tropics during the boreal summer (Figs. 4, S2, S4), horizontal mixing is primarily associated with the Asian monsoon anticyclone, and it causes a decrease in N_2O (Konopka et al., 2010; Tweedy et al., 2017). In the lower stratosphere, the contributions from M_y combine with that from A_z in the total impact of the shallow branch of the BDC on N_2O all year round (Diallo et al., 2012).

The vertical mixing contribution M_z is very small during boreal winter, except in the middle and lower stratosphere poleward of 60° N, where it tends to balance the M_y contribution (Figs. S1, S3). In austral winter, there is a strong

disagreement between WACCM-CCMI and the reanalyses around 60° S between 5 and 15 hPa (Fig. S2). WACCM-CCMI simulates a strong M_z contribution at the polar jet core that decreases the N_2O abundances and tends to balance M_y, whereas M_z is weaker and increases N_2O in the higher stratosphere in the reanalyses.

In the next section, we focus on a single level in the middle stratosphere to quantitatively study the disagreement between WACCM-CCMI and the reanalyses.

4 Climatological seasonal cycles

After investigating the seasonal means of A_z and M_y, it is interesting to examine their climatological mean annual cycles in order to study the month-to-month variations over the year and their dependance on the latitude in the middle stratosphere. The cycles are shown for three latitude bands in each hemisphere corresponding to the tropics (0–20°), the surf zones (40–60°) and the polar regions (60–80°). For WACCM-CCMI, we examine the envelope (the yellow shaded areas in Figs. 5–12) of the three model realizations in order to evaluate the role of the internal variability and its relative importance for each month and latitude band. In the following, we will consider BRAM2 as the reference when comparing N_2O mixing ratios between datasets, because its dynamics and chemistry are both constrained by observational datasets.

4.1 Polar regions

The EPFD is often used to quantify the forcing of the wave drag due to resolved (planetary) waves (e.g., Gerber, 2012; Konopka et al., 2015). We first show the monthly mean climatological annual cycles of EPFD averaged between 3 and 50 hPa and the residual vertical velocity $\overline{w}^*$ at 15 hPa for the polar regions (60–80° S and N, Fig. 5). We arbitrarily average the EPFD between 3 and 50 hPa in order to identify the wave forcing for the deep branch of the BDC (Plumb, 2002; Konopka et al., 2015). However, the qualitative results do not depend on the choice of the lower boundary level. We also show one realization of the earlier version WACCM4 that suffered from a larger cold bias above the Antarctic (see Sect. 2.1). In WACCM-CCMI, the parameterization of gravity waves was adjusted in order to reduce this issue while not significantly changing the dynamics in the NH, which results in an enhanced polar downwelling above the southern polar region (Garcia et al., 2017). Above the Antarctic, the forcing from resolved waves peaks in October in the reanalyses as a result of the vortex breakup that allows enhanced wave activity compared with austral winter (Randel and Newman, 1998). The WACCM simulations miss this strong springtime peak, and they are in good agreement with the reanalyses during the rest of the year (Fig. 5a). The residual vertical velocity w^* above the Antarctic is shown in Fig. 5c. This comparison

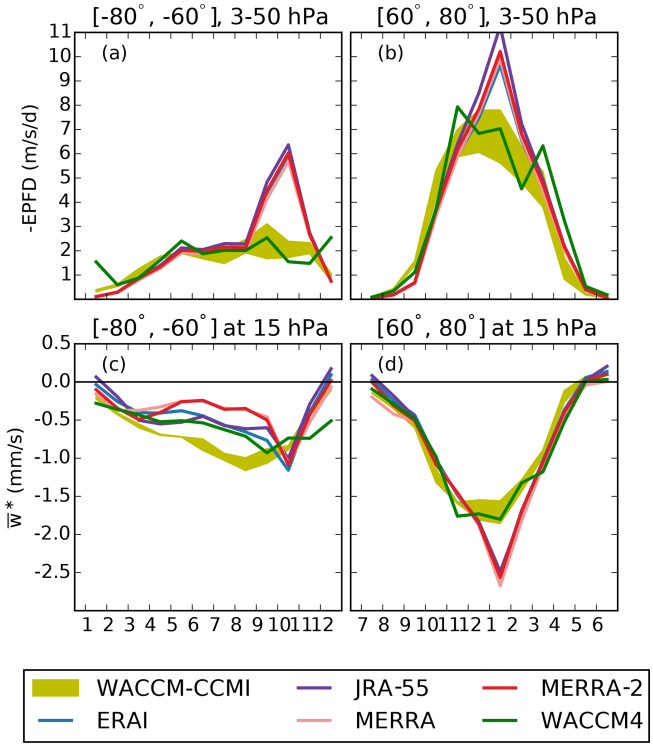

Figure 5. Monthly mean annual cycle of **(a, b)** the EPFD ($m\,s^{-1}\,d^{-1}$) averaged between 3 and 50 hPa and **(c, d)** $\overline{w}^*$ ($mm\,s^{-1}$) at 15 hPa for **(a, c)** the Antarctic region (60–80° S) and **(b, d)** the Arctic region (60–80° N). The color code is shown in the legend. The yellow envelope shows the three realizations of the WACCM-CCMI simulation.

between the WACCM versions was already shown in Garcia et al. (2017, Fig. 10), but we repeat it here adding the dynamical reanalyses. In November–December the weaker downwelling in WACCM-CCMI agrees well with the reanalyses. Throughout the rest of the year WACCM-CCMI simulates a stronger downwelling than all reanalyses (also at lower levels, not shown). This difference raises the question of whether the residual vertical velocity is correctly represented in WACCM-CCMI or in the dynamical reanalyses. Above the Arctic, the WACCM simulations underestimate the EPFD contribution during boreal winter compared with the reanalyses (Fig. 5b), and the downwelling velocities simulated by WACCM are weaker than the reanalyses during that period, with no significant differences between the WACCM versions (Fig. 5d). The differences between WACCM and the reanalyses in EPFD and w^* in the polar regions will help with the interpretation of the differences in A_z and M_y.

Figure 6 shows the monthly mean climatological annual cycle of the N_2O mixing ratio, A_z and M_y for the polar regions (60–80° S and N) at 15 hPa for all of the datasets. First, we investigate the N_2O mixing ratio in the Antarctic region (Fig. 6a). During winter, the N_2O abundances are smaller than the rest of the year due to the suppressed trans-

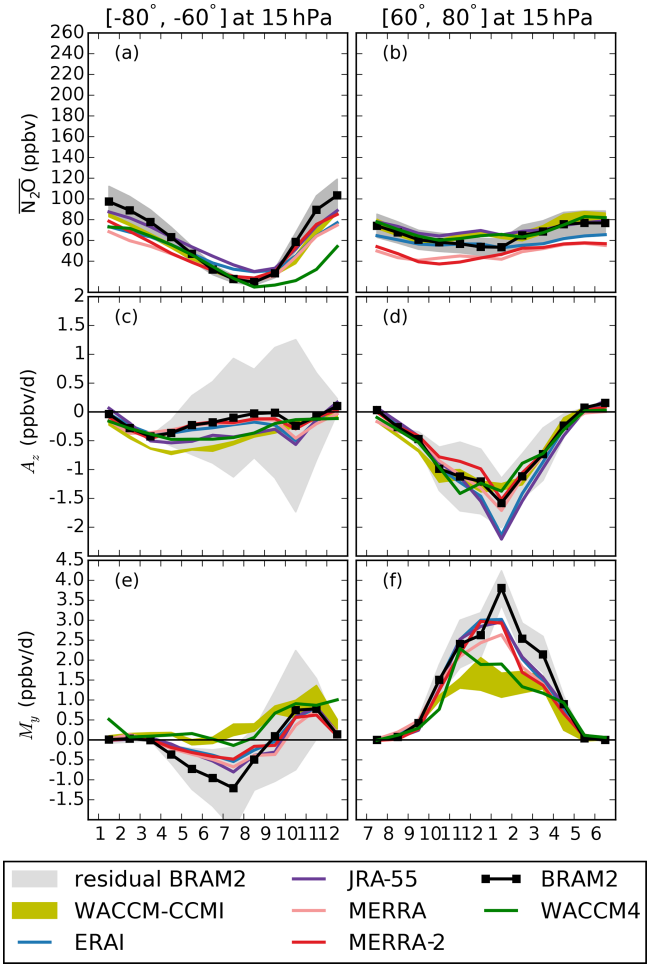

Figure 6. Annual cycles over the 2005–2014 period at 15 hPa for **(a, b)** the N_2O volume mixing ratio (ppbv), **(c, d)** M_y (ppbv d^{-1}) and **(e, f)** A_z (ppbv d^{-1}) in the **(a, c, e)** Antarctic region (60–80° S) and the **(b, d, f)** Arctic region (60–80° N). Note that the vertical scale differs for M_y and A_z. The olive envelope shows the three realizations of the WACCM-CCMI simulation. The color codes for the four CTM simulations follow the conventions of S-RIP (Fujiwara et al., 2017). BRAM2 is depicted using a black line and symbols, as usually done for observations, because it is constrained by both dynamical and chemical observations. As the N_2O mixing ratio in BRAM2 has been evaluated with a 15 % uncertainty (1σ standard deviation) at 15 hPa (Errera et al., 2019), this is highlighted by a dark gray region in panels **(a)** and **(b)**. The light gray shading around the BRAM2 cycles represents the uncertainty arising from the residual term in the TEM budget, i.e., it is entirely interpreted first as an uncertainty on A_z and then as an uncertainty on M_y in order to remain cautious.

port from the lower latitudes caused by the onset of the polar barrier. After the vortex breakup, the N_2O increase during spring and early summer is smaller in all of the simulations than in BRAM2. In WACCM-CCMI, the modification of the parameterization of gravity waves also results in a shift towards earlier vortex breakup dates in the austral spring compared with WACCM4 (Garcia et al., 2017). The earlier vortex breakup in WACCM-CCMI allows for the transport of N_2O-rich air from lower latitudes for a longer period compared with WACCM4, resulting in larger and more realistic simulations of the N_2O mixing ratios during austral spring and early summer (Fig. 6a).

In the Antarctic region, the downwelling decreases N_2O during most of the year (A_z term in Fig. 6c). Here, JRA-55 and WACCM-CCMI are outliers: both present stronger A_z contributions in fall and winter, especially WACCM-CCMI, which reaches values that are 3 times stronger than BRAM2 in early winter, as a result of the stronger downwelling velocity simulated by WACCM-CCMI in that region. While this strong disagreement is questioned by the large residuals, we note that all of the reanalyses confirm it except JRA-55. During fall and summer, A_z is stronger in WACCM-CCMI than in WACCM4 as a consequence of the stronger downwelling in WACCM-CCMI that results from the modification of the gravity wave parameterization.

We now turn to the contribution from M_y. In the Antarctic region, M_y is very different among the datasets during winter: in BRAM2 it contributes to the N_2O decrease during fall and winter, with the strongest contribution in July; however, this contribution is 2 times weaker with the CTM simulations, and the horizontal mixing has almost no effect on N_2O in WACCM-CCMI (Fig. 6e). As already mentioned, the TEM analysis suffers from large residuals in the wintertime Antarctic region. Nevertheless, we note that the disagreement between WACCM-CCMI and BRAM2 is significant, because the envelope of WACCM-CCMI realizations falls completely outside of the possible BRAM2 values in fall and winter when accounting for the residual. During the austral spring, the vortex breakup leads to an increased wave activity reaching the Antarctic, and M_y is in better agreement among all datasets compared with austral winter. Note that WACCM-CCMI exhibits large internal variability in this season (Fig. 6e).

It is interesting to highlight the differences between the wintertime Arctic and Antarctic regions, because the hemispheric differences in wave activity (Scaife and James, 2000; Kidston et al., 2015) play a crucial role in the N_2O abundances and TEM budget. Above the Arctic, the N_2O abundances simulated by WACCM agree with the BRAM2 reanalysis, except in December and January, and the CTM experiments driven by MERRA and MERRA-2 deliver smaller N_2O mixing ratios compared with BRAM2 (Fig. 6b). A_z is also in good agreement between the datasets above the Arctic, with the exception of ERAI and JRA-55 which provide stronger contributions (Fig. 6d). The Arctic is characterized by a very variable polar vortex with a shorter life span than the Antarctic vortex (Randel and Newman, 1998; Waugh and Randel, 1999), resulting in an enhanced contribution of the horizontal mixing to the N_2O budget during winter compared with the Antarctic (Fig. 6f). In contrast to the dynamical reanalyses and BRAM2, WACCM shows a 2-

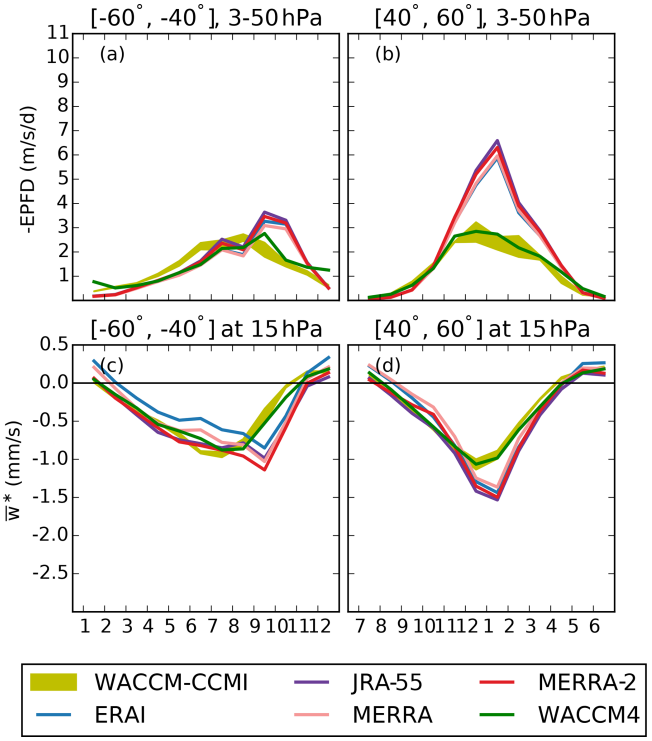

Figure 7. As for Fig. 5 but for the middle latitudes: **(a, c)** southern midlatitudes (40–60° S); **(b, d)** northern midlatitudes (40–60° N).

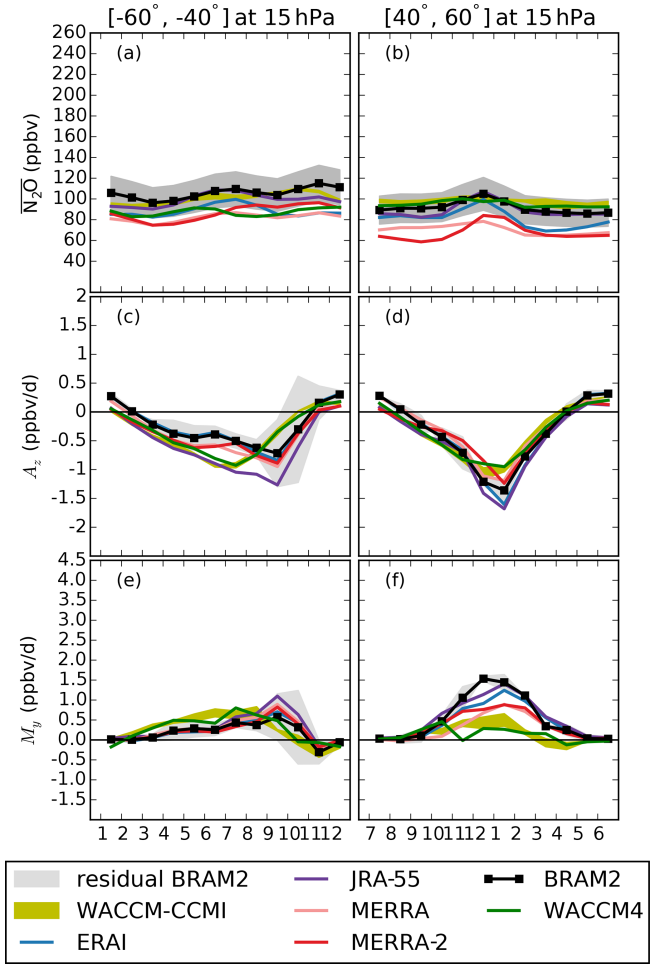

Figure 8. As for Fig. 6 but for the middle latitudes: **(a, c, e)** southern midlatitudes (40–60° S); **(b, d, f)** northern midlatitudes (40–60° N).

fold underestimation of the N_2O changes in the Arctic due to horizontal mixing during winter. Note that the Arctic extended winter presents the largest internal variability compared with the other regions, as shown by the spread in the WACCM realizations. The weaker contribution from M_y in WACCM is meaningful because the relative importance of the residual term is small in the NH. The horizontal mixing is predominately influenced by the forcing from the breaking of resolved (planetary) waves (Plumb, 2002; Dietmüller et al., 2018). In the Arctic region, WACCM underestimates the forcing from resolved waves compared with the dynamical reanalyses in the middle stratosphere (see Fig. 5d). This discrepancy in the resolved wave driving could contribute to the large differences in the wintertime M_y between the CCM simulations and the CTM experiments above the Arctic. On the other hand, the role of different waves in driving mixing processes is an ongoing research topic, and additional data and sensitivity tests are needed in order to establish a clear separation of the waves' contributions (e.g., gravity wave parameterization, spatial resolution, etc.; Dietmüller et al., 2018). It should also be emphasized that WACCM is among the CCMI models with the lowest contribution of aging by mixing to the age of air (Fig. 2 in Dietmüller et al., 2018).

4.2 Middle latitudes

Figure 7 shows the monthly mean climatological annual cycle of w^* at 15 hPa and the EPFD averaged between 3 and 50 hPa over the surf zones (40–60° S and N), and Fig. 8 shows the monthly mean climatological annual cycle of the N_2O mixing ratio, A_z and M_y at 15 hPa averaged over the same latitudes. The subtropical barriers are not shown because M_y and A_z change sign in these regions and averaging across the regions would hinder the interpretation of their means.

In the southern midlatitudes, the EPFD peaks in austral spring in the reanalyses, due to the enhanced wave activity in the Southern Hemisphere (SH) during austral spring compared with winter (Konopka et al., 2015), whereas the WACCM simulations deliver an earlier and weaker peak during austral winter (Fig. 7a). The downwelling velocity w^* shows a similar pattern to the EPFD (Fig. 7c), as it is also driven by the breaking of resolved waves (Abalos et al., 2015). In the northern midlatitudes, the EPFD peaks in win-

ter in all of the datasets, reflecting the stronger wave forcing in the surf zone in this season, and WACCM simulates lower EPFD values compared with the reanalyses (Fig. 7b) that leads to a weaker downwelling velocity in the WACCM simulations (Fig. 7d). As for the polar regions, the differences in EPFD and w^* between the WACCM simulations and the reanalyses will help with the interpretation of the differences in A_z and M_y.

With regard to the N_2O mixing ratio in both hemispheres, the CTMs driven by JRA-55 and ERAI are in good agreement with BRAM2, whereas MERRA-2 and MERRA underestimate it (Fig. 8a, b). The WACCM-CCMI simulations agree well with the BRAM2 chemical reanalysis, confirming the results obtained through the direct comparison with MLS observations (Froidevaux et al., 2019).

We now investigate the contribution from A_z and M_y. In the southern midlatitudes, A_z is negative in all seasons except during summer and there is again a good agreement among the datasets except for WACCM-CCMI and JRA-55 (Fig. 8c). These two datasets appear to have a purely annual cycle in this region, whereas the other four show a semi-annual component. The peak in the A_z contribution in the reanalyses in September results from the increased forcing from the resolved waves (see Fig. 7a) and from the stronger contribution from gravity waves to the mass flux during spring (Sato and Hirano, 2019, Fig. 11). In the same region, M_y increases throughout the winter, reflecting the mixing associated with the surf zone, and also peaks in early spring in the reanalyses (Fig. 8e). During summer and early fall, M_y does not contribute significantly to the TEM budget, and M_y reaches negative values in November which are comparable to the residual term. Both A_z and M_y peak in mid-winter in the WACCM-CCMI simulations, whereas these maxima are reached 3 months later in the reanalyses. This difference is related to the earlier minimum in the downwelling velocity $\overline{w}^*$ simulated by WACCM-CCMI (see Fig. 7c), which directly affects A_z (Fig. 8c) and, due to compensation, M_y (Fig. 8e). Among the reanalyses, the compensating contributions of A_z and M_y are stronger for JRA-55 than for the other reanalyses (up to 2 times larger in September, see Fig. 8c, e). This reflects the strong BDC in JRA-55 that resulted in the youngest mean AoA in the whole stratosphere (Chabrillat et al., 2018).

In the northern middle latitudes, A_z shows the effect of the wintertime downwelling to lower levels on N_2O, with the WACCM experiments simulating a slightly weaker contribution than the reanalyses (Fig. 8d). Such disagreement mostly originates from the weaker downwelling velocity in the CCM compared with the reanalyses shown in Fig. 7b. In the northern midlatitudes, the strong M_y contribution tends to increase the N_2O abundances in the surf zone during winter (Fig. 8f). The reanalyses show a large spread, with values reaching ~ 1.5 in BRAM2 and $\sim 0.9\,\mathrm{ppbv\,d^{-1}}$ in the MERRA runs, and WACCM-CCMI presents a large underestimation with respect to the reanalyses. While the spread across the reanalyses cannot be explained by the forcing from the resolved waves, the weaker M_y contribution simulated by WACCM could be partly attributed to the weaker EPFD in the CCM compared with the reanalyses (see Fig. 7d).

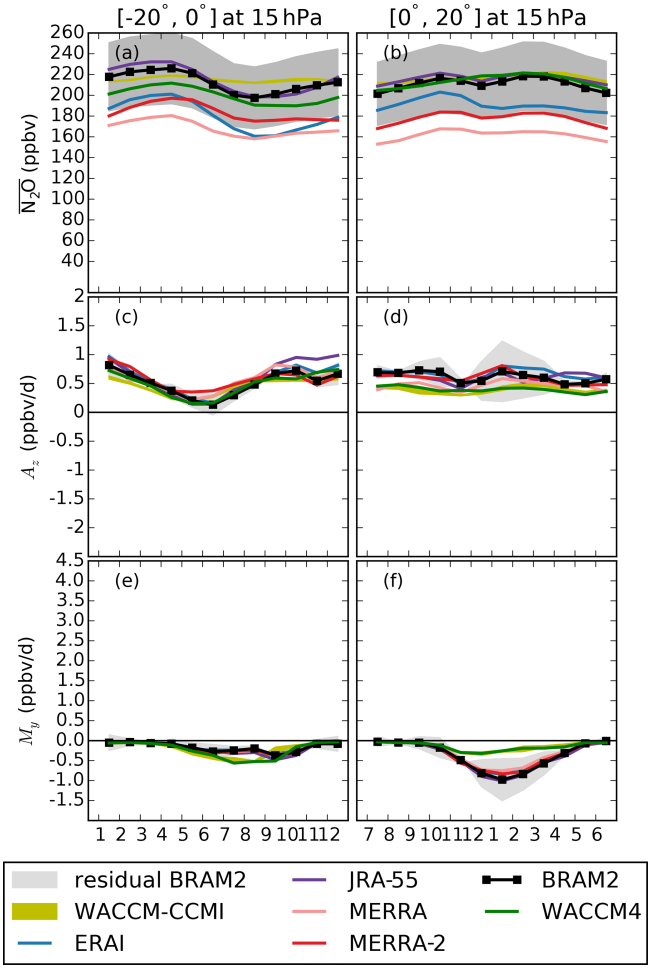

Figure 9. As for Fig. 6 but for the tropics: **(a, c, e)** southern tropics (0–20° S); **(b, d, f)** northern tropics (0–20° N).

4.3 Tropics

Figure 9 shows the climatological annual cycle for the N_2O mixing ratio, A_z and M_y for the southern and northern tropics (0–20° S and N) at 15 hPa across all of the datasets. The same latitude bands for the cycles of w^* and EPFD are shown in the Supplement (Fig. S7). In the tropical regions, the N_2O mixing ratio in WACCM-CCMI agrees well with the reanalysis of the Aura MLS, whereas the CTM results show large differences in the N_2O abundances depending on the input reanalysis (Fig. 9a, b). In regions where the AoA is less than 4.5 years and N_2O is greater than 150 ppb, i.e., in the tropical regions and lower stratospheric middle latitudes (Strahan et al., 2011), the N_2O mixing ratio is inversely proportional to the mAoA, because faster upwelling (younger air) implies

more N_2O transported from lower levels, decreasing its residence time and resulting in a limited chemical destruction (Hall et al., 1999; Galytska et al., 2019). The dynamical reanalyses also produce large differences in mAoA at 15 hPa: MERRA delivers the oldest mAoA, and MERRA-2, ERAI and JRA-55 progressively show a younger mAoA (Fig. 4b in Chabrillat et al., 2018). Hence, the large discrepancies in the N_2O mixing ratio can be explained by the large differences in the mAoA, while M_y and A_z contribute to rates of change of N_2O.

We continue by investigating the contribution from A_z. In both of the tropical regions, the upwelling term A_z is positive all year round, showing the effect of tropical upwelling, and agrees very well in the reanalyses (Fig. 9c, d), as a result of the good agreement in the tropical upwelling velocity at 15 hPa (Fig. S7 bottom row), and also as depicted by mAoA diagnostics (Fig. 4d in Chabrillat et al., 2018). Large interhemispheric differences arise in the seasonality of A_z between the tropical regions. The largest values of A_z in the southern tropics are in the boreal late-fall and winter (Fig. 9c), whereas no large seasonal variations can be detected in the annual cycle of the A_z in the northern tropics (Fig. 9d). This is the result of the more pronounced seasonality of the upwelling velocity in the southern tropics compared with the northern tropics (Fig. S7 bottom row).

We now turn to the contribution from M_y. In the southern tropics, M_y causes a decrease in the N_2O abundances from May to October (when N_2O is transported to the middle latitudes), and it has a near-zero contribution over the rest of the year, which is generally common in all of the datasets considered (Fig. 9e). The BRAM2 uncertainty is smaller than for the polar region and middle latitudes, indicating better performance of the TEM analysis outside of the high latitudes. In the northern tropics, M_y is negative from November to April and presents a marked seasonality in the reanalyses that is much weaker in WACCM-CCMI (Fig. 9f). With respect to interhemispheric differences, WACCM disagrees with the reanalyses: according to WACCM, M_y has a larger impact in the southern tropics than in the northern tropics, but M_y has a much larger impact in the northern tropics according to the reanalyses (Fig. 9e, f). These interhemispheric differences in the M_y contributions can be partly attributed to different forcings from the resolved waves between northern and southern tropics. The EPFD presents a stronger seasonality in the northern tropics than in the southern tropics in all of the datasets (Fig. S7 top row), which could partly explain the differences in the seasonality of M_y in the reanalyses, but it does not impact the M_y simulated by WACCM.

5 Interannual variability of the seasonal cycles

To analyze the interannual variability of the annual cycle, we compute for each month the 1σ standard deviations of the N_2O mixing ratio, M_y and A_z across the 10 simulated years.

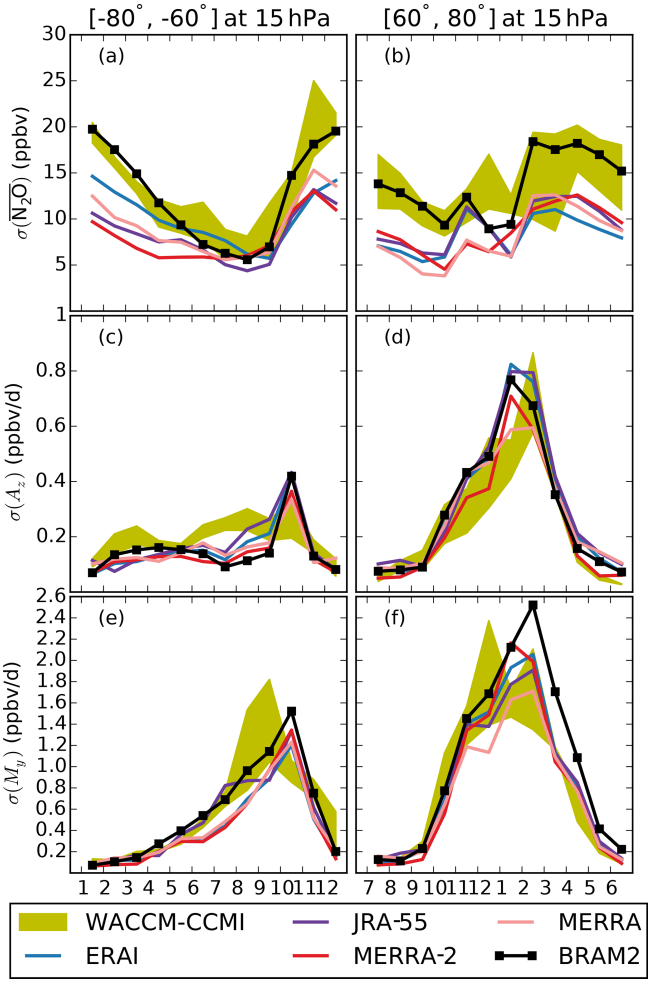

Figure 10. Monthly standard deviation over the 2005–2014 period at 15 hPa for **(a, b)** the N_2O volume mixing ratio (ppb), **(c, d)** the horizontal mixing term (ppbv d^{-1}) and **(e, f)** the vertical residual advection term (ppbv d^{-1}) in **(a, c, e)** the Antarctic region (60–80° S) and **(b, d, f)** the Arctic region (60–80° N). The color code is shown in the legend. The yellow envelope shows the three realizations of the WACCM-CCMI simulation.

Figure 10 shows the annual cycles of these standard deviations for each dataset in the polar regions (60–80° S and N) at 15 hPa for both hemispheres. First, we consider the variabilities of the N_2O mixing ratio. In the Antarctic, during austral winter and early spring the year-to-year change in the N_2O abundances is very small (Fig. 10a) because the duration, extension and strength of the polar vortex are very stable in a climatological sense, isolating air masses in the vortex from the highly variable midlatitudes (Waugh and Randel, 1999). The variability of the N_2O mixing ratio increases in October, i.e., during the breaking vortex period that is highly variable in time (Strahan et al., 2015). Furthermore, the midlatitude air masses, which have more variable composition, become free to reach the higher latitudes during this period. In the Arctic region, the interannual variability of the N_2O mixing

ratio is also largest during springtime but this is spread over a longer period, i.e., from February to June (Fig. 10b), reflecting the large interannual variability in the duration, extension and zonal asymmetry of the Arctic polar vortex (Waugh and Randel, 1999). In both polar regions, WACCM-CCMI agrees well with BRAM2, whereas the CTM experiments simulate a smaller variability.

We now look at the interannual variability of A_z and M_y in the polar regions. Above the Antarctic, the interannual variabilities of A_z and M_y are maximum during spring (Fig. 10c, e), due to the large interannual variability in vortex breakup dates (Strahan et al., 2015). While the maximum variability of M_y is consistently reached in October in all of the reanalyses, WACCM-CCMI simulates an earlier maximum (September) that does not correspond to the maximum in its mean values. The lower wintertime variability of both A_z and M_y would increase if a longer period was considered that included the exceptional Antarctic vortices of 2002 (Newman and Nash, 2005) and 2019 (Yamazaki et al., 2019). Above the Arctic, M_y and A_z are most variable during winter, reflecting the frequent disruptions of the northern polar vortex by sudden stratospheric warmings (SSWs; Butler et al., 2017). A case study of the effect of a SSW on the N_2O TEM budget showed that A_z and M_y contribute more to this budget during the SSW event than in the seasonal mean (Randel et al., 1994). Thus, the large wintertime variabilities of A_z and M_y are explained by the occurrence of seven major SSWs detected in the reanalyses for the 2005–2014 period (Butler et al., 2017).

In Fig. 11, we show the interannual variabilities of the N_2O mixing ratio, M_y and A_z for each dataset in the surf zones (40–60° S and N) at 15 hPa for both hemispheres. Regarding the N_2O mixing ratio, the interannual variability in the southern middle latitudes reaches the lowest values during austral winter. The datasets deliver very diverse values, with WACCM showing the largest variability and JRA-55 showing the least variability across the climatological year (Fig. 11a). In the northern midlatitudes, the interannual variability of the N_2O mixing ratio increases in late winter across all of the datasets as a response to the increased wintertime variability of the surf zone (Fig. 11b). The variability of WACCM-CCMI largely depends on the realization considered, except in October and November. Strong differences between ensemble members with respect to interannual variability indicate that the period considered is not long enough to explore the interannual variability in the northern midlatitudes and that the mean variability from this ensemble (with only three members) would not be representative of the internal variability of WACCM. The interannual variabilities of A_z and M_y in the southern midlatitudes are shown in Fig. 11c and e, respectively. As their mean value, A_z and M_y are most variable during austral spring and late summer in the reanalyses, whereas WACCM simulates an earlier peak during winter in the interannual variabilities of A_z and M_y compared with the reanalyses. In the northern midlatitudes,

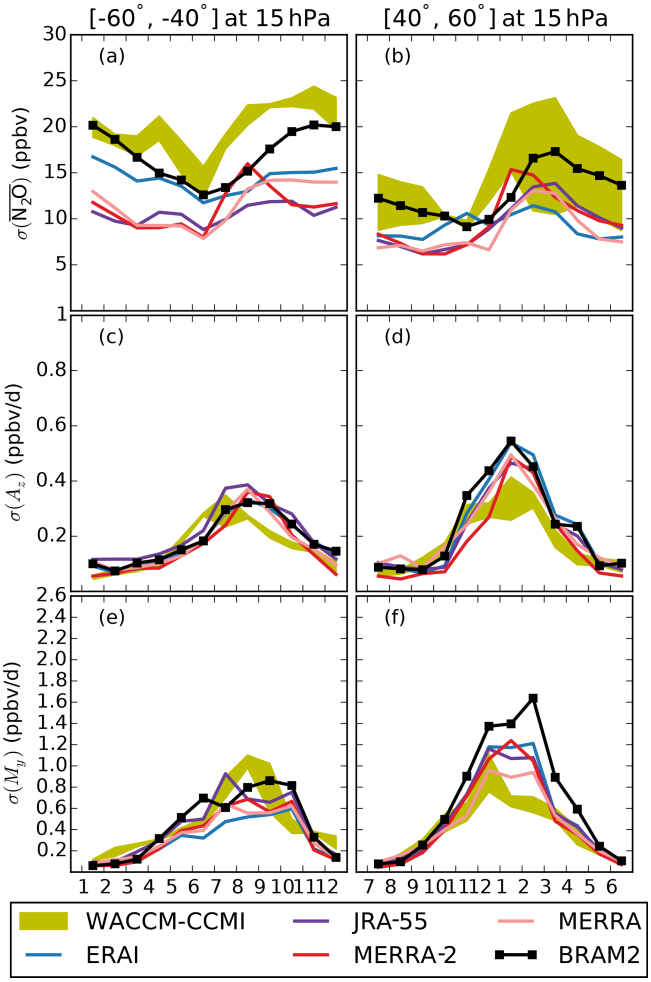

Figure 11. As for Fig. 10 but for the middle latitudes: **(a, c, e)** southern midlatitudes (40–60° S); **(b, d, f)** northern midlatitudes (40–60° N).

the interannual variabilities of A_z and M_y peak in winter, as do their mean values, and WACCM simulates smaller variabilities compared with the reanalyses (Fig. 11d, f).

Figure 12 shows the annual cycles of the standard deviations of the N_2O mixing ratio, M_y and A_z for each dataset in the tropical regions (0–20° S and N) at 15 hPa for both hemispheres. The interannual variability of the N_2O mixing ratio in both the southern and northern tropics depends considerably on the dataset (Fig.12a, b). WACCM-CCMI and the BASCOE reanalysis of the Aura MLS show very similar variabilities, especially in the southern tropics. As the QBO is the major source of variability in the tropical stratosphere (Baldwin et al., 2001), this confirms an earlier comparison that showed a good agreement between the WACCM model and MLS observations in the middle stratosphere in terms of the interannual variability of N_2O due to the QBO (Park et al., 2017). Among the CTM simulations, ERAI succeeds at delivering $\sigma(\overline{X})$ values that are as large as BRAM2 and

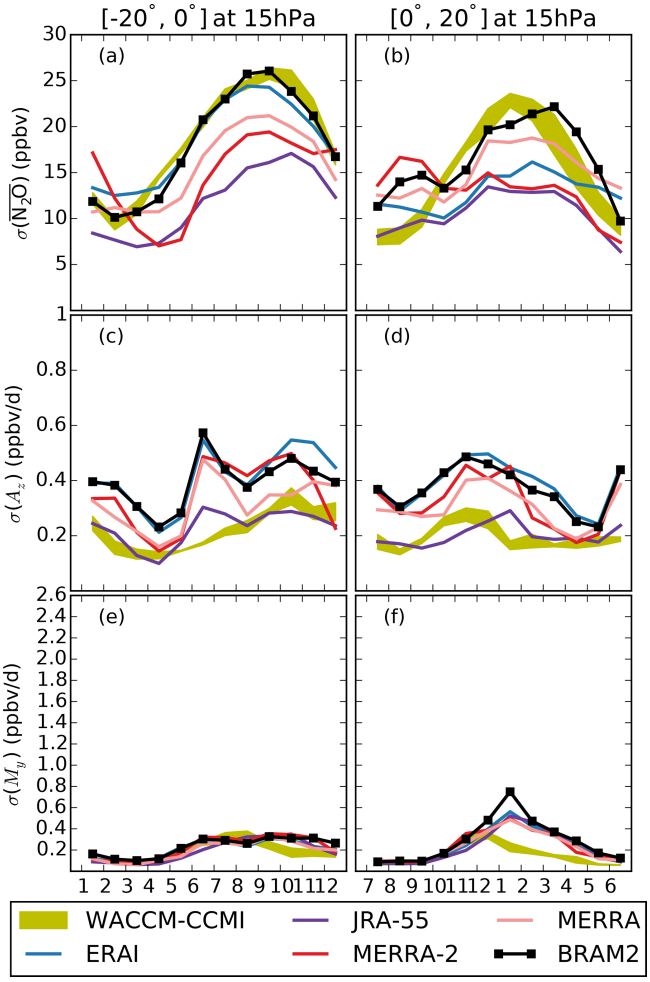

Figure 12. As for Fig. 10 but for the tropics: **(a, c, e)** southern tropics (0–20° S); **(b, d, f)** northern tropics (0–20° N).

WACCM-CCMI in the southern tropics, although this is not the case in the northern tropics.

The interannual variability of A_z in both hemispheres can be related to the impact of the QBO on the tropical upwelling (Flury et al., 2013). Among MERRA, ERAI and JRA-55, the fraction of variance in deseasonalized tropical upwelling $\overline{w}^*$ that is associated with the QBO is the largest with ERAI (Abalos et al., 2015). Our findings support this conclusion, as the largest $\sigma(\overline{A_z})$ among the reanalyses is again found with ERAI (Fig. 12c, d). However, a detailed analysis of the impact of the QBO on the BDC as illustrated here goes beyond the scope of this study. The variability of M_y in the tropical regions is small compared with the extra-tropical regions (Fig. 12e, f), which is in agreement with calculations of effective diffusivity that show small variabilities within the tropical pipe (Abalos et al., 2016a). The reanalyses deliver a larger interannual variability in the northern tropics during boreal winter, whereas the variability of M_y presents a much weaker annual cycle in the southern tropics. WACCM-CCMI does not reproduce this hemispheric asymmetry, with a rather flat profile in both hemispheres and a clear underestimation in the northern tropics, as is also shown for its mean values. In the tropical regions, both the variabilities of M_y and A_z fail to explain the good agreement in the variability of N_2O between WACCM and BRAM2, as well as their disagreement with the dynamical reanalyses, because M_y and A_z directly contribute to the N_2O tendency rather than its mixing ratio.

6 Summary and conclusions

We have evaluated the climatological (2005–2014) N_2O transport processes in the stratosphere using the tracer continuity equation in the TEM formalism. In particular, we emphasized the horizontal mixing and the vertical advection terms (M_y and A_z, respectively). The upwelling term A_z reduces the N_2O concentrations in the tropics and increases them in the extra-tropics, whereas M_y tends to reduce the meridional gradients of N_2O and presents large hemispheric differences. As M_y or A_z contribute to the local rates of change of N_2O, this analysis is complementary to time-integrated diagnostics such as mAoA. The comparison investigates a variety of datasets, from a free-running chemistry climate model to a reanalysis where dynamics and chemistry are both constrained. The former comprises three realizations of the CCMI REF-C1 experiment by WACCM, and the latter is the chemical reanalysis of Aura MLS driven by ERA-Interim: BRAM2. The intercomparison also includes the BASCOE CTM driven by four dynamical reanalyses – ERAI, JRA-55, MERRA and MERRA-2 – in order to contribute to the S-RIP.

Considering the N_2O mixing ratio in the middle stratosphere, all of the datasets agree with respect to the annual cycle, with the large spread in the N_2O abundances of the CTM experiments ($\sim 20\,\%$) reflecting the diversity of mAoA obtained with the same model (Chabrillat et al., 2018). The upwelling term A_z also agrees among the datasets, especially in the NH where WACCM closely follows the reanalyses. The horizontal mixing term M_y in the NH is weaker in WACCM compared with the reanalyses. In the extra-tropics, this could be attributed to the weaker forcing from the planetary waves in WACCM compared with the reanalyses. The differences in M_y become striking in the wintertime Antarctic, where the polar vortex plays a major role. According to the reanalyses, horizontal mixing plays an important role in that region, but that is not found by WACCM. However, this large wintertime M_y in the reanalyses is challenged by an almost as large residual term. It should be noted that the residual term also includes effects from mixing by diffusion. An additional WACCM run with different gravity waves in the SH is used as a sensitivity test. Over the Antarctic, this test has small impact on M_y, but it significantly modifies A_z in the austral fall and winter due to the enhanced downwelling, and the

N_2O mixing ratio during spring as a consequence of a more realistic timing of the vortex breakup.

The interannual variability of the mid-stratospheric horizontal mixing term M_y is largest in the polar regions. It is related to the variability in the vortex breakup dates during spring in the Antarctic, whereas it is related to the highly variable polar vortex in winter in the Arctic. The interannual variability of A_z is characterized by a large spread in the mid-stratospheric tropical regions where WACCM-CCMI and JRA-55 deliver a smaller contribution than the other reanalyses. This variability reflects the impact of the QBO on the tropical upwelling (Abalos et al., 2015).

The application of the TEM framework to tracer transport with reanalyses suffers from a poor closure of the budget in the polar regions. We chose to analyze these regions nonetheless, because the differences in M_y between WACCM and the reanalyses are larger than the residual term, but it remains important to better understand the causes of these large uncertainties. To this end, detailed studies of transport in the polar stratosphere are needed, e.g., comparing the residual circulations with indirect estimates derived from momentum and thermodynamic balances as well as evaluating the effective diffusivity in each dataset (Abalos et al., 2015, 2016a).

The next step of this research consists of the analysis of the interannual variations of the BDC, including the impact of the QBO and the El Niño–Southern Oscillation. Further extensions of this work would include the addition of new reanalysis products such as ERA5 and an intercomparison of several CCMs as already done for the residual circulation itself (Chrysanthou et al., 2019).

Data availability. The nine monthly climatologies of the N_2O mixing ratios and TEM budget terms are freely available at the BIRA-IASB repository (http://repository.aeronomie.be, https://doi.org/10.18758/71021057, Minganti, 2020).

Supplement. The supplement related to this article is available online at: https://doi.org/10.5194/acp-20-12609-2020-supplement.

Author contributions. DM, SC and EM designed the study. YC provided support with installing and running the models. QE provided the BRAM2 chemical reanalysis and helped with its interpretation. MP ran the CTM experiments. DK provided the WACCM-CCMI realizations and helped with the interpretation of the WACCM datasets. DM wrote and ran the software tools to compute the TEM budgets and realized all of the figures. DM, MA and SC analyzed the TEM budgets. DM and SC wrote the text. All co-authors contributed to the interpretation of the results and the reviews of the drafts of this paper.

Competing interests. The authors declare that they have no conflict of interest.

Special issue statement. This article is part of the special issue "The SPARC Reanalysis Intercomparison Project (S-RIP) (ACP/ESSD inter-journal SI)". It is not associated with a conference.

Acknowledgements. Emmanuel Mahieu is a research associate with the F.R.S. – FNRS. Marta Abalos acknowledges funding from the Atracción de Talento Comunidad de Madrid (grant no 2016-T2/AMB-1405) and the Spanish National STEADY project (grant no. CGL2017-83198-R). We thank the reanalysis centers (ECMWF, NASA GSFC and JMA) for providing their support and data products. WACCM is a component of NCAR's CESM, which is supported by the NSF and the Office of Science of the U.S. Department of Energy. The authors wish to acknowledge the contribution of Rolando Garcia in the discussion of the paper, specifically regarding the WACCM model results.

Financial support. This research has been supported by the F.R.S. – FNRS (Brussels) (grant no. PDR.T.0040.16).

Review statement. This paper was edited by Peter Haynes and reviewed by Mohamadou Diallo and one anonymous referee.

References

Abalos, M., Randel, W. J., Kinnison, D. E., and Serrano, E.: Quantifying tracer transport in the tropical lower stratosphere using WACCM, Atmos. Chem. Phys., 13, 10591–10607, https://doi.org/10.5194/acp-13-10591-2013, 2013.

Abalos, M., Legras, B., Ploeger, F., and Randel, W. J.: Evaluating the advective Brewer-Dobson circulation in three reanalyses for the period 1979–2012, J. Geophys. Res.-Atmos., 120, 7534–7554, 2015.

Abalos, M., Legras, B., and Shuckburgh, E.: Interannual variability in effective diffusivity in the upper troposphere/lower stratosphere from reanalysis data, Q. J. Roy. Meteorol. Soc., 142, 1847–1861, 2016a.

Abalos, M., Randel, W. J., and Birner, T.: Phase-speed spectra of eddy tracer fluxes linked to isentropic stirring and mixing in the upper troposphere and lower stratosphere, J. Atmos. Sci., 73, 4711–4730, 2016b.

Abalos, M., Randel, W. J., Kinnison, D. E., and Garcia, R. R.: Using the artificial tracer e90 to examine present and future UTLS tracer transport in WACCM, J. Atmos. Sci., 74, 3383–3403, 2017.

Andrews, D. G., Holton, J. R., and Leovy, C. B.: Middle atmosphere dynamics, 40, Academic press, USA, 489 pp., 1987.

Baldwin, M., Gray, L., Dunkerton, T., Hamilton, K., Haynes, P., Randel, W., Holton, J., Alexander, M., Hirota, I., Horinouchi, T., Jones, D. B. A., Kinnersley, J. S., Marquardt, C., Sato, K., and Takahashi, M.: The quasi-biennial oscillation, Rev. Geophys., 39, 179–229, 2001.

Birner, T. and Bönisch, H.: Residual circulation trajectories and transit times into the extratropical lowermost stratosphere, At-

mos. Chem. Phys., 11, 817–827, https://doi.org/10.5194/acp-11-817-2011, 2011.

Bönisch, H., Engel, A., Birner, Th., Hoor, P., Tarasick, D. W., and Ray, E. A.: On the structural changes in the Brewer-Dobson circulation after 2000, Atmos. Chem. Phys., 11, 3937–3948, https://doi.org/10.5194/acp-11-3937-2011, 2011.

Brasseur, G. P. and Solomon, S.: Aeronomy of the middle atmosphere: chemistry and physics of the stratosphere and mesosphere, Vol. 32, Springer Science & Business Media, the Netherlands, 637 pp., 2006.

Brewer, A.: Evidence for a world circulation provided by the measurements of helium and water vapour distribution in the stratosphere, Q. J. Roy. Meteorol. Soc., 75, 351–363, 1949.

Butchart, N.: The Brewer-Dobson circulation, Rev. Geophys., 52, 157–184, 2014.

Butchart, N., Cionni, I., Eyring, V., Shepherd, T., Waugh, D., Akiyoshi, H., Austin, J., Brühl, C., Chipperfield, M., Cordero, E., Dameris, M., Deckert, R., Dhomse, S., Frith, S. M., Garcia, R. R., Gettelman, A., Giorgetta, M. A., Kinnison, D. E., Li, F., Mancini, E., Mclandress, C., Pawson, S., Pitari, G., Plummer, D. A., Rozanov, E., Sassi, F., Scinocca, J. F., Shibata, K., Steil, B., and Tian, W.: Chemistry–climate model simulations of twenty-first century stratospheric climate and circulation changes, J. Clim., 23, 5349–5374, 2010.

Butler, A. H., Sjoberg, J. P., Seidel, D. J., and Rosenlof, K. H.: A sudden stratospheric warming compendium, Earth Syst. Sci. Data, 9, 63–76, https://doi.org/10.5194/essd-9-63-2017, 2017.

Cameron, C., Bodeker, G. E., Conway, J. P., Stuart, S., and Renwick, J.: Simulating the Antarctic stratospheric vortex transport barrier: comparing the Unified Model to reanalysis, Clim. Dynam., 53, 441–452, 2019.

Chabrillat, S., Vigouroux, C., Christophe, Y., Engel, A., Errera, Q., Minganti, D., Monge-Sanz, B. M., Segers, A., and Mahieu, E.: Comparison of mean age of air in five reanalyses using the BASCOE transport model, Atmos. Chem. Phys., 18, 14715–14735, https://doi.org/10.5194/acp-18-14715-2018, 2018.

Charney, J. G. and Drazin, P. G.: Propagation of planetary-scale disturbances from the lower into the upper atmosphere, J. Geophys. Res., 66, 83–109, 1961.

Chipperfield, M. P.: New version of the TOMCAT/SLIMCAT offline chemical transport model: Intercomparison of stratospheric tracer experiments, Q. J. Roy. Meteorol. Soc., 132, 1179–1203, https://doi.org/10.1256/qj.05.51, 2006.

Chrysanthou, A., Maycock, A. C., Chipperfield, M. P., Dhomse, S., Garny, H., Kinnison, D., Akiyoshi, H., Deushi, M., Garcia, R. R., Jöckel, P., Kirner, O., Pitari, G., Plummer, D. A., Revell, L., Rozanov, E., Stenke, A., Tanaka, T. Y., Visioni, D., and Yamashita, Y.: The effect of atmospheric nudging on the stratospheric residual circulation in chemistry–climate models, Atmos. Chem. Phys., 19, 11559–11586, https://doi.org/10.5194/acp-19-11559-2019, 2019.

Conley, A. J., Garcia, R., Kinnison, D., Lamarque, J.-F., Marsh, D., Mills, M., Smith, A. K., Tilmes, S., Vitt, F., Morrison, H., Cameron-Smith, P., Collins, W. D., Iacono, M. J., Easter, R. C., Ghan, S. I., Liu, X., Rasch, P. J., and Taylor, M. A.: Description of the NCAR community atmosphere model (CAM 5.0), NCAR Technical note, 254 pp., 2012.

Davis, S. M., Rosenlof, K. H., Hassler, B., Hurst, D. F., Read, W. G., Vömel, H., Selkirk, H., Fujiwara, M., and Damadeo, R.: The Stratospheric Water and Ozone Satellite Homogenized (SWOOSH) database: a long-term database for climate studies, Earth Syst. Sci. Data, 8, 461–490, https://doi.org/10.5194/essd-8-461-2016, 2016.

de la Cámara, A., Mechoso, C. R., Mancho, A. M., Serrano, E., and Ide, K.: Isentropic Transport within the Antarctic Polar-Night Vortex: Rossby Wave Breaking Evidence and Lagrangian Structures, J. Atmos. Sci., 70, 2982–3001, https://doi.org/10.1175/JAS-D-12-0274.1, 2013.

Dee, D. P., Uppala, S., Simmons, A., Berrisford, P., Poli, P., Kobayashi, S., Andrae, U., Balmaseda, M., Balsamo, G., Bauer, P., Bechtold, P., Beljaars, A. C. M., van de Berg, L., Bidlot, J., Bormann, N., Delsol, C., Dragani, R., Fuentes, M., Geer, A. J., Haimberger, L., Healy, S. B., Hersbach, H., Holm, E. V., Isaksen, L., Källberg, P., Köhler, M., Matricardi, M., McNally, A. P., Monge-Sanz, B. M., Morcrette, J.-J., Park, B.-K., Peubey, C., de Rosnay, P., Tavolato, C., Thepaut, J.-N., and Vitarta, F.: The ERA-Interim reanalysis: Configuration and performance of the data assimilation system, Q. J. Roy. Meteorol. Soc., 137, 553–597, 2011.

Diallo, M., Legras, B., and Chédin, A.: Age of stratospheric air in the ERA-Interim, Atmos. Chem. Phys., 12, 12133–12154, https://doi.org/10.5194/acp-12-12133-2012, 2012.

Diallo, M., Riese, M., Birner, T., Konopka, P., Müller, R., Hegglin, M. I., Santee, M. L., Baldwin, M., Legras, B., and Ploeger, F.: Response of stratospheric water vapor and ozone to the unusual timing of El Niño and the QBO disruption in 2015–2016, Atmos. Chem. Phys., 18, 13055–13073, https://doi.org/10.5194/acp-18-13055-2018, 2018.

Diallo, M., Konopka, P., Santee, M. L., Müller, R., Tao, M., Walker, K. A., Legras, B., Riese, M., Ern, M., and Ploeger, F.: Structural changes in the shallow and transition branch of the Brewer–Dobson circulation induced by El Niño, Atmos. Chem. Phys., 19, 425–446, https://doi.org/10.5194/acp-19-425-2019, 2019.

Dietmüller, S., Garny, H., Plöger, F., Jöckel, P., and Cai, D.: Effects of mixing on resolved and unresolved scales on stratospheric age of air, Atmos. Chem. Phys., 17, 7703–7719, https://doi.org/10.5194/acp-17-7703-2017, 2017.

Dietmüller, S., Eichinger, R., Garny, H., Birner, T., Boenisch, H., Pitari, G., Mancini, E., Visioni, D., Stenke, A., Revell, L., Rozanov, E., Plummer, D. A., Scinocca, J., Jöckel, P., Oman, L., Deushi, M., Kiyotaka, S., Kinnison, D. E., Garcia, R., Morgenstern, O., Zeng, G., Stone, K. A., and Schofield, R.: Quantifying the effect of mixing on the mean age of air in CCMVal-2 and CCMI-1 models, Atmos. Chem. Phys., 18, 6699–6720, https://doi.org/10.5194/acp-18-6699-2018, 2018.

Dobson, G. M. B.: Origin and distribution of the polyatomic molecules in the atmosphere, Proc. Roy. Soc. London Ser. A, 236, 187–193, 1956.

Dobson, G. M. B., Harrison, D., and Lawrence, J.: Measurements of the amount of ozone in the Earth's atmosphere and its relation to other geophysical conditions – Part III, Proc. Roy. Soc. London Ser. A, 122, 456–486, 1929.

Edmon, H., Hoskins, B., and McIntyre, M.: Eliassen-Palm cross sections for the troposphere, J. Atmos. Sci., 37, 2600–2616, 1980.

Engel, A., Möbius, T., Bönisch, H., Schmidt, U., Heinz, R., Levin, I., Atlas, E., Aoki, S., Nakazawa, T., Sugawara, S., Moore, F., Hurst, D., Elkins, J., Schauffler, S., Andrews, A., and Boering,

K.: Age of stratospheric air unchanged within uncertainties over the past 30 years, Nat. Geosci., 2, 28–31, 2009.

Engel, A., Bönisch, H., Ullrich, M., Sitals, R., Membrive, O., Danis, F., and Crevoisier, C.: Mean age of stratospheric air derived from AirCore observations, Atmos. Chem. Phys., 17, 6825–6838, https://doi.org/10.5194/acp-17-6825-2017, 2017.

Errera, Q., Daerden, F., Chabrillat, S., Lambert, J. C., Lahoz, W. A., Viscardy, S., Bonjean, S., and Fonteyn, D.: 4D-Var assimilation of MIPAS chemical observations: ozone and nitrogen dioxide analyses, Atmos. Chem. Phys., 8, 6169-6187, https://doi.org/10.5194/acp-8-6169-2008, 2008.

Errera, Q., Chabrillat, S., Christophe, Y., Debosscher, J., Hubert, D., Lahoz, W., Santee, M. L., Shiotani, M., Skachko, S., von Clarmann, T., and Walker, K.: Technical note: Reanalysis of Aura MLS chemical observations, Atmos. Chem. Phys., 19, 13647–13679, https://doi.org/10.5194/acp-19-13647-2019, 2019.

Flury, T., Wu, D. L., and Read, W. G.: Variability in the speed of the Brewer–Dobson circulation as observed by Aura/MLS, Atmos. Chem. Phys., 13, 4563–4575, https://doi.org/10.5194/acp-13-4563-2013, 2013.

Fritsch, F., Garny, H., Engel, A., Bönisch, H., and Eichinger, R.: Sensitivity of age of air trends to the derivation method for non-linear increasing inert SF_6, Atmos. Chem. Phys., 20, 8709–8725, https://doi.org/10.5194/acp-20-8709-2020, 2020.

Froidevaux, L., Kinnison, D. E., Wang, R., Anderson, J., and Fuller, R. A.: Evaluation of CESM1 (WACCM) free-running and specified dynamics atmospheric composition simulations using global multispecies satellite data records, Atmos. Chem. Phys., 19, 4783–4821, https://doi.org/10.5194/acp-19-4783-2019, 2019.

Fueglistaler, S., Dessler, A., Dunkerton, T., Folkins, I., Fu, Q., and Mote, P. W.: Tropical tropopause layer, Rev. Geophys., 47, RG1004, https://doi.org/10.1029/2008RG000267, 2009.

Fujiwara, M., Wright, J. S., Manney, G. L., Gray, L. J., Anstey, J., Birner, T., Davis, S., Gerber, E. P., Harvey, V. L., Hegglin, M. I., Homeyer, C. R., Knox, J. A., Krüger, K., Lambert, A., Long, C. S., Martineau, P., Molod, A., Monge-Sanz, B. M., Santee, M. L., Tegtmeier, S., Chabrillat, S., Tan, D. G. H., Jackson, D. R., Polavarapu, S., Compo, G. P., Dragani, R., Ebisuzaki, W., Harada, Y., Kobayashi, C., McCarty, W., Onogi, K., Pawson, S., Simmons, A., Wargan, K., Whitaker, J. S., and Zou, C.-Z.: Introduction to the SPARC Reanalysis Intercomparison Project (S-RIP) and overview of the reanalysis systems, Atmos. Chem. Phys., 17, 1417–1452, https://doi.org/10.5194/acp-17-1417-2017, 2017.

Galytska, E., Rozanov, A., Chipperfield, M. P., Dhomse, Weber, M., Arosio, C., Feng, W., and Burrows, J. P.: Dynamically controlled ozone decline in the tropical mid-stratosphere observed by SCIAMACHY, Atmos. Chem. Phys., 19, 767–783, https://doi.org/10.5194/acp-19-767-2019, 2019.

Garcia, R. R., Randel, W. J., and Kinnison, D. E.: On the determination of age of air trends from atmospheric trace species, J. Atmos. Sci., 68, 139–154, 2011.

Garcia, R. R., Smith, A. K., Kinnison, D. E., Cámara, Á. d. l., and Murphy, D. J.: Modification of the gravity wave parameterization in the Whole Atmosphere Community Climate Model: Motivation and results, J. Atmos. Sci., 74, 275–291, 2017.

Gelaro, R., McCarty, W., Suárez, M. J., Todling, R., Molod, A., Takacs, L., Randles, C. A., Darmenov, A., Bosilovich, M. G., Reichle, R., Wargan, K., Coy, L., Cullather, R., Draper, C., Akella, S., Buchard, V., Conaty, A., da Silva, A. M., Gu, W., Kim, G.-K., Koster, R., Lucchesi, R., Merkova, D., Nielsen, J. E., Partyka, G., Pawson, S., Putman, W., Rienecker, M., Schubert, S. D., Sienkiewicz, M., and Zhao, B.: The modern-era retrospective analysis for research and applications, version 2 (MERRA-2), J. Clim., 30, 5419–5454, 2017.

Gerber, E. P.: Stratospheric versus tropospheric control of the strength and structure of the Brewer–Dobson circulation, J. Atmos. Sci., 69, 2857–2877, 2012.

Gerber, E. P., Baldwin, M. P., Akiyoshi, H., Austin, J., Bekki, S., Braesicke, P., Butchart, N., Chipperfield, M., Dameris, M., Dhomse, S., Frith, S. M., Garcia, R. R., Garny, H., Getterlman, A., Hardiman, S. C., Karpechko, A., Marchand, M., Morgenstern, O., Nielsen, J. E., Pawson, S., Peter, T., Plummer, D. A., Pyle, J. A., Rozanov, E., Scinnocca, J. F., Shepherd, T. G., and Smale, D.: Stratosphere-troposphere coupling and annular mode variability in chemistry-climate models, J. Geophys. Res.-Atmos., 115, D00M06, https://doi.org/10.1029/2009JD013770, 2010.

Haenel, F. J., Stiller, G. P., von Clarmann, T., Funke, B., Eckert, E., Glatthor, N., Grabowski, U., Kellmann, S., Kiefer, M., Linden, A., and Reddmann, T.: Reassessment of MIPAS age of air trends and variability, Atmos. Chem. Phys., 15, 13161–13176, https://doi.org/10.5194/acp-15-13161-2015, 2015.

Hall, T. M., Waugh, D. W., Boering, K. A., and Plumb, R. A.: Evaluation of transport in stratospheric models, J. Geophys. Res.-Atmos., 104, 18815–18839, 1999.

Hardiman, S. C., Butchart, N., and Calvo, N.: The morphology of the Brewer–Dobson circulation and its response to climate change in CMIP5 simulations, Q. J. Roy. Meteorol. Soc., 140, 1958–1965, 2014.

Hardiman, S. C., Lin, P., Scaife, A. A., Dunstone, N. J., and Ren, H.-L.: The influence of dynamical variability on the observed Brewer-Dobson circulation trend, Geophys. Res. Lett., 44, 2885–2892, 2017.

Haynes, P. and Shuckburgh, E.: Effective diffusivity as a diagnostic of atmospheric transport: 2. Troposphere and lower stratosphere, J. Geophys. Res.-Atmos., 105, 22795–22810, 2000.

Haynes, P., McIntyre, M., Shepherd, T., Marks, C., and Shine, K. P.: On the downward control of extratropical diabatic circulations by eddy-induced mean zonal forces, J. Atmos. Sci.s, 48, 651–678, 1991.

Hegglin, M., Plummer, D., Shepherd, T., Scinocca, J., Anderson, J., Froidevaux, L., Funke, B., Hurst, D., Rozanov, A., Urban, J., von Clarmann, T., Walker, K. A., Wang, H. J., Tegtmeier, S., and Weigel, K.: Vertical structure of stratospheric water vapour trends derived from merged satellite data, Nat. Geosci., 7, 768–776, 2014.

Holton, J.: An Introduction to Dynamic Meteorology, no. v. 1 in An Introduction to Dynamic Meteorology, Elsevier Science, available at: https://books.google.be/books?id=fhW5oDv3EPsC (last access: 28 October 2020), 2004.

Hurrell, J. W., Holland, M. M., Gent, P. R., Ghan, S., Kay, J. E., Kushner, P. J., Lamarque, J.-F., Large, W. G., Lawrence, D., Lindsay, K., Lipscomb, W. H., Long, M. C., Mahowald, N., Marsh, D. R., Neale, R. B., Rasch, P., Vavrus, S., Vertenstein, M., Bader, D., Collins, W. D., Hack, J. J., Kiehl, J., and Marshall, S.: The community earth system model: a framework for

collaborative research, B. Am. Meteorol. Soc., 94, 1339–1360, 2013.

Kawatani, Y., Hamilton, K., Miyazaki, K., Fujiwara, M., and Anstey, J. A.: Representation of the tropical stratospheric zonal wind in global atmospheric reanalyses, Atmos. Chem. Phys., 16, 6681–6699, https://doi.org/10.5194/acp-16-6681-2016, 2016.

Kidston, J., Scaife, A. A., Hardiman, S. C., Mitchell, D. M., Butchart, N., Baldwin, M. P., and Gray, L. J.: Stratospheric influence on tropospheric jet streams, storm tracks and surface weather, Nat. Geosci., 8, 433–440, 2015.

Kinnison, D., Brasseur, G., Walters, S., Garcia, R., Marsh, D., Sassi, F., Harvey, V., Randall, C., Emmons, L., Lamarque, J.-F., Hess, P., Orlando, J. J., Tie, X. X., Randel, W., Pan, L. L., Gettelman, A., Granier, C., Diehl, T., Niemeier, U., and Simmons, A. J.: Sensitivity of chemical tracers to meteorological parameters in the MOZART-3 chemical transport model, J. Geophys. Res.-Atmos., 112, D20302, https://doi.org/10.1029/2006JD007879, 2007.

Kobayashi, S., Ota, Y., Harada, Y., Ebita, A., Moriya, M., Onoda, H., Onogi, K., Kamahori, H., Kobayashi, C., Endo, H., Miyaoka, K., and Takahashi, K.: The JRA-55 reanalysis: General specifications and basic characteristics, J. Meteorol. Soc. Jpn. Ser. II, 93, 5–48, 2015.

Konopka, P., Grooß, J.-U., Günther, G., Ploeger, F., Pommrich, R., Müller, R., and Livesey, N.: Annual cycle of ozone at and above the tropical tropopause: observations versus simulations with the Chemical Lagrangian Model of the Stratosphere (CLaMS), Atmos. Chem. Phys., 10, 121–132, https://doi.org/10.5194/acp-10-121-2010, 2010.

Konopka, P., Ploeger, F., Tao, M., Birner, T., and Riese, M.: Hemispheric asymmetries and seasonality of mean age of air in the lower stratosphere: Deep versus shallow branch of the Brewer-Dobson circulation, J. Geophys. Res.-Atmos., 120, 2053–2066, 2015.

Lahoz, W. and Errera, Q.: Data Assimilation: Making Sense of Observations, Constituent Assimilation, Springer, Berlin, Heidelberg, 449–490, 2010.

Lean, J., Rottman, G., Harder, J., and Kopp, G.: SORCE contributions to new understanding of global change and solar variability, in: The Solar Radiation and Climate Experiment (SORCE), Springer, New York, NY, 27–53, 2005.

Li, F., Waugh, D. W., Douglass, A. R., Newman, P. A., Pawson, S., Stolarski, R. S., Strahan, S. E., and Nielsen, J. E.: Seasonal variations of stratospheric age spectra in the Goddard Earth Observing System Chemistry Climate Model (GEOSCCM), J. Geophys. Res.-Atmos., 117, D5, https://doi.org/10.1029/2011JD016877, 2012.

Lin, P. and Fu, Q.: Changes in various branches of the Brewer–Dobson circulation from an ensemble of chemistry climate models, J. Geophys. Res.-Atmos., 118, 73–84, 2013.

Lin, S.-J.: A "vertically Lagrangian" finite-volume dynamical core for global models, Mon. Weather Rev., 132, 2293–2307, 2004.

Lin, S.-J. and Rood, R. B.: Multidimensional flux-form semi-Lagrangian transport schemes, Mon. Weather Rev., 124, 2046–2070, 1996.

Livesey, N., Read, W., Wagner, P., Froidevaux, L., Lambert, A., Manney, G., Pumphrey, H., Santee, M., Schwartz, M., Wang, S., Fuller, R. A., Jarnot, R. F., Knosp, B. W., and Martinez, E.: Earth Observing System (EOS) Aura Microwave Limb Sounder (MLS) version 4.2x level 2 data quality and description document, JPL D-33509 rev. A, A, JPL publication, Pasadena, CA, USA, 174 pp., 2015.

Long, C. S., Fujiwara, M., Davis, S., Mitchell, D. M., and Wright, C. J.: Climatology and interannual variability of dynamic variables in multiple reanalyses evaluated by the SPARC Reanalysis Intercomparison Project (S-RIP), Atmos. Chem. Phys., 17, 14593–14629, https://doi.org/10.5194/acp-17-14593-2017, 2017.

Mahieu, E., Chipperfield, M., Notholt, J., Reddmann, T., Anderson, J., Bernath, P., Blumenstock, T., Coffey, M., Dhomse, S., Feng, W., Franco, B., Froidevaux, L., Griffith, D. W. T., Hannigan, J. W., Hase, F., Hossaini, R., Jones, N. B., Morino, I., Murata, I., Nakajima, H., Palm, M., Paton-Walsh, C., Russell III, J. M., Schneider, M., Servais, C., Smale, D., and Walker, K. A.: Recent Northern Hemisphere stratospheric HCl increase due to atmospheric circulation changes, Nature, 515, 104–107, 2014.

Manney, G. L., Sabutis, J. L., Pawson, S., Santee, M. L., Naujokat, B., Swinbank, R., Gelman, M. E., and Ebisuzaki, W.: Lower stratospheric temperature differences between meteorological analyses in two cold Arctic winters and their impact on polar processing studies, J. Geophys. Res.-Atmos., 108, 8328, https://doi.org/10.1029/2001JD001149, 2003.

Marsh, D. R., Mills, M. J., Kinnison, D. E., Lamarque, J.-F., Calvo, N., and Polvani, L. M.: Climate change from 1850 to 2005 simulated in CESM1 (WACCM), J. Clim., 26, 7372–7391, 2013.

Matthes, K., Marsh, D. R., Garcia, R. R., Kinnison, D. E., Sassi, F., and Walters, S.: Role of the QBO in modulating the influence of the 11 year solar cycle on the atmosphere using constant forcings, J. Geophys. Res.-Atmos., 115, D18110, https://doi.org/10.1029/2009JD013020, 2010.

McIntyre, M. E. and Palmer, T.: Breaking planetary waves in the stratosphere, Nature, 305, 593–600, 1983.

Ménard, R., Chabrillat, S., Robichaud, A., de Grandpré, J., Charron, M., Rochon, Y., Batchelor, R., Kallaur, A., Reszka, M., and Kaminski, J.: Coupled Stratospheric Chemistry-Meteorology Data Assimilation, Part I: Physical Background and Coupled Modeling Aspects, Atmosphere, 11, 150, https://doi.org/10.3390/atmos11020150, 2020.

Minganti, D.: Supplement for: Climatological impact of the Brewer-Dobson Circulation on the N_2O budget in WACCM, a chemical reanalysis and a CTM driven by four dynamical reanalyses, https://doi.org/10.18758/71021057, 2020.

Miyazaki, K. and Iwasaki, T.: Diagnosis of meridional ozone transport based on mass-weighted isentropic zonal means, J. Atmos. Sci., 62, 1192–1208, 2005.

Monge-Sanz, B. M., Chipperfield, M. P., Dee, D. P., Simmons, A. J., and Uppala, S. M.: Improvements in the stratospheric transport achieved by a chemistry transport model with ECMWF (re)analyses: identifying effects and remaining challenges, Q. J. Roy. Meteorol. Soc., 139, 654–673, https://doi.org/10.1002/qj.1996, 2012.

Morgenstern, O., Hegglin, M. I., Rozanov, E., O'Connor, F. M., Abraham, N. L., Akiyoshi, H., Archibald, A. T., Bekki, S., Butchart, N., Chipperfield, M. P., Deushi, M., Dhomse, S. S., Garcia, R. R., Hardiman, S. C., Horowitz, L. W., Jöckel, P., Josse, B., Kinnison, D., Lin, M., Mancini, E., Manyin, M. E., Marchand, M., Marécal, V., Michou, M., Oman, L. D., Pitari, G., Plummer, D. A., Revell, L. E., Saint-Martin, D., Schofield, R., Stenke, A., Stone, K., Sudo, K., Tanaka, T. Y., Tilmes, S., Yamashita, Y., Yoshida, K., and Zeng, G.: Review of the

global models used within phase 1 of the Chemistry–Climate Model Initiative (CCMI), Geosci. Model Dev., 10, 639–671, https://doi.org/10.5194/gmd-10-639-2017, 2017.

Neale, R. B., Richter, J., Park, S., Lauritzen, P. H., Vavrus, S. J., Rasch, P. J., and Zhang, M.: The mean climate of the Community Atmosphere Model (CAM4) in forced SST and fully coupled experiments, J. Clim., 26, 5150–5168, 2013.

Newman, P. A. and Nash, E. R.: Quantifying the wave driving of the stratosphere, J. Geophys. Res.-Atmos., 105, 12485–12497, 2000.

Newman, P. A. and Nash, E. R.: The unusual Southern Hemisphere stratosphere winter of 2002, J. Atmos. Sci., 62, 614–628, 2005.

Palmeiro, F. M., Calvo, N., and Garcia, R. R.: Future changes in the Brewer–Dobson circulation under different greenhouse gas concentrations in WACCM4, J. Atmos. Sci., 71, 2962–2975, 2014.

Park, M., Randel, W., Kinnison, D., Bourassa, A., Degenstein, D., Roth, C., McLinden, C., Sioris, C., Livesey, N., and Santee, M.: Variability of stratospheric reactive nitrogen and ozone related to the QBO, J. Geophys. Res.-Atmos., 122, 10–103, 2017.

Ploeger, F. and Birner, T.: Seasonal and inter-annual variability of lower stratospheric age of air spectra, Atmos. Chem. Phys., 16, 10195–10213, https://doi.org/10.5194/acp-16-10195-2016, 2016.

Ploeger, F., Legras, B., Charlesworth, E., Yan, X., Diallo, M., Konopka, P., Birner, T., Tao, M., Engel, A., and Riese, M.: How robust are stratospheric age of air trends from different reanalyses?, Atmos. Chem. Phys., 19, 6085–6105, https://doi.org/10.5194/acp-19-6085-2019, 2019.

Plumb, R. A.: Stratospheric transport, J. Meteorol. Soc. Jpn. Ser. II, 80, 793–809, 2002.

Polvani, L. M., Abalos, M., Garcia, R., Kinnison, D., and Randel, W. J.: Significant Weakening of Brewer-Dobson Circulation Trends Over the 21st Century as a Consequence of the Montreal Protocol, Geophys. Res. Lett., 45, 401–409, 2018.

Prignon, M., Chabrillat, S., Minganti, D., O'Doherty, S., Servais, C., Stiller, G., Toon, G. C., Vollmer, M. K., and Mahieu, E.: Improved FTIR retrieval strategy for HCFC-22 (CHClF2), comparisons with in situ and satellite datasets with the support of models, and determination of its long-term trend above Jungfraujoch, Atmos. Chem. Phys., 19, 12309–12324, https://doi.org/10.5194/acp-19-12309-2019, 2019.

Randel, W. J. and Newman, P. A.: The stratosphere in the Southern Hemisphere, in: Meteorology of the Southern Hemisphere, Springer, Boston, MA, 243–282, 1998.

Randel, W. J., Boville, B. A., Gille, J. C., Bailey, P. L., Massie, S. T., Kumer, J., Mergenthaler, J., and Roche, A.: Simulation of stratospheric N2O in the NCAR CCM2: Comparison with CLAES data and global budget analyses, Journal of the atmospheric sciences, 51, 2834–2845, 1994.

Rao, J., Ren, R., and Yang, Y.: Parallel comparison of the northern winter stratospheric circulation in reanalysis and in CMIP5 models, Adv. Atmos. Sci., 32, 952–966, 2015.

Richter, J. H., Sassi, F., and Garcia, R. R.: Toward a physically based gravity wave source parameterization in a general circulation model, J. Atmos. Sci., 67, 136–156, 2010.

Rienecker, M. M., Suarez, M. J., Gelaro, R., Todling, R., Bacmeister, J., Liu, E., Bosilovich, M. G., Schubert, S. D., Takacs, L., Kim, G.-K., Bloom, S., Junye, C., Collins, D., Conaty, A., da Silva, A., Gu, W., Joiner, J., Koster, R. D., Lucchesi, R., Molod, A., Owens, T., Pawson, S., Pegion, P., Redder, C. R., Reichle, R., Robertson, F. R., Ruddick, A. G., Sienkiewicz, M., and Woollen, J.: MERRA: NASA' modern-era retrospective analysis for research and applications, J. Clim., 24, 3624–3648, 2011.

Riese, M., Ploeger, F., Rap, A., Vogel, B., Konopka, P., Dameris, M., and Forster, P.: Impact of uncertainties in atmospheric mixing on simulated UTLS composition and related radiative effects, J. Geophys. Res.-Atmos., 117, D16305, https://doi.org/10.1029/2012JD017751, 2012.

Roscoe, H. K., Feng, W., Chipperfield, M. P., Trainic, M., and Shuckburgh, E. F.: The existence of the edge region of the Antarctic stratospheric vortex, J. Geophys. Res.-Atmos., 117, D04301, https://doi.org/10.1029/2011JD015940, 2012.

Rosenlof, K. H. and Holton, J. R.: Estimates of the stratospheric residual circulation using the downward control principle, J. Geophys. Res.-Atmos., 98, 10465–10479, 1993.

Salby, M. L. and Callaghan, P. F.: Interaction between the Brewer–Dobson circulation and the Hadley circulation, J. Clim., 18, 4303–4316, 2005.

Sato, K. and Hirano, S.: The climatology of the Brewer–Dobson circulation and the contribution of gravity waves, Atmos. Chem. Phys., 19, 4517–4539, https://doi.org/10.5194/acp-19-4517-2019, 2019.

Scaife, A. and James, I.: Response of the stratosphere to interannual variability of tropospheric planetary waves, Q. J. Roy. Meteorol. Soc., 126, 275–297, 2000.

Schoeberl, M., Douglass, A., Stolarski, R., Pawson, S., Strahan, S., and Read, W.: Comparison of lower stratospheric tropical mean vertical velocities, J. Geophys. Res.-Atmos., 113, D24109, https://doi.org/10.1029/2008JD010221, 2008.

Seinfeld, J. H. and Pandis, S. N.: Atmospheric chemistry and physics: from air pollution to climate change, John Wiley & Sons, 1152 pp., 2016.

Shepherd, T. G.: Transport in the middle atmosphere, J. Meteorol. Soc. Jpn. Ser. II, 85, 165–191, 2007.

Solomon, S., Kinnison, D., Bandoro, J., and Garcia, R.: Simulation of polar ozone depletion: An update, J. Geophys. Res.-Atmos., 120, 7958–7974, 2015.

Stiller, G. P., von Clarmann, T., Haenel, F., Funke, B., Glatthor, N., Grabowski, U., Kellmann, S., Kiefer, M., Linden, A., Lossow, S., and López-Puertas, M.: Observed temporal evolution of global mean age of stratospheric air for the 2002 to 2010 period, Atmos. Chem. Phys., 12, 3311–3331, https://doi.org/10.5194/acp-12-3311-2012, 2012.

Strahan, S., Oman, L., Douglass, A., and Coy, L.: Modulation of Antarctic vortex composition by the quasi-biennial oscillation, Geophys. Res. Lett., 42, 4216–4223, 2015.

Strahan, S. E., Douglass, A., Stolarski, R., Akiyoshi, H., Bekki, S., Braesicke, P., Butchart, N., Chipperfield, M., Cugnet, D., Dhomse, S., Frith, S. M., Gettelman, A., Hardiman, S. C., Kinnison, D. E., Lamarque, J. F., Mancini, E., Marchand, M., Michou, M., Morgenstern, O., Nakamura, T., Olivie, D., Pawson, S., Pitari, G., Plummer, D. A., Pyle, J. A., Scinocca, J. F., Shepherd, T. G., Shibata, K., Smale, D., Teyssedre, H., Tian, W., and Yamashita, Y.: Using transport diagnostics to understand chemistry climate model ozone simulations, J. Geophys. Res.-Atmos., 116, D17302, https://doi.org/10.1029/2010JD015360, 2011.

Tao, M., Konopka, P., Ploeger, F., Yan, X., Wright, J. S., Diallo, M., Fueglistaler, S., and Riese, M.: Multitimescale variations in modeled stratospheric water vapor derived from three mod-

ern reanalysis products, Atmos. Chem. Phys., 19, 6509–6534, https://doi.org/10.5194/acp-19-6509-2019, 2019.

Tweedy, O., Waugh, D., Stolarski, R., Oman, L. D., Randel, W., and Abalos, M.: Hemispheric differences in the annual cycle of tropical lower stratosphere transport and tracers, J. Geophys. Res.-Atmos., 122, 7183–7199, 2017.

Waugh, D. and Hall, T.: Age of stratospheric air: Theory, observations, and models, Rev. Geophys., 40, 1–1010, 2002.

Waugh, D. W. and Randel, W. J.: Climatology of Arctic and Antarctic polar vortices using elliptical diagnostics, J. Atmos. Sci., 56, 1594–1613, 1999.

Yamazaki, Y., Matthias, V., Miyoshi, Y., Stolle, C., Siddiqui, T., Kervalishvili, G., Laštovička, J., Kozubek, M., Ward, W., Themens, D. R., Kristoffersen, S., and Alken, P.: September 2019 Antarctic sudden stratospheric warming: quasi-6-day wave burst and ionospheric effects, Geophys. Res. Lette., 47, e2019GL086577, https://doi.org/10.1029/2019GL086577, 2019.

Yang, H., Chen, G., and Domeisen, D. I.: Sensitivities of the lower-stratospheric transport and mixing to tropical SST heating, J. Atmos. Sci., 71, 2674–2694, 2014.

6.2 Addition of the BASCOE CTM driven by ERA5 and WACCM-REFD1 simulations

This Section replicates Figures 5 to 9 of the previous Section with the inclusion of the BASCOE CTM simulation driven by ERA5 and the WACCM-REFD1 realization (Figs. 6.1 to 6.6), which were not available for use at the time of the published study (Minganti et al., 2020).

The annual climatological cycles of the residual vertical velocity $\overline{w}^*$ and of the divergence of the Eliassen-Palm flux $\nabla \cdot \mathbf{F}$ (EPFD), together with the annual cycles of N_2O, A_z and M_y, obtained from the ERA5 simulation are very similar to those obtained using the ERAI simulation. The only exception is above the northern Tropics, where the N_2O abundances simulated by the ERA5 experiment are closer to BRAM2 than achieved with the ERAI experiment (Fig. 6.5b). Regarding WACCM-REFD1, there are no significant differences compared with the WACCM-REFC1 version.

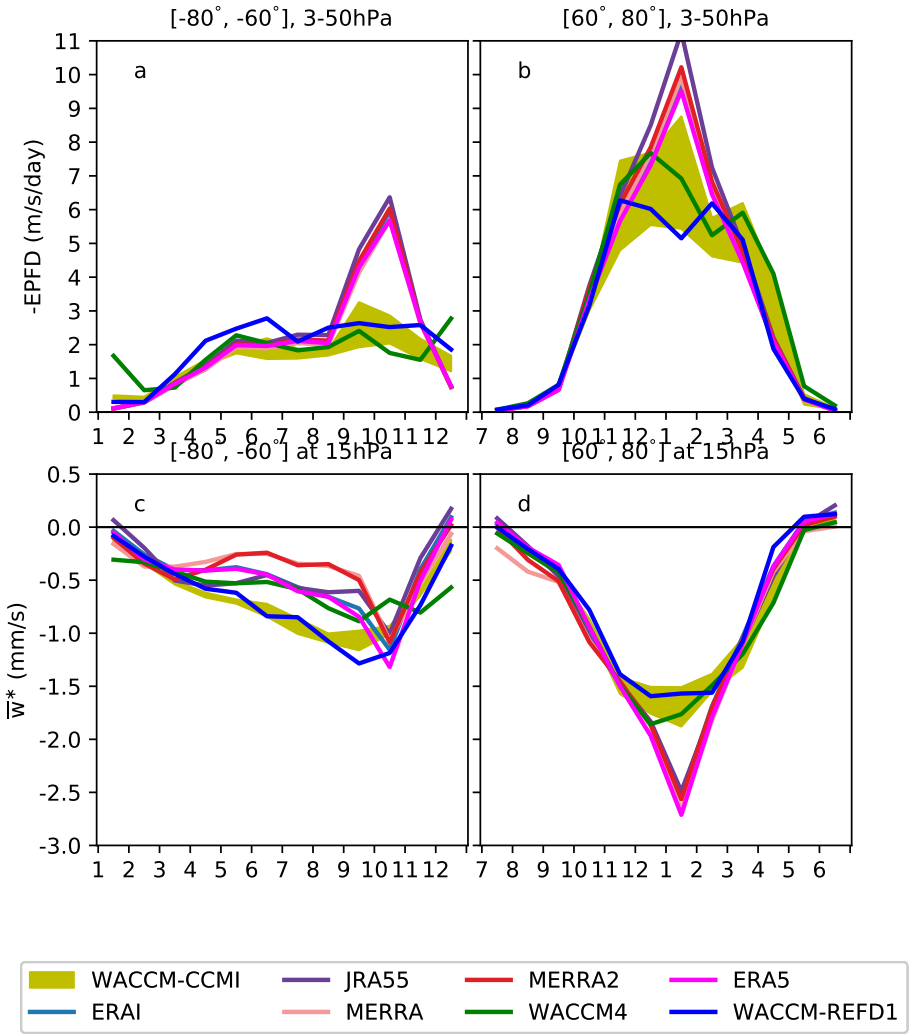

Figure 6.1: As Fig. 5 of the previous Section, with the addition of the BASCOE CTM driven by ERA5 and the WACCM-REFD1 simulation.

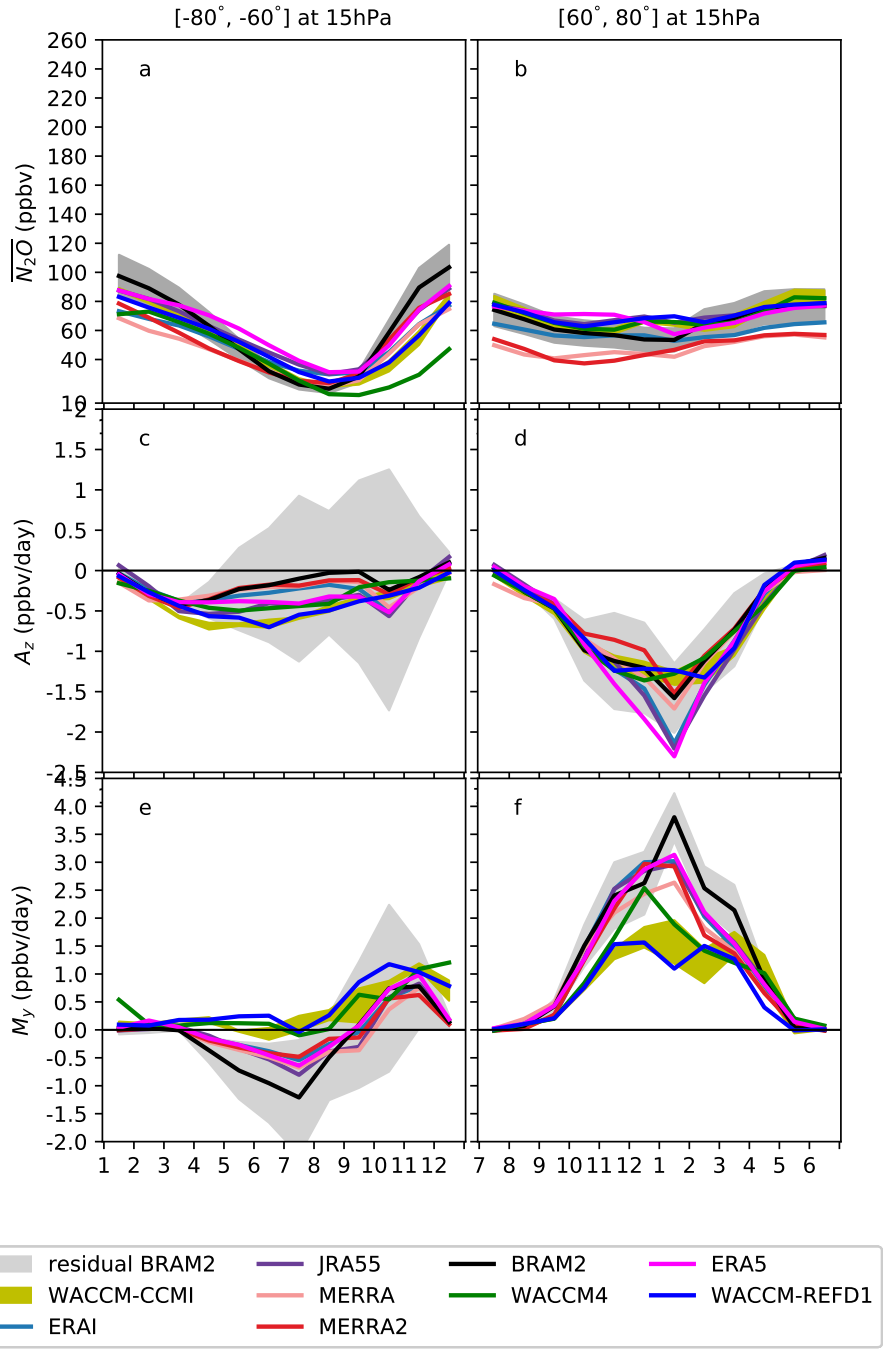

Figure 6.2: As Fig. 6 of the previous Section, with the addition of the BASCOE CTM simulation driven by ERA5 and the WACCM-REFD1 realization.

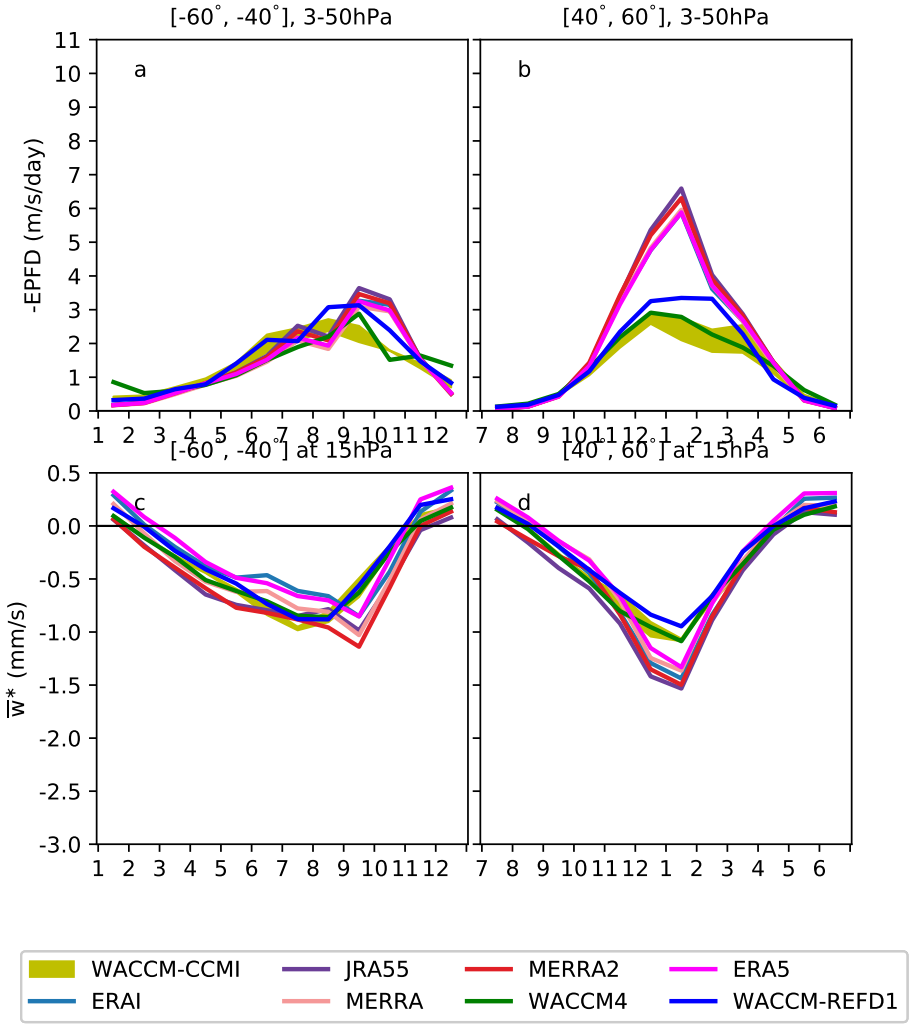

Figure 6.3: As Fig. 7 of the previous Section, with the addition of the BAS-COE CTM simulation driven by ERA5 and the WACCM-REFD1 realization.

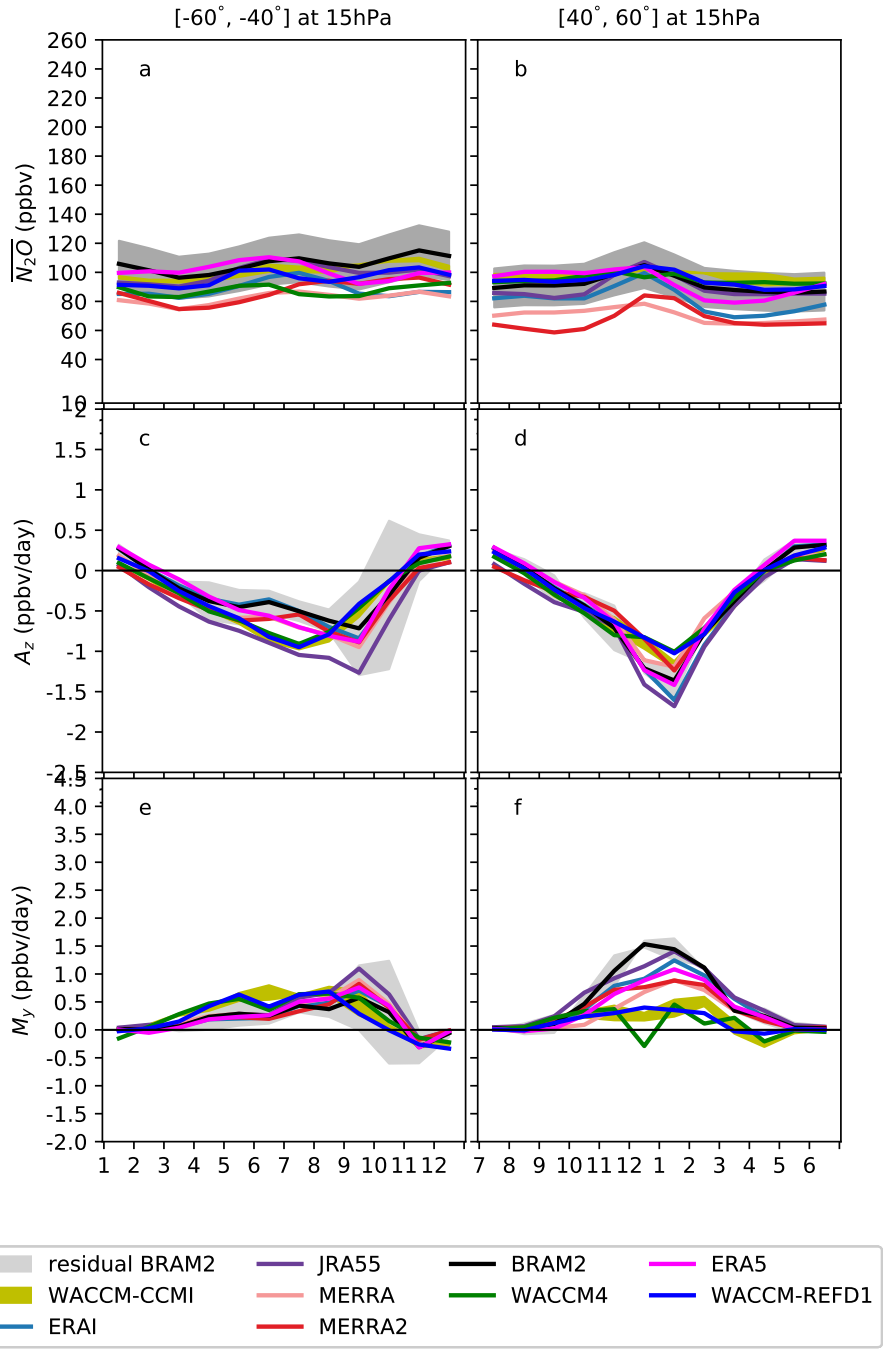

Figure 6.4: As Fig. 8 of the previous Section, with the addition of the BASCOE CTM simulation driven by ERA5 and the WACCM-REFD1 realization.

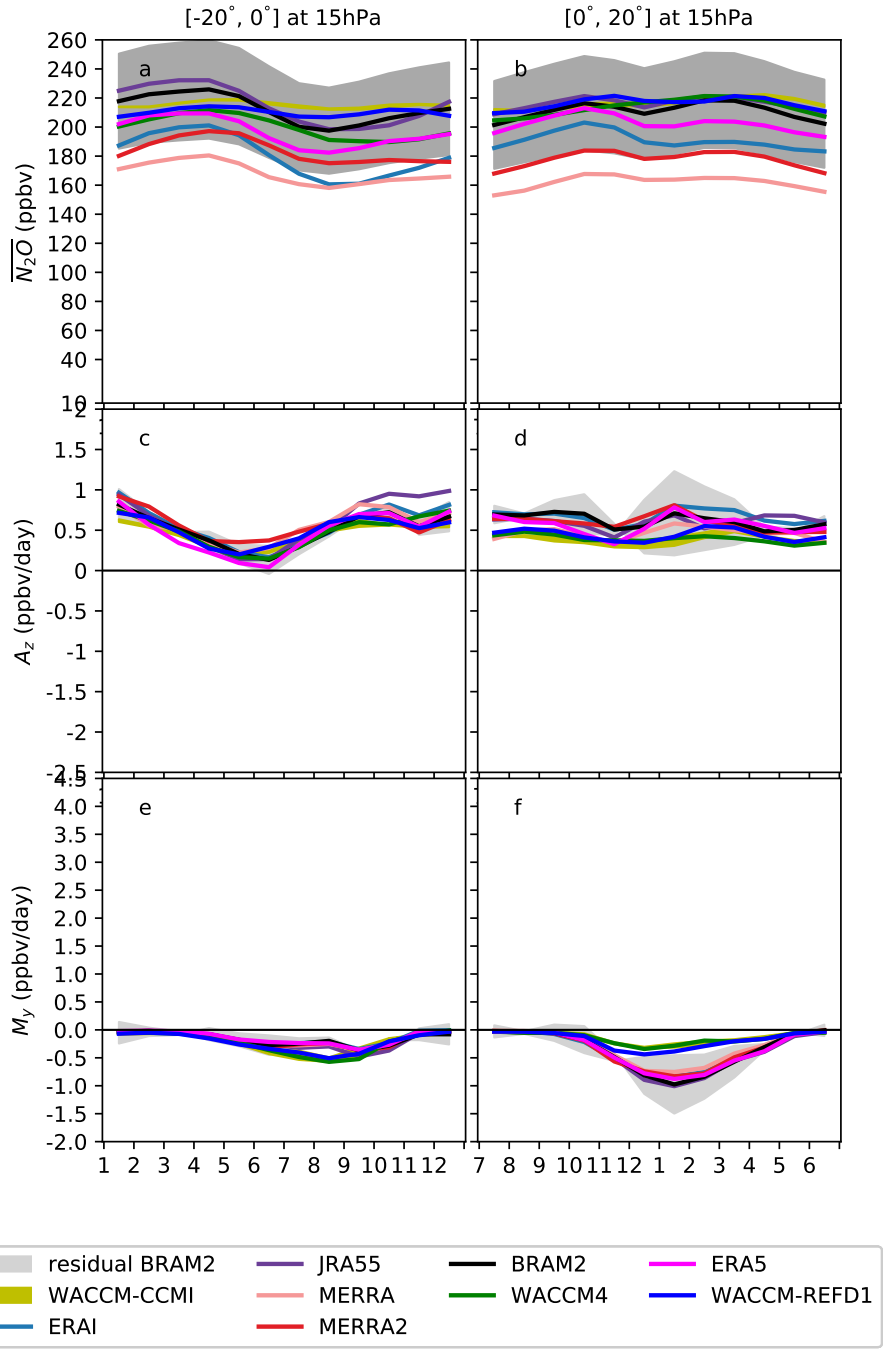

Figure 6.5: As Fig. 9 of the previous Section, with the addition of the BASCOE CTM simulation driven by ERA5 and the WACCM-REFD1 realization.

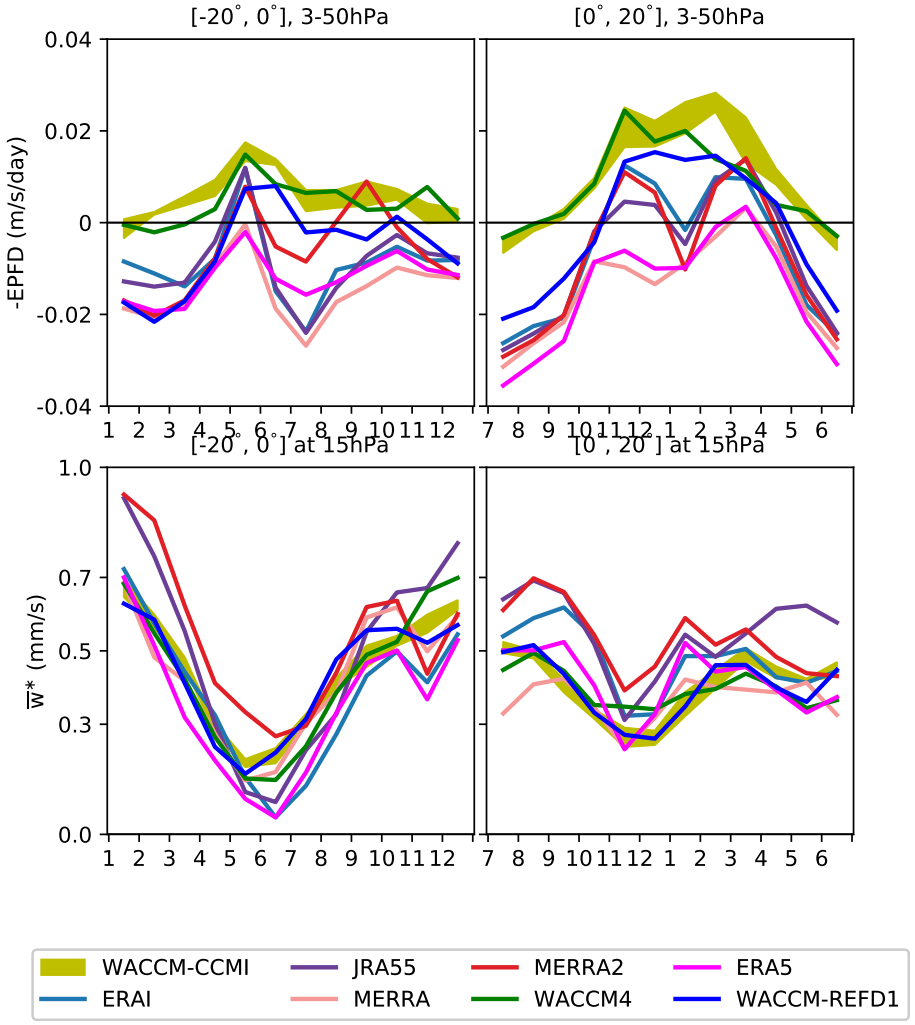

Figure 6.6: As Fig. 10 of the previous Section, with the addition of the BASCOE CTM simulation driven by ERA5 and the WACCM-REFD1 realization.

7 Decadal changes of N_2O and impact of BDC

This Chapter addresses the main objective of this thesis: it investigates the interannual variability of N_2O in the stratosphere and evaluates the impact of the stratospheric transport on its changes. The present Chapter is divided as follows: Section 7.1 investigates the decadal N_2O changes in the stratosphere and relates them to changes in the stratospheric transport and was submitted to the Journal of Geophysical Research (JGR): Atmospheres; Section 7.2 contains additional elements of discussion that were not selected for publication in Sect. 7.1.

7.1 N_2O rate of change as a diagnostic of the Brewer-Dobson Circulation in the stratosphere

This Section investigates the decadal changes of the N_2O stratospheric volume mixing rations and columns from ground-based (FTIR) and satellite (ACE-FTS) observations, and compares them with model simulations from the BASCOE CTM driven by ERAI, ERA5, MERRA and JRA55 and with the climate model simulations WACCM-REFD1 and WACCM-REC1. This Section was submitted in December 2021 to the peer-reviewed Journal of Geophysical Research Atmospheres and is available through the public repository Earth and Space Science Open Archive (ESSOAr):

Minganti, D., Chabrillat, S., Errera, Q., Prignon, M., Kinnison, D.E., Garcia, R.R., Abalos, M., Alsing, J., Schneider, M., Smale, D., Jones, N., Mahieu, E. (2022). N2O rate of change as a diagnostic of the Brewer-Dobson Circulation in the stratosphere, Journal of Geophysical Research: Atmospheres, under review, `https://doi.org/10.1002/essoar.10510213.1`

N_2O rate of change as a diagnostic of the Brewer-Dobson Circulation in the stratosphere

Daniele Minganti [1], Simon Chabrillat [1], Quentin Errera [1], Maxime Prignon [2*], Douglas E. Kinnison [3], Rolando R. Garcia [3], Marta Abalos[4], Justin Alsing[59], Matthias Schneider [6], Dan Smale [7], Nicholas Jones [8], Emmanuel Mahieu [2]

[1]Royal Belgian Institute for Space Aeronomy, BIRA-IASB, Brussels, Belgium
[2]Institute of Astrophysics and Geophysics, UR SPHERES, University of Liège, Liège, Belgium
[3]National Center for Atmospheric Research, Boulder, CO, USA
[4]Universidad Complutense de Madrid, Madrid, Spain
[5]Oskar Klein Centre for Cosmoparticle Physics, Department of Physics, Stockholm University, Stockholm SE-106 91, Sweden
[6]Karlsruhe Institute of Technology, Karlsruhe, Germany
[7]National Institute of Water and Atmospheric Research, Lauder, New Zealand
[8]School of Chemistry, University of Wollongong, Wollongong, Australia
[9]Imperial Centre for Inference and Cosmology, Department of Physics, Imperial College London, Blackett Laboratory, Prince Consort Road, London SW7 2AZ, UK

Key Points:

- The poor sampling of the Atmospheric Chemistry Experiment Fourier Transform Spectrometer exaggerates the stratospheric nitrous oxide trends
- Decadal trends of nitrous oxide are less significant in the northern extratropics due to a larger short-timescale variability of transport
- The Transformed Eulerian Mean analysis shows that the residual advection contributes to the positive nitrous oxide trends over the Tropics

*Currently at: Department of Earth, Space and Environment, Chalmers University of Technology, 41296, Gothenburg, Sweden

Corresponding author: Daniele Minganti, daniele.minganti@aeronomie.be

Abstract

The Brewer-Dobson Circulation (BDC) determines the distribution of long-lived tracers in the stratosphere; therefore, their changes can be used to diagnose changes in the BDC. We investigate decadal (2005-2018) trends of nitrous oxide (N_2O) stratospheric columns (12-40 km) as measured by four Fourier transform infrared (FTIR) ground-based instruments and by the Atmospheric Chemistry Experiment Fourier Transform Spectrometer (ACE-FTS), and compare them with simulations by two models: a chemistry-transport model (CTM) driven by four different reanalyses, and the Whole Atmosphere Chemistry-Climate Model (WACCM). The limited sensitivity of the FTIR instruments can hide negative N_2O trends in the mid-stratosphere because of the large increase in the lowermost stratosphere. When applying the ACE-FTS sampling on model datasets, the reanalyses by the European Centre for Medium Range Weather Forecast (ECMWF) compare best with ACE-FTS, but the N_2O trends are consistently exaggerated. Model sensitivity tests show that while decadal N_2O trends reflect changes in transport, these trends are less significant in the northern extratropics due to the larger variability of transport over timescales shorter than two years in that region. We further investigate the N_2O Transformed Eulerian Mean (TEM) budget in three model datasets. The TEM analysis shows that enhanced advection affects the stratospheric N_2O trends more than changes in mixing. While no ideal observational dataset currently exists, this model study of N_2O trends still provides new insights about the BDC and its changes thanks to relevant sensitivity tests and the TEM analysis.

Plain Language Summary

The circulation in the stratosphere is characterized by upward motion above the Tropics, followed by poleward and downward motions above the high latitudes. Changes in the pattern of this stratospheric circulation are currently a challenging topic of research. We investigate the decennial changes of this stratospheric circulation using observations and numerical simulations of the long-lived tracer nitrous oxide. Observations are obtained from ground-based and satellite instruments. Numerical simulations include complex atmospheric models that reproduce the chemistry and dynamics of the stratosphere. Both observations and models show differences between the hemispheres in the nitrous oxide decennial changes. Unfortunately, the current observations of nitrous oxide are not perfect. The ground-based instruments cannot correctly measure the changes of nitrous oxide in the northern hemisphere. The satellite does not measure at all times, and it spatially covers more the high latitudes, which negatively affects the measurements of nitrous oxide. On the other side, model simulations can provide valuable insights into the changes in the stratospheric circulation. They show that changes in the stratospheric circulation cause the differences between hemispheres in the nitrous oxide tendencies. In addition, the model simulations show that the circulation changes can be associated with different physical contributions.

1 Introduction

Nitrous oxide (N_2O) is continuously emitted in the troposphere, with a nearly constant rate of change of 2% per decade, and transported into the stratosphere, where it is destroyed by photodissociation mainly in the Tropics (Tian et al., 2020). The atmospheric lifetime of N_2O is approximately 120 years, which makes it an excellent tracer for stratospheric transport studies (Seinfeld & Pandis, 2016). Changes in ozone abundances have been studied and attributed to chemical and dynamical contributions (Petropavlovskikh et al., 2019). Recently, Ball et al. (2018) discussed positive ozone trends in the lower stratosphere and attributed them to changes in transport. However, the ozone distribution in the middle and upper stratosphere is largely impacted by changes in its chemistry. Hence,

long-lived tracers as N_2O are more relevant than ozone to investigate transport changes with little interference from the chemistry.

The transport in the stratosphere is enabled by the Brewer-Dobson Circulation (BDC), a wave-driven circulation that consists of upwelling in the Tropics followed by poleward transport and downwelling in the extratropics (Plumb, 2002). For tracer transport, the BDC is often separated into an advective component, the residual meridional circulation, and a quasi-horizontal mixing component (Shepherd, 2007). The BDC has a significant impact in determining the stratospheric distribution of chemical tracers, like ozone and greenhouse gases (GHGs), and in the momentum and heat budgets of the stratosphere (e.g., Butchart, 2014).

Long-term changes in the BDC could have significant impacts on the climate system. One of the most important is the effect on the recovery of stratospheric ozone, as a changing BDC would result in changes of the meridional distribution of ozone (e.g., Shepherd, 2008; Dhomse et al., 2018). The lifetime of Ozone Depleting Substances (ODS) in the stratosphere is also impacted by changes in the BDC (Butchart & Scaife, 2001; Waugh & Hall, 2002), as well as the water vapor entering the stratosphere in the Tropics (e.g., W. Randel & Park, 2019). The troposphere is also impacted by the BDC changes in terms of mass exchange with the stratosphere (e.g., ozone, Meul et al., 2018), and of the harmful ultra-violet radiation reaching the surface (Meul et al., 2016).

Understanding the changes in the BDC is thus fundamental to fully comprehend the past and future evolution of climate. Simulations by Chemistry-Climate Models (CCMs) robustly project an acceleration of the BDC throughout the stratosphere in recent and coming decades due to the increase of GHGs (e.g., Hardiman et al., 2014; Abalos et al., 2021). On the other hand, Oberländer-Hayn et al. (2016) argue that the global BDC trends in the lower stratosphere in CCMs are caused by a lift of the tropopause in response to global warming rather than an actual speedup of the circulation. Other modeling studies have shown that mixing also plays an important role in the simulated BDC changes, and is also the primary reason for the differences in the simulated BDC changes among CCMs (e.g., Eichinger et al., 2019). Recent studies have also shown that ODS, through their impact on ozone, play a significant role in the modeled BDC changes, and that ODS decreases resulting from the Montreal Protocol, will reduce the global warming-induced acceleration of the BDC (e.g., Polvani et al., 2019; Abalos et al., 2020).

The BDC can be quantified indirectly from measurements of long-lived tracers or temperature (e.g., Fu et al., 2015; Engel et al., 2009). Recently, Strahan et al. (2020) used ground-based observations of nitric acid and hydrogen chloride to investigate hemispheric-dependent BDC changes in the stratosphere. The Age of Air (AoA) is a widely used diagnostic for stratospheric transport, and is defined as the transit time of an air parcel from the tropical tropopause (or the surface, depending on the definition) to a certain point of the stratosphere (Waugh & Hall, 2002). Engel et al. (2017) used balloon-borne observations of carbon dioxide and methane to derive mean AoA trends above the northern mid-latitudes in the mid-lower stratosphere. They found positive but not statistically significant AoA trends over about 40 years (corresponding to a slowdown of the BDC), which is in contrast with model results that anticipate a significant acceleration of the BDC. These discrepancies can be partly attributed to the temporal and spatial sparseness of the measurements and to uncertainties in the AoA trends derived from real tracers (Garcia et al., 2011; Fritsch et al., 2020).

Satellite measurements of long-lived tracers have been used to compute AoA trends as well (e.g., Stiller et al., 2012; Haenel et al., 2015). These observational studies using remote sensing measurements have shown a hemispheric asymmetry in the AoA trends over the last decade, with positive changes in the Northern Hemisphere (NH) and a negative change in the Southern Hemisphere (SH) (e.g., Mahieu et al., 2014; Stiller et al., 2017; Fu et al., 2019). However, the mean AoA indirectly obtained from satellite mea-

surements does not allow the separation between residual advection and mixing, which was proven to be important in CCMs (Dietmüller et al., 2018). The recent study of von Clarmann and Grabowski (2021) proposes an alternative method to infer the stratospheric circulation from satellite measurements of long-lived tracers by a direct inversion of the continuity equation. When studying BDC trends, it is crucial to consider time scales longer than around 12 years, as the natural variability of the BDC can mask trends computed over shorter periods (Hardiman et al., 2017).

Reanalysis datasets try to fill the gap between observations and free-running models, providing a global multi-decadal and consistent state of the past atmosphere by assimilating available observations. Dynamical fields from reanalyses can be used to drive Chemistry-Transport Models (CTMs) to simulate the distribution of real and synthetic tracers in the atmosphere. In the past decade, these CTMs experiments have been used to investigate BDC changes in reanalyses, providing similar results as the satellite measurements for decadal time scales, as first shown by Monge-Sanz et al. (2013). However, recent studies have shown significant differences in BDC changes obtained from different reanalyses, especially over decadal time scales (e.g., Chabrillat et al., 2018). Furthermore, the computation of AoA largely depends on whether the velocities or the heating rates are used to drive the CTMs, leading to significant differences within the same reanalysis (Ploeger et al., 2019).

Minganti et al. (2020, hereafter M2020) investigated the climatology of stratospheric N_2O and its Transformed Eulerian Mean (TEM) budget in a CCM and in a CTM driven by dynamical reanalyses. The TEM diagnostic allows separating the effects of transport and chemistry on the rate of change of a stratospheric tracer such as N_2O (Andrews et al., 1987; W. J. Randel et al., 1994). Within the TEM framework, the impact of transport can be further separated into the impact from the residual mean advection and mixing, as was done for ozone in Abalos et al. (2013). In this study, we aim to investigate multi-decadal and decadal changes of stratospheric N_2O and the impact of the BDC on those changes in both observations and model simulations. We use ground-based observations of N_2O from Fourier transform infrared (FTIR) spectrometers that are part of the Network for the Detection of Atmospheric Composition Change (NDACC) at four stations in the SH and NH subtropics as well as at mid-latitudes (De Mazière et al., 2018, `http://www.ndaccdemo.org/`). We compare these FTIR observations with satellite measurements from the Atmospheric Chemistry Experiment Fourier Transform Spectrometer (ACE-FTS, P. Bernath et al., 2021). Contrary to M2020, who used the chemical reanalysis of N_2O measured by the Aura Microwave Limb Sounder (MLS) within their comparison (Errera et al., 2019), we cannot use such reanalysis because of the drift in the MLS N_2O dataset (Livesey et al., 2021).

We use four modern reanalyses that are part of the SPARC (Stratosphere-troposphere Processes and their Role in Climate) Reanalysis Intercomparison Project (S-RIP, Fujiwara et al., 2017). These reanalyses drive simulations of the Belgian Assimilation System for Chemical ObsErvation Chemistry-Transport Model CTM (BASCOE CTM, Chabrillat et al., 2018). We compare the observations and the BASCOE CTM simulations with the Whole Atmosphere Community Climate Model (WACCM) version 4 (Garcia et al., 2017) and version 6 (Gettelman et al., 2019).

The present study is structured as follows. Section 2 describes the observational and modeling datasets used in this study, as well as the TEM diagnostics and the regression model used to derive linear trends. In Section 3, we use FTIR observations to evaluate the trends in the N_2O stratospheric columns obtained from satellite measurements and models. In Section 4, using ACE-FTS as a reference, we study the global N_2O trends in the stratosphere and focus on the differences in the trend patterns among datasets. In Section 5, we investigate the N_2O TEM budget for two BASCOE simulations and WACCM version 6 in order to separate the impact of the residual advection and mixing on the

177 N_2O trends. Finally, Section 6 concludes the study with a summary of the principal find-
178 ings.

179 2 Data and Methods

180 This section describes the observational and model data as well as the methods used
181 in this study (see Tables 1 and 2). Throughout the study, we will refer to the CCMs and
182 the BASCOE CTM simulations as "models" to distinguish them from the observations
183 obtained from the FTIR and ACE-FTS. For the sake of brevity, we refer to M2020 for
184 a more detailed description of the dataset (BASCOE CTM, WACCM version 4, and S-
RIP reanalyses) and methods (TEM framework) already used there.

Dataset name	Full Name	Reference	Year range	Vertical resolution
WACCM-REFC1	Whole Atmosphere Community Climate Model	Garcia et al. (2017)	1985-2018	L66, 5.96 10^{-6} hPa
WACCM-REFD1	Whole Atmosphere Community Climate Model	Gettelman et al. (2019)	1985-2018	L70, 5.96 10^{-6} hPa
CTM+ERAI	ECMWF Reanalysis Interim	Dee et al. (2011)	1985-2018	L60, 0.1 hPa
CTM+ERA5	ECMWF Reanalysis 5	Hersbach et al. (2020)	1985-2019	L86, 0.01 hPa
CTM+JRA55	Japanese 55-year Reanalysis	Kobayashi et al. (2015)	1985-2018	L60, 0.2 hPa
CTM+MERRA2	Modern-Era Retrospective analysis for Research and Applications	Gelaro et al. (2017)	1985-2018	L72, 0.01 hPa
ACE-FTS	Atmospheric Chemistry Experiment Fourier Transform Spectrometer	P. Bernath et al. (2021)	2005-present	L42, 150 km

Table 1. Overview of the models and satellite measurements used in this study.

Station name	Reference	Location (lat and lon)	Altitude	strato DOFS
Lauder	Zhou et al. (2019)	45.4°S and 169.68°E	370 m	2
Wollongong	Griffith et al. (2012)	34.45°S and 150.88°E	30 m	2
Izãna	García et al. (2021)	28.30°N and 16.48°E	2367 m	1.5
Jungfraujoch	Zander et al. (2008)	46.55°N and 7.98°E	3580 m	1.1

Table 2. Overview of FTIR stations considered in this study.

185

186 2.1 Ground-based FTIR Observations

187 We use ground-based measurements of stratospheric N_2O columns obtained at four
188 stations that are part of NDACC: Lauder (New Zealand, 45°S), Wollongong (Australia,
189 34°S), Izãna(Spain, 28°N) and Jungfraujoch (Switzerland, 46°N) (Zhou et al., 2019). The
190 FTIR technique allows the acquisition of long-term consistent ensembles of very high-
191 resolution solar absorption spectra under clear-sky conditions. The stations have been
192 chosen at the mid-latitudes and subtropics where the observed BDC changes are the largest
193 (e.g., Engel et al., 2017; Strahan et al., 2020).

At Jungfraujoch, measurements have been obtained from two spectrometers: an instrument developed at the University of Liège (1984-2008), and a Bruker IFS 120HR (early 1990's-present) (Zander et al., 2008; Prignon et al., 2019). In this study, we use the Bruker spectrometer to investigate the most recent period. Ground-based measurements of N_2O profiles at Lauder started in 2001 with a Bruker 120HR spectrometer, replaced in 2018 (with 6 months overlap) by a Bruker 125HR (Strong et al., 2008; Zhou et al., 2019). The Lauder station is particularly relevant as is the only FTIR site of NDACC located in the SH mid-latitudes. The Wollongong station has provided data for the SH subtropics since 1996. Solar spectra were measured with a Bomem instrument until 2007, which was then replaced by a Bruker 125HR (Griffith et al., 2012). N_2O profiles are also measured at the IzãnaObservatory since 1999. This high-altitude station is characterized by excellent conditions for FTIR spectroscopy, with clear sky conditions for most of the year. Observations started using a Bruker 120M spectrometer and continued, since 2005, with a Bruker 125HR (García et al., 2021). The retrieval code for the N_2O profiles is the SFIT-v4 (v0.9.4.4) for the Jungfraujoch, Lauder and Wollongong stations, and PROFITT9 for the Izãnastation (Zhou et al., 2019).

We consider stratospheric N_2O columns between 12 and 40 km because the instruments at all stations are the most sensitive to the measured N_2O profiles over that layer (not shown). The degrees of freedom for signal (DOFS), which quantify the vertical resolution of the measurement (Rodgers, 2000), largely vary among the stations. For N_2O, the stratospheric DOFS between 12 and 40 km of the instruments above the SH are around 2, allowing the separation of two stratospheric layers. On the other hand, the stratospheric DOFS of the instruments above the NH are around 1.5 for Izãna, and 1 for Jungfraujoch, limiting the analysis to one stratospheric layer between 12 and 40 km. Thus, in order to perform a fair comparison, we compute one stratospheric N_2O column between 12 and 40 km for all stations.

2.2 Spaceborne Measurements - ACE-FTS

ACE-FTS, onboard the SCISAT Canadian satellite, was launched in August 2003 on a high inclination (74°) low earth orbit (650 km) and is still in operation in 2021 (P. F. Bernath et al., 2005; P. Bernath, 2017). ACE-FTS instrument measures the infrared absorptions from solar occultations between 2.2 and 13.3 μm with a spectral resolution of 0.02 cm^{-1}. This allows the retrieval of vertically resolved mixing ratio profiles for 44 molecules and 24 isotopologues from each measurement (P. Bernath et al., 2020).

In this study, we use version 4.1 of the ACE-FTS data. It differs from previous versions by significantly better retrievals at low altitudes and led to substantially improved trends compared to earlier version 3.5 (P. Bernath et al., 2021). For N_2O, previous comparisons of v3.6 with independent satellite instruments showed a good agreement below 35 km (within 10%) and larger biases above that level (within 20%, Sheese et al., 2017). In our study, N_2O profiles are filtered for outliers using the method described in Sheese et al. (2017) and are then vertically regridded to a constant pressure vertical grid using a mass-conservative scheme (Bader et al., 2017). When compared to ground-based measurements, ACE-FTS profiles are vertically interpolated to the grid of the FTIR data applying the averaging kernels of the FTIR retrieval as described in Langerock et al. (2015). For trend analysis, profiles are monthly averaged on latitude bins with 5°spacing from pole to pole.

In order to compare trend analysis of model simulations with those obtained by ACE-FTS, model datasets are first re-sampled as ACE-FTS (this is important in particular due to the low sampling of ACE-FTS - only 30 daily profiles due to the solar occultation method). This is done by finding model output adjacent it time to each ACE-FTS profile (BASCOE and WACCM datasets used in this study have, respectively, 6 hourly and daily output) and then by linearly interpolating the model values in time and space

at the profile geolocation. The re-sampled model datasets are then monthly averaged as done with ACE-FTS.

2.3 BASCOE CTM and Driving Reanalyses

In this study, we use the BASCOE CTM driven by four dynamical reanalyses: the European Centre for Medium-Range Weather Forecast Interim reanalysis (ERAI, Dee et al., 2011), and its newer version ERA5 (Hersbach et al., 2020), the Modern-Era Retrospective analysis for Research and Applications (MERRA2, Gelaro et al., 2017), and the Japanese 55-year Reanalysis (JRA55, Kobayashi et al., 2015). In the following, we provide a brief overview of the CTM and the ERAI, MERRA2 and JRA55 reanalyses, because those datasets are already described in a number of companion studies (Chabrillat et al., 2018; Prignon et al., 2019, 2021, M2020). On the other hand, we provide a more detailed description of ERA5, as is the newest reanalysis in this study.

The BASCOE CTM is built on a kinematic transport module (that takes in input the surface pressure and the horizontal winds) with a flux-form semi-Lagrangian (FFSL) advection scheme (S.-J. Lin & Rood, 1996). The FFSL scheme is run on a common horizontal grid of 2°x2.5°for all the reanalyses, while the vertical grid depends on the input reanalysis. The chemical scheme explicitly solves for stratospheric chemistry, and includes 65 chemical species and 243 reactions (Prignon et al., 2019). ERAI and JRA55 have 60 levels up to 0.1 hPa, MERRA2 has 72 levels up to 0.01 hPa. The model setup, as well as the boundary conditions, are the ones used in Prignon et al. (2019), M2020 and Prignon et al. (2021). Refer to Chabrillat et al. (2018) for a detailed description of the BASCOE CTM and its driving by the ERAI, JRA55 and MERRA2 reanalyses.

The ERA5 reanalysis is the fifth generation of reanalysis produced by the ECMWF and covers the 1979-present period, with a programmed extension back to 1950 (Hersbach et al., 2020). The horizontal resolution is 31 km, with hourly output frequency, and the vertical grid ranges from the surface to 0.01 hPa with 137 levels and with 300-600 m vertical spacing in the troposphere and stratosphere, which increases to 1-3 km above 30 km. ERA5 suffers from a cold bias in the lower stratosphere from 2000 and 2006. For this reason, a new analysis (ERA5.1) has been produced for that period to correct for that bias (Simmons et al., 2020). In this study, the BASCOE CTM was driven by ERA5.1 for the 2000-2006 period. For computational reasons, the vertical resolution is reduced to 86 levels from the original 137 keeping the original vertical spacing in the stratosphere, and we used 6-hourly (0000, 0600, 1200, 1800 UTC) data. As done for the other reanalyses, the ERA5 data on the fine 31-km grid were truncated at wavenumber 47 to avoid aliasing on the target 2.5°x2°horizontal grid (Chabrillat et al., 2018).

In order to investigate more the contribution of transport for ERA5, we performed two sensitivity tests with the BASCOE CTM driven by that reanalysis. In order to isolate the contribution of transport, the first sensitivity test consisted of a BASCOE CTM experiment where the N_2O does not increase over time. We accomplished that by performing a BASCOE CTM run exactly as the ERA5 simulation but keeping the N_2O volume mixing ratios at the surface fixed to their values at the beginning of the simulation (cst-N_2O run). Variations in the rate of change of N_2O for cst-N_2O are therefore due only to the effect of transport. The other sensitivity test is complementary to cst-N_2O, and consists of an experiment where the transport does not change over time (cst-dyn). In order to include a complete Quasi Biennial Oscillation cycle (QBO, Baldwin et al., 2001), we used the years 2006 and 2007 from ERA5.1 and ERA5, respectively. Those years are unusual (but convenient) because the QBO lasted exactly 24 months (see the zonal wind data at Singapore `https://www.geo.fu-berlin.de/met/ag/strat/produkte/qbo/singapore.dat`). We used the dynamics of the year 2006 to simulate even years and from the year 2007 for odd years. All the N_2O changes simulated by cst-dyn are due to its constant increase at the surface.

2.4 WACCM

In this study, we use two versions of WACCM: version 4 (Marsh et al., 2013) and version 6 (Gettelman et al., 2019). WACCM version 4 (WACCM4) is the atmospheric component of the Community Earth System Model version 1.2.2 (CESM, Hurrell et al., 2013), which has been developed by the U.S. National Center of Atmospheric Research. It is the extended (whole atmosphere) version of the Community Atmosphere Model version 4 (CAM4, Neale et al., 2013). WACCM4 has a longitude-latitude grid of 2.5°x1.9°and 66 vertical levels from the surface to about 140 km altitude, with 1.1-1.75 km vertical spacing in the stratosphere. The physics of WACCM4 is the same as CAM4 and the dynamical core is a finite volume with a horizontal discretization based on a conservative flux-form semi Lagrangian (FFSL) scheme (S.-J. Lin, 2004). WACCM4 is not able to internally generate the QBO; thus, it is nudged towards observations of stratospheric winds (Matthes et al., 2010). In this study, we use the WACCM4 version included within the SPARC (Stratosphere-troposphere Processes And their Role in Climate) Chemistry-Climate Model Intercomparison phase 1 (CCMI-1, Morgenstern et al., 2017). In particular, we use the REFC1 experiments (WACCM-REFC1), which consist of simulations of the recent past (1960-2018) using state-of-the-art historical forcings and observed sea-surface temperatures (Morgenstern et al., 2017). Compared to the default WACCM4 version, WACCM-REFC1 includes important modifications of the treatment of heterogeneous chemistry and of the gravity waves parameterization, which ultimately improve the simulation of ozone above the Southern Hemispheric (Garcia et al., 2017). In this study, we use three realizations of the WACCM-REFC1 configuration for the 1985-2018 period.

Version 6 of WACCM (WACCM6) is the extension to the whole atmosphere of version 6 of CAM that is part of version 2 of CESM (Danabasoglu et al., 2020). The default horizontal resolution of WACCM6 is 0.9°x1.25°latitude-longitude, with 70 levels in the vertical from the ground to around 140 km, with vertical resolution similar to WACCM4. The transition from WACCM4 to WACCM6 involved several changes in the physics and chemistry that are described in Gettelman et al. (2019). WACCM6 is part of the Coupled Model Intercomparison Project Phase 6 (CMIP6, Eyring et al., 2016), and is used in the CCMI-2022 activity (i.e., the successor of CCMI-1, Plummer et al., 2021). Within CCMI-2022, we use the REFD1 WACCM6 experiments (WACCM-REFD1), i.e., a suite of hindcast experiments for the recent past (1960-2018) used to compare with observations. The REFD1 experiments use the databases for historical forcings and observed sea surface temperatures developed for the CMIP6. Although WACCM6 can internally produce the QBO, the REFD1 experiments require a nudged QBO towards observed winds to ensure synchronization with historical variability. In this study, we use one realization of the WACCM-REFD1 experiments for the 1985-2018 period.

2.5 TEM Diagnostics

For stratospheric tracers, the TEM diagnostics (Andrews et al., 1987) allows separating the impact of transport and chemistry on the zonal mean local rate of change of a tracer with mixing ratio χ:

$$\overline{\chi}_t = -v^*\overline{\chi}_y - w^*\overline{\chi}_z + e^{z/H}\nabla\cdot\mathbf{M} + \overline{S} + \overline{\epsilon}, \tag{1}$$

where χ represents N_2O, $\mathbf{M} = -e^{-z/H}(\overline{v'\chi'} - \overline{v'\theta'}\bar{\chi}_z/\bar{\theta}_z, \overline{w'\chi'} + \overline{v'\theta'}\bar{\chi}_y/\bar{\theta}_z)$ is the eddy flux vector, and (v^*, w^*) are the meridional and vertical components of the residual circulation, respectively. Overbars denote zonal means and prime quantities indicate deviations from it, while subscripts indicate partial derivatives. $H = 7\ km$ is the scale height, and $z \equiv -Hlog_e(p/p_s)$ is the log-pressure altitude, with the surface pressure $p_s = 10^5 Pa$. The S term is the net rate of change due to chemistry, defined as the difference between the production ($\bar{P}$) and loss ($\bar{L}$) rates $\bar{S} = \bar{P} - \bar{L}$. The $\bar{\epsilon}$ contribution

represents the residual of the budget, i.e., the difference between the actual rate of change of χ and the sum of the transport and chemistry terms on the right-side hand of Eq. 1.

The transport terms in Eq. 1 can be grouped as follows:

$$\overline{\chi}_t = ADV + MIX + \overline{S} + \bar{\epsilon}, \tag{2}$$

where $ADV = (-v^*\overline{\chi}_y - w^*\overline{\chi}_z)$ and $MIX = e^{z/H}\nabla \cdot \mathbf{M}$ represent the contribution of the residual advection and of the resolved mixing, respectively. We refer to M2020 for a more detailed description of the TEM framework applied to the N_2O mixing ratios in the stratosphere and for a comprehensive discussion of the contribution of each term to the N_2O budget.

2.6 Derivation of Trends with the Dynamical Linear Modelling Tool

In this study, we investigate decadal trends using the Dynamical Linear Modeling (DLM, Alsing, 2019). DLM is based on Bayesian inference and provides a number of possible models to analyze time series. Each model is characterized by some unknown parameters, and the DLM computes the posterior probability distribution of those parameters using a combination of Kalman filtering and Markov chain Monte Carlo method.

For a given atmospheric time-series y_t, a generic DLM model is composed of four components: a linear background trend, a seasonal cycle with 12- and 6-months periods, forcing terms decribed by a number of regressor variables and an auto-regressive component:

$$\begin{aligned} y_t \quad = \quad & \beta_{1,t}z_{1,t} + \beta_{2,t}z_{2,t} ... + \beta_{n,t}z_{n,t} \\ & + \beta^{12}_{1,t}\sin(2\pi t/12) + \beta^{12}_{2,t}\cos(2\pi t/12) \\ & + \beta^{6}_{1,t}\sin(2\pi t/6) + \beta^{6}_{2,t}\cos(2\pi t/6) \\ & + \mu_t \\ & + z^{AR}_t \\ & + \epsilon_t. \end{aligned} \tag{3}$$

In Eq. 3, the terms $\beta_{i,t}z_{i,t}$ represent the contribution to y_t from each of the regressors. The 6- and 12-months seasonal cycles are modeled respectively by $\beta^{6}_{1,t}\sin(2\pi t/6)+\beta^{6}_{2,t}\cos(2\pi t/6)$ and $\beta^{12}_{1,t}\sin(2\pi t/12)+\beta^{12}_{2,t}\cos(2\pi t/12)$. The μ_t term denotes the linear fit term, and z^{AR}_t the auto-regressive term, defined similarly to the Cochrane-Orcutt correction (Kyrölä et al., 2013), and ϵ_t is the uncertainty.

Contrarily to a multi-linear regression (MLR) model, the background linear fit μ_t and the amplitudes of the seasonal cycles $\beta^{6,12}_{i,t}$ in DLM can vary with time (i.e., they are non-parametric). Their degrees of time-dependence are the unknown model parameters and are initially set by the user and inferred from the data during the model run. Furthermore, the auto-regressive process in the DLM is computed within the model run together with the other parameters, not as a post-run correction as done in the MLR, and its uncertainties are carefully taken into account within the error propagation. In addition, the standard DLM implementation has time-varying (heteroscedastic) uncertainty distribution, when time-varying uncertainties are available. DLM was recently used to investigate stratospheric ozone trends in observations and models (Ball et al., 2017, 2018). A more detailed description of the DLM models and their implementation can be found in Laine et al. (2014). For a more comprehensive review of time-series analysis using DLM, refer to Durbin and Koopman (2012).

As regressor variables, we used the 30 cm radio flux as a solar proxy (de Wit et al., 2014), an index for the El-Nino Southern Oscillation (Wolter & Timlin, 2011) from the National Oceanic and Atmospheric Administration (`http://www.esrl.noaa.gov/psd/`

enso/mei/), and two indices for the QBO at 30 and 50 hPa from the Freie Universität Berlin (http://www.geo.fu-berlin.de/en/met/ag/strat/produkte/qbo/index.html). We fed the DLM model with monthly data, running 3000 samples where the first 1000 were considered as a warmup and discarded. We also tried 10000 realizations and 3000 as warmup with very similar results (not shown). We performed several sensitivity tests to determine the appropriate values of the initial model parameters, i.e., the degree of time-dependence of the linear trend and seasonal cycles, in order to allow a reasonable time-dependence without being unrealistic. The different combinations of these values did not provide significant differences, so we kept the recommended values.

The linear trends are computed from the distribution of the fit samples as the difference of the model realizations between the end and start dates of the period considered (delta), weighted by the number of the years considered. The uncertainties associated with the trend are computed as the percentage of the delta values that are positive (negative). This percentage can be interpreted as the posterior probability that the overall change in the fit is positive (negative) between the considered dates. In this way, we do not make any assumption on the shape of the distribution of the trends. In this study, we show three values of the posterior probability, 80, 90 and 95 %.

3 Stratospheric N_2O Columns and their Trends

Figure 1 shows the monthly linear fits of the N_2O stratospheric columns (12-40 km) at the four FTIR stations, together with the initial N_2O columns for the observations and the ERA5 simulation. In this analysis, we do not apply the FTIR time sampling to the model outputs, because sensitivity tests using the WACCM-REFD1 outputs at each station showed no significant impact of the FTIR time sampling on the recovered trends of the N_2O columns (not shown). The stratospheric N_2O columns computed between 12 and 40 km of altitude are highly sensitive to the N_2O increase in the lower stratosphere, which is the result of the continuous growth in the troposphere (Tian et al., 2020; P. Bernath et al., 2020). Consequently, all datasets exhibit an increase in the stratospheric N_2O columns over the last two decades.

Above Lauder, the linear fit of the stratospheric N_2O columns from the ERA5 simulation is in agreement with the observations, similarly to JRA55 and ERAI. WACCM-REFD1 underestimates the N_2O stratospheric columns compared to the observations by around 10%, and performs worse than its earlier version WACCM-REFC1. At Wollongong, the slope of the linear fit of the N_2O columns measured by the FTIR, and to a lesser extent by ACE-FTS, is steeper before 2005 compared to the following period. This change of gradient is not visible in any of the model simulations. On the contrary, some of the models show a slower increase before 2005, followed by a more rapid increase.

Above Izãna, all the model simulations underestimate the stratospheric N_2O columns with respect to the FTIR observations, with the largest difference reaching 14% for MERRA2. Concerning ACE-FTS, the bias with FTIR measurements is around 8%, which is qualitatively consistent with the results of Strong et al. (2008), even though they used v2.2 of ACE-FTS. However, García et al. (2021) showed good agreement above Izãnafor tropospheric N_2O abundances and total N_2O columns obtained from independent measurements. The difference between the stratospheric N_2O columns measured by FTIR and ACE-FTS could be explained by the poor coverage of ACE-FTS over the tropical and subtropical regions. Since the ACE-FTS measurements represent a latitude band, the observed N_2O results biased towards the values measured at higher latitudes, where more occultations are available (Kolonjari et al., 2018). Since the N_2O abundances decrease poleward (Jin et al., 2009), this could explain the low bias in the stratospheric N_2O columns measured by ACE-FTS compared to those obtained from FTIR.

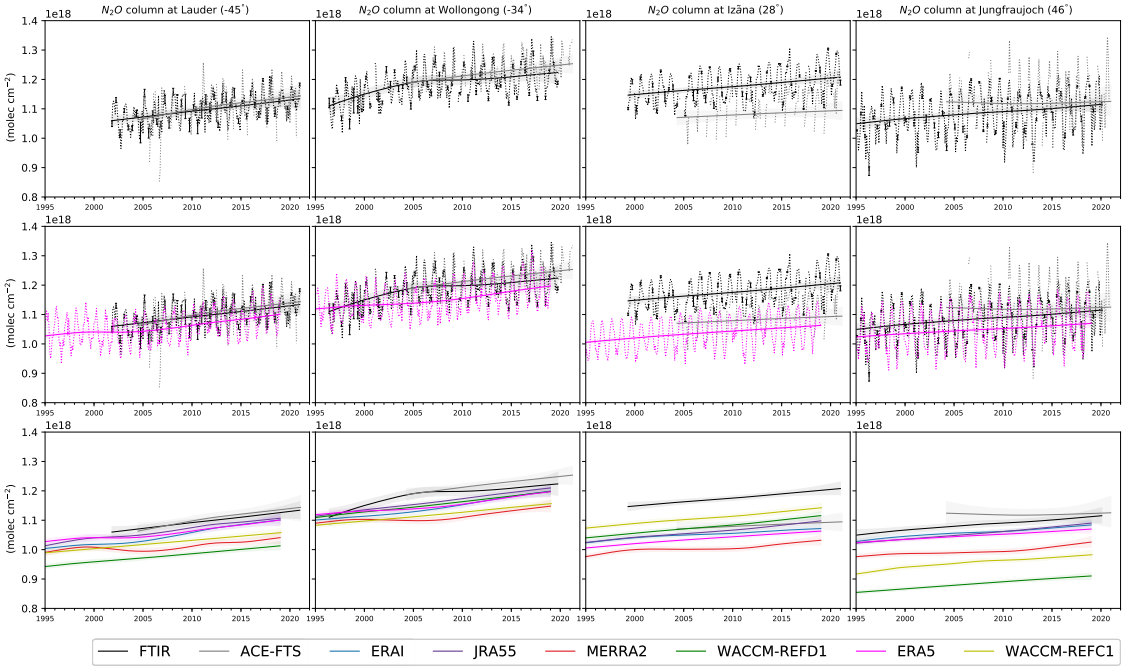

Figure 1. Time-series of N_2O stratospheric columns (12-40 km) from observations and models at four stations. Continuous lines show the linear fit obtained by the DLM regression, dashed lines depict the N_2O column data. The color code is shown in the legend. First row: DLM fits and data for FTIR and ACE-FTS measurements. Second row: DLM fits and data for FTIR and ACE-FTS measurements and the BASCOE simulation driven by ERA5. Third row: DLM fits for all the datasets considered. The model and satellite data are interpolated to the longitude and latitude of the station, and vertically regridded to match the retrieval layering schemes. After the regridding, the data were smoothed using the FTIR averaging kernels. The colored shadings represent the uncertainties from the 2.5 and 97.5 percentiles of the distributions from the DLM.

Above Jungfraujoch, there is the largest spread in the linear fits of the stratospheric N_2O columns, with differences reaching around 25% between ACE-FTS and WACCM-REFD1. Prignon et al. (2019) compared lower stratospheric columns of chlorodifluoromethane (HCFC-22) between an earlier WACCM version and FTIR measurements, and showed that WACCM consistently underestimates the HCFC-22 columns compared to the FTIR measurements. Since both N_2O and HCFC-22 (which has an atmospheric lifetime of 12 years, Prignon et al., 2019) are produced at the surface and transported into the stratosphere, this underestimation in WACCM could indicate a shortcoming in simulating the accumulation of long-lived tracers in the stratosphere above Northern mid-latitudes. Indeed, Angelbratt et al. (2011) already highlighted that the stratospheric transport has a large impact on the N_2O columns above Jungfraujoch compared to stations at higher latitudes. Regarding the observational datasets, there is a considerable disagreement between the FTIR instrument and ACE-FTS before 2012, showing increasing and decreasing N_2O columns, respectively. This is in contrast with the remarkably good agreement in the SH between the two datasets. This difference between the stratospheric N_2O columns in ACE-FTS and FTIR measurements will be further addressed in Sect. 4.

In the Tropics and above the lower stratospheric mid-latitudes, the N_2O mixing ratio is inversely proportional to the mean AoA (Galytska et al., 2019). The N_2O stratospheric columns at mid-latitudes considered here are highly sensitive to the N_2O abundances in the lower stratosphere, hence the inverse relationship also holds for the stratospheric N_2O columns above the mid-latitudes. Thus, the lower N_2O stratospheric columns in MERRA2 compared to the other datasets across the stations are consistent with the older mean AoA throughout the stratosphere found using MERRA2 by Chabrillat et al. (2018). The N_2O distribution in the stratosphere is opposite also to the total inorganic fluorine F_y. N_2O is emitted in the troposphere while F_y is produced in the stratosphere, and the transport due to the BDC tends to remove N_2O and increase F_y in the stratospheric mid-latitudes. In the light of this relationship between N_2O and F_y, the underestimated N_2O columns above Lauder and Jungfraujoch in MERRA2 are consistent with larger F_y stratospheric columns in MERRA2 compared to the other reanalyses above those stations (Prignon et al., 2021).

Figure 2 shows distributions of the trend of the stratospheric N_2O columns obtained from the respective linear fits over the common period 2005-2018. The N_2O trends at the surface have already been validated for a number of FTIR stations (including Lauder, Wollongong and Izãna) against observations from flask samples, showing an excellent agreement (Zhou et al., 2019).

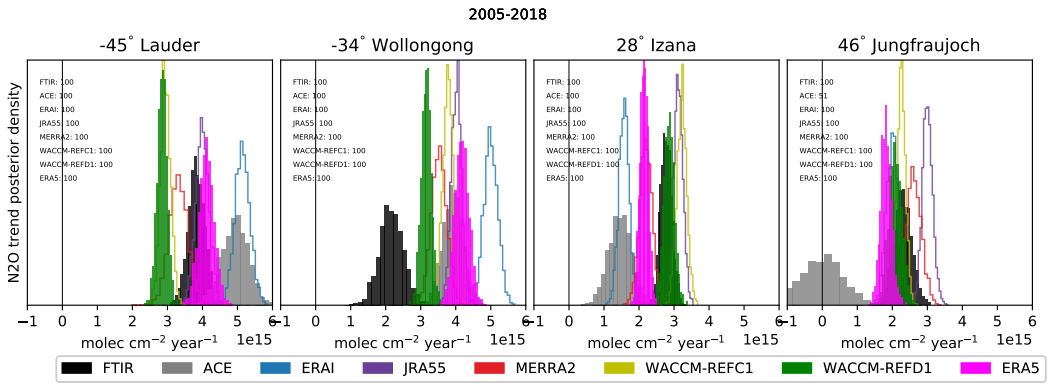

Figure 2. Posterior probability of positive changes of the DLM linear trend of the stratospheric N_2O columns (12-40 km) for the four FTIR stations (2005-2018). The color code is shown in the legend.

Above Lauder, the N_2O trends obtained with ERA5 are in good agreement with the FTIR measurements, but are underestimated in WACCM-REFD1 (around 25%) with no particular improvement with respect to WACCM-REFC1. At Wollongong, the N_2O trend obtained with the FTIR measurements is the smallest because the N_2O increase above that station is smoother compared to the other datasets. Interestingly, the N_2O trend simulated by WACCM-REFD1 is the closest to the trend obtained from the FTIR observations, while the trend obtained with ERA5 is almost twice as large. Above Izãna, WACCM-REFD1 agrees remarkably well with the FTIR (difference around 3%), while the trend from ERA5 lies between the trends measured from FTIR and ACE-FTS, with around 20% difference compared to FTIR. Above Jungfraujoch, the trend in the N_2O columns from WACCM-REFD1 agrees with the trend from the FTIR station within 10% difference and is similar to what is obtained with ERA5. The decreasing N_2O stratospheric column in ACE-FTS before 2012 results in a near-zero trend, which is in contrast with the trends obtained by the other datasets, which approximately range from 2 to 3×10^{15} molec cm^{-2} $year^{-1}$.

Considering decadal changes, the observations and the ERA5 simulation show larger trends of the stratospheric N_2O columns in the SH than in the NH, especially at mid-latitudes (respectively Lauder and Jungfraujoch). WACCM-REFD1 also shows this hemispheric difference at mid-latitudes, which is a clear improvement with respect to WACCM-REFC1. Those asymmetries are consistent with the results of Strahan et al. (2020), who found significantly negative AoA trends in the SH compared to the NH using HCl and HNO_3 measured at several ground-based FTIR stations. In addition, the hemispheric differences of the N_2O trends are also consistent with the results of Prignon et al. (2021), who found larger and more significant Fy trends above Jungfraujoch than above Lauder.

We conclude the section by providing a short description of the limits of using stratospheric columns of N_2O from FTIR measurements. As mentioned earlier, the stratospheric N_2O columns between 12 and 40 km are primarily influenced by the steady increase in the lowermost stratosphere. The DOFS of the FTIR instrument at Jungfraujoch for the stratosphere (12-40 km) is close to 1.1. Thus, the measurements cannot resolve more than one partial column between 12 and 40 km, which can hinder the detection of N_2O trends in the middle and upper stratosphere (i.e., above 30 km) because of the influence of the increase in the lowermost stratosphere. Indeed, it was shown that stratospheric N_2O trends over the last decades, obtained both from satellite measurements and model simulations, do not consist of just a global increase, but largely depend on latitude and height (e.g., Froidevaux et al., 2019). Therefore, we will consider latitudinal- and vertical-dependent trends of N_2O mixing ratios in the following section.

4 Global N_2O Linear Trends

Figure 3 shows latitude-vertical cross sections of the linear trends of the N_2O mixing ratios for the various datasets, over the 2005-2018 period. In order to perform a fair comparison, the model datasets are sampled in space and time as ACE-FTS before the computation of the trends. We use the ACE-FTS measurements as a reference, because they encompass this relatively long period with global coverage and good stability (P. Bernath et al., 2020, 2021).

In the upper stratosphere above 10 hPa, the N_2O trends from ACE-FTS are positive, with larger trends in the NH that are found significant at lower levels than in the SH. The ERAI-driven simulation qualitatively reproduces these patterns in the upper stratosphere, while the other model datasets differ from ACE-FTS, especially ERA5. A common feature among all datasets is an increase in N_2O above the Equator in the upper stratosphere, around 5 hPa. At those altitudes of the tropical pipe, the upward trans-

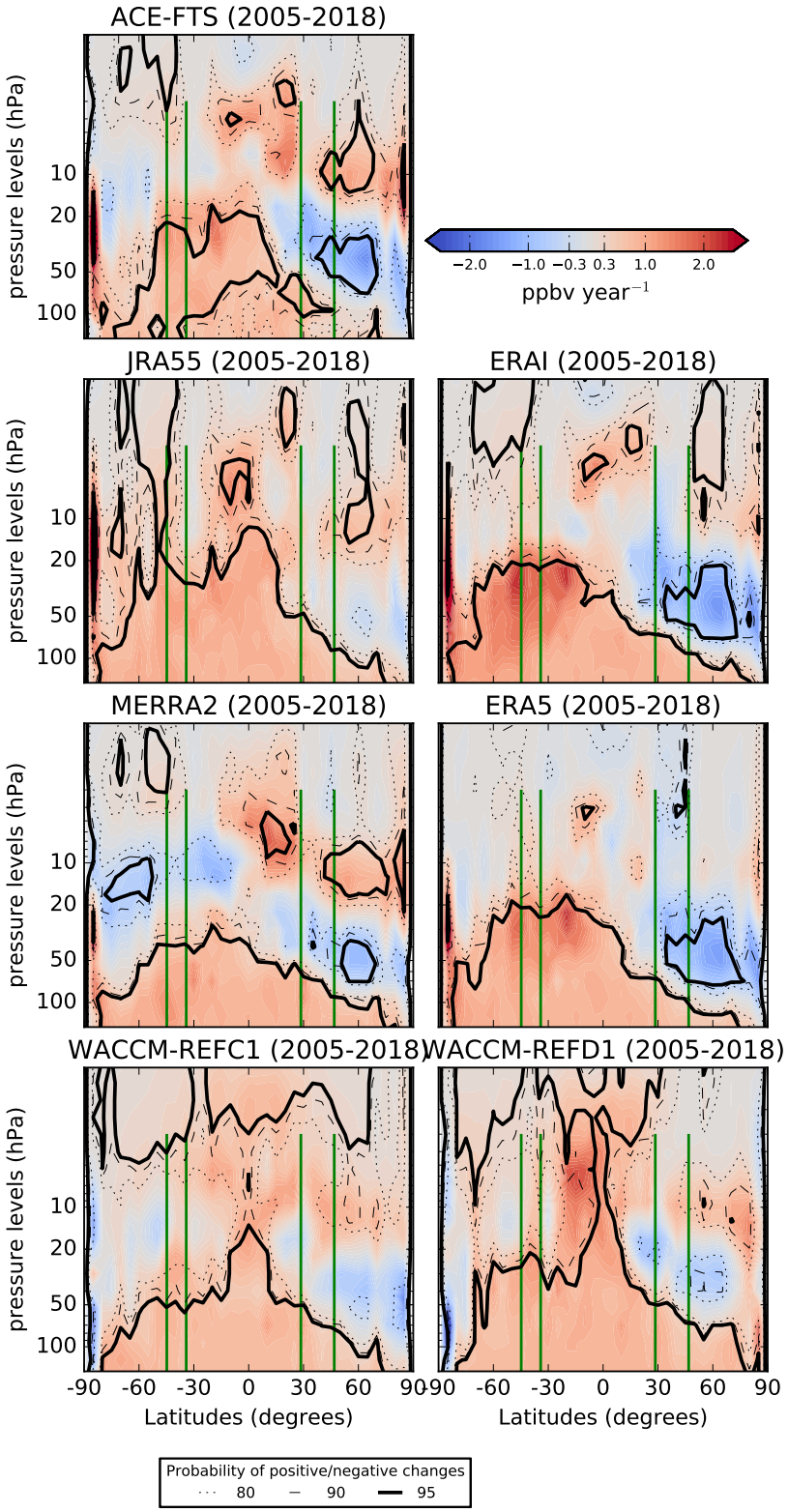

Figure 3. Latitude-pressure cross-sections of N_2O linear trends (pptv year^{-1}) obtained from the DLM (2005-2018). The N_2O simulated by the model is interpolated to the location and timing of the observations, see text for details. The dotted, dashed and continue lines represent the probability at 80, 90 and 95% of positive/negative N_2O changes respectively. The green vertical lines identify the position of the FTIR stations together with their vertical coverage.

port of N_2O by the mean advection reaches its maximum (see M2020). In the mid-lower stratosphere below 20 hPa, ACE-FTS shows a clear hemispherical asymmetry (meridional dipole) in the N_2O trends, with significantly negative values in the NH and significantly positive in the SH, that is generally reproduced by the models with ERAI and ERA5 delivering trends that are most similar to those derived from ACE-FTS.

Prignon et al. (2021) used the same simulations as the present study to investigate global stratospheric trends of total inorganic fluorine Fy. The dipoles obtained here in the N_2O trends from ACE-FTS and the ECMWF reanalyses are consistent with the opposite trends of Fy for almost the same period (Prignon et al., 2021). Above the location of Jungfraujoch (the most northern vertical green line), the negative N_2O trend detected by ACE-FTS in the mid-lower stratosphere is responsible for the disagreement with the FTIR observations discussed in the previous section, as the layer of the stratospheric N_2O column encompasses regions of both positive (lowermost and upper stratosphere) and negative (mid-lower stratosphere) N_2O trends. In the lowermost stratosphere (pressure larger than 100 hPa), all models and ACE-FTS show positive N_2O trends, resulting from the constant increase in the troposphere. However, the N_2O increase in the equatorial lowermost stratosphere is not significant in ACE-FTS, contrary to the model simulations.

Figure 4 shows the N_2O trends as in Fig. 3, but in the model space, i.e., the sampling from the observations is not applied. A comparison between each model simulation in the observation and model space (respectively Fig. 3 and Fig. 4) reveals large differences in the N_2O decadal trends. Generally, the sampling of the ACE-FTS observations enhances the trends simulated by the models, both in the negative and positive directions. For the ERA5 simulation, the significantly negative trend in the NH observational space becomes insignificant in model space. In addition, one notes immediately that the N_2O trends in the WACCM simulations change sign, with negative trends in the NH in the observational space becoming weakly positive in model space. However, this difference is not significant because neither of the trends above that region is statistically significant at 95%.

For satellite measurements, the impact of the sampling in the detection of trends in long-lived species (including N_2O) has been evaluated in Millán et al. (2016). They concluded that large errors may arise in the detected trends for coarse and non-uniform sampling obtained with occultation instruments (such as ACE-FTS), and that long time scales are required for a robust trend detection from these datasets. Such errors propagate to the models when they are sampled in space and time as the observations. In particular, within the DLM, the non-uniform time sampling considerably increases the standard deviation of the error in the time series, which is zero for regular time sampling. This difference plays a role when deriving trends over these relatively short (decadal) time scales. For example, the non-uniform ACE-FTS sampling applied to the ERA5 output results in negative N_2O trends that are 4 times stronger compared to the native grid above the northern mid-latitudes between 50 and 70 hPa. For WACCM, the issue of downsampling was also raised by Garcia et al. (2011) when comparing AoA trends obtained from balloon-borne observations and simulated by the model. They showed that sampling the model as the observations would deliver positive and non-significant AoA trends, similarly to the observations. We find consistent results with the WACCM simulations: sampling the WACCM output as the observations drives the N_2O trends towards the observed values. In addition, the non-significant negative N_2O trends simulated by WACCM are compatible with the non-significant positive AoA trends found by Garcia et al. (2011) when downsampling WACCM at the AoA observations. Hence, the ACE-FTS sampling exaggerates the simulated N_2O trends in the stratosphere.

In order to understand the actual trends and compare them with other modeling studies, we now focus on the N_2O trends obtained from the model datasets in model space (Fig. 4). We mentioned earlier that the mean AoA and the N_2O abundancies are inversely

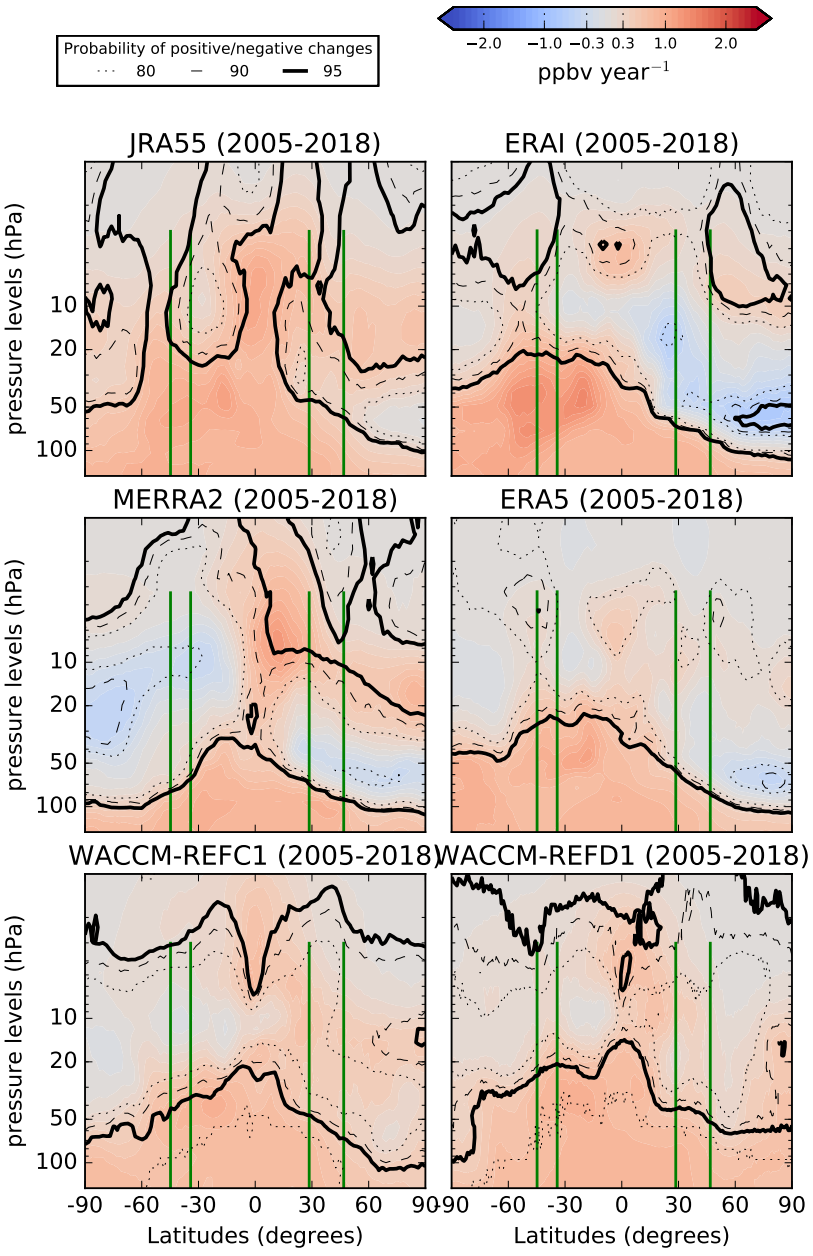

Figure 4. As in Figure 3, but in the model space.

correlated in the Tropics and above the lower stratospheric mid-latitudes. Thus, the stratospheric N_2O trends have opposite signs compared to trends of mean AoA. For ERAI, the meridional N_2O trend dipole is consistent with AoA trends derived over a shorter period with the same CTM (Chabrillat et al., 2018) and also with different CTMs (Ploeger et al., 2019; Han et al., 2019). ERAI shows positive N_2O trends in the upper stratosphere, around 5 hPa, above the Equator, which is consistent with the findings of Galytska et al. (2019) using the same reanalysis to drive a different CTM in that region, but ERA5 does not allow us to find any significant trend in the upper stratosphere. The ERA5 simulation confirms the meridional dipole in the mid-lower stratosphere of ERAI, and is consistent with recent AoA trend results over a shorter period (Ploeger et al., 2021).

Above the SH mid-latitudes in the mid-lower stratosphere, the N_2O trends obtained with MERRA2 are biased low compared to the other models, and do not replicate the hemispheric asymmetry that is visible in the ECMWF reanalyses. Wargan et al. (2018) have shown that the tropopause height has changed in MERRA2 in the past decades, with a decrease in the extratropics and an increase above the Tropics. The pattern of the N_2O trends in MERRA2 is qualitatively consistent with the changing tropopause height: a rise of the tropopause would lead to positive N_2O trends, while a sinking tropopause to negative N_2O trends. In addition, the N_2O trends with MERRA2 do not match the AoA trends obtained with the same CTM (Chabrillat et al., 2018), at least in the regions where the inverse relationship between N_2O and AoA holds (Galytska et al., 2019). Ploeger et al. (2019) found that AoA trends in the stratosphere for MERRA2 are opposite with their diabatic transport model than with our kinematic transport model. The large differences between JRA55 and MERRA2 and the ECMWF reanalyses highlight the fact that decadal changes in the stratospheric transport are not as robustly detected in JRA55 and MERRA2 as in the ERAI and ERA5. The WACCM simulations do not simulate the vertical and meridional gradients of the N_2O trends, especially compared to the CTM experiments driven by MERRA2 above the southern polar latitudes and by the ECMWF reanalyses above the northern polar latitudes, but rather a global N_2O increase that is largest in the lower stratosphere. This N_2O increase in the tropical lower stratosphere can be related to the AoA decrease due to the projected BDC acceleration in response to global warming (e.g., Butchart, 2014). However, WACCM-REFD1 improved the representation of the N_2O trends with respect to WACCM-REFC1 in the SH mid-latitudes. The newer WACCM version simulates significant N_2O increase up to 20 hPa, which makes the N_2O trends in the mid-lower stratosphere slightly more similar to the meridional dipole seen in ERAI and ERA5, even though the decreasing N_2O trends in the NH are not reproduced.

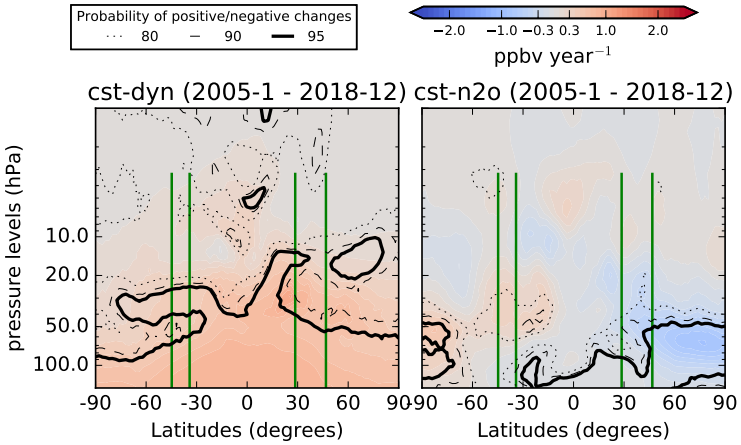

Figure 5. Latitude-pressure cross sections of N_2O linear trends (pptv year^{-1}) obtained from the DLM from a BASCOE run driven by ERA5 with fixed dynamics and increasing N_2O (left panel), and from the same model setup but with N_2O kept constant at the surface and time-varying dynamics (right panel).

The two sensitivity tests done with ERA5 (cst-dyn and cst-N_2O) are shown in Fig. 5. As expected, the cst-dyn experiment does not simulate any N_2O decrease in the stratosphere, showing only a steady N_2O increase as a consequence of the constant buildup at the surface. Between 30 and 50 hPa, the N_2O increase in the SH is significant with 95% probability, while this is not the case over the NH. This difference can be attributed to the larger variability of the NH over one QBO cycle compared to the SH due to its larger wave activity (Scaife & James, 2000), and was already shown for the significance of ozone trends (Shepherd, 2008). This highlights the importance of considering a sufficiently long period for the trend detection in the stratosphere (Garcia et al., 2011; Hardiman et al., 2017). In particular, the 14 years considered here are sufficient to propagate the N_2O increase to the mid-stratospheric mid-latitudes in the SH but not in the NH. The cst-N_2O sensitivity test confirms that the extratropical N_2O trends in the mid-lower stratosphere are due to the impact of changes in the stratospheric transport. Contrarily to the cst-dyn experiment, a changing dynamics impacts the sign of the obtained trends, with an N_2O decrease above the NH and increase in the SH. The mean stratospheric transport contributes to the hemispheric asymmetry through differences in the significance of the trends between the hemispheres, and the decadal changes in the transport contribute to the recovered trends through changes in their signs.

5 N_2O TEM Budget

This section further investigates the N_2O trends from the model simulations using the TEM budget. Equation 2 allows separating the contributions of the residual advection and mixing terms (respectively ADV and MIX) to the N_2O rate of change. In particular, we aim to identify the contributions from changes in the ADV and MIX terms to the N_2O trends shown in the previous section. To that end, we compute the changes of the ADV and MIX terms as the differences between their linear fits (i.e., the μ_t term of Eq. 3) at the end and the beginning of the considered period. A similar analysis was also done by the recent study of Abalos et al. (2020), who used the outputs of several CCMs to compute changes of the TEM budget terms of synthetic tracers. For a detailed description of the climatologies of the ADV and MIX terms, we refer to M2020.

We highlight that we do not aim to provide a quantitative analysis of the contributions of the changes of each transport term to the N_2O trends. The complete TEM budget also includes the chemistry term $\overline{S}$ (i.e., loss due to photolysis, Tian et al., 2020), which is large in the tropical mid-high stratosphere, and the residual term $\bar{\epsilon}$, which accounts for all the processes not resolved by the TEM analysis (Eq. 2). Here, we provide a qualitative estimate of the contributions from changes in the advection and mixing to the N_2O trends, by comparing the signs of the changes of ADV and MIX with those of the N_2O trends discussed in the previous section. Figure 6 shows the latitude-vertical cross sections of those changes in the ADV and MIX terms over the 2005-2018 period. We limit the analysis to the simulations by ERA5, WACCM-REFD1 and MERRA2 in order to investigate further the differences in their N_2O trends discussed in the previous section. In the following, we refer to N_2O trends discussed in the previous section as "direct" N_2O trends, in order to distinguish them from the N_2O changes derived from changes in the ADV and MIX contributions.

Looking at the changes in the ADV term in ERA5, the N_2O abundances increase in the tropical high stratosphere (between 4 and 10 hPa) because of the impact of advection, similarly to the weak positive direct N_2O trends above the same region. These changes are mainly due to an enhanced tropical upwelling over that region (not shown), and agree with a recent study showing a strengthening of the advective part of the BDC obtained from ERA5 over a longer period (Diallo et al., 2021). Above the lower stratospheric subtropics, the positive N_2O changes due to an enhanced ADV contribution are small but significant and can contribute to the positive direct N_2O trend above the SH. Such increased contribution from ADV above the lower stratospheric subtropics can be associated with the strengthening of the shallow branch of the BDC (P. Lin & Fu, 2013), which was recently detected in ERA5 using the AoA diagnostic (Ploeger et al., 2021).

Above the extratropical latitudes, the changes of the ADV term differ between the two hemispheres. Above the northern polar latitudes below 50 hPa, the negative changes of the ADV term can explain the negative direct N_2O trend and are consistent with the enhanced advection term over the tropical region. Above the southern mid-latitudes, the ADV term shows positive changes between 30 and 70 hPa. Over that region, N_2O-rich air is advected upward and southward from the lower tropical region (M2020 and their Supplement). Therefore, the positive ADV changes can indicate a strengthening of the residual advection over that region and can contribute to the positive direct N_2O trend, which is part of the hemispheric asymmetry described in the previous section.

Concerning the MIX term in ERA5, its changes are more irregular compared to those of the ADV term, and do not correspond to the direct N_2O trends over the NH. Above the SH between 10 and 30 hPa, there is enhanced poleward N_2O mixing from the subtropics (where MIX changes are negative), and increased N_2O abundances over the mid-latitudes (positive MIX changes). Such positive N_2O changes above the southern mid-latitudes can be associated with the positive but not significant direct N_2O trends over the same region. The role of mixing in the decadal BDC trends has been studied in ECMWF reanalyses, especially using AoA (e.g., Ploeger et al., 2015; Dietmüller et al., 2017). Recent studies have associated the N_2O trend dipole discussed in the previous section with a southward shift of the circulation pattern, which in turn is related to the impact of mixing on the BDC changes (Stiller et al., 2017; Ploeger et al., 2019). Our results with N_2O from ERA5 confirm the role of mixing processes above the southern mid-latitudes in determining changes in the N_2O abundances, and indirectly support the hypothesis of the southward shift of the circulation as the reason for the dipole structure. Considering AoA results, Ploeger et al. (2015) showed that mixing plays a major role in the SH in determining the negative AoA trend over the 2002-2012 period for ERAI, which is consistent with the impact of mixing on the positive N_2O changes in ERA5 outlined here.

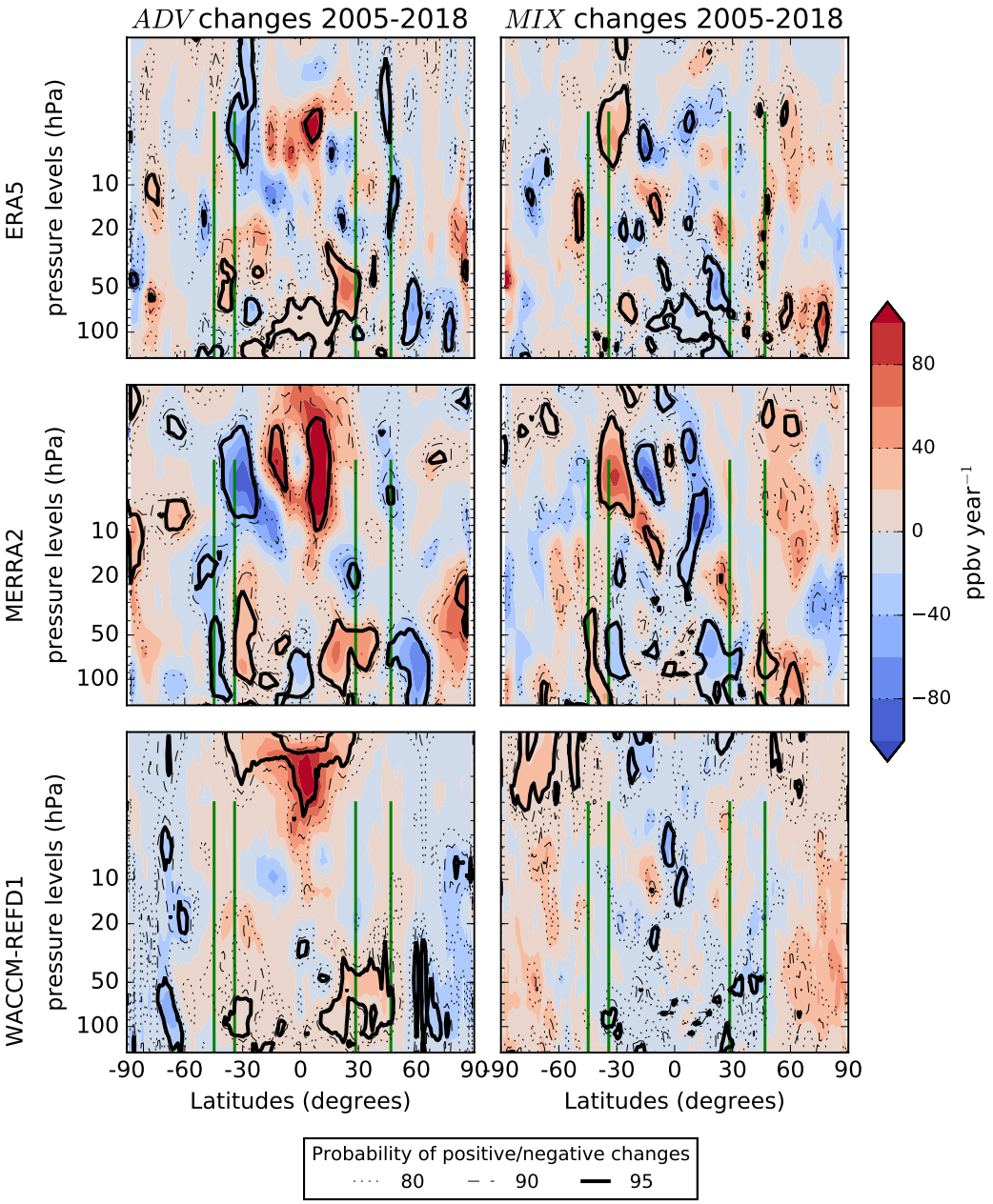

Figure 6. Latitude-pressure cross sections of the changes of the advection term (A_z+A_y, central panel, ppbv year^{-1}) and mixing term (M_z+M_y, left panel, ppbv year^{-1}) of the TEM N_2O budget for ERA5, WACCM-REFD1 and MERRA2 (2005-2018). The dotted, dashed and continue lines represent the probability at 80, 90 and 95% of positive/negative N_2O changes respectively. The green vertical lines identify the position of the FTIR stations together with their vertical coverage.

We now consider the MERRA2 simulation, starting with the changes in the *ADV* term. Similar to the ERA5 simulation, the MERRA2 experiment shows positive *ADV* changes over the tropical region above 10 hPa, which correspond to positive direct N_2O trends over the same region. These changes are due to an enhanced tropical upwelling at those levels (not shown), and qualitatively agree with the negative trends of mean AoA simulated by MERRA2 over a similar period (Ploeger et al., 2019). Above the subtropics in the lower stratosphere, the changes of the *ADV* term are positive and stronger than those obtained from the ERA5 simulation, and can be associated with the strengthening of the shallow branch of the BDC in MERRA2, as was already argued by Wargan et al. (2018). Above the southern mid-latitudes between 10 and 30 hPa, the decreasing *ADV* term leads to negative N_2O changes, indicating an enhanced downwelling over that region. Those negative *ADV* changes, possibly combined with larger chemical losses, correspond to the negative but not significant direct N_2O trends over the same region.

Regarding the *MIX* term in the MERRA2 simulation, there are no significant changes that correspond to direct N_2O trends. An intercomparison of AoA trends among reanalyses showed that significant differences in mixing exist between MERRA2 and ERAI that contribute to the mean AoA, as well as differences in the trends of the AoA spectrum in the lower and middle stratosphere (Ploeger et al., 2019). Indeed, we find large differences in the mixing contribution to the N_2O trends between MERRA2 and ERA5 (which is very similar to ERAI, not shown).

After discussing the TEM terms in the BASCOE simulations driven by ERA5 and MERRA2, we now investigate those simulated by WACCM-REFD1, starting with the *ADV* contribution. Similar to the BASCOE experiments, the positive changes in the *ADV* term simulated by WACCM-REFD1 consistently result in an N_2O increase in the Tropics above 5 hPa, which contributes to the positive direct N_2O trend over the same region. In addition, the *ADV* term is also enhanced above the subtropical lower stratosphere, possibly as a consequence of the strengthening of the shallow branch of the BDC that was robustly detected in CCMs (Butchart, 2014). Above the polar latitudes of both hemispheres, the *ADV* term decreases, resulting in negative N_2O changes, which are not visible in the direct N_2O trends because masked by the constant N_2O increase in the lowermost stratosphere. These patterns of positive and negative N_2O changes due to changes in the *ADV* term across the whole stratosphere are driven by a strengthening of the upwelling in the Tropics and downwelling in the extratropics (not shown), and can be associated with the acceleration of the BDC, which was robustly detected in several CCMs studies over longer periods (e.g., Abalos et al., 2021).

The changes in the *MIX* term in WACCM-REFD1 have a small impact on the N_2O trends compared to those of the *ADV* term. Large differences between WACCM and reanalyses were shown already by M2020 for WACCM-REFC1 for the climatologies of the mixing terms of the TEM budget. Furthermore, the weaker effect of mixing in WACCM-REFD1 compared to ERA5 is consistent with AoA studies that found weaker trends in aging by mixing in a free-running CCM compared to its specified-dynamics version and a reanalysis (Dietmüller et al., 2017).

From this section, we highlight that, within the TEM framework, changes in the residual advection have a stronger impact on the direct N_2O trends compared to those in mixing, for all datasets. However, the ERA5 simulation also delivers significant N_2O changes due to mixing that are consistent with previous studies using ECMWF reanalysis. We also notice that the hemispheric asymmetry in the direct N_2O trends simulated by ERA5 can be attributed to changes in both advection and mixing.

6 Summary and Conclusions

We have investigated the N_2O stratospheric columns (12-40 km) and their decadal (2005-2018) rates of change at four ground-based FTIR stations: Lauder (45°S), Wollongong (34°S), Izãna (28°N) and Jungfraujoch (46°N). We compared those ground-based observations with space-borne measurements from ACE-FTS, with the output of the BASCOE CTM driven by four modern reanalyses: ERAI, ERA5, JRA55 and MERRA2, and with two versions of WACCM: WACCM-REFC1 (version 4) and WACCM-REFD1 (version 6). We also studied the latitudinal and vertical distributions of these trends of the N_2O mixing ratios from model output and satellite measurements, both in the observation and model space, and used the Transformed Eulerian Mean (TEM) budget to investigate further the trends above the SH mid-latitudes in the BASCOE CTM driven by ERA5 and MERRA2 and in WACCM-REFD1.

The comparison of the stratospheric N_2O columns reveals a good agreement above Wollongong, and Lauder to a lesser extent, and larger differences above Jungfraujoch and Izãna. The trends in the N_2O stratospheric columns are larger in the SH compared to the NH, which is consistent with hemispherical differences in trends of stratospheric tracers measured at FTIR stations over the past decade (Strahan et al., 2020; Prignon et al., 2021). We find that the decadal trends in the N_2O columns are consistently positive in all cases except for ACE-FTS observations above Jungfraujoch. However, the vertical resolution of the FTIR retrievals above the Northern Hemisphere for N_2O limits our analysis to one stratospheric column, hence (in this analysis) the detection of potentially negative N_2O trends in the mid-stratosphere is hindered by the large N_2O increase in the lowermost stratosphere which arises from its continuous increase at the surface.

Global and vertically resolved trends of N_2O volume mixing ratios provide a more detailed picture compared to N_2O profiles obtained from FTIR measurements. The ACE-FTS measurements show a meridional dipole in the N_2O trends in the mid-lower stratosphere, with negative values in the NH mid-latitudes and positive values in the SH. When applying the temporal and spatial sampling of ACE-FTS on model datasets, ERAI and ERA5 compare best with the satellite measurements while the other reanalyses and the CCMs do not reproduce the meridional dipole in the mid-lower stratosphere as clearly as the ECMWF reanalyses. However, this application of the irregular sampling of ACE-FTS to the model output consistently enhances the N_2O trends, both positive and negative. Using continuous time sampling on native model grids, ERAI, and ERA5 to a lesser extent, still simulate the meridional dipole in the N_2O trends, consistently with a large number of modeling studies using both idealized and real tracers (e.g., Chabrillat et al., 2018; Ploeger et al., 2021; Prignon et al., 2021), but MERRA2, JRA55 and WACCM fail to reproduce the meridional dipole. WACCM-REFD1 is still an improvement compared to WACCM-REFC1, because it simulates the positive trend above the SH mid-latitudes also in the mid-lower stratosphere. The inherently limited spatial and temporal sampling of ACE-FTS, and its effect on N_2O trends, highlight how a regular coverage in the measurements, as in MLS, is essential to deliver reliable trends of long-lived tracers in the stratosphere. Because of this, the N_2O trends discussed here should be revisited using a newer version of MLS, once its drift in the N_2O retrievals will have been corrected.

We carried out two sensitivity tests using the BASCOE CTM driven by ERA5: one keeping N_2O constant at the surface with time-dependent dynamics (cst-N_2O), and the other using fixed dynamics with increasing N_2O at the surface (cst-dyn). The cst-N_2O experiment confirms that the extratropical N_2O trends in the mid-lower stratosphere are due to the impact of changes in the stratospheric transport. As expected, the cst-dyn simulation shows that N_2O increases everywhere, but the trend over 2005-2018 is not significantly positive in the NH mid-stratosphere. From these sensitivity tests with ERA5, we confirm that the hemispheric asymmetry of the decadal N_2O trends arises from decadal changes in transport. For the 2005-2018 period and in the 20-50 hPa layer, the hemispheric asymmetry in the significance of these trends arises from the larger dynamical

variability which is found in the northern extratropics on shorter timescales, i.e. with one single QBO cycle repeating indefinitely.

We found a strong impact of transport on the stratospheric trends of N_2O volume mixing ratios for the ERA5 simulations and large differences between ERA5, MERRA2 and WACCM-REFD1. This prompted us to study the TEM budget of N_2O in these datasets, in order to separate the possible impacts of the residual advection and mixing. For all datasets, the analysis of the TEM budget reveals positive N_2O changes in the tropical mid-high stratosphere and negative changes in the northern extratropical lower stratosphere, as a result of enhanced tropical upwelling and extratropical downwelling, respectively. This is in agreement with the acceleration of the advective part of the BDC over this relatively short period both in models (Butchart, 2014) and reanalyses (Ploeger et al., 2019). For the ERA5 simulation, the positive N_2O trend above the southern midlatitudes (part of the meridional dipole) can be due to the impact of changes in both advection and mixing, the latter is consistent with previous studies, both using Age of Air (AoA, Ploeger et al., 2015) and N_2O (Stiller et al., 2017). The TEM budget obtained with MERRA2 delivers different results, with a larger impact of the residual advection in forcing the N_2O trends. This discrepancy is consistent with the large differences between MERRA2 and other reanalyses when considering stratospheric mixing on decadal time scales (e.g., Ploeger et al., 2019).

Using a measurable tracer for stratospheric transport studies allows direct comparisons with observations. The rate of change of N_2O at the surface is well-known and approximately linear and the chemical losses are limited to the higher stratosphere. In theory, this relatively simple chemistry, combined with its long life, makes N_2O a very good tracer for stratospheric transport studies. Unfortunately, no ideal observational dataset currently exists for N_2O-based investigations such as the present study: FTIR observations generally lack adequate vertical resolution, the N_2O product from the latest MLS version suffers from an unrealistic drift, and ACE-FTS has poor spatial and temporal sampling. Here, we showed how model studies of N_2O trends still provide new insights about the BDC and its changes thanks to properly taking into account the ACE-FTS sampling, complementary sensitivity tests, and the TEM analysis. Despite the shortcomings of the TEM approach, i.e., the difficulty of closing its budget, its combination with sensitivity tests provides new insights on transport changes and their impacts on the composition of the stratosphere. This approach could be extended to other tracers that are both measured and modeled - e.g., carbon monoxide, methane, and inorganic fluorine.

Acknowledgments

We thank P. Bernath for his leadership of the ACE mission, which is supported by the Canadian Space Agency. Measurements at Lauder are core-funded by the National Institute of Water and Atmospheric Research Ltd. (NIWA) through New Zealand's Ministry of Business, Innovation and Employment Strategic Science Investment Fund. The ULiège team is grateful to the International Foundation High Altitude Research Stations Jungfraujoch and Gornergrat (HFSJG, Bern) for supporting the facilities needed to perform the FTIR observations at Jungfraujoch. D. Minganti and M. Prignon were financially supported by the Fonds de la Recherche Scientifique (F.R.S.-FNRS, Brussels) through the ACCROSS research project (Grant no. PDR.T.0040.16). The University of Liège contribution was further supported by the GAW-CH program of MeteoSwiss and by the F.R.S.-FNRS Grant no J.0126.21. E. Mahieu is a senior research associate with the F.R.S.-FNRS. D. Kinnison was funded in part by National Aeronautics and Space Administration (NASA) grant (NNH19ZDA001N-AURAST). This research was enabled by the computational and storage resources of NCAR's Computational and Information Systems Laboratory (CISL), sponsored by the NSF. Cheyenne: HPE/SGI ICE XA System (NCAR Community Computing). Boulder, CO: National Center for Atmospheric Research. https://doi.org/10.5065/D6RX99HX. The WACCM and BASCOE CTM data used for the N_2O

trends and TEM comparisons in the study are available at the BIRA-IASB repository (`http://repository.aeronomie.be`) via https://dx.doi.org/10.18758/71021071 with CC BY license (Minganti & Errera, 2022). FTIR data at the various stations are available at `https://www-air.larc.nasa.gov/pub/NDACC/PUBLIC/stations/`. ACE-FTS data are available at `https://databace.scisat.ca/level2/ace_v4.1/display_data.php`. ERA5 data are available at `https://cds.climate.copernicus.eu/`. ERA-Interim data are available at `https://apps.ecmwf.int/datasets/`. JRA-55 data are available at `https://rda.ucar.edu/`. MERRA2 data are available at `https://disc.gsfc.nasa.gov/datasets/`. The DLM source code is available at `https://github.com/justinalsing/dlmmc`.

References

Abalos, M., Calvo, N., Benito-Barca, S., Garny, H., Hardiman, S. C., Lin, P., ... others (2021). The Brewer-Dobson circulation in CMIP6. *Atmospheric Chemistry and Physics Discussions*, 1–27.

Abalos, M., Orbe, C., Kinnison, D. E., Plummer, D., Oman, L. D., Jöckel, P., ... others (2020). Future trends in stratosphere-to-troposphere transport in CCMI models. *Atmospheric chemistry and physics*, *20*(11), 6883–6901.

Abalos, M., Randel, W., Kinnison, D., & Serrano, E. (2013). Quantifying tracer transport in the tropical lower stratosphere using WACCM. *Atmos. Chem. Phys*, *13*(10), 591–10.

Alsing, J. A. (2019). dlmmc: Dynamical linear model regression for atmospheric time-series analysis. *Journal of Open Source Software*, *4*(37), 1157.

Andrews, D. G., Holton, J. R., & Leovy, C. B. (1987). *Middle atmosphere dynamics* (No. 40). Academic press.

Angelbratt, J., Mellqvist, J., Blumenstock, T., Borsdorff, T., Brohede, S., Duchatelet, P., ... Urban, J. (2011). A new method to detect long term trends of methane (CH_4) and nitrous oxide (N_2O) total columns measured within the NDACC ground-based high resolution solar FTIR network. *Atmospheric Chemistry and Physics*, *11*(13), 6167–6183. Retrieved from `https://acp.copernicus.org/articles/11/6167/2011/` doi: 10.5194/acp-11-6167-2011

Bader, W., Bovy, B., Conway, S., Strong, K., Smale, D., Turner, A. J., ... Mahieu, E. (2017). The recent increase of atmospheric methane from 10 years of ground-based ndacc ftir observations since 2005. *Atmospheric Chemistry and Physics*, *17*(3), 2255–2277. Retrieved from `https://acp.copernicus.org/articles/17/2255/2017/` doi: 10.5194/acp-17-2255-2017

Baldwin, M., Gray, L., Dunkerton, T., Hamilton, K., Haynes, P., Randel, W., ... others (2001). The quasi-biennial oscillation. *Reviews of Geophysics*, *39*(2), 179–229.

Ball, W. T., Alsing, J., Mortlock, D. J., Rozanov, E. V., Tummon, F., & Haigh, J. D. (2017). Reconciling differences in stratospheric ozone composites. *Atmospheric Chemistry and Physics*, *17*(20), 12269–12302. Retrieved from `https://acp.copernicus.org/articles/17/12269/2017/` doi: 10.5194/acp-17-12269-2017

Ball, W. T., Alsing, J., Mortlock, D. J., Staehelin, J., Haigh, J. D., Peter, T., ... Rozanov, E. V. (2018). Evidence for a continuous decline in lower stratospheric ozone offsetting ozone layer recovery. *Atmospheric Chemistry and Physics*, *18*(2), 1379–1394. Retrieved from `https://acp.copernicus.org/articles/18/1379/2018/` doi: 10.5194/acp-18-1379-2018

Bernath, P. (2017). The atmospheric chemistry experiment (ACE). *Journal of Quantitative Spectroscopy and Radiative Transfer*, *186*, 3-16. Retrieved from `https://www.sciencedirect.com/science/article/pii/S0022407316300176` (Satellite Remote Sensing and Spectroscopy: Joint ACE-Odin Meeting, October 2015) doi: https://doi.org/10.1016/j.jqsrt.2016.04.006

Bernath, P., Crouse, J., Hughes, R., & Boone, C. (2021). The Atmospheric Chemistry Experiment Fourier transform spectrometer (ACE-FTS) version 4.1 retrievals: Trends and seasonal distributions. *Journal of Quantitative Spectroscopy and Radiative Transfer*, *259*, 107409.

Bernath, P., Steffen, J., Crouse, J., & Boone, C. (2020). Sixteen-year trends in atmospheric trace gases from orbit. *Journal of Quantitative Spectroscopy and Radiative Transfer*, *253*, 107178. Retrieved from `https://www.sciencedirect.com/science/article/pii/S0022407320302958` doi: https://doi.org/10.1016/j.jqsrt.2020.107178

Bernath, P. F., McElroy, C. T., Abrams, M. C., Boone, C. D., Butler, M., Camy-Peyret, C., ... Zou, J. (2005). Atmospheric chemistry experiment (ACE): Mis-

sion overview. *Geophysical Research Letters*, *32*(15). Retrieved from https://agupubs.onlinelibrary.wiley.com/doi/abs/10.1029/2005GL022386 doi: https://doi.org/10.1029/2005GL022386

Butchart, N. (2014). The Brewer-Dobson circulation. *Reviews of Geophysics*, *52*(2), 157-184. Retrieved from https://agupubs.onlinelibrary.wiley.com/doi/abs/10.1002/2013RG000448 doi: https://doi.org/10.1002/2013RG000448

Butchart, N., & Scaife, A. A. (2001). Removal of chlorofluorocarbons by increased mass exchange between the stratosphere and troposphere in a changing climate. *Nature*, *410*(6830), 799–802.

Chabrillat, S., Vigouroux, C., Christophe, Y., Engel, A., Errera, Q., Minganti, D., ... Mahieu, E. (2018). Comparison of mean age of air in five reanalyses using the BASCOE transport model. *Atmospheric Chemistry and Physics*, *18*(19), 14715–14735.

Danabasoglu, G., Lamarque, J.-F., Bacmeister, J., Bailey, D., DuVivier, A., Edwards, J., ... others (2020). The community earth system model version 2 (CESM2). *Journal of Advances in Modeling Earth Systems*, *12*(2).

Dee, D. P., Uppala, S., Simmons, A., Berrisford, P., Poli, P., Kobayashi, S., ... others (2011). The ERA-interim reanalysis: Configuration and performance of the data assimilation system. *Quarterly Journal of the royal meteorological society*, *137*(656), 553–597.

De Mazière, M., Thompson, A. M., Kurylo, M. J., Wild, J. D., Bernhard, G., Blumenstock, T., ... others (2018). The Network for the Detection of Atmospheric Composition Change (NDACC): history, status and perspectives. *Atmospheric Chemistry and Physics*, *18*(7), 4935–4964.

de Wit, T. D., Bruinsma, S., & Shibasaki, K. (2014). Synoptic radio observations as proxies for upper atmosphere modelling. *Journal of Space Weather and Space Climate*, *4*, A06.

Dhomse, S. S., Kinnison, D., Chipperfield, M. P., Salawitch, R. J., Cionni, I., Hegglin, M. I., ... Zeng, G. (2018). Estimates of ozone return dates from Chemistry-Climate Model Initiative simulations. *Atmospheric Chemistry and Physics*, *18*(11), 8409–8438. Retrieved from https://acp.copernicus.org/articles/18/8409/2018/ doi: 10.5194/acp-18-8409-2018

Diallo, M., Ern, M., & Ploeger, F. (2021). The advective brewer–dobson circulation in the era5 reanalysis: climatology, variability, and trends. *Atmospheric Chemistry and Physics*, *21*(10), 7515–7544.

Dietmüller, S., Eichinger, R., Garny, H., Birner, T., Boenisch, H., Pitari, G., ... others (2018). Quantifying the effect of mixing on the mean age of air in ccmval-2 and ccmi-1 models. *Atmospheric Chemistry and Physics*, *18*(9), 6699–6720.

Dietmüller, S., Garny, H., Plöger, F., Jöckel, P., & Cai, D. (2017). Effects of mixing on resolved and unresolved scales on stratospheric age of air. *Atmospheric chemistry and physics*, *17*(12), 7703–7719.

Durbin, J., & Koopman, S. J. (2012). *Time series analysis by state space methods*. Oxford university press.

Eichinger, R., Dietmüller, S., Garny, H., Šácha, P., Birner, T., Bönisch, H., ... others (2019). The influence of mixing on the stratospheric age of air changes in the 21st century. *Atmospheric chemistry and physics*, *19*(2), 921–940.

Engel, A., Bönisch, H., Ullrich, M., Sitals, R., Membrive, O., Danis, F., & Crevoisier, C. (2017). Mean age of stratospheric air derived from AirCore observations. *Atmospheric Chemistry and Physics*, *17*(11), 6825–6838.

Engel, A., Möbius, T., Bönisch, H., Schmidt, U., Heinz, R., Levin, I., ... others (2009). Age of stratospheric air unchanged within uncertainties over the past 30 years. *Nature Geoscience*, *2*(1), 28–31.

Errera, Q., Chabrillat, S., Christophe, Y., Debosscher, J., Hubert, D., Lahoz, W., ... Walker, K. (2019). Technical note: Reanalysis of Aura MLS Chemical Observations. *Atmospheric Chemistry and Physics Discussions*, *2019*, 1–60.

Retrieved from https://www.atmos-chem-phys-discuss.net/acp-2019-530/ doi: 10.5194/acp-2019-530

Eyring, V., Bony, S., Meehl, G. A., Senior, C. A., Stevens, B., Stouffer, R. J., & Taylor, K. E. (2016). Overview of the coupled model intercomparison project phase 6 (cmip6) experimental design and organization. *Geoscientific Model Development*, *9*(5), 1937–1958.

Fritsch, F., Garny, H., Engel, A., Bönisch, H., & Eichinger, R. (2020). Sensitivity of age of air trends to the derivation method for non-linear increasing inert SF_6. *Atmospheric Chemistry and Physics*, *20*(14), 8709–8725. Retrieved from https://www.atmos-chem-phys.net/20/8709/2020/ doi: 10.5194/acp-20-8709-2020

Froidevaux, L., Kinnison, D. E., Wang, R., Anderson, J., & Fuller, R. A. (2019). Evaluation of CESM1 (WACCM) free-running and specified dynamics atmospheric composition simulations using global multispecies satellite data records. *Atmospheric Chemistry and Physics*, *19*(7), 4783–4821. Retrieved from https://acp.copernicus.org/articles/19/4783/2019/ doi: 10.5194/acp-19-4783-2019

Fu, Q., Lin, P., Solomon, S., & Hartmann, D. (2015). Observational evidence of strengthening of the Brewer–Dobson circulation since 1980. *Journal of Geophysical Research: Atmospheres*, *120*(19), 10–214.

Fu, Q., Solomon, S., Pahlavan, H. A., & Lin, P. (2019). Observed changes in Brewer–Dobson circulation for 1980–2018. *Environmental Research Letters*, *14*(11), 114026.

Fujiwara, M., Wright, J. S., Manney, G. L., Gray, L. J., Anstey, J., Birner, T., ... others (2017). Introduction to the SPARC Reanalysis Intercomparison Project (S-RIP) and overview of the reanalysis systems. *Atmospheric Chemistry and Physics*, *17*(2), 1417–1452.

Galytska, E., Rozanov, A., Chipperfield, M. P., Dhomse, Weber, M., Arosio, C., ... Burrows, J. P. (2019). Dynamically controlled ozone decline in the tropical mid-stratosphere observed by SCIAMACHY. *Atmospheric Chemistry and Physics*, *19*(2), 767–783. Retrieved from https://www.atmos-chem-phys.net/19/767/2019/ doi: 10.5194/acp-19-767-2019

García, O. E., Schneider, M., Sepúlveda, E., Hase, F., Blumenstock, T., Cuevas, E., ... López, C. (2021). Twenty years of ground-based NDACC FTIR spectrometry at Izaña Observatory – overview and long-term comparison to other techniques. *Atmospheric Chemistry and Physics*, *21*(20), 15519–15554. Retrieved from https://acp.copernicus.org/articles/21/15519/2021/ doi: 10.5194/acp-21-15519-2021

Garcia, R. R., Randel, W. J., & Kinnison, D. E. (2011). On the determination of age of air trends from atmospheric trace species. *Journal of the Atmospheric Sciences*, *68*(1), 139–154.

Garcia, R. R., Smith, A. K., Kinnison, D. E., de la Cámara, A., & Murphy, D. J. (2017). Modification of the Gravity Wave Parameterization in the Whole Atmosphere Community Climate Model: Motivation and Results. *Journal of the Atmospheric Sciences*, *74*(1), 275 - 291. Retrieved from https://journals.ametsoc.org/view/journals/atsc/74/1/jas-d-16-0104.1.xml doi: 10.1175/JAS-D-16-0104.1

Gelaro, R., McCarty, W., Suárez, M. J., Todling, R., Molod, A., Takacs, L., ... others (2017). The modern-era retrospective analysis for research and applications, version 2 (MERRA-2). *Journal of Climate*, *30*(14), 5419–5454.

Gettelman, A., Mills, M., Kinnison, D., Garcia, R., Smith, A., Marsh, D., ... others (2019). The whole atmosphere community climate model version 6 (WACCM6). *Journal of Geophysical Research: Atmospheres*, *124*(23), 12380–12403.

Griffith, D. W. T., Deutscher, N. M., Caldow, C., Kettlewell, G., Riggenbach, M.,

& Hammer, S. (2012). A Fourier transform infrared trace gas and isotope analyser for atmospheric applications. *Atmospheric Measurement Techniques*, *5*(10), 2481–2498. Retrieved from https://amt.copernicus.org/articles/5/2481/2012/ doi: 10.5194/amt-5-2481-2012

Haenel, F. J., Stiller, G. P., von Clarmann, T., Funke, B., Eckert, E., Glatthor, N., ... Reddmann, T. (2015). Reassessment of MIPAS age of air trends and variability. *Atmospheric Chemistry and Physics*, *15*(22), 13161–13176. Retrieved from https://acp.copernicus.org/articles/15/13161/2015/ doi: 10.5194/acp-15-13161-2015

Han, Y., Tian, W., Chipperfield, M. P., Zhang, J., Wang, F., Sang, W., ... Tian, H. (2019). Attribution of the Hemispheric Asymmetries in Trends of Stratospheric Trace Gases Inferred From Microwave Limb Sounder (MLS) Measurements. *Journal of Geophysical Research: Atmospheres*, *124*(12), 6283-6293. Retrieved from https://agupubs.onlinelibrary.wiley.com/doi/abs/10.1029/2018JD029723 doi: https://doi.org/10.1029/2018JD029723

Hardiman, S. C., Butchart, N., & Calvo, N. (2014). The morphology of the Brewer–Dobson circulation and its response to climate change in CMIP5 simulations. *Quarterly Journal of the Royal Meteorological Society*, *140*(683), 1958–1965.

Hardiman, S. C., Lin, P., Scaife, A. A., Dunstone, N. J., & Ren, H.-L. (2017). The influence of dynamical variability on the observed Brewer–Dobson circulation trend. *Geophysical Research Letters*, *44*(6), 2885–2892.

Hersbach, H., Bell, B., Berrisford, P., Hirahara, S., Hornyi, A., Muoz-Sabater, J., ... Thpaut, J.-N. (2020). The ERA5 global reanalysis. *Quarterly Journal of the Royal Meteorological Society*, *146*(730), 1999-2049. Retrieved from https://rmets.onlinelibrary.wiley.com/doi/abs/10.1002/qj.3803 doi: https://doi.org/10.1002/qj.3803

Hurrell, J. W., Holland, M. M., Gent, P. R., Ghan, S., Kay, J. E., Kushner, P. J., ... others (2013). The community earth system model: a framework for collaborative research. *Bulletin of the American Meteorological Society*, *94*(9), 1339–1360.

Jin, J. J., Semeniuk, K., Beagley, S. R., Fomichev, V. I., Jonsson, A. I., McConnell, J. C., ... Dupuy, E. (2009). Comparison of cmam simulations of carbon monoxide (co), nitrous oxide (n_2o), and methane (ch_4) with observations from odin/smr, ace-fts, and aura/mls. *Atmospheric Chemistry and Physics*, *9*(10), 3233–3252. Retrieved from https://acp.copernicus.org/articles/9/3233/2009/ doi: 10.5194/acp-9-3233-2009

Kobayashi, S., Ota, Y., Harada, Y., Ebita, A., Moriya, M., Onoda, H., ... others (2015). The JRA-55 reanalysis: General specifications and basic characteristics. *Journal of the Meteorological Society of Japan. Ser. II*, *93*(1), 5–48.

Kolonjari, F., Plummer, D. A., Walker, K. A., Boone, C. D., Elkins, J. W., Heglin, M. I., ... Stiller, G. P. (2018). Assessing stratospheric transport in the cmam30 simulations using ace-fts measurements. *Atmospheric Chemistry and Physics*, *18*(9), 6801–6828. Retrieved from https://acp.copernicus.org/articles/18/6801/2018/ doi: 10.5194/acp-18-6801-2018

Kyrölä, E., Laine, M., Sofieva, V., Tamminen, J., Päivärinta, S.-M., Tukiainen, S., ... Thomason, L. (2013). Combined sage ii–gomos ozone profile data set for 1984–2011 and trend analysis of the vertical distribution of ozone. *Atmospheric Chemistry and Physics*, *13*(21), 10645–10658.

Laine, M., Latva-Pukkila, N., & Kyrölä, E. (2014). Analysing time-varying trends in stratospheric ozone time series using the state space approach. *Atmospheric Chemistry and Physics*, *14*(18), 9707–9725.

Langerock, B., De Mazière, M., Hendrick, F., Vigouroux, C., Desmet, F., Dils, B., & Niemeijer, S. (2015). Description of algorithms for co-locating and comparing gridded model data with remote-sensing observations. *Geoscientific Model Development*, *8*(3), 911–921. Retrieved from https://gmd.copernicus.org/

articles/8/911/2015/ doi: 10.5194/gmd-8-911-2015

Lin, P., & Fu, Q. (2013). Changes in various branches of the Brewer–Dobson circulation from an ensemble of chemistry climate models. *Journal of Geophysical Research: Atmospheres*, *118*(1), 73–84.

Lin, S.-J. (2004). A "vertically lagrangian" finite-volume dynamical core for global models. *Monthly Weather Review*, *132*(10), 2293–2307.

Lin, S.-J., & Rood, R. B. (1996). Multidimensional flux-form semi-lagrangian transport schemes. *Monthly Weather Review*, *124*(9), 2046–2070.

Livesey, N. J., Read, W. G., Froidevaux, L., Lambert, A., Santee, M. L., Schwartz, M. J., ... Nedoluha, G. E. (2021). Investigation and amelioration of long-term instrumental drifts in water vapor and nitrous oxide measurements from the aura microwave limb sounder (MLS) and their implications for studies of variability and trends. *Atmospheric Chemistry and Physics*, *21*(20), 15409–15430. Retrieved from https://acp.copernicus.org/articles/21/15409/2021/ doi: 10.5194/acp-21-15409-2021

Mahieu, E., Chipperfield, M., Notholt, J., Reddmann, T., Anderson, J., Bernath, P., ... others (2014). Recent northern hemisphere stratospheric HCl increase due to atmospheric circulation changes. *Nature*, *515*(7525), 104.

Marsh, D. R., Mills, M. J., Kinnison, D. E., Lamarque, J.-F., Calvo, N., & Polvani, L. M. (2013). Climate change from 1850 to 2005 simulated in cesm1(waccm). *Journal of Climate*, *26*(19), 7372 - 7391. Retrieved from https://journals.ametsoc.org/view/journals/clim/26/19/jcli-d-12-00558.1.xml doi: 10.1175/JCLI-D-12-00558.1

Matthes, K., Marsh, D. R., Garcia, R. R., Kinnison, D. E., Sassi, F., & Walters, S. (2010). Role of the qbo in modulating the influence of the 11 year solar cycle on the atmosphere using constant forcings. *Journal of Geophysical Research: Atmospheres*, *115*(D18).

Meul, S., Dameris, M., Langematz, U., Abalichin, J., Kerschbaumer, A., Kubin, A., & Oberlnder-Hayn, S. (2016). Impact of rising greenhouse gas concentrations on future tropical ozone and UV exposure. *Geophysical Research Letters*, *43*(6), 2919-2927. Retrieved from https://agupubs.onlinelibrary.wiley.com/doi/abs/10.1002/2016GL067997 doi: https://doi.org/10.1002/2016GL067997

Meul, S., Langematz, U., Kröger, P., Oberländer-Hayn, S., & Jöckel, P. (2018). Future changes in the stratosphere-to-troposphere ozone mass flux and the contribution from climate change and ozone recovery. *Atmospheric Chemistry and Physics*, *18*(10), 7721–7738. Retrieved from https://acp.copernicus.org/articles/18/7721/2018/ doi: 10.5194/acp-18-7721-2018

Millán, L. F., Livesey, N. J., Santee, M. L., Neu, J. L., Manney, G. L., & Fuller, R. A. (2016). Case studies of the impact of orbital sampling on stratospheric trend detection and derivation of tropical vertical velocities: solar occultation vs. limb emission sounding. *Atmospheric Chemistry and Physics*, *16*(18), 11521–11534. Retrieved from https://acp.copernicus.org/articles/16/11521/2016/ doi: 10.5194/acp-16-11521-2016

Minganti, D., Chabrillat, S., Christophe, Y., Errera, Q., Abalos, M., Prignon, M., ... Mahieu, E. (2020). Climatological impact of the Brewer–Dobson circulation on the N_2O budget in WACCM, a chemical reanalysis and a CTM driven by four dynamical reanalyses. *Atmospheric Chemistry and Physics*, *20*(21), 12609–12631. Retrieved from https://acp.copernicus.org/articles/20/12609/2020/ doi: 10.5194/acp-20-12609-2020

Minganti, D., & Errera, Q. (2022). *Supplement for: N_2O rate of change as a diagnostic of the brewer-dobson circulation in the stratosphere* [dataset]. Royal Belgian Institute for Space Aeronomy. Retrieved from https://repository.aeronomie.be/?doi=10.18758/71021071 doi: https://dx.doi.org/10.18758/71021071

Monge-Sanz, B. M., Chipperfield, M. P., Dee, D. P., Simmons, A. J., & Uppala, S. M. (2013). Improvements in the stratospheric transport achieved by a chemistry transport model with ECMWF (re)analyses: identifying effects and remaining challenges. *Quarterly Journal of the Royal Meteorological Society*, *139*(672), 654-673. Retrieved from `https://rmets.onlinelibrary.wiley.com/doi/abs/10.1002/qj.1996` doi: https://doi.org/10.1002/qj.1996

Morgenstern, O., Hegglin, M. I., Rozanov, E., O'Connor, F. M., Abraham, N. L., Akiyoshi, H., ... Zeng, G. (2017). Review of the global models used within phase 1 of the chemistry–climate model initiative (ccmi). *Geoscientific Model Development*, *10*(2), 639–671. Retrieved from `https://gmd.copernicus.org/articles/10/639/2017/` doi: 10.5194/gmd-10-639-2017

Neale, R. B., Richter, J., Park, S., Lauritzen, P. H., Vavrus, S. J., Rasch, P. J., & Zhang, M. (2013). The mean climate of the Community Atmosphere Model (CAM4) in forced SST and fully coupled experiments. *Journal of Climate*, *26*(14), 5150–5168.

Oberländer-Hayn, S., Gerber, E. P., Abalichin, J., Akiyoshi, H., Kerschbaumer, A., Kubin, A., ... Oman, L. D. (2016). Is the Brewer-Dobson circulation increasing or moving upward? *Geophysical Research Letters*, *43*(4), 1772-1779. Retrieved from `https://agupubs.onlinelibrary.wiley.com/doi/abs/10.1002/2015GL067545` doi: https://doi.org/10.1002/2015GL067545

Petropavlovskikh, I., Godin-Beekmann, S., Hubert, D., Damadeo, R., Hassler, B., & Sofieva, V. (2019). SPARC/IO3C/GAW report on Long-term Ozone Trends and Uncertainties in the Stratosphere.

Ploeger, F., Abalos, M., Birner, T., Konopka, P., Legras, B., Müller, R., & Riese, M. (2015). Quantifying the effects of mixing and residual circulation on trends of stratospheric mean age of air. *Geophysical Research Letters*, *42*(6), 2047–2054.

Ploeger, F., Diallo, M., Charlesworth, E., Konopka, P., Legras, B., Laube, J. C., ... Riese, M. (2021). The stratospheric Brewer–Dobson circulation inferred from age of air in the ERA5 reanalysis. *Atmospheric Chemistry and Physics*, *21*(11), 8393–8412.

Ploeger, F., Legras, B., Charlesworth, E., Yan, X., Diallo, M., Konopka, P., ... Riese, M. (2019). How robust are stratospheric age of air trends from different reanalyses? *Atmospheric Chemistry and Physics*, *19*(9), 6085–6105.

Plumb, R. A. (2002). Stratospheric transport. *Journal of the Meteorological Society of Japan. Ser. II*, *80*(4B), 793–809.

Plummer, D., Nagashima, T., Tilmes, S., Archibald, A., Chiodo, G., Fadnavis, S., ... others (2021). Ccmi-2022: A new set of chemistry-climate model initiative (ccmi) community simulations to update the assessment of models and support upcoming ozone assessment activities. *Newsletter n 57 July 2021*, 22.

Polvani, L. M., Wang, L., Abalos, M., Butchart, N., Chipperfield, M. P., Dameris, M., ... Stone, K. A. (2019). Large Impacts, Past and Future, of Ozone-Depleting Substances on Brewer-Dobson Circulation Trends: A Multimodel Assessment. *Journal of Geophysical Research: Atmospheres*, *124*(13), 6669-6680. Retrieved from `https://agupubs.onlinelibrary.wiley.com/doi/abs/10.1029/2018JD029516` doi: https://doi.org/10.1029/2018JD029516

Prignon, M., Chabrillat, S., Friedrich, M., Smale, D., Strahan, S., Bernath, P., ... others (2021). Stratospheric fluorine as a tracer of circulation changes: comparison between infrared remote-sensing observations and simulations with five modern reanalyses. *Journal of Geophysical Research: Atmospheres*, e2021JD034995.

Prignon, M., Chabrillat, S., Minganti, D., O'Doherty, S., Servais, C., Stiller, G., ... Mahieu, E. (2019). Improved FTIR retrieval strategy for HCFC-22 ($CHClF_2$), comparisons with in situ and satellite datasets with the support of models, and determination of its long-term trend above Jungfraujoch. *Atmospheric Chemistry and Physics Discussions*.

Randel, W., & Park, M. (2019). Diagnosing observed stratospheric water vapor relationships to the cold point tropical tropopause. *Journal of Geophysical Research: Atmospheres*, *124*(13), 7018–7033.

Randel, W. J., Boville, B. A., Gille, J. C., Bailey, P. L., Massie, S. T., Kumer, J., ... Roche, A. (1994). Simulation of stratospheric N_2O in the NCAR CCM2: Comparison with CLAES data and global budget analyses. *Journal of the atmospheric sciences*, *51*(20), 2834–2845.

Rodgers, C. D. (2000). *Inverse methods for atmospheric sounding: theory and practice* (Vol. 2). World scientific.

Scaife, A., & James, I. (2000). Response of the stratosphere to interannual variability of tropospheric planetary waves. *Quarterly Journal of the Royal Meteorological Society*, *126*(562), 275–297.

Seinfeld, J. H., & Pandis, S. N. (2016). *Atmospheric chemistry and physics: from air pollution to climate change*. John Wiley & Sons.

Sheese, P. E., Walker, K. A., Boone, C. D., Bernath, P. F., Froidevaux, L., Funke, B., ... von Clarmann, T. (2017). ACE-FTS ozone, water vapour, nitrous oxide, nitric acid, and carbon monoxide profile comparisons with MIPAS and MLS. *Journal of Quantitative Spectroscopy and Radiative Transfer*, *186*, 63–80.

Shepherd, T. G. (2007). Transport in the middle atmosphere. *Journal of the Meteorological Society of Japan. Ser. II*, *85*, 165–191.

Shepherd, T. G. (2008). Dynamics, stratospheric ozone, and climate change. *Atmosphere-Ocean*, *46*(1), 117-138. Retrieved from `https://doi.org/10.3137/ao.460106` doi: 10.3137/ao.460106

Simmons, A., Soci, C., Nicolas, J., Bell, B., Berrisford, P., Dragani, R., ... others (2020). *Global stratospheric temperature bias and other stratospheric aspects of ERA5 and ERA5. 1.* European Centre for Medium Range Weather Forecasts.

Stiller, G., Clarmann, T. v., Haenel, F., Funke, B., Glatthor, N., Grabowski, U., ... others (2012). Observed temporal evolution of global mean age of stratospheric air for the 2002 to 2010 period. *Atmospheric Chemistry and Physics*, *12*(7), 3311–3331.

Stiller, G., Fierli, F., Ploeger, F., Cagnazzo, C., Funke, B., Haenel, F. J., ... Clarmann, T. v. (2017). Shift of subtropical transport barriers explains observed hemispheric asymmetry of decadal trends of age of air. *Atmospheric Chemistry and Physics*, *17*(18), 11177–11192.

Strahan, S. E., Smale, D., Douglass, A. R., Blumenstock, T., Hannigan, J. W., Hase, F., ... others (2020). Observed hemispheric asymmetry in stratospheric transport trends from 1994 to 2018. *Geophysical Research Letters*, *47*(17), e2020GL088567.

Strong, K., Wolff, M. A., Kerzenmacher, T. E., Walker, K. A., Bernath, P. F., Blumenstock, T., ... Wood, S. (2008). Validation of ACE-FTS N_2O measurements. *Atmospheric Chemistry and Physics*, *8*(16), 4759–4786. Retrieved from `https://acp.copernicus.org/articles/8/4759/2008/` doi: 10.5194/acp-8-4759-2008

Tian, H., Xu, R., Canadell, J. G., Thompson, R. L., Winiwarter, W., Suntharalingam, P., ... Yao, Y. (2020). A comprehensive quantification of global nitrous oxide sources and sinks. *Nature*, *586*(7828), 248?256. doi: 10.1038/s41586-020-2780-0

von Clarmann, T., & Grabowski, U. (2021). Direct inversion of circulation from tracer measurements–Part 2: Sensitivity studies and model recovery tests. *Atmospheric Chemistry and Physics*, *21*(4), 2509–2526.

Wargan, K., Orbe, C., Pawson, S., Ziemke, J. R., Oman, L. D., Olsen, M. A., ... Emma Knowland, K. (2018). Recent Decline in Extratropical Lower Stratospheric Ozone Attributed to Circulation Changes. *Geophysical Research Letters*, *45*(10), 5166-5176. Retrieved from `https://`

agupubs.onlinelibrary.wiley.com/doi/abs/10.1029/2018GL077406 doi: https://doi.org/10.1029/2018GL077406

Waugh, D., & Hall, T. (2002). Age of stratospheric air: Theory, observations, and models. *Reviews of Geophysics*, *40*(4), 1–1.

Wolter, K., & Timlin, M. S. (2011). El Niño/Southern Oscillation behaviour since 1871 as diagnosed in an extended multivariate ENSO index (MEI. ext). *International Journal of Climatology*, *31*(7), 1074–1087.

Zander, R., Mahieu, E., Demoulin, P., Duchatelet, P., Roland, G., Servais, C., ... Rinsland, C. (2008). Our changing atmosphere: Evidence based on long-term infrared solar observations at the jungfraujoch since 1950. *Science of The Total Environment*, *391*(2), 184-195. Retrieved from https://www.sciencedirect.com/science/article/pii/S0048969707010789 (Research at Jungfraujoch - Contributions to the International conference in celebration of the 75th anniversary of the High Altitude Research Station Jungfraujoch at Interlaken, Switzerland (11-13 September, 2006)) doi: https://doi.org/10.1016/j.scitotenv.2007.10.018

Zhou, M., Langerock, B., Wells, K. C., Millet, D. B., Vigouroux, C., Sha, M. K., ... De Mazière, M. (2019). An intercomparison of total column-averaged nitrous oxide between ground-based FTIR TCCON and NDACC measurements at seven sites and comparisons with the GEOS-Chem model. *Atmospheric Measurement Techniques*, *12*(2), 1393–1408. Retrieved from https://amt.copernicus.org/articles/12/1393/2019/ doi: 10.5194/amt-12-1393-2019

7.2 Additional discussion

This Section contains complementary and additional elements of discussion that could not find a place in the manuscript submitted to Journal of Geophysical Research - Atmospheres. Section 7.2.1 discusses the additional components of the recovered fit of the N_2O stratospheric columns at the four FTIR stations: the impacts of the seasonal cycle and the forcings from the regressors. Section 7.2.2 expands the discussion about the hemispheric asymmetries of the N_2O stratospheric columns and their trends above the FTIR stations. Section 7.2.3 discusses the changes of the ADV and MIX terms for the datasets that are not included in the previous Section.

7.2.1 Impact of the seasonal cycle and regressors on the N_2O stratospheric columns

This Section discusses the impact of the seasonal cycle and regressor variables on the fits of the N_2O stratospheric columns obtained with the DLM for all datasets above the location of the FTIR stations. Figures 7.1 and 7.2 show the time-dependent coefficients of the seasonal cycle terms ($\beta_{1,2,t}^{6,12}$ in Eq. 5.16) for the stations above the SH and NH, respectively. Above Lauder, there is an excellent agreement among the datasets, as well as above Wollongong, except for WACCM-REFC1, which simulates a weaker seasonal contribution than the other datasets (around 25% smaller). Above Izãna, both WACCM versions simulate a much weaker contribution of the seasonal cycle than the other datasets (more than twice smaller), while above Jungfraujoch there is an excellent agreement among the datasets. Among the considered stations, the coefficients of the seasonal cycles are the largest above Jungfraujoch, because of the larger variability above the wintertime northern mid-latitudes compared to subtropical regions and the wintertime southern mid-latitudes (Scaife and James, 2000). From these two figures, we conclude that WACCM underestimates seasonal variations of transport in the subtropics, while it models this aspect in a more realistic manner in the mid-latitudes.

Figure 7.3 shows vertical profiles of the regressor coefficients for the QBO, the solar cycle and the ENSO obtained with the DLM regression. As mentioned in Sect. 5.2.3, those coefficients do not depend on time. Above the stations in the SH, the QBO contribution is the largest below 20 km and decreases above. Above the NH stations, the QBO contribution is generally weaker than the SH (coefficients approximately twice smaller, depending on the dataset), with the largest values below 25 km above Izãna and below 17-18 km above Jungfraujoch. Above Jungfraujoch, the QBO contribution to the fit of the N_2O stratospheric columns is relatively small (around $2\text{x}10^{15}$

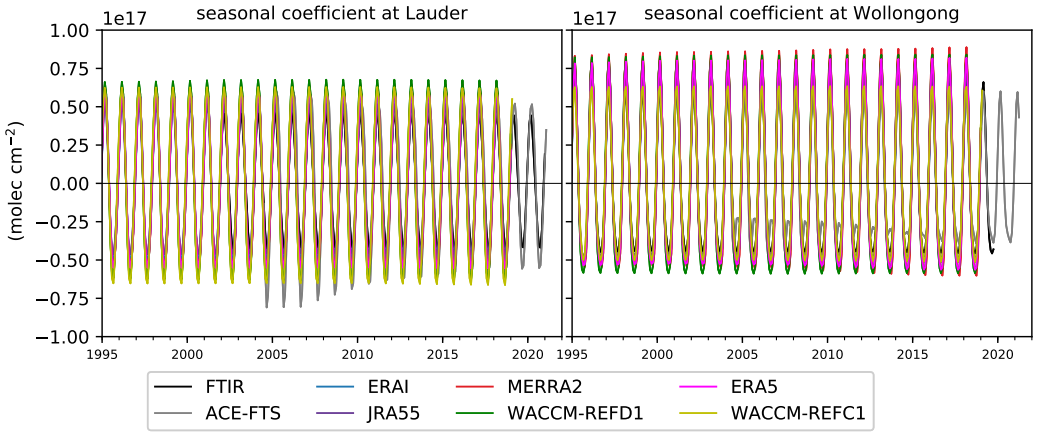

Figure 7.1: Coefficients of the seasonal cycles from the fit of the stratospheric N_2O columns obtained from the DLM regression. Left panel: all datasets above Lauder; right panel: all datasets above Wollongong.

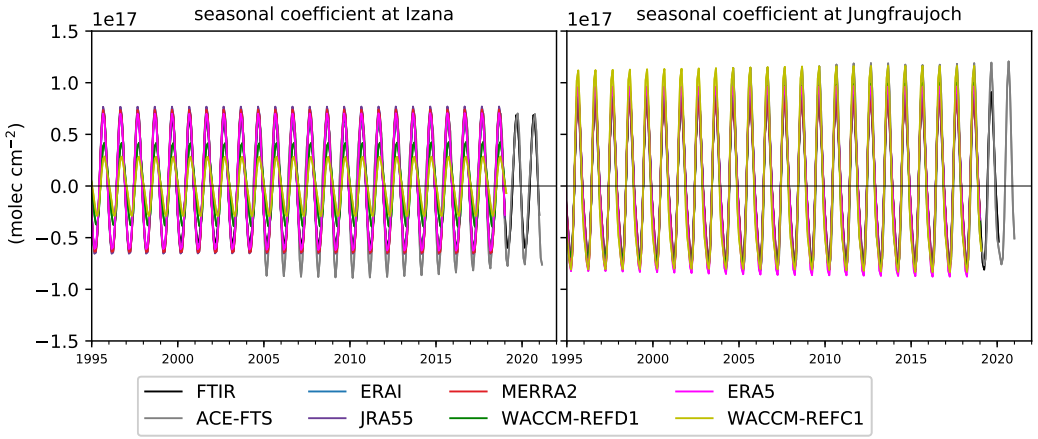

Figure 7.2: Coefficients of the seasonal cycles from the fit of the stratospheric N_2O columns obtained from the DLM regression. Left panel: all datasets above Izãna ; right panel: all datasets above Jungfraujoch.

molec cm^{-2} compared to 3x10^{15} molec cm^{-2} above Lauder). Hendrick et al. (2012) showed that the QBO contribution is minimal for the primary N_2O product (nitrous dioxide, NO_2) columns above Jungfraujoch. Such small impact is found here also for the N_2O stratospheric columns themselves. From the comparison of the panels in the top row of Fig. 7.3, we conclude that version 6 of WACCM underestimates the QBO contribution to the variability of the N_2O columns in the Southern Hemisphere, performing worse than its version 4.

The contribution from the solar cycle to the recovered fit is generally smaller than the QBO contribution and largely varies among the datasets. The ENSO has negligible impact on the fits of the N_2O stratospheric columns.

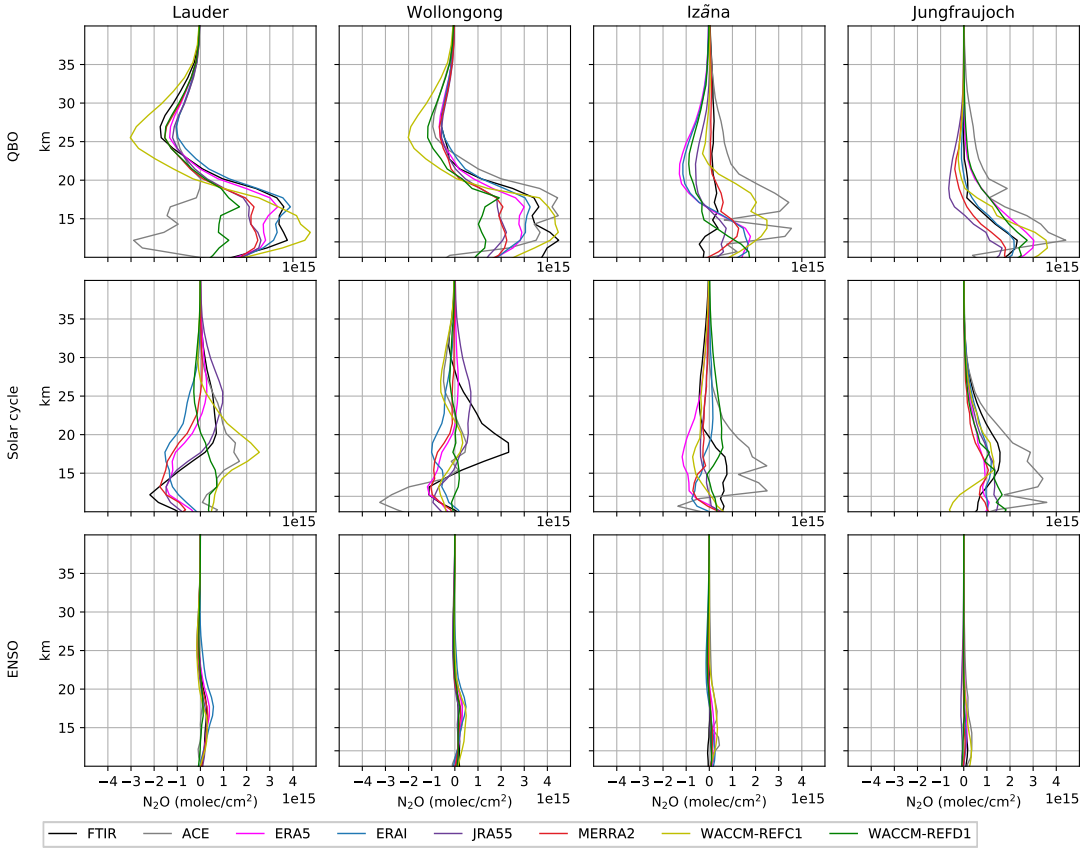

Figure 7.3: Vertical profiles of the coefficients of the DLM regressors (QBO, solar, ENSO) on the N_2O stratospheric columns at the four stations for all the datasets. First row: QBO, second row: solar cycle, third row: ENSO. Columns from left to right: Lauder, Wollongong, Izãna, Jungfraujoch. The color code is in the legend.

7.2.2 Hemispherical Differences of N_2O columns

This Section discusses the inter-hemispheric differences between corresponding latitudes for the linear fits of the N_2O stratospheric columns obtained with the observations and model simulations. This comparison aims to provide additional insights about the hemispheric differences of the N_2O stratospheric columns investigated in the previous Section, similarly to the works of Strahan et al. (2020) for HNO_3 and HCl and Prignon et al. (2021) for F_y. Here, these differences were found too challenging to interpret for inclusion in the manuscript submitted to JGR: Atmospheres (Sect. 7.1). Figure 7.4 shows these inter-hemispheric differences between the FTIR stations at mid-latitudes (Lauder-Jungfraujoch) and subtropical latitudes (Wollongong-Izãna) for all the datasets.

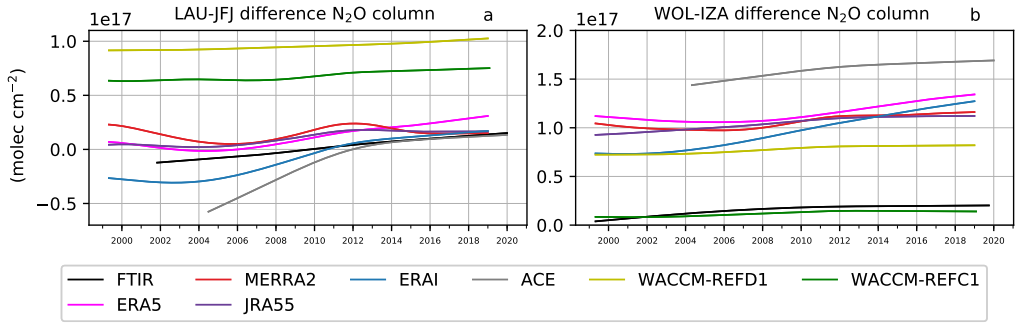

Figure 7.4: Hemispheric differences of N_2O stratospheric columns between mid-latitudes (Lauder, LAU - Jungfraujoch, JFJ; panel a) and subtropical (Wollongong, WOL - Izãna, IZA; panel b) stations. The color code is in the legend. The model data are interpolated and vertically regridded to fit the station needs, and the AVKs have been applied.

At mid-latitudes (Fig. 7.4a), the N_2O columns obtained with the FTIR observations are smaller in the SH than in the NH before 2010. After 2010, they become larger in the SH, indicating a more rapid accumulation of N_2O in the SH compared to the NH. Similarly to FTIR, the N_2O columns measured by ACE-FTS are smaller in the SH compared to the NH until 2012, and afterward the opposite becomes true. However, as discussed in Sect. 7.1, the ACE-FTS measurements are characterized by a poor sampling, and their N_2O stratospheric columns do not provide a complete picture above the northern mid-latitudes. Regarding the BASCOE CTM simulations, ERAI simulates negative hemispheric differences twice larger than those from the FTIR observations before 2011. Afterward, ERAI delivers larger N_2O stratospheric columns in the SH compared to the NH, in excellent agreement with

the FTIR observations. ERA5 simulates near-zero hemispheric differences before 2007 and larger stratospheric columns in the SH than in the NH afterward. For the observations and the CTM simulations driven by ECMWF reanalyses, the larger N_2O stratospheric columns above the SH compared to the NH after 2009/2010 confirm the differences in transport between the hemispheres over the last decade. These differences are consistent with the findings of the previous Section and with the results of Strahan et al. (2020) and Prignon et al. (2021).

The BASCOE CTM simulations driven by JRA55 and MERRA2 do not deliver results as clear as the experiments driven by the ECMWF reanalyses: their simulated hemispheric differences undulate around zero. Ultimately, the WACCM simulations consistently deliver larger N_2O columns in the SH than in the NH, especially WACCM-REFC1, and both model versions simulate a faster N_2O accumulation above the SH compared to the NH.

Above the subtropical latitudes (Fig. 7.4b), the N_2O stratospheric columns are consistently larger above the SH than above the NH for all the datasets. This difference is due to the smaller N_2O columns above Izãna compared to Wollongong as discussed in the previous Section. The hemispheric differences are nearly constant for all the datasets except for the ECMWF reanalyses. The BASCOE CTM simulations driven by ERAI and ERA5 initially show constant hemispheric differences until 2004 and 2009, respectively, followed by increasing N_2O columns above the SH compared to the NH, which is consistent with the pattern above the mid-latitudes, but this is not seen in the FTIR observations nor with the other reanalyses.

The inter-hemispheric differences reported in Fig. 7.4 confirm the findings of the previous Section for the observations and the BASCOE runs driven by ERA5 and ERAI. However, they do not show the 5- to 7-years variability discussed in Strahan et al. (2020) and Prignon et al. (2021), which was attributed to the contribution of the QBO on the BDC transport changes on such "short" time scales. The lack of short-term variability in Fig. 7.4 is due to the methods used in the different studies to obtain the hemispheric differences. In particular, the present study treats the QBO differently from Strahan et al. (2020) and Prignon et al. (2021). Within the DLM, the QBO is treated as a regressor (see Sect. 5.2.3), and the linear fit μ_t in Fig. 7.4 does not include any variability related to the QBO. On the contrary, Strahan et al. (2020) used time series of anomalies of the HNO_3 and HCl columns, and Prignon et al. (2021) used the bootstrap method that does not include any regressor (see Sect. 5.2.1). Those methods do not eliminate the variability due to the QBO in the time series of their stratospheric columns, allowing this shorter-term variability to appear in the linear fit.

7.2.3 Changes of ADV and MIX in the remaining datasets

This Section discusses the changes of the ADV and MIX terms of the N_2O TEM budget for those model simulations not included in Sect. 7.1: the BASCOE CTM experiments driven by JRA55 and MERRA2 and the WACCM-REFC1 simulation. Figure 7.5 shows those changes in the ADV and MIX terms, computed as for Fig. 6 of Sect. 7.1. In this Section (as in subsect. 5 of Sect. 7.1), we will refer to the N_2O trends shown in Fig. 4 of Sect. 7.1 as "direct" trends, in order to distinguish them from the N_2O changes derived from changes in ADV and MIX.

Considering the ADV term, it is enhanced above the Tropics in the upper stratosphere (i.e., above 10 hPa) in all datasets, leading to an N_2O increase over that region. This is consistent with the positive direct N_2O trends for the respective datasets and reinforces the hypothesis of a contribution from enhanced advection in driving the N_2O trends over that region. Above the northern subtropics in the lower stratosphere, all datasets show an N_2O increase due to a stronger ADV term, which corresponds to the positive direct N_2O trends over the same region. As discussed in Sect. 7.1, this confirms the role of a strengthening shallow branch of the BDC as a contribution to the N_2O trends. In the lower stratosphere of the northern polar latitudes, the negative changes in the ADV term in ERAI and JRA55 result in an N_2O decrease, which is consistent with their negative direct N_2O trends over the same region, especially for ERAI. This negative ADV term results from enhanced downwelling over the northern polar region, consistent with the enhanced tropical upwelling (see discussion in Sect. 7.1).

The impact of the changes in the MIX term on the N_2O abundances varies among the datasets. For the BASCOE simulation driven by ERAI, the positive changes in the MIX term contribute to the positive direct N_2O changes only above the lower stratospheric southern polar region. This contribution is in agreement with the enhanced mixing over the SH found using this reanalysis (e.g., Ploeger et al., 2015a). Considering the JRA55 simulation, the positive changes in the MIX term can contribute to the positive direct N_2O trends over several regions, e.g., above 10 hPa over the northern mid-latitudes. However, the contributions from enhanced mixing to the N_2O changes in the JRA55 simulation need further studies using additional methods that do not involve tracers (e.g., effective diffusivity). For the WACCM-REFC1 simulation, the changes in the MIX term have little impact on the direct N_2O trends, except for around 60°S between 50 and 80 hPa, where they correspond to positive direct N_2O trends.

In conclusion, the enhanced advection term contributes to the N_2O trends above the Tropics and the polar latitudes, while changes in the mixing terms

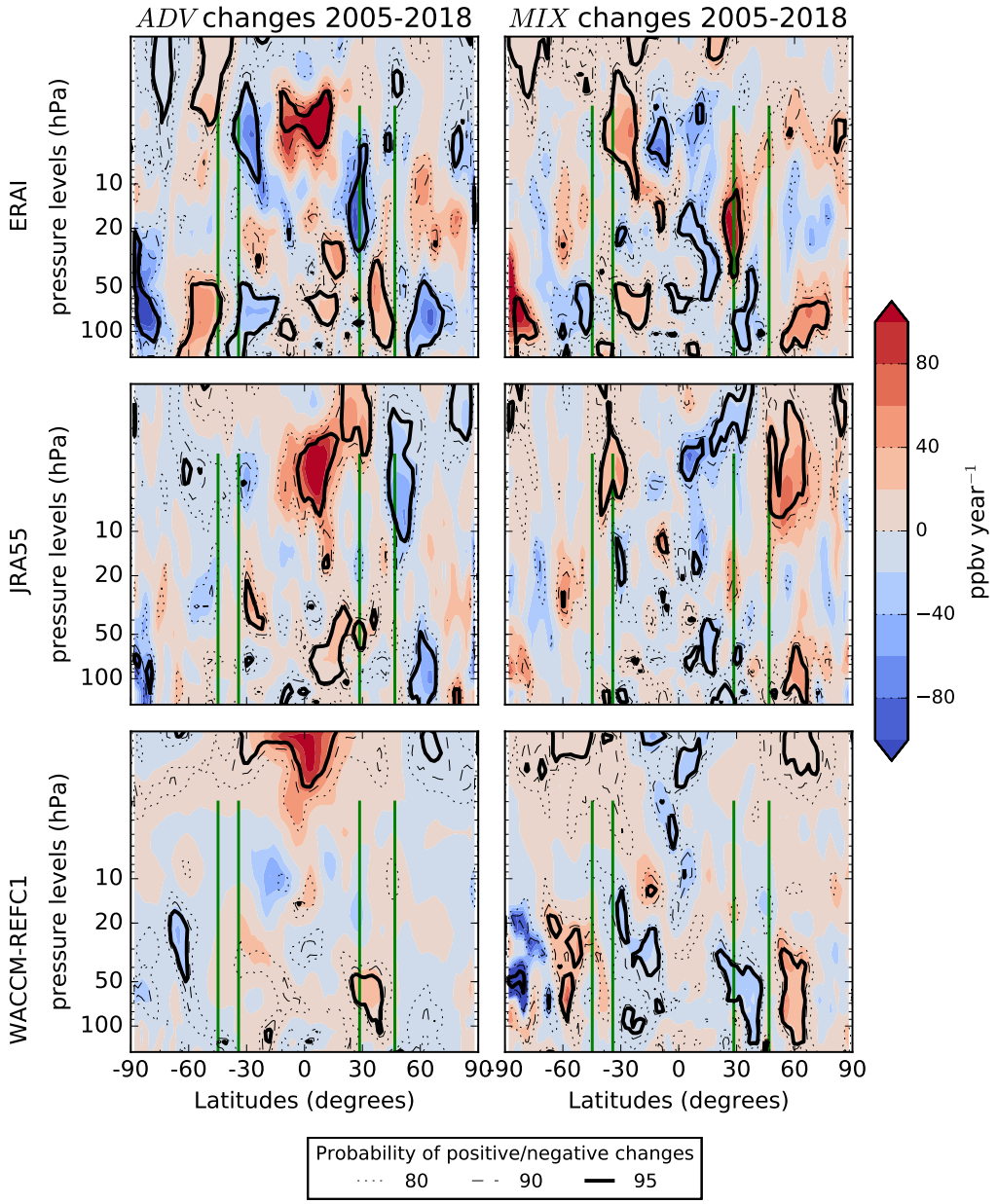

Figure 7.5: Latitude-pressure cross sections of the changes of the *ADV* term (A_z+A_y, central panel, ppbv year^{-1}) and *MIX* term (M_z+M_y, left panel, ppbv year^{-1}) of the TEM N_2O budget for ERAI, JRA55 and WACCM-REFC1 (2005-2018). The dotted, dashed and continuous lines represent the probability at 80, 90 and 95% of positive/negative N_2O changes, respectively. The green vertical lines identify the position of the FTIR stations together with their vertical coverage.

do not significantly impact the N_2O trends, for all the datasets considered here. These results agree with the findings discussed in the subsect. 5 of Sect. 7.1.

8 Conclusions and Outlook

This thesis investigated the climatology and the decadal changes of the N_2O abundances and the transport contributions to their TEM budget. We performed this investigation using a variety of datasets. As observational datasets, we used ground-based FTIR observations at four NDACC stations: Lauder (45°S, New Zealand), Wollongong (34°S, Australia), Izãna (28°N, Spain) and Jungfraujoch (46°N, Switzerland), and satellite observations from the ACE-FTS instrument. We also used the chemical reanalysis BRAM2, internally developed at BIRA-IASB. We compared the observations and BRAM2 with the output of the BASCOE CTM driven by five meteorological reanalyses (ERAI, ERA5, JRA55, MERRA and MERRA2), and with the output of the Whole Atmosphere Community Climate Model: two configurations of its version 4 generated the datasets WACCM4 and WACCM-REFC1, and its version 6 generated the dataset WACCM-REFD1.

The main conclusions of the thesis are presented in Section 8.1 and the possible future perspectives are outlined in Section 8.2.

8.1 Conclusions

In the following, we present the most relevant conclusions obtained in this thesis relative to the two thesis objectives outlined in Sect. 3. **Objective 1** - Evaluate the realism of the BDC in a CCM by investigating and evaluating the climatological abundances of N_2O and the impact of the BDC on those abundacies, and comparing them with CTM simulations and a chemical reanalysis. **Objective 2** - Evaluate the changing BDC in the same CCM by studying multi-decadal and decadal changes of N_2O in the stratosphere, comparing them with observations and CTM simulations, and calculating the impact of the BDC on those changes.

8.1.1 Conclusions for Objective 1

At the beginning of this thesis, it was decided to use the TEM analysis as an additional tool to study the N_2O changes; in particular, the N_2O TEM budget was computed to investigate the impact of transport on the N_2O rates of change in the stratosphere. Then, the climatologies of the transport terms of the N_2O TEM budget were evaluated, focusing on the contributions from the vertical advection (A_z) and horizontal mixing (M_y), together with the N_2O mixing ratios themselves in the mid-stratosphere. Within this evaluation, we used the REFC1 configuration of the WACCM model (WACCM-REFC1) together with a sensitivity test with a different representation of the gravity

waves parametrization over the SH (WACCM4). We compared the WACCM simulations with four simulations of the BASCOE CTM driven by ERAI, JRA55, MERRA and MERRA2 and also with the chemical reanalysis of Aura MLS, BRAM2, which we used as a reference, because it is the dataset that is most constrained by observations.

We showed that the WACCM and the BASCOE simulations generally agree with BRAM2 regarding the climatologies of N_2O mixing ratios. However, the BASCOE simulations present a large spread of the N_2O abundances over the tropical regions, reflecting the spread of the mean AoA obtained with the same driving reanalyses by Chabrillat et al. (2018).

Concerning the transport terms of the TEM budget, the A_z contribution agrees well among the datasets, notably above the NH, while larger differences arise for M_y. Over the NH, the differences in M_y between WACCM and the BASCOE simulations could be attributed to the weaker forcing from resolved waves in WACCM compared to the reanalyses driving the CTM. Over the SH and, in particular, over the Antarctic, there are significant differences between WACCM and the BASCOE simulations in M_y (five times larger in the CTM than WACCM), but the residual of the budget challenges these differences in M_y.

The sensitivity test with WACCM confirms that the updated parameterization of the gravity waves results in a more realistic simulation of the downwelling over the Antarctic mid-stratosphere. The new parameterization leads to enhanced contribution from A_z and more realistic N_2O volume mixing ratios because of the improved timing of the polar vortex breakup.

8.1.2 Conclusions for Objective 2

After evaluating the climatologies of the mid-stratospheric N_2O abundances and their TEM budget terms, we investigated their interannual variability in Chapter 7 in order to address the main objective of the ACCROSS project. Compared to Chapter 6, we added observations of N_2O mixing ratios from the ACE-FTS satellite and ground-based FTIR instruments, together with the newer version of ERAI, ERA5, and version 6 of the WACCM model. The simulation from the BASCOE CTM driven by MERRA is not included because that reanalysis ended in 2015.

First, the N_2O stratospheric columns from the model simulations and the ACE-FTS observations were compared with those obtained from the four FTIR stations. This comparison revealed a good agreement above Lauder and Wollongong, and larger differences above Izãna and Jungfraujoch. Concerning the WACCM model, the stratospheric N_2O columns are underestimated compared with the FTIR observations at all stations, especially in the

NH, with the largest differences above Jungfraujoch. In addition, version 6 of WACCM performs worse than version 4, with larger differences compared to the FTIR, except above Wollongong. The trends in the N_2O stratospheric columns over the 2005-2018 period are generally larger above the SH than the NH. This reveals differences in the transport between the hemispheres and is consistent with recent studies that revealed hemispherical differences in trends of HNO_3 and HCl (Strahan et al., 2020) and F_y (Prignon et al., 2021) columns measured at FTIR stations over the past decade. The trends in the N_2O stratospheric columns simulated by the WACCM model do not show significant hemispherical differences, but their agreement with the FTIR observations depends on the hemisphere. Both the WACCM versions largely disagree with the FTIR observations above the SH (approximately 40% difference in the N_2O stratospheric trends at the Wollongong station), while they are in excellent agreement above the NH.

The vertical resolution of the FTIR retrievals is quantified with the stratospheric DOFS, which are around 2 for the stations in the SH but are 1.5 for Izãna and 1.1 for Jungfraujoch. These lower DOFS for the instruments above the NH limit our analysis to one stratospheric column. Hence, within this thesis, the detection of potentially negative trends of N_2O columns in the mid-stratosphere is hindered by the large N_2O increase in the lowermost stratosphere, which arises from its continuous increase at the surface.

In order to have a complete depiction of the decadal changes in the N_2O columns, we investigated latitudinal and vertical cross sections of the trends in the N_2O mixing ratios obtained from the ACE-FTS observations and the model simulations. Since the temporal and spatial sampling of ACE-FTS is limited (see Sect. 4.3.3), the same sampling was first applied to the model output as to the satellite measurements in order to perform a fair comparison. The ACE-FTS measurements show a meridional dipole in the N_2O trends in the mid-lower stratosphere, with negative values in the northern mid-latitudes and positive values in the SH. However, ACE-FTS samples more often the high latitudes and the application of this sampling to the model output consistently enhances the N_2O trends, both in the positive and negative directions. Using continuous time sampling on the native model grids, ERAI and, to a lesser extent, ERA5 still simulate the meridional dipole in the N_2O trends, consistently with a large number of modeling studies using both idealized and real tracers (e.g., Chabrillat et al., 2018; Ploeger et al., 2021; Prignon et al., 2021), but MERRA2, JRA55 and WACCM fail to reproduce the meridional dipole. We show that WACCM-REFD1 is an improvement over WACCM-REFC1 because it simulates the positive trend above the southern mid-latitudes not only in the lowermost stratosphere but also in the mid-lower stratosphere.

Two sensitivity tests using the BASCOE CTM driven by ERA5 were performed: one keeping N_2O constant at the surface with time-dependent dynamics (cst-N_2O), and the other using a biennial repetition of the dynamics with increasing N_2O at the surface (cst-dyn). The cst-N_2O experiment shows that the extratropical N_2O trends in the mid-lower stratosphere are due to the impact of changes in the stratospheric transport. The cst-dyn simulation shows that, while N_2O does increase everywhere, its trend over 2005-2018 would not be significantly positive in the northern mid-stratosphere if it was not for the changing dynamics. Furthermore, the hemispheric asymmetry in the significance of these trends between 20 and 50 hPa arises from the larger dynamical variability in the northern extratropics on shorter timescales, i.e., with one single QBO cycle repeating indefinitely.

The N_2O TEM budget for the model datasets reveals a significant N_2O increase in the tropical mid-high stratosphere and a significant decrease in the northern extratropical lower stratosphere, which result from enhanced tropical upwelling and extratropical downwelling, respectively. For the ERA5 simulation, the positive N_2O trend above the southern mid-latitudes (part of the meridional dipole) can be attributed to the impact of changes in both advection and mixing; this is consistent with previous studies, both using AoA (Ploeger et al., 2015a) and N_2O (Stiller et al., 2017).

Concerning the WACCM simulations, the lack of strong hemispheric asymmetries in the trends of the N_2O stratospheric columns and volume mixing ratios highlights small inter-hemispheric differences in the stratospheric transport. As already stated in the previous Section, this is a consequence of the irrealistic stratospheric transport simulated by WACCM over the SH. However, version 6 of WACCM still is an improvement compared to version 4 because it simulates more realistic trends in N_2O volume mixing ratios above the southern mid-latitudes. This improvement can be related to the changes in the parametrization of the gravity waves in WACCM version 6 that followed the increase of the horizontal resolution. Concerning the N_2O TEM budget, both WACCM versions confirm the strengthening of the tropical upwelling through its impact on the N_2O rates of change. On the other hand, while WACCM version 6 simulates a strengthening of the polar downwelling as the CTM simulations, version 4 of WACCM does not succeed in doing so. Overall, version 6 of WACCM performs better than version 4 concerning changes in N_2O volume mixing ratios over the SH and to changes in downwelling over the north pole.

We have shown the relevance of N_2O as a tracer for stratospheric transport studies. Since it is a measurable tracer, N_2O allows direct comparisons with ground-based and satellite observations. Furthermore, the rate of change of N_2O at the surface is well-known and approximately linear and the chemical

losses are limited to the higher stratosphere. This relatively simple chemistry, combined with its long life, makes N_2O an excellent tracer for stratospheric transport studies.

8.1.3 General Conclusions

From what discussed earlier, we can draw some general conclusions common to Chapters 6 and 7. We have confirmed that the N_2O abundances measured from satellite have changed in the past decades, decreasing over the Southern Hemisphere and increasing above the Northern Hemisphere. However, the analysis of the satellite and the ground-based observations and chemical reanalysis revealed different sorts of dataset-dependent shortcomings. The chemical reanalysis BRAM2 assimilated N_2O data from a version of MLS that does not allow trend studies. The FTIR observational datasets are very valuable because of their long data record, but they would need improvements in terms of vertical resolution and spatial and temporal coverage to enable full evaluation of model transport as attempted here.

Sensitivity tests have shown that the observed N_2O changes are caused by changes in the stratospheric transport due to the BDC. The N_2O climatologies and decadal changes simulated by the WACCM and BASCOE CTM experiments show differences among each other, with the CTM simulations driven by the ECMWF reanalyses that agree best with the observations. This indicates a better representation of the BDC and its changes in the ECMWF reanalyses than in the other reanalyses. On the other hand, the WACCM model does not correctly simulate the BDC in the Southern Hemisphere and provides too small inter-hemispheric differences with regard to its decadal changes. The CCM is not expected to perform as well as the CTM since its dynamics is not constrained by the observations.

Using the N_2O TEM budget, we found that the residual advection contribution agrees well among datasets and that its changes are robust and contribute to the tropical N_2O trends consistently with previous studies. On the other hand, the mixing contribution largely differs among the datasets and its trends are more uncertain, and do not explain the modeled trends of N_2O. Overall, CTM simulations provide valuable and additional insights compared to direct observations and allow useful evaluations of the representation of the BDC in CCMs such as WACCM.

8.2 Outlook

The results obtained within this thesis raise several questions and call for further studies and actions on several topics. In the following, the major

perspectives for future research that stem from this thesis are outlined.

8.2.1 Need of Improved Long-Term Observations of N_2O

The N_2O observations used in this thesis suffer from instrument-dependent shortcomings. Ground-based observations obtained from FTIR instruments at Izãna and Jungfraujoch lack adequate vertical resolution to resolve more than one stratospheric layer. In the future, the information content available for the Jungfraujoch and Izãna stations should be improved in order to be able to resolve more layers in the stratosphere.

Satellite measurements from ACE-FTS are robust but suffer from poor temporal and spatial sampling, which affects the retrieved trends of N_2O. This shortcoming highlights that more regular coverage in the satellite measurements is essential to derive reliable trends of long-lived tracers. The MLS measurements in the limb geometry are characterized by a much better spatial and temporal sampling compared to those obtained with ACE-FTS. However, even the latest MLS version (v5) suffers from an unrealistic drift that makes the N_2O product not suitable for trend studies. When the newer MLS version of the drift in the N_2O product is corrected, the present study should be repeated using these high-value observations and also a chemical reanalysis similar to BRAM2 in order to provide a reference for the changing TEM budget.

8.2.2 Added Value of Modelling Studies

Model simulations from WACCM and the BASCOE CTM provide valuable insights into transport changes and their impact on the stratospheric composition. In particular, sensitivity tests and the TEM analysis have proven to be necessary to understand the role of transport in the N_2O changes.

Within the TEM framework, the climatologies and trends of the contribution from the mixing present considerable disagreements among the datasets. In addition, the TEM analysis suffers from large uncertainties due to the difficulty of closing its budget in regions with strong gradients, e.g., the Antarctic region. Thus, it is important to better understand the causes of these large uncertainties. To this end, the recent study of Sato et al. (2021) is helpful, as it proposes a new formulation of the residual flow and its governing equations in 3-D. This formulation should be extended to tracer transport (similarly to the TEM budget in Sect. 5.1). This framework would reveal the impact of the inclusion of longitudinal variations on the resolved mixing and, consequently, on the residual of the tracer budget. Complementary methods such as evaluating the effective diffusivity in each dataset (Abalos

et al., 2016a,b) would also help to understand the effect of mixing in regions of strong gradients of N_2O.

We showed that sensitivity tests with WACCM and the BASCOE CTM driven by ERA5 provide an added value that allows us to better understand the role of dynamics and transport on the N_2O changes. The WACCM4 sensitivity test allowed us to assess the impact of an updated parametrization of OGW in the SH on the simulated N_2O and its transport over the Antarctic. Given the diversity of the gravity waves parametrizations in the forecast models that create the reanalyses, similar tests could be performed with these unconstrained models. Such tests could provide insights to improve the parametrizations of gravity waves in numerical weather prediction and climate models.

Sensitivity tests such as cst-N_2O and cst-dyn should be extended to other datasets, e.g., the BASCOE simulation driven by MERRA2 and WACCM. Future sensitivity tests could investigate the differences in the transport between the hemispheres. Such investigation could be done by running a model with fixed tracer mixing ratios at the surface for one hemisphere and running the same model but fixing the mixing ratios for the other hemisphere. Comparing the trends of long-lived tracers between the two experiments could provide additional insights into the differences in the build-up of such tracers in the stratosphere between the hemispheres.

Given the importance of the modelling studies, it is important to extend investigations like the present one to a larger number of models. In particular, it would be beneficial to use the latest generation CCMs that participate in the CCMI-2022 and CMIP6 initiatives. In addition, an added value would be the use of those models in specified dynamics mode, to be compared with their free-running configuration to assess their representation of the transport and the impact of nudging reanalyses to a free-running CCM.

8.2.3 General Outlook

When we first started working on the ACCROSS project in October 2016, the knowledge of the scientific community on BDC changes was uncertain: model projections simulated a strengthening of the BDC across the stratosphere in the past and future decades, while indirect measurements did not confirm such findings for the past decades. At the same time, the hemispheric asymmetry in the indirect and direct measurements of the BDC trends was emerging.

Within these uncertainties, the ACCROSS project aimed to improve our understanding of the past circulation changes using long-lived tracers, combining robust long-term observations and state-of-the-art models. Within

the ACCROSS project, we started looking at the mean AoA, then we moved to the long-lived tracer N_2O, and we ended up characterizing its abundances and decadal changes together with its TEM budget. The present work confirmed the acceleration of the BDC in the Tropics and the recently discovered hemispheric asymmetry in the BDC changes in the extra-tropics. It was also found that the N_2O observations lack the necessary resolution and sampling frequency to adequately resolve its changes in the stratosphere. However, the BASCOE CTM simulations have proven to be highly beneficial because they provided a valuable understanding of the N_2O and BDC changes, complementary to those derived from the observations. Concerning the WACCM model, its free-running dynamics does not allow its simulations to correctly represent the inter-hemispherical differences in the BDC and its changes as in the CTM simulations. At the same time, despite differences with the CTM simulations remain, the changes between the different WACCM configurations and versions have significantly improved the CCM performances in that regard.

Given the promising results obtained with the BASCOE CTM and the improvements in the newest WACCM version, future research on the BDC changes must exploit the full capabilities of CTM and CCM simulations: from appropriate sensitivity tests to the extension to the next-generation models. At the same time, the current long-term N_2O observations need improvements in terms of vertical resolution and quality of the retrieval. While modelling studies without the inclusion of observations are undoubtedly incomplete, this work shows that the opposite is also true for studies of BDC changes: current N_2O observations do not provide sufficient insights on stratospheric trends, and the inclusion of relevant and complementary model simulations is necessary to the interpretation of the results and increases the relevance of such studies.

Appendix A List of Acronyms

3D-Var Three-dimensional variational

4D-Var Four-dimensional variational

ACE-FTS Atmospheric Chemistry Experiment - Fourier Transform Spectrometer

ANA Analysis state

AoA Age of Air

AR Autoregressive process

ASM Assimilation state

AVK AVeraging Kernel

BASCOE Belgian Assimilation System of ObsErvations

BDC Brewer-Dobson Circulation

BIRA-IASB Belgisch Instituut voor Ruimte-Aeronomie - Institut d'Aéronomie Spatiale de Belgique

BRAM BASCOE reanalysis of Aura MLS

CAM Community Atmosphere Model

CCM Chemistry-Climate Model

CCMI Chemistry-Climate Model Intercomparison

CEM Conventional Eulerian Mean

CESM Community Earth System Model

CFC Chlorofluorocarbon

CMIP Coupled Model Intercomparison Project

CTM Chemistry-Transport Model

DLM Dynamical Linear Modelling

DOFS Degree of Freedom for Signal

ECMWF European Centre for Medium-Range Weather Forecast

EnKF Ensemble Kalman Filter

ENSO El-Niño Southern Oscillation

ERA5 ECMWF fifth-generation reanalysis

ERA-Interim ECMWF-Interim reanalysis

ESM Earth System Model

FFSL Flux-Form Semi Lagrangian

FGAT First Guess at Appropriate Time

FTIR Fourier Transform Infrared

FV Finite Volume

GCM General Circulation Model

GEOS Goddard Earth Observing System

GHG Greenhouse Gases

GSM Global Spectral Model

GWP Global Warming Potential

HCFC Hydrochlorofluorocarbon

HPC High Performance Computer

IFS Integrated Forecast System

IR Infrared

JMA Japanese Meteorological Agency

JPL Jet Propulsion Laboratory

JRA-55 JMA 55-year reanalysis

MAESTRO Measurement of Aerosol Extinction in the Stratosphere and Troposphere Retrieved by Occultation

MERRA Modern-Era Retrospective analysis for Research and Applications

MERRA-2 Modern-Era Retrospective analysis for Research and Applications version 2

MIPAS Michelson Interferometer for Passive Atmospheric Sounding

MLR Multiple Linear Regression

MLS Microwave Limb Sounder

MOZART Model for Ozone and Related Chemical Tracers

NASA National Aeronautic Space Agency

NCAR National Center for Atmospheric Research

NCEP National Centers for Environmental Prediction

NDACC Network for the Detection of Atmospheric Composition Change

NH Northern Hemisphere

NOAA National Oceanic and Atmospheric Administration

NOGW Non-Orographic Gravity Waves

ODS Ozone Depleting Substance

OGW Orographic Gravity Waves

PSC Polar Stratospheric Cloud

QBO Quasi-Biennial Oscillation

SD Specified Dynamics

SH Southern Hemisphere

SPARC Stratosphere-troposphere Processes And their Role in Climate

S-RIP SPARC Reanalysis Intercomparison Poject

TEM Transformed Eulerian Mean

TILS Tracer Increasing Linearly at the Surface

TTL Tropical Tropopause Layer

UK United Kingdom

UNEP United Nations Environment Programme

UNFCC United Nations Framework Convention on Climate Change

UV UltraViolet

VIS Visible

vmr volume mixing ratio

WACCM Whole Atmosphere Community-Climate Model

WMO World Meteorological Organization

Appendix B List of Papers

Chabrillat, S., Vigouroux, C., Christophe, Y., Engel, A., Errera, Q., **Minganti, D.**, Monge-Sanz, B. M., Segers, A., and Mahieu, E.: Comparison of mean age of air in five reanalyses using the BASCOE transport model, Atmos. Chem. Phys., 18, 14715-14735, https://doi.org/10.5194/acp-18-14715-2018, 2018.

Prignon, M., Chabrillat, S., **Minganti, D.**, O'Doherty, S., Servais, C., Stiller, G., Toon, G. C., Vollmer, M. K., and Mahieu, E.: Improved FTIR retrieval strategy for HCFC-22 (CHClF2), comparisons with in situ and satellite datasets with the support of models, and determination of its long-term trend above Jungfraujoch, Atmos. Chem. Phys., 19, 12309-12324, https://doi.org/10.5194/acp-19-12309-2019, 2019.

Minganti, D., Chabrillat, S., Christophe, Y., Errera, Q., Abalos, M., Prignon, M., Kinnison, D. E., and Mahieu, E.: Climatological impact of the Brewer-Dobson circulation on the N2O budget in WACCM, a chemical reanalysis and a CTM driven by four dynamical reanalyses, Atmos. Chem. Phys., 20, 12609-12631, https://doi.org/10.5194/acp-20-12609-2020, 2020.

Prignon, M., Chabrillat, S., Friedrich, M., Smale, D., Strahan, S. E., Bernath, P. F., Chipperfield, M. P., Dhomse, S. S., Feng, W., **Minganti, D.**, Servais, C., Mahieu, E. (2021). Stratospheric fluorine as a tracer of circulation changes: Comparison between infrared remote-sensing observations and simulations with five modern reanalyses. Journal of Geophysical Research: Atmospheres, 126, e2021JD034995. https://doi.org/10.1029/2021JD034995

Minganti, D., Chabrillat, S., Errera, Q., Prignon, M., Kinnison, D.E., Garcia, R.R., Abalos, M., Alsing, J., Schneider, M., Smale, D., Jones, N., Mahieu, E. (2022). N2O rate of change as a diagnostic of the Brewer-Dobson Circulation in the stratosphere, Journal of Geophysical Research: Atmospheres, under review https://doi.org/10.1002/essoar.10510213.1

References

Abalos, M., Legras, B., and Shuckburgh, E. (2016a). Interannual variability in effective diffusivity in the upper troposphere/lower stratosphere from reanalysis data. *Quarterly Journal of the Royal Meteorological Society*, 142(697):1847–1861.

Abalos, M., Polvani, L., Calvo, N., Kinnison, D., Ploeger, F., Randel, W., and Solomon, S. (2019). New insights on the impact of ozone-depleting substances on the Brewer-Dobson circulation. *Journal of Geophysical Research: Atmospheres*, 124(5):2435–2451.

Abalos, M., Randel, W., Kinnison, D., and Serrano, E. (2013). Quantifying tracer transport in the tropical lower stratosphere using WACCM. *Atmospheric Chemistry and Physics*, 13(21):10591–10607.

Abalos, M., Randel, W. J., and Birner, T. (2016b). Phase-speed spectra of eddy tracer fluxes linked to isentropic stirring and mixing in the upper troposphere and lower stratosphere. *Journal of the Atmospheric Sciences*, 73(12):4711–4730.

Abalos, M., Randel, W. J., Kinnison, D. E., and Garcia, R. R. (2017). Using the artificial tracer e90 to examine present and future UTLS tracer transport in WACCM. *Journal of the Atmospheric Sciences*, 74(10):3383–3403.

Alsing, J. A. (2019). dlmmc: Dynamical linear model regression for atmospheric time-series analysis. *Journal of Open Source Software*, 4(37):1157.

Andrews, D. and McIntyre, M. (1978a). Generalized Eliassen-Palm and Charney-Drazin theorems for waves on axismmetric mean flows in compressible atmospheres. *Journal of the Atmospheric Sciences*, 35(2):175–185.

Andrews, D. and Mcintyre, M. E. (1976). Planetary waves in horizontal and vertical shear: The generalized Eliassen-Palm relation and the mean zonal acceleration. *Journal of the Atmospheric Sciences*, 33(11):2031–2048.

Andrews, D. G., Holton, J. R., and Leovy, C. B. (1987). *Middle atmosphere dynamics*. Number 40. Academic press.

Andrews, D. G. and McIntyre, M. (1978b). An exact theory of nonlinear waves on a lagrangian-mean flow. *Journal of fluid Mechanics*, 89(4):609–646.

Andrews, D. G. and McIntyre, M. (1978c). On wave-action and its relatives. *Journal of Fluid Mechanics*, 89(4):647–664.

Assmann, R. (1902). *Über die Existenz eines wärmeren Luftstromes in der Höhe von 10 bis 15km.*

Austin, J. and Li, F. (2006). On the relationship between the strength of the Brewer-Dobson circulation and the age of stratospheric air. *Geophysical research letters*, 33(17).

Bader, W., Bovy, B., Conway, S., Strong, K., Smale, D., Turner, A. J., Blumenstock, T., Boone, C., Collaud Coen, M., Coulon, A., et al. (2017). The recent increase of atmospheric methane from 10 years of ground-based NDACC FTIR observations since 2005. *Atmospheric Chemistry and Physics*, 17(3):2255–2277.

Baines, P. G. and Palmer, T. (1990). Rationale for a new physically-based parameterization of subgridscale orographic effects.

Baldwin, M., Gray, L., Dunkerton, T., Hamilton, K., Haynes, P., Randel, W., Holton, J., Alexander, M., Hirota, I., Horinouchi, T., et al. (2001). The quasi-biennial oscillation. *Reviews of Geophysics*, 39(2):179–229.

Baldwin, M. P., Ayarzagena, B., Birner, T., Butchart, N., Butler, A. H., Charlton-Perez, A. J., Domeisen, D. I. V., Garfinkel, C. I., Garny, H., Gerber, E. P., Hegglin, M. I., Langematz, U., and Pedatella, N. M. (2021). Sudden Stratospheric Warmings. *Reviews of Geophysics*, 59(1):e2020RG000708. e2020RG000708 10.1029/2020RG000708.

Baldwin, M. P., Birner, T., Brasseur, G., Burrows, J., Butchart, N., Garcia, R., Geller, M., Gray, L., Hamilton, K., Harnik, N., Hegglin, M. I., Langematz, U., Robock, A., Sato, K., and Scaife, A. A. (01 Jan. 2019). 100 Years of Progress in Understanding the Stratosphere and Mesosphere. *Meteorological Monographs*, 59:27.1 – 27.62.

Ball, W. T., Alsing, J., Mortlock, D. J., Rozanov, E. V., Tummon, F., and Haigh, J. D. (2017). Reconciling differences in stratospheric ozone composites. *Atmospheric Chemistry and Physics*, 17(20):12269–12302.

Ball, W. T., Alsing, J., Mortlock, D. J., Staehelin, J., Haigh, J. D., Peter, T., Tummon, F., Stübi, R., Stenke, A., Anderson, J., Bourassa, A., Davis, S. M., Degenstein, D., Frith, S., Froidevaux, L., Roth, C., Sofieva, V., Wang, R., Wild, J., Yu, P., Ziemke, J. R., and Rozanov, E. V. (2018). Evidence for a continuous decline in lower stratospheric ozone offsetting

ozone layer recovery. *Atmospheric Chemistry and Physics*, 18(2):1379–1394.

Banks, P. M. and Kockarts, G. (2013). *Aeronomy*. Elsevier.

Barret, B., Gouzenes, Y., Le Flochmoen, E., and Ferrant, S. (2021). Retrieval of Metop-A/IASI N_2O Profiles and Validation with NDACC FTIR Data. *Atmosphere*, 12(2).

Bates, D. R. and Nicolet, M. (1950). The photochemistry of atmospheric water vapor. *Journal of Geophysical Research*, 55(3):301–327.

Bekki, S. and Lefèvre, F. (2009). Stratospheric ozone: History and concepts and interactions with climate. In *EPJ Web of Conferences*, volume 1, pages 113–136. EDP Sciences.

Beljaars, A. (1995). The impact of some aspects of the boundary layer scheme in the ECMWF model. In *Proc. Seminar on Parameterization of Sub-Grid Scale Physical Processes*.

Beljaars, A. C., Brown, A. R., and Wood, N. (2004). A new parametrization of turbulent orographic form drag. *Quarterly Journal of the Royal Meteorological Society*, 130(599):1327–1347.

Bellouin, N., Davies, W., Shine, K. P., Quaas, J., Mülmenstädt, J., Forster, P. M., Smith, C., Lee, L., Regayre, L., Brasseur, G., et al. (2020). Radiative forcing of climate change from the Copernicus reanalysis of atmospheric composition. *Earth System Science Data*, 12(3):1649–1677.

Bengtsson, L. and Shukla, J. (1988). Integration of space and in situ observations to study global climate change. *Bulletin of the American Meteorological Society*, 69(10):1130–1143.

Beres, J. H., Garcia, R. R., Boville, B. A., and Sassi, F. (2005). Implementation of a gravity wave source spectrum parameterization dependent on the properties of convection in the Whole Atmosphere Community Climate Model (WACCM). *Journal of Geophysical Research: Atmospheres*, 110(D10).

Bernath, P. (2017). The atmospheric chemistry experiment (ACE). *Journal of Quantitative Spectroscopy and Radiative Transfer*, 186:3–16.

Bernath, P., Crouse, J., Hughes, R., and Boone, C. (2021). The Atmospheric Chemistry Experiment Fourier transform spectrometer (ACE-FTS) version 4.1 retrievals: Trends and seasonal distributions. *Journal of Quantitative Spectroscopy and Radiative Transfer*, 259:107409.

Best, N., Havens, R., and LaGow, H. (1947). Pressure and Temperature of the Atmosphere to 120 km. *Physical Review*, 71(12):915.

Birner, T. and Bönisch, H. (2011). Residual circulation trajectories and transit times into the extratropical lowermost stratosphere. *Atmospheric Chemistry and Physics*, 11(2):817–827.

Bloom, S., Takacs, L., Da Silva, A., and Ledvina, D. (1996). Data assimilation using incremental analysis updates. *Monthly Weather Review*, 124(6):1256–1271.

Bönisch, H., Engel, A., Birner, T., Hoor, P., Tarasick, D., and Ray, E. (2011). On the structural changes in the Brewer-Dobson circulation after 2000. *Atmospheric Chemistry and Physics*, 11(8):3937–3948.

Boone, C., Bernath, P., Cok, D., Jones, S., and Steffen, J. (2020). Version 4 retrievals for the atmospheric chemistry experiment Fourier transform spectrometer (ACE-FTS) and imagers. *Journal of Quantitative Spectroscopy and Radiative Transfer*, 247:106939.

Boville, B. A. and Bretherton, C. S. (2003). Heating and kinetic energy dissipation in the NCAR Community Atmosphere Model. *Journal of climate*, 16(23):3877–3887.

Box, G. E. and Tiao, G. C. (2011). *Bayesian inference in statistical analysis*, volume 40. John Wiley & Sons.

Boyd, J. P. (1976). The noninteraction of waves with the zonally averaged flow on a spherical earth and the interrelationships on eddy fluxes of energy, heat and momentum. *Journal of the Atmospheric Sciences*, 33(12):2285–2291.

Braathen, G. (2016). WMO Arctic Ozone Bulletin no. 1 - 2016.

Bracewell, R. N. (1986). *The Fourier transform and its applications*, volume 31999. McGraw-Hill New York.

Brasseur, G. P. and Solomon, S. (2005). *Aeronomy of the middle atmosphere: Chemistry and physics of the stratosphere and mesosphere*, volume 32. Springer Science & Business Media.

Brewer, A. W. (1949). Evidence for a world circulation provided by the measurements of helium and water vapour distribution in the stratosphere. *Quarterly Journal of the Royal Meteorological Society*, 75(326):351–363.

Briegleb, B. P. (1992). Delta-Eddington approximation for solar radiation in the NCAR Community Climate Model. *Journal of Geophysical Research: Atmospheres*, 97(D7):7603–7612.

Bron, F.-M. and Ciais, P. (2010). Spaceborne remote sensing of greenhouse gas concentrations. *Comptes Rendus GEOScience*, 342(4):412–424. Atmosphre vue de l'espace.

Butchart, N. (2014). The Brewer-Dobson circulation. *Reviews of Geophysics*, 52(2):157–184.

Butchart, N., Cionni, I., Eyring, V., Shepherd, T., Waugh, D., Akiyoshi, H., Austin, J., Brühl, C., Chipperfield, M., Cordero, E., et al. (2010). Chemistry–climate model simulations of twenty-first century stratospheric climate and circulation changes. *Journal of Climate*, 23(20):5349–5374.

Butchart, N., Scaife, A., Bourqui, M., De Grandpré, J., Hare, S., Kettleborough, J., Langematz, U., Manzini, E., Sassi, F., Shibata, K., et al. (2006). Simulations of anthropogenic change in the strength of the Brewer–Dobson circulation. *Climate Dynamics*, 27(7-8):727–741.

Butchart, N. and Scaife, A. A. (2001). Removal of chlorofluorocarbons by increased mass exchange between the stratosphere and troposphere in a changing climate. *Nature*, 410(6830):799–802.

Butler, A. H., Sjoberg, J. P., Seidel, D. J., and Rosenlof, K. H. (2017). A sudden stratospheric warming compendium. *Earth System Science Data*, 9(1):63–76.

Canziani, P. O., Holton, J. R., Fishbein, E., Froidevaux, L., and Waters, J. W. (1994). Equatorial Kelvin waves: a UARS MLS view. *Journal of Atmospheric Sciences*, 51(20):3053–3076.

Chabrillat, S., Kockarts, G., Fonteyn, D., and Brasseur, G. (2002). Impact of molecular diffusion on the CO_2 distribution and the temperature in the mesosphere. *Geophysical research letters*, 29(15):19–1.

Chabrillat, S., Vigouroux, C., Christophe, Y., Engel, A., Errera, Q., Minganti, D., Monge-Sanz, B. M., Segers, A., and Mahieu, E. (2018). Comparison of mean age of air in five reanalyses using the BASCOE transport model. *Atmospheric Chemistry and Physics*, 18(19):14715–14735.

Chapman, S. (1930). XXXV. on ozone and atomic oxygen in the upper atmosphere. *The London, Edinburgh, and Dublin Philosophical Magazine and Journal of Science*, 10(64):369–383.

Charney, J. G. and Drazin, P. G. (1961). Propagation of planetary-scale disturbances from the lower into the upper atmosphere. *Journal of Geophysical Research (1896-1977)*, 66(1):83–109.

Chipperfield, M. P., Bekki, S., Dhomse, S., Harris, N. R., Hassler, B., Hossaini, R., Steinbrecht, W., Thiéblemont, R., and Weber, M. (2017). Detecting recovery of the stratospheric ozone layer. *Nature*, 549(7671):211–218.

Chirkov, M., Stiller, G. P., Laeng, A., Kellmann, S., vonClarmann, T., Boone, C. D., Elkins, J. W., Engel, A., Glatthor, N., Grabowski, U., Harth, C. M., Kiefer, M., Kolonjari, F., Krummel, P. B., Linden, A., Lunder, C. R., Miller, B. R., Montzka, S. A., Mühle, J., O'Doherty, S., Orphal, J., Prinn, R. G., Toon, G., Vollmer, M. K., Walker, K. A., Weiss, R. F., Wiegele, A., and Young, D. (2016). Global HCFC – 22 measurements with MIPAS: retrieval, validation, global distribution and its evolution over 2005–2012. *Atmospheric Chemistry and Physics*, 16(5):3345–3368.

Chou, M.-D. and Suarez, M. J. (1999). *A solar radiation parameterization for atmospheric studies*, volume 15. National Aeronautics and Space Administration, Goddard Space Flight Center ŏ2026.

Chou, M.-D., Suarez, M. J., Liang, X.-Z., Yan, M. M.-H., and Cote, C. (2001). A thermal infrared radiation parameterization for atmospheric studies.

Cicerone, R. J., Stolarski, R. S., and Walters, S. (1974). Stratospheric ozone destruction by man-made chlorofluoromethanes. *Science*, 185(4157):1165–1167.

Cohen, N. Y., Gerber, E. P., and Bühler, O. (2013). Compensation between resolved and unresolved wave driving in the stratosphere: Implications for downward control. *Journal of the Atmospheric Sciences*, 70(12):3780–3798.

Cohen, N. Y., Gerber, E. P., and Bühler, O. (2014). What drives the Brewer–Dobson circulation? *Journal of the Atmospheric Sciences*, 71(10):3837–3855.

Collins, W. D. (2001). Parameterization of generalized cloud overlap for radiative calculations in general circulation models. *Journal of the atmospheric sciences*, 58(21):3224–3242.

Cornu, A. M. (1879). Ii. Sur la limite ultraviolette du spectre solaire. *Proceedings of the Royal Society of London*, 29(196-199):47–55.

Courtier, P., Thépaut, J.-N., and Hollingsworth, A. (1994). A strategy for operational implementation of 4D-Var, using an incremental approach. *Quarterly Journal of the Royal Meteorological Society*, 120(519):1367–1387.

Craig, A. P., Vertenstein, M., and Jacob, R. (2012). A new flexible coupler for earth system modeling developed for CCSM4 and CESM1. *The International Journal of High Performance Computing Applications*, 26(1):31–42.

Crutzen, P. J. (1970). The influence of nitrogen oxides on the atmospheric ozone content. *Quarterly Journal of the Royal Meteorological Society*, 96(408):320–325.

Daerden, F., Larsen, N., Chabrillat, S., Errera, Q., Bonjean, S., Fonteyn, D., Hoppel, K., and Fromm, M. (2007). A 3D-CTM with detailed online PSC-microphysics: analysis of the Antarctic winter 2003 by comparison with satellite observations. *Atmospheric Chemistry and Physics*, 7(7):1755–1772.

Danabasoglu, G., Lamarque, J.-F., Bacmeister, J., Bailey, D., DuVivier, A., Edwards, J., Emmons, L., Fasullo, J., Garcia, R., Gettelman, A., et al. (2020). The community earth system model version 2 (CESM2). *Journal of Advances in Modeling Earth Systems*, 12(2).

Davis, N. A., Callaghan, P., Simpson, I. R., and Tilmes, S. (2022). Specified dynamics scheme impacts on wave-mean flow dynamics, convection, and tracer transport in CESM2 (WACCM6). *Atmospheric Chemistry and Physics*, 22(1):197–214.

Davis, S. M., Rosenlof, K. H., Hassler, B., Hurst, D. F., Read, W. G., Vömel, H., Selkirk, H., Fujiwara, M., and Damadeo, R. (2016). The stratospheric water and ozone satellite homogenized (swoosh) database: a long-term database for climate studies. *Earth System Science Data*, 8(2):461–490.

De Laat, A., Gloudemans, A., Schrijver, H., Aben, I., Nagahama, Y., Suzuki, K., Mahieu, E., Jones, N., Paton-Walsh, C., Deutscher, N., et al. (2010). Validation of five years (2003–2007) of SCIAMACHY CO total column measurements using ground-based spectrometer observations. *Atmospheric Measurement Techniques*, 3(5):1457–1471.

De Mazière, M., Thompson, A. M., Kurylo, M. J., Wild, J. D., Bernhard, G., Blumenstock, T., Braathen, G. O., Hannigan, J. W., Lambert, J.-C.,

Leblanc, T., et al. (2018). The Network for the Detection of Atmospheric Composition Change (NDACC): history, status and perspectives. *Atmospheric Chemistry and Physics*, 18(7):4935–4964.

de Wit, T. D., Bruinsma, S., and Shibasaki, K. (2014). Synoptic radio observations as proxies for upper atmosphere modelling. *Journal of Space Weather and Space Climate*, 4:A06.

Dee, D. P., Uppala, S. M., Simmons, A. J., Berrisford, P., Poli, P., Kobayashi, S., Andrae, U., Balmaseda, M. A., Balsamo, G., Bauer, P., Bechtold, P., Beljaars, A. C. M., van de Berg, L., Bidlot, J., Bormann, N., Delsol, C., Dragani, R., Fuentes, M., Geer, A. J., Haimberger, L., Healy, S. B., Hersbach, H., Hlm, E. V., Isaksen, L., Kllberg, P., Khler, M., Matricardi, M., McNally, A. P., Monge-Sanz, B. M., Morcrette, J.-J., Park, B.-K., Peubey, C., de Rosnay, P., Tavolato, C., Thpaut, J.-N., and Vitart, F. (2011). The ERA-Interim reanalysis: configuration and performance of the data assimilation system. *Quarterly Journal of the Royal Meteorological Society*, 137(656):553–597.

Deushi, M. and Shibata, K. (2011). Impacts of increases in greenhouse gases and ozone recovery on lower stratospheric circulation and the age of air: Chemistry-climate model simulations up to 2100. *Journal of Geophysical Research: Atmospheres*, 116(D7).

Diallo, M., Konopka, P., Santee, M. L., Müller, R., Tao, M., Walker, K. A., Legras, B., Riese, M., Ern, M., and Ploeger, F. (2019). Structural changes in the shallow and transition branch of the Brewer–Dobson circulation induced by El Niño. *Atmospheric chemistry and physics*, 19(1):425–446.

Diallo, M., Legras, B., and Chédin, A. (2012). Age of stratospheric air in the ERA-Interim. *Atmospheric Chemistry and Physics*, 12(24):12133–12154.

Dietmüller, S., Eichinger, R., Garny, H., Birner, T., Boenisch, H., Pitari, G., Mancini, E., Visioni, D., Stenke, A., Revell, L., et al. (2018). Quantifying the effect of mixing on the mean age of air in CCMVal-2 and CCMI-1 models. *Atmospheric Chemistry and Physics*, 18(9):6699–6720.

Dietmüller, S., Garny, H., Plöger, F., Jöckel, P., and Cai, D. (2017). Effects of mixing on resolved and unresolved scales on stratospheric age of air. *Atmospheric chemistry and physics*, 17(12):7703–7719.

Dobson, G. (1931). A photoelectric spectrophotometer for measuring the amount of atmospheric ozone. *Proceedings of the Physical Society (1926-1948)*, 43(3):324.

Dobson, G. M. B., Harrison, D. N., and Lawrence, J. (1929). Measurements of the amount of ozone in the earth's atmosphere and its relation to other geophysical conditions.part iii. *Proceedings of the Royal Society of London. Series A, Containing Papers of a Mathematical and Physical Character*, 122(790):456–486.

Domeisen, D. I., Garfinkel, C. I., and Butler, A. H. (2019). The Teleconnection of El Niño Southern Oscillation to the Stratosphere. *Reviews of Geophysics*, 57(1):5–47.

Dunkerton, T. (1978). On the mean meridional mass motions of the stratosphere and mesosphere. *Journal of the Atmospheric Sciences*, 35(12):2325–2333.

Dunkerton, T. J. (1997). The role of gravity waves in the quasi-biennial oscillation. *Journal of Geophysical Research: Atmospheres*, 102(D22):26053–26076.

Durbin, J. and Koopman, S. J. (2012). *Time series analysis by state space methods*. Oxford university press.

Edmon Jr, H., Hoskins, B., and McIntyre, M. (1980). Eliassen-Palm cross sections for the troposphere. *Journal of Atmospheric Sciences*, 37(12):2600–2616.

Emmons, L. K., Walters, S., Hess, P. G., Lamarque, J.-F., Pfister, G. G., Fillmore, D., Granier, C., Guenther, A., Kinnison, D., Laepple, T., et al. (2010). Description and evaluation of the Model for Ozone and Related chemical Tracers, version 4 (MOZART-4). *GEOScientific Model Development*, 3(1):43–67.

Engel, A., Bönisch, H., Ullrich, M., Sitals, R., Membrive, O., Danis, F., and Crevoisier, C. (2017). Mean age of stratospheric air derived from AirCore observations. *Atmospheric Chemistry and Physics*, 17(11):6825–6838.

Engel, A., Möbius, T., Bönisch, H., Schmidt, U., Heinz, R., Levin, I., Atlas, E., Aoki, S., Nakazawa, T., Sugawara, S., et al. (2009). Age of stratospheric air unchanged within uncertainties over the past 30 years. *Nature GEOScience*, 2(1):28–31.

Errera, Q., Chabrillat, S., Christophe, Y., Debosscher, J., Hubert, D., Lahoz, W., Santee, M. L., Shiotani, M., Skachko, S., von Clarmann, T., and Walker, K. (2019). Technical note: Reanalysis of Aura MLS chemical observations. *Atmospheric Chemistry and Physics*, 19(21):13647–13679.

Errera, Q., Daerden, F., Chabrillat, S., Lambert, J., Lahoz, W., Viscardy, S., Bonjean, S., and Fonteyn, D. (2008). 4D-Var assimilation of MIPAS chemical observations: ozone and nitrogen dioxide analyses. *Atmospheric Chemistry and Physics*, 8(20):6169–6187.

Errera, Q. and Ménard, R. (2012). Technical Note: Spectral representation of spatial correlations in variational assimilation with grid point models and application to the Belgian Assimilation System for Chemical Observations (BASCOE). *Atmospheric Chemistry and Physics*, 12(21):10015–10031.

Evensen, G. (2009). *Data assimilation: the ensemble Kalman filter*. Springer Science & Business Media.

Eyring, V., Bony, S., Meehl, G. A., Senior, C. A., Stevens, B., Stouffer, R. J., and Taylor, K. E. (2016). Overview of the Coupled Model Intercomparison Project Phase 6 (CMIP6) experimental design and organization. *GEOScientific Model Development*, 9(5):1937–1958.

Eyring, V., Butchart, N., Waugh, D. W., Akiyoshi, H., Austin, J., Bekki, S., Bodeker, G. E., Boville, B. A., Brühl, C., Chipperfield, M. P., et al. (2006). Assessment of temperature, trace species, and ozone in chemistry-climate model simulations of the recent past. *Journal of Geophysical Research: Atmospheres*, 111(D22).

Eyring, V., Chipperfield, M. P., Giorgetta, M. A., Kinnison, D. E., Manzini, E., Matthes, K., Newman, P. A., Pawson, S., Shepherd, T. G., and Waugh, D. W. (2008). Overview of the new CCMVal reference and sensitivity simulations in support of upcoming ozone and climate assessments and the planned SPARC CCMVal report. *SPARC Newsl*, 30:20–26.

Eyring, V., Shepherd, T., Waugh, D., et al. (2010). SPARC report on the evaluation of chemistry-climate models.

Fahey, D. W. and Hegglin, M. I. (2010). Twenty questions and answers about the ozone layer: 2010 update. *Scientific assessment of ozone depletion*, pages 4–1.

Fang, X., Pyle, J. A., Chipperfield, M. P., Daniel, J. S., Park, S., and Prinn, R. G. (2019). Challenges for the recovery of the ozone layer. *Nature GEOScience*, 12(8):592–596.

Farman, J. C., Gardiner, B. G., and Shanklin, J. D. (1985). Large losses of total ozone in antarctica reveal seasonal ClO_x/NO_x interaction. *Nature*, 315(6016):207–210.

Fiedler, F. and Panofsky, H. (1972). The geostrophic drag coefficient and the "effective" roughness length. *Quarterly Journal of the Royal Meteorological Society*, 98(415):213–220.

Flato, G. M. (2011). Earth system models: an overview. *Wiley Interdisciplinary Reviews: Climate Change*, 2(6):783–800.

Fouquart, Y. et al. (1980). Computations of solar heating of the earth's atmosphere: A new parameterization.

Freidenreich, S. and Ramaswamy, V. (1999). A new multiple-band solar radiative parameterization for general circulation models. *Journal of Geophysical Research: Atmospheres*, 104(D24):31389–31409.

Friedrich, M., Smeekes, S., and Urbain, J.-P. (2020). Autoregressive wild bootstrap inference for nonparametric trends. *Journal of Econometrics*, 214(1):81 – 109. Annals Issue: Econometric Models of Climate Change.

Fritsch, F., Garny, H., Engel, A., Bönisch, H., and Eichinger, R. (2020). Sensitivity of age of air trends to the derivation method for non-linear increasing inert SF_6. *Atmospheric Chemistry and Physics*, 20(14):8709–8725.

Fritts, D. C. and Alexander, M. J. (2003). Gravity wave dynamics and effects in the middle atmosphere. *Reviews of Geophysics*, 41(1).

Froidevaux, L., Kinnison, D. E., Wang, R., Anderson, J., and Fuller, R. A. (2019). Evaluation of CESM1 (WACCM) free-running and specified dynamics atmospheric composition simulations using global multispecies satellite data records. *Atmospheric Chemistry and Physics*, 19(7):4783–4821.

Fu, Q., Lin, P., Solomon, S., and Hartmann, D. (2015). Observational evidence of strengthening of the Brewer-Dobson circulation since 1980. *Journal of Geophysical Research: Atmospheres*, 120(19):10–214.

Fu, Q., Solomon, S., Pahlavan, H. A., and Lin, P. (2019). Observed changes in Brewer–Dobson circulation for 1980–2018. *Environmental Research Letters*, 14(11):114026.

Fueglistaler, S., Dessler, A. E., Dunkerton, T. J., Folkins, I., Fu, Q., and Mote, P. W. (2009). Tropical tropopause layer. *Reviews of Geophysics*, 47(1).

Fujiwara, M., Wright, J. S., Manney, G. L., Gray, L. J., Anstey, J., Birner, T., Davis, S., Gerber, E. P., Harvey, V. L., Hegglin, M. I., et al. (2017). Introduction to the SPARC Reanalysis Intercomparison Project (S-RIP) and overview of the reanalysis systems. *Atmospheric Chemistry and Physics*, 17(2):1417–1452.

Gamerman, D. and Lopes, H. F. (2006). *Markov chain Monte Carlo: stochastic simulation for Bayesian inference*. CRC Press.

García, O. E., Schneider, M., Sepúlveda, E., Hase, F., Blumenstock, T., Cuevas, E., Ramos, R., Gross, J., Barthlott, S., Röhling, A. N., Sanromá, E., González, Y., Gómez-Peláez, A. J., Navarro-Comas, M., Puentedura, O., Yela, M., Redondas, A., Carreño, V., León-Luis, S. F., Reyes, E., García, R. D., Rivas, P. P., Romero-Campos, P. M., Torres, C., Prats, N., Hernández, M., and López, C. (2021). Twenty years of ground-based NDACC FTIR spectrometry at Izaña Observatory – overview and long-term comparison to other techniques. *Atmospheric Chemistry and Physics*, 21(20):15519–15554.

Garcia, R. R. and Boville, B. A. (1994). Downward control of the mean meridional circulation and temperature distribution of the polar winter stratosphere. *Journal of Atmospheric Sciences*, 51(15):2238–2245.

Garcia, R. R. and Randel, W. J. (2008). Acceleration of the Brewer–Dobson circulation due to increases in greenhouse gases. *Journal of the Atmospheric Sciences*, 65(8):2731–2739.

Garcia, R. R., Randel, W. J., and Kinnison, D. E. (2011). On the determination of age of air trends from atmospheric trace species. *Journal of the Atmospheric Sciences*, 68(1):139–154.

Garcia, R. R., Smith, A. K., Kinnison, D. E., Álvaro de la Cámara, and Murphy, D. J. (2017). Modification of the gravity wave parameterization in the whole atmosphere community climate model: Motivation and results. *Journal of the Atmospheric Sciences*, 74(1):275 – 291.

Gardiner, T., Forbes, A., de Mazière, M., Vigouroux, C., Mahieu, E., Demoulin, P., Velazco, V., Notholt, J., Blumenstock, T., Hase, F., Kramer, I., Sussmann, R., Stremme, W., Mellqvist, J., Strandberg, A., Ellingsen, K., and Gauss, M. (2008). Trend analysis of greenhouse gases over Europe measured by a network of ground-based remote FTIR instruments. *Atmospheric Chemistry and Physics*, 8(22):6719–6727.

Garfinkel, C. I., Aquila, V., Waugh, D. W., and Oman, L. D. (2017). Time-varying changes in the simulated structure of the Brewer–Dobson circulation. *Atmospheric Chemistry and Physics*, 17(2):1313–1327.

Garny, H., Birner, T., Bönisch, H., and Bunzel, F. (2014). The effects of mixing on age of air. *Journal of Geophysical Research: Atmospheres*, 119(12):7015–7034.

Gelaro, R., McCarty, W., Suárez, M. J., Todling, R., Molod, A., Takacs, L., Randles, C. A., Darmenov, A., Bosilovich, M. G., Reichle, R., Wargan, K., Coy, L., Cullather, R., Draper, C., Akella, S., Buchard, V., Conaty, A., da Silva, A. M., Gu, W., Kim, G.-K., Koster, R., Lucchesi, R., Merkova, D., Nielsen, J. E., Partyka, G., Pawson, S., Putman, W., Rienecker, M., Schubert, S. D., Sienkiewicz, M., and Zhao, B. (15 Jul. 2017). The Modern-Era Retrospective Analysis for Research and Applications, Version 2 (MERRA-2). *Journal of Climate*, 30(14):5419 – 5454.

Geller, M. A., Zhou, T., Ruedy, R., Aleinov, I., Nazarenko, L., Tausnev, N. L., Sun, S., Kelley, M., and Cheng, Y. (2011). New gravity wave treatments for GISS climate models. *Journal of climate*, 24(15):3989–4002.

Gerber, E. P., Baldwin, M. P., Akiyoshi, H., Austin, J., Bekki, S., Braesicke, P., Butchart, N., Chipperfield, M., Dameris, M., Dhomse, S., Frith, S. M., Garcia, R. R., Garny, H., Gettelman, A., Hardiman, S. C., Karpechko, A., Marchand, M., Morgenstern, O., Nielsen, J. E., Pawson, S., Peter, T., Plummer, D. A., Pyle, J. A., Rozanov, E., Scinocca, J. F., Shepherd, T. G., and Smale, D. (2010). Stratosphere-troposphere coupling and annular mode variability in chemistry-climate models. *Journal of Geophysical Research: Atmospheres*, 115(D3).

Gettelman, A., Mills, M., Kinnison, D., Garcia, R., Smith, A., Marsh, D., Tilmes, S., Vitt, F., Bardeen, C., McInerny, J., et al. (2019). The whole atmosphere community climate model version 6 (WACCM6). *Journal of Geophysical Research: Atmospheres*, 124(23):12380–12403.

Gettelman, A. and Morrison, H. (2015). Advanced two-moment bulk microphysics for global models. Part I: Off-line tests and comparison with other schemes. *Journal of Climate*, 28(3):1268–1287.

Giacomo, P. (1987). The Michelson interferometer. *Microchimica Acta*, 93(1):19–31.

Glatthor, N., Höpfner, M., Leyser, A., Stiller, G. P., Clarmann, T. v., Grabowski, U., Kellmann, S., Linden, A., Sinnhuber, B.-M., Krysztofiak,

G., et al. (2017). Global carbonyl sulfide (OCS) measured by MIPAS/Envisat during 2002–2012. *Atmospheric Chemistry and Physics*, 17(4):2631–2652.

Götz, F. P., Meetham, A. R., and Dobson, G. M. B. (1934). The vertical distribution of ozone in the atmosphere. *Proceedings of the Royal Society of London. Series A, Containing Papers of a Mathematical and Physical Character*, 145(855):416–446.

Gray, L. and Pyle, J. (1989). A two-dimensional model of the quasi-biennial oscillation of ozone. *Journal of Atmospheric Sciences*, 46(2):203–220.

Griffith, D. W. T., Deutscher, N. M., Caldow, C., Kettlewell, G., Riggenbach, M., and Hammer, S. (2012). A Fourier transform infrared trace gas and isotope analyser for atmospheric applications. *Atmospheric Measurement Techniques*, 5(10):2481–2498.

Hack, J. J., Boville, B. A., Briegleb, B. P., Kiehl, J. T., Rasch, P. J., and Williamson, D. L. (1993). Description of the NCAR community climate model (CCM2). Technical report, Technical Report NCAR/TN-382+ STR, National Center for Atmospheric Research ŏ026.

Haenel, F. J., Stiller, G. P., von Clarmann, T., Funke, B., Eckert, E., Glatthor, N., Grabowski, U., Kellmann, S., Kiefer, M., Linden, A., and Reddmann, T. (2015). Reassessment of mipas age of air trends and variability. *Atmospheric Chemistry and Physics*, 15(22):13161–13176.

Hall, T. M. and Plumb, R. A. (1994). Age as a diagnostic of stratospheric transport. *Journal of Geophysical Research: Atmospheres*, 99(D1):1059–1070.

Hardiman, S. C., Butchart, N., and Calvo, N. (2014). The morphology of the Brewer–Dobson circulation and its response to climate change in CMIP5 simulations. *Quarterly Journal of the Royal Meteorological Society*, 140(683):1958–1965.

Hardiman, S. C., Lin, P., Scaife, A. A., Dunstone, N. J., and Ren, H.-L. (2017). The influence of dynamical variability on the observed Brewer-Dobson circulation trend. *Geophysical Research Letters*, 44(6):2885–2892.

Harrison, J. J., Chipperfield, M. P., Boone, C. D., Dhomse, S. S., Bernath, P. F., Froidevaux, L., Anderson, J., and Russell III, J. (2016). Satellite observations of stratospheric hydrogen fluoride and comparisons with SLIMCAT calculations. *Atmospheric Chemistry and Physics*, 16(16):10501–10519.

Hartley, W. (1880). On the probable absorption of solar radiation by atmospheric ozone. *Chem. News*, 42(268).

Harvey, L. D. (2018). *Global warming*. Routledge.

Hase, F., Hannigan, J., Coffey, M., Goldman, A., Höpfner, M., Jones, N., Rinsland, C., and Wood, S. (2004). Intercomparison of retrieval codes used for the analysis of high-resolution, ground-based FTIR measurements. *Journal of Quantitative Spectroscopy and Radiative Transfer*, 87(1):25–52.

Haynes, P. (2005). Stratospheric dynamics. *Annu. Rev. Fluid Mech.*, 37:263–293.

Haynes, P. H., McIntyre, M., Shepherd, T., Marks, C., and Shine, K. P. (1991). On the "downward control" of extratropical diabatic circulations by eddy-induced mean zonal forces. *Journal of the Atmospheric Sciences*, 48(4):651–678.

Haynes, P. H. and McIntyre, M. E. (1987). On the evolution of vorticity and potential vorticity in the presence of diabatic heating and frictional or other forces. *Journal of the Atmospheric Sciences*, 44(5):828–841.

Hegglin, M., Plummer, D., Shepherd, T., Scinocca, J., Anderson, J., Froidevaux, L., Funke, B., Hurst, D., Rozanov, A., Urban, J., et al. (2014). Vertical structure of stratospheric water vapour trends derived from merged satellite data. *Nature GEOScience*, 7(10):768–776.

Helfand, H. M. and Schubert, S. D. (1995). Climatology of the simulated Great Plains low-level jet and its contribution to the continental moisture budget of the United States. *Journal of Climate*, 8(4):784–806.

Hendrick, F., Mahieu, E., Bodeker, G., Boersma, K., Chipperfield, M., Mazière, M. D., Smedt, I. D., Demoulin, P., Fayt, C., Hermans, C., et al. (2012). Analysis of stratospheric NO_2 trends above jungfraujoch using ground-based UV-visible, FTIR, and satellite nadir observations. *Atmospheric Chemistry and Physics*, 12(18):8851–8864.

Hersbach, H., Bell, B., Berrisford, P., Hirahara, S., Horányi, A., Muñoz-Sabater, J., Nicolas, J., Peubey, C., Radu, R., Schepers, D., et al. (2020). The ERA5 global reanalysis. *Quarterly Journal of the Royal Meteorological Society*, 146(730):1999–2049.

Hoesly, R. M., Smith, S. J., Feng, L., Klimont, Z., Janssens-Maenhout, G., Pitkanen, T., Seibert, J. J., Vu, L., Andres, R. J., Bolt, R. M., et al.

(2018). Historical (1750–2014) anthropogenic emissions of reactive gases and aerosols from the Community Emissions Data System (CEDS). *GEO-Scientific Model Development*, 11(1):369–408.

Hoinka, K. P. (1997). The tropopause: discovery, definition and demarcation. *Meteorologische Zeitschrift*, 6(6):281–303.

Holland, M. M., Bailey, D. A., Briegleb, B. P., Light, B., and Hunke, E. (2012). Improved sea ice shortwave radiation physics in CCSM4: The impact of melt ponds and aerosols on Arctic sea ice. *Journal of Climate*, 25(5):1413–1430.

Holton, J. (2004). *An Introduction to Dynamic Meteorology*. Number v. 1 in An Introduction to Dynamic Meteorology. Elsevier Academic Press.

Holton, J. R. and Alexander, M. J. (2000). The role of waves in the transport circulation of the middle atmosphere. *Atmospheric science across the stratopause*, 123:21–35.

Holton, J. R., Haynes, P. H., McIntyre, M. E., Douglass, A. R., Rood, R. B., and Pfister, L. (1995). Stratosphere-troposphere exchange. *Reviews of geophysics*, 33(4):403–439.

Holton, J. R. and Lindzen, R. S. (1972). An updated theory for the quasi-biennial cycle of the tropical stratosphere. *Journal of Atmospheric Sciences*, 29(6):1076–1080.

Holton, J. R. and Tan, H.-C. (1982). The Quasi-Biennial Oscillation in the Northern Hemisphere Lower Stratosphere. *Journal of the Meteorological Society of Japan. Ser. II*, 60(1):140–148.

Holtslag, A. and Boville, B. (1993). Local versus nonlocal boundary-layer diffusion in a global climate model. *Journal of climate*, 6(10):1825–1842.

Houghton, J. (2005). Global warming. *Reports on progress in physics*, 68(6):1343.

Howard, L. N. (1961). Note on a paper of John W. Miles. *Journal of Fluid Mechanics*, 10(4):509–512.

Huijnen, V., Flemming, J., Chabrillat, S., Errera, Q., Christophe, Y., Blechschmidt, A.-M., Richter, A., and Eskes, H. (2016). C-IFS-CB05-BASCOE: stratospheric chemistry in the Integrated Forecasting System of ECMWF. *GEOScientific Model Development*, 9(9):3071–3091.

Hunke, E. C., Lipscomb, W. H., Turner, A. K., Jeffery, N., and Elliott, S. (2010). Cice: the los alamos sea ice model documentation and software user's manual version 4.1 la-cc-06-012. *T-3 Fluid Dynamics Group, Los Alamos National Laboratory*, 675:500.

Hurrell, J. W., Holland, M. M., Gent, P. R., Ghan, S., Kay, J. E., Kushner, P. J., Lamarque, J.-F., Large, W. G., Lawrence, D., Lindsay, K., et al. (2013). The community earth system model: a framework for collaborative research. *Bulletin of the American Meteorological Society*, 94(9):1339–1360.

Iacono, M. J., Delamere, J. S., Mlawer, E. J., Shephard, M. W., Clough, S. A., and Collins, W. D. (2008). Radiative forcing by long-lived greenhouse gases: Calculations with the AER radiative transfer models. *Journal of Geophysical Research: Atmospheres*, 113(D13).

Inness, A., Ades, M., Agustí-Panareda, A., Barré, J., Benedictow, A., Blechschmidt, A.-M., Dominguez, J. J., Engelen, R., Eskes, H., Flemming, J., Huijnen, V., Jones, L., Kipling, Z., Massart, S., Parrington, M., Peuch, V.-H., Razinger, M., Remy, S., Schulz, M., and Suttie, M. (2019). The CAMS reanalysis of atmospheric composition. *Atmospheric Chemistry and Physics*, 19(6):3515–3556.

Inness, A., Chabrillat, S., Flemming, J., Huijnen, V., Langenrock, B., Nicolas, J., Polichtchouk, I., and Razinger, M. (2020). Exceptionally low Arctic stratospheric ozone in spring 2020 as seen in the CAMS reanalysis. *Journal of Geophysical Research: Atmospheres*, 125(23):e2020JD033563.

Iwasaki, T., Yamada, S., and Tada, K. (1989a). A parameterization scheme of orographic gravity wave drag with two different vertical partitionings part I: Impacts on Medium-range forecasts. *Journal of the Meteorological Society of Japan. Ser. II*, 67(1):11–27.

Iwasaki, T., Yamada, S., and Tada, K. (1989b). A parameterization scheme of orographic gravity wave drag with two different vertical partitionings part II: Zonally averaged budget analyses based on transformed eulerian mean method. *Journal of the Meteorological Society of Japan*, 67(1):29–41.

Jacob, D. J. (1999). *Introduction to atmospheric chemistry*. Princeton University Press.

Johnston, H. (1971). Reduction of stratospheric ozone by nitrogen oxide catalysts from supersonic transport exhaust. *Science*, 173(3996):517–522.

Kalman, R. E. (1960). A new approach to linear filtering and prediction problems.

Kalnay, E. (2003). *Atmospheric modeling, data assimilation and predictability*. Cambridge university press.

Kida, H. (1983). General circulation of air parcels and transport characteristics derived from a hemispheric GCM. *Journal of the Meteorological Society of Japan. Ser. II*, 61(2):171–187.

Kiehl, J., Hack, J., Bonan, G., Boville, B., Williamson, D., and Rasch, P. (1998). The national center for atmospheric research community climate model: CCM3. *Journal of Climate*, 11(6):1131–1149.

Kinnison, D., Brasseur, G. P., Walters, S., Garcia, R., Marsh, D., Sassi, F., Harvey, V., Randall, C., Emmons, L., Lamarque, J., et al. (2007). Sensitivity of chemical tracers to meteorological parameters in the MOZART-3 chemical transport model. *Journal of Geophysical Research: Atmospheres*, 112(D20).

Kobayashi, S., OTA, Y., HARADA, Y., EBITA, A., MORIYA, M., ONODA, H., ONOGI, K., KAMAHORI, H., KOBAYASHI, C., ENDO, H., MIYAOKA, K., and TAKAHASHI, K. (2015). The JRA-55 reanalysis: General specifications and basic characteristics. *Journal of the Meteorological Society of Japan. Ser. II*, 93(1):5–48.

Kodama, C., Iwasaki, T., Shibata, K., and Yukimoto, S. (2007). Changes in the stratospheric mean meridional circulation due to increased CO_2: Radiation- and sea surface temperature-induced effects. *Journal of Geophysical Research: Atmospheres*, 112(D16).

Kodera, K. and Kuroda, Y. (2002). Dynamical response to the solar cycle. *Journal of Geophysical Research: Atmospheres*, 107(D24):ACL 5–1–ACL 5–12.

Köhler, M., Ahlgrimm, M., and Beljaars, A. (2011). Unified treatment of dry convective and stratocumulus-topped boundary layers in the ECMWF model. *Quarterly Journal of the Royal Meteorological Society*, 137(654):43–57.

Kolonjari, F., Plummer, D. A., Walker, K. A., Boone, C. D., Elkins, J. W., Hegglin, M. I., Manney, G. L., Moore, F. L., Pendlebury, D., Ray, E. A., Rosenlof, K. H., and Stiller, G. P. (2018). Assessing stratospheric transport

in the CMAM30 simulations using ACE-FTS measurements. *Atmospheric Chemistry and Physics*, 18(9):6801–6828.

Konopka, P., Ploeger, F., Tao, M., Birner, T., and Riese, M. (2015). Hemispheric asymmetries and seasonality of mean age of air in the lower stratosphere: Deep versus shallow branch of the Brewer-Dobson circulation. *Journal of Geophysical Research: Atmospheres*, 120(5):2053–2066.

Kovács, T., Feng, W., Totterdill, A., Plane, J., Dhomse, S., Gómez-Martín, J. C., Stiller, G. P., Haenel, F. J., Smith, C., Forster, P. M., et al. (2017). Determination of the atmospheric lifetime and global warming potential of sulfur hexafluoride using a three-dimensional model. *Atmospheric Chemistry and Physics*, 17(2):883–898.

Kovilakam, M., Thomason, L. W., Ernest, N., Rieger, L., Bourassa, A., and Millán, L. (2020). The Global Space-based Stratospheric Aerosol Climatology (version 2.0): 1979–2018. *Earth System Science Data*, 12(4):2607–2634.

Kunz, A., Pan, L., Konopka, P., Kinnison, D., and Tilmes, S. (2011). Chemical and dynamical discontinuity at the extratropical tropopause based on START08 and WACCM analyses. *Journal of Geophysical Research: Atmospheres*, 116(D24).

Laine, M., Latva-Pukkila, N., and Kyrölä, E. (2014). Analysing time-varying trends in stratospheric ozone time series using the state space approach. *Atmospheric Chemistry and Physics*, 14(18):9707–9725.

Lamarque, J.-F., Emmons, L., Hess, P., Kinnison, D. E., Tilmes, S., Vitt, F., Heald, C., Holland, E. A., Lauritzen, P., Neu, J., et al. (2012). CAM-chem: Description and evaluation of interactive atmospheric chemistry in the Community Earth System Model. *GEOScientific Model Development*, 5(2):369–411.

Langematz, U., Tully, M., Calvo, N., Dameris, M., de Laat, J., Klekociuk, A. R., Müller, R., and Young, P. (2018). Polar Stratospheric Ozone: Past, Present, and Future, Chapter 4 in WMO Scientific Assessment of Ozone Depletion (2018). *UNEP/WMO Scientific Assessment of Ozone Depletion: 2018 (Report)*, 58.

Langerock, B., De Mazière, M., Hendrick, F., Vigouroux, C., Desmet, F., Dils, B., and Niemeijer, S. (2015). Description of algorithms for co-locating and comparing gridded model data with remote-sensing observations. *GEOScientific Model Development*, 8(3):911–921.

Larson, V. E. (2017). CLUBB-SILHS: A parameterization of subgrid variability in the atmosphere. *arXiv preprint arXiv:1711.03675*.

Lawless, A. (2010). A note on the analysis error associated with 3D-FGAT. *Quarterly Journal of the Royal Meteorological Society*, 136(649):1094–1098.

Lawrence, D. M., Oleson, K. W., Flanner, M. G., Thornton, P. E., Swenson, S. C., Lawrence, P. J., Zeng, X., Yang, Z.-L., Levis, S., Sakaguchi, K., et al. (2011). Parameterization improvements and functional and structural advances in version 4 of the Community Land Model. *Journal of Advances in Modeling Earth Systems*, 3(1).

Li, F., Newman, P., Pawson, S., and Perlwitz, J. (2018). Effects of Greenhouse Gas Increase and Stratospheric Ozone Depletion on Stratospheric Mean Age of Air in 19602010. *Journal of Geophysical Research: Atmospheres*, 123(4):2098–2110.

Li, F., Waugh, D. W., Douglass, A. R., Newman, P. A., Pawson, S., Stolarski, R. S., Strahan, S. E., and Nielsen, J. E. (2012). Seasonal variations of stratospheric age spectra in the Goddard Earth Observing System Chemistry Climate Model (GEOSCCM). *Journal of Geophysical Research: Atmospheres*, 117(D5).

Lin, P. and Fu, Q. (2013). Changes in various branches of the Brewer–Dobson circulation from an ensemble of chemistry climate models. *Journal of Geophysical Research: Atmospheres*, 118(1):73–84.

Lin, S.-J. (2004). A "vertically lagrangian" finite-volume dynamical core for global models. *Monthly Weather Review*, 132(10):2293–2307.

Lin, S.-J. and Rood, R. B. (1996). Multidimensional flux-form semi-Lagrangian transport schemes. *Monthly Weather Review*, 124(9):2046–2070.

Lindemann, F. A. and Dobson, G. M. B. (1923). A theory of meteors, and the density and temperature of the outer atmosphere to which it leads. *Proceedings of the Royal Society of London. Series A, Containing Papers of a Mathematical and Physical Character*, 102(717):411–437.

Lindsay, K., Bonan, G. B., Doney, S. C., Hoffman, F. M., Lawrence, D. M., Long, M. C., Mahowald, N. M., Keith Moore, J., Randerson, J. T., and Thornton, P. E. (2014). Preindustrial-control and twentieth-century carbon cycle experiments with the Earth System Model CESM1 (BGC). *Journal of Climate*, 27(24):8981–9005.

Lindzen, R. S. (1981). Turbulence and stress owing to gravity wave and tidal breakdown. *Journal of Geophysical Research: Oceans*, 86(C10):9707–9714.

Lindzen, R. S. and Holton, J. R. (1968). A theory of the quasi-biennial oscillation. *Journal of Atmospheric Sciences*, 25(6):1095–1107.

Liu, X., Ma, P.-L., Wang, H., Tilmes, S., Singh, B., Easter, R., Ghan, S., and Rasch, P. (2016). Description and evaluation of a new four-mode version of the Modal Aerosol Module (MAM4) within version 5.3 of the Community Atmosphere Model. *GEOScientific Model Development*, 9(2):505–522.

Livesey, N. J., Read, W. G., Froidevaux, L., Lambert, A., Santee, M. L., Schwartz, M. J., Millán, L. F., Jarnot, R. F., Wagner, P. A., Hurst, D. F., Walker, K. A., Sheese, P. E., and Nedoluha, G. E. (2021). Investigation and amelioration of long-term instrumental drifts in water vapor and nitrous oxide measurements from the Aura Microwave Limb Sounder (MLS) and their implications for studies of variability and trends. *Atmospheric Chemistry and Physics*, 21(20):15409–15430.

Livesey, N. J., Read, W. G., Wagner, P. A., Froidevaux, L., Lambert, A., Manney, G. L., Millan Valle, L. F., Pumphrey, H. C., Santee, M. L., Schwartz, M. J., Wang, S., Fuller, R. A., Jarnot, R. F., Knosp, B. W., and Martinez, E. (2015). Earth Observing System (EOS) Aura Microwave Limb Sounder (MLS) version 4.2x level 2 data quality and description document. Technical Report D-33509 Rev. A, JPL.

Lock, A., Brown, A., Bush, M., Martin, G., and Smith, R. (2000). A new boundary layer mixing scheme. part I: Scheme description and single-column model tests. *Monthly weather review*, 128(9):3187–3199.

Loeffel, S., Eichinger, R., Garny, H., Reddmann, T., Fritsch, F., Versick, S., Stiller, G., and Haenel, F. (2022). The impact of sulfur hexafluoride (SF_6) sinks on age of air climatologies and trends. *Atmospheric Chemistry and Physics*, 22(2):1175–1193.

Lott, F. and Miller, M. J. (1997). A new subgrid-scale orographic drag parametrization: Its formulation and testing. *Quarterly Journal of the Royal Meteorological Society*, 123(537):101–127.

Louis, J. F. (1982). A short history of the operational pbl-parameterization at ECMWF. In *ECMWF Workshop Planetary Boundary Layer Parameterization, 1982*. ECMWF.

Mahfouf, J., Cariolle, D., Royer, J., Geleyn, J., and Timbal, B. (1994). Response of the météo-france climate model to changes in CO_2 and sea surface temperature. *Climate Dynamics*, 9(7):345–362.

Mahieu, E., Chipperfield, M., Notholt, J., Reddmann, T., Anderson, J., Bernath, P., Blumenstock, T., Coffey, M., Dhomse, S., Feng, W., et al. (2014). Recent Northern Hemisphere stratospheric HCl increase due to atmospheric circulation changes. *Nature*, 515(7525):104–107.

Manney, G. L., Santee, M. L., Rex, M., Livesey, N. J., Pitts, M. C., Veefkind, P., Nash, E. R., Wohltmann, I., Lehmann, R., Froidevaux, L., et al. (2011). Unprecedented Arctic ozone loss in 2011. *Nature*, 478(7370):469–475.

Marsh, D. R., Mills, M. J., Kinnison, D. E., Lamarque, J.-F., Calvo, N., and Polvani, L. M. (01 Oct. 2013). Climate change from 1850 to 2005 simulated in CESM1(WACCM). *Journal of Climate*, 26(19):7372 – 7391.

Matsuno, T. (1966). Quasi-geostrophic Motions in the Equatorial Area. *Journal of the Meteorological Society of Japan. Ser. II*, 44(1):25–43.

Matthes, K., Funke, B., Andersson, M. E., Barnard, L., Beer, J., Charbonneau, P., Clilverd, M. A., Dudok de Wit, T., Haberreiter, M., Hendry, A., et al. (2017). Solar forcing for CMIP6 (v3. 2). *GEOScientific Model Development*, 10(6):2247–2302.

Matthes, K., Marsh, D. R., Garcia, R. R., Kinnison, D. E., Sassi, F., and Walters, S. (2010). Role of the QBO in modulating the influence of the 11 year solar cycle on the atmosphere using constant forcings. *Journal of Geophysical Research: Atmospheres*, 115(D18).

McElroy, C. T., Nowlan, C. R., Drummond, J. R., Bernath, P. F., Barton, D. V., Dufour, D. G., Midwinter, C., Hall, R. B., Ogyu, A., Ullberg, A., et al. (2007). The ACE-MAESTRO instrument on SCISAT: description, performance, and preliminary results. *Applied Optics*, 46(20):4341–4356.

McFarlane, N. (1987). The effect of orographically excited gravity wave drag on the general circulation of the lower stratosphere and troposphere. *Journal of Atmospheric Sciences*, 44(14):1775–1800.

McIntyre, M. and Palmer, T. (1984). The "surf zone" in the stratosphere. *Journal of atmospheric and terrestrial physics*, 46(9):825–849.

McIntyre, M. E. and Norton, W. A. (2000). Potential vorticity inversion on a hemisphere. *Journal of Atmospheric Sciences*, 57(9):1214–1235.

Meinshausen, M., Nicholls, Z. R., Lewis, J., Gidden, M. J., Vogel, E., Freund, M., Beyerle, U., Gessner, C., Nauels, A., Bauer, N., et al. (2020). The shared socio-economic pathway (SSP) greenhouse gas concentrations and their extensions to 2500. *GEOScientific Model Development*, 13(8):3571–3605.

Meinshausen, M., Vogel, E., Nauels, A., Lorbacher, K., Meinshausen, N., Etheridge, D. M., Fraser, P. J., Montzka, S. A., Rayner, P. J., Trudinger, C. M., et al. (2017). Historical greenhouse gas concentrations for climate modelling (CMIP6). *GEOScientific Model Development*, 10(5):2057–2116.

Mellor, G. L. and Yamada, T. (1974). A hierarchy of turbulence closure models for planetary boundary layers. *Journal of Atmospheric Sciences*, 31(7):1791–1806.

Miller, M., Palmer, T., and Swinbank, R. (1989). Parametrization and influence of subgridscale orography in general circulation and numerical weather prediction models. *Meteorology and Atmospheric Physics*, 40(1):84–109.

Mills, M. J., Schmidt, A., Easter, R., Solomon, S., Kinnison, D. E., Ghan, S. J., Neely III, R. R., Marsh, D. R., Conley, A., Bardeen, C. G., et al. (2016). Global volcanic aerosol properties derived from emissions, 1990–2014, using CESM1 (WACCM). *Journal of Geophysical Research: Atmospheres*, 121(5):2332–2348.

Minganti, D., Chabrillat, S., Christophe, Y., Errera, Q., Abalos, M., Prignon, M., Kinnison, D. E., and Mahieu, E. (2020). Climatological impact of the Brewer-Dobson circulation on the N_2O budget in WACCM, a chemical reanalysis and a CTM driven by four dynamical reanalyses. *Atmospheric Chemistry and Physics*, 20(21):12609–12631.

Mlawer, E. J., Taubman, S. J., Brown, P. D., Iacono, M. J., and Clough, S. A. (1997). Radiative transfer for inhomogeneous atmospheres: RRTM, a validated correlated-k model for the longwave. *Journal of Geophysical Research: Atmospheres*, 102(D14):16663–16682.

Molina, M. J. and Rowland, F. S. (1974). Stratospheric sink for chlorofluoromethanes: chlorine atom-catalysed destruction of ozone. *Nature*, 249(5460):810–812.

Molod, A., Takacs, L., Suarez, M., and Bacmeister, J. (2015). Development of the GEOS-5 atmospheric general circulation model: evolution from

MERRA to MERRA2. *GEOScientific Model Development*, 8(5):1339–1356.

Monge-Sanz, B., Chipperfield, M., Dee, D., Simmons, A., and Uppala, S. (2013). Improvements in the stratospheric transport achieved by a chemistry transport model with ECMWF (re) analyses: Identifying effects and remaining challenges. *Quarterly Journal of the Royal Meteorological Society*, 139(672):654–673.

Morgenstern, O., Hegglin, M. I., Rozanov, E., O'Connor, F. M., Abraham, N. L., Akiyoshi, H., Archibald, A. T., Bekki, S., Butchart, N., Chipperfield, M. P., Deushi, M., Dhomse, S. S., Garcia, R. R., Hardiman, S. C., Horowitz, L. W., Jöckel, P., Josse, B., Kinnison, D., Lin, M., Mancini, E., Manyin, M. E., Marchand, M., Marécal, V., Michou, M., Oman, L. D., Pitari, G., Plummer, D. A., Revell, L. E., Saint-Martin, D., Schofield, R., Stenke, A., Stone, K., Sudo, K., Tanaka, T. Y., Tilmes, S., Yamashita, Y., Yoshida, K., and Zeng, G. (2017). Review of the global models used within phase 1 of the Chemistry–Climate Model Initiative (CCMI). *GEOScientific Model Development*, 10(2):639–671.

Müller, J.-F., Stavrakou, T., Bauwens, M., George, M., Hurtmans, D., Coheur, P.-F., Clerbaux, C., and Sweeney, C. (2018). Top-down CO emissions based on IASI observations and hemispheric constraints on OH levels. *Geophysical Research Letters*, 45(3):1621–1629.

Murai, S., Yabu, S., and Kitagawa, H. (2005). Development of a new radiation scheme for the global atmospheric NWP model. In *Proceeding of 21st Conference on Weather Analysis and Forecasting/17th Conference on Numerical Weather Prediction P*, volume 1, page 66. Citeseer.

Murgatroyd, R. and Singleton, F. (1961). Possible meridional circulations in the stratosphere and mesosphere. *Quarterly Journal of the Royal Meteorological Society*, 87(372):125–135.

Nappo, C. J. (2013). *An introduction to atmospheric gravity waves*. Academic press.

Neale, R. B., Chen, C.-C., Gettelman, A., Lauritzen, P. H., Park, S., Williamson, D. L., Conley, A. J., Garcia, R., Kinnison, D., Lamarque, J.-F., et al. (2010a). Description of the NCAR community atmosphere model (CAM 5.0). *NCAR Tech. Note NCAR/TN-486+ STR*, 1(1):1–12.

Neale, R. B., Richter, J., Conley, A., Park, S., Lauritzen, P., Gettelman, A., Williamson, D., Rasch, P., Vavrus, S., Taylor, M., et al. (2010b). Description of the NCAR Community Atmosphere Model (CAM 4.0), NCAR Tech. *Note, TN–485*, page 212.

Neale, R. B., Richter, J., Park, S., Lauritzen, P. H., Vavrus, S. J., Rasch, P. J., and Zhang, M. (2013). The mean climate of the community atmosphere model (CAM4) in forced SST and fully coupled experiments. *Journal of Climate*, 26(14):5150–5168.

Nedoluha, G. E., Boyd, I. S., Parrish, A., Gomez, R. M., Allen, D. R., Froidevaux, L., Connor, B. J., and Querel, R. R. (2015). Unusual stratospheric ozone anomalies observed in 22 years of measurements from Lauder, New Zealand. *Atmospheric Chemistry and Physics*, 15(12):6817–6826.

Neu, J. L. and Plumb, R. A. (1999). Age of air in a "leaky pipe" model of stratospheric transport. *Journal of Geophysical Research: Atmospheres*, 104(D16):19243–19255.

Newell, R. E. (1963). Transfer through the tropopause and within the stratosphere. *Quarterly Journal of the Royal Meteorological Society*, 89(380):167–204.

Newman, P. A., Coy, L., Pawson, S., and Lait, L. R. (2016). The anomalous change in the QBO in 2015-2016. *Geophysical Research Letters*, 43(16):8791–8797.

Newman, P. A. and Nash, E. R. (2005). The unusual Southern Hemisphere stratosphere winter of 2002. *Journal of the atmospheric sciences*, 62(3):614–628.

Oberheide, J., Hagan, M., Richmond, A., and Forbes, J. (2015). DYNAMICAL METEOROLOGY — Atmospheric Tides. In North, G. R., Pyle, J., and Zhang, F., editors, *Encyclopedia of Atmospheric Sciences (Second Edition)*, pages 287–297. Academic Press, Oxford, second edition edition.

Oberländer, S., Langematz, U., and Meul, S. (2013). Unraveling impact factors for future changes in the Brewer-Dobson circulation. *Journal of Geophysical Research: Atmospheres*, 118(18):10–296.

Oberländer-Hayn, S., Gerber, E. P., Abalichin, J., Akiyoshi, H., Kerschbaumer, A., Kubin, A., Kunze, M., Langematz, U., Meul, S., Michou, M., Morgenstern, O., and Oman, L. D. (2016). Is the Brewer-Dobson

circulation increasing or moving upward? *Geophysical Research Letters*, 43(4):1772–1779.

Oberländer-Hayn, S., Meul, S., Langematz, U., Abalichin, J., and Haenel, F. (2015). A chemistry-climate model study of past changes in the Brewer-Dobson circulation. *Journal of Geophysical Research: Atmospheres*, 120(14):6742–6757.

Oman, L., Waugh, D. W., Pawson, S., Stolarski, R. S., and Newman, P. A. (2009). On the influence of anthropogenic forcings on changes in the stratospheric mean age. *Journal of Geophysical Research: Atmospheres*, 114(D3).

Orr, A., Bracegirdle, T. J., Hosking, J. S., Feng, W., Roscoe, H. K., and Haigh, J. D. (2012). Strong dynamical modulation of the cooling of the polar stratosphere associated with the Antarctic ozone hole. *Journal of Climate*, 26(2):662–668.

Osprey, S. M., Butchart, N., Knight, J. R., Scaife, A. A., Hamilton, K., Anstey, J. A., Schenzinger, V., and Zhang, C. (2016). An unexpected disruption of the atmospheric quasi-biennial oscillation. *Science*, 353(6306):1424–1427.

Palmer, P. I. (2008). Quantifying sources and sinks of trace gases using spaceborne measurements: current and future science. *Philosophical Transactions of the Royal Society A: Mathematical, Physical and Engineering Sciences*, 366(1885):4509–4528.

Palmer, T., Shutts, G., and Swinbank, R. (1986). Alleviation of a systematic westerly bias in general circulation and numerical weather prediction models through an orographic gravity wave drag parametrization. *Quarterly Journal of the Royal Meteorological Society*, 112(474):1001–1039.

Paneth, F. (1939). Composition and temperature of the upper atmosphere.

Park, S. K. and Županski, D. (2003). Four-dimensional variational data assimilation for mesoscale and storm-scale applications. *Meteorology and Atmospheric Physics*, 82(1):173–208.

Pascoe, C. L., Gray, L. J., Crooks, S. A., Juckes, M. N., and Baldwin, M. P. (2005). The quasi-biennial oscillation: Analysis using ERA-40 data. *Journal of Geophysical Research: Atmospheres*, 110(D8).

Paton-Walsh, C., Jones, N. B., Wilson, S. R., Haverd, V., Meier, A., Griffith, D. W. T., and Rinsland, C. P. (2005). Measurements of trace gas emissions

from Australian forest fires and correlations with coincident measurements of aerosol optical depth. *Journal of Geophysical Research: Atmospheres*, 110(D24).

Patra, A., Min, S.-K., and Seong, M.-G. (2020). Climate variability impacts on global extreme wave heights: seasonal assessment using satellite data and ERA5 reanalysis. *Journal of Geophysical Research: Oceans*, 125(12):e2020JC016754.

Petersen, A. K., Warneke, T., Lawrence, M. G., Notholt, J., and Schrems, O. (2008). First ground-based FTIR observations of the seasonal variation of carbon monoxide in the tropics. *Geophysical Research Letters*, 35(3).

Petris, G., Petrone, S., and Campagnoli, P. (2009). Dynamic linear models. In *Dynamic Linear Models with R*, pages 31–84. Springer.

Ploeger, F., Abalos, M., Birner, T., Konopka, P., Legras, B., Müller, R., and Riese, M. (2015a). Quantifying the effects of mixing and residual circulation on trends of stratospheric mean age of air. *Geophysical Research Letters*, 42(6):2047–2054.

Ploeger, F. and Birner, T. (2016). Seasonal and inter-annual variability of lower stratospheric age of air spectra. *Atmospheric Chemistry and Physics*, 16(15):10195–10213.

Ploeger, F., Diallo, M., Charlesworth, E., Konopka, P., Legras, B., Laube, J. C., Grooß, J.-U., Günther, G., Engel, A., and Riese, M. (2021). The stratospheric Brewer–Dobson circulation inferred from age of air in the ERA5 reanalysis. *Atmospheric Chemistry and Physics*, 21(11):8393–8412.

Ploeger, F., Legras, B., Charlesworth, E., Yan, X., Diallo, M., Konopka, P., Birner, T., Tao, M., Engel, A., and Riese, M. (2019). How robust are stratospheric age of air trends from different reanalyses? *Atmospheric Chemistry and Physics*, 19(9):6085–6105.

Ploeger, F., Riese, M., Haenel, F., Konopka, P., Müller, R., and Stiller, G. (2015b). Variability of stratospheric mean age of air and of the local effects of residual circulation and eddy mixing. *Journal of Geophysical Research: Atmospheres*, 120(2):716–733.

Plumb, R. A. (1996). A "tropical pipe" model of stratospheric transport. *Journal of Geophysical Research: Atmospheres*, 101(D2):3957–3972.

Plumb, R. A. (2002). Stratospheric transport. *Journal of the Meteorological Society of Japan. Ser. II*, 80(4B):793–809.

Plumb, R. A. (2007). Tracer interrelationships in the stratosphere. *Reviews of Geophysics*, 45(4).

Plumb, R. A. and Bell, R. C. (1982). A model of the quasi-biennial oscillation on an equatorial beta-plane. *Quarterly Journal of the Royal Meteorological Society*, 108(456):335–352.

Plumb, R. A. and Eluszkiewicz, J. (1999). The Brewer–Dobson circulation: Dynamics of the tropical upwelling. *Journal of the atmospheric sciences*, 56(6):868–890.

Poli, P., Hersbach, H., Dee, D. P., Berrisford, P., Simmons, A. J., Vitart, F., Laloyaux, P., Tan, D. G., Peubey, C., Thépaut, J.-N., et al. (2016). ERA-20C: An atmospheric reanalysis of the twentieth century. *Journal of Climate*, 29(11):4083–4097.

Polvani, L. M., Wang, L., Abalos, M., Butchart, N., Chipperfield, M. P., Dameris, M., Deushi, M., Dhomse, S. S., Jckel, P., Kinnison, D., Michou, M., Morgenstern, O., Oman, L. D., Plummer, D. A., and Stone, K. A. (2019). Large Impacts, Past and Future, of Ozone-Depleting Substances on Brewer-Dobson Circulation Trends: A Multimodel Assessment. *Journal of Geophysical Research: Atmospheres*, 124(13):6669–6680.

Polvani, L. M., Wang, L., Aquila, V., and Waugh, D. W. (2017). The impact of ozone-depleting substances on tropical upwelling, as revealed by the absence of lower-stratospheric cooling since the late 1990s. *Journal of Climate*, 30(7):2523–2534.

Polvani, L. M., Waugh, D., and Plumb, R. A. (1995). On the subtropical edge of the stratospheric surf zone. *Journal of Atmospheric Sciences*, 52(9):1288–1309.

Pommereau, J.-P., Goutail, F., Pazmino, A., Lefèvre, F., Chipperfield, M. P., Feng, W., Van Roozendael, M., Jepsen, N., Hansen, G., Kivi, R., et al. (2018). Recent Arctic ozone depletion: Is there an impact of climate change? *Comptes Rendus GEOScience*, 350(7):347–353.

Pougatchev, N. S., Connor, B. J., and Rinsland, C. P. (1995). Infrared measurements of the ozone vertical distribution above Kitt Peak. *Journal of Geophysical Research: Atmospheres*, 100(D8):16689–16697.

Prather, M. J., Hsu, J., DeLuca, N. M., Jackman, C. H., Oman, L. D., Douglass, A. R., Fleming, E. L., Strahan, S. E., Steenrod, S. D., Søvde, O. A., et al. (2015). Measuring and modeling the lifetime of nitrous oxide including its variability. *Journal of Geophysical Research: Atmospheres*, 120(11):5693–5705.

Previdi, M. and Polvani, L. M. (2014). Climate system response to stratospheric ozone depletion and recovery. *Quarterly Journal of the Royal Meteorological Society*, 140(685):2401–2419.

Prignon, M., Chabrillat, S., Friedrich, M., Smale, D., Strahan, S., Bernath, P., Chipperfield, M., Dhomse, S., Feng, W., Minganti, D., et al. (2021). Stratospheric Fluorine as a Tracer of Circulation Changes: Comparison Between Infrared Remote-Sensing Observations and Simulations With Five Modern Reanalyses. *Journal of Geophysical Research: Atmospheres*, 126(19):e2021JD034995.

Prignon, M., Chabrillat, S., Minganti, D., O'Doherty, S., Servais, C., Stiller, G., Toon, G. C., Vollmer, M. K., and Mahieu, E. (2019). Improved FTIR retrieval strategy for HCFC−22 ($CHClF_2$), comparisons with in situ and satellite datasets with the support of models, and determination of its long-term trend above Jungfraujoch. *Atmospheric Chemistry and Physics*, 19(19):12309–12324.

Ramanathan, V. and Downey, P. (1986). A nonisothermal emissivity and absorptivity formulation for water vapor. *Journal of Geophysical Research: Atmospheres*, 91(D8):8649–8666.

Randel, W. J. and Jensen, E. J. (2013). Physical processes in the tropical tropopause layer and their roles in a changing climate. *Nature GEOScience*, 6(3):169–176.

Rasch, P. and Kristjánsson, J. (1998). A comparison of the CCM3 model climate using diagnosed and predicted condensate parameterizations. *Journal of Climate*, 11(7):1587–1614.

Ravishankara, A., Daniel, J. S., and Portmann, R. W. (2009). Nitrous oxide (N_2O): the dominant ozone-depleting substance emitted in the 21st century. *science*, 326(5949):123–125.

Raymond, D. J. and Blyth, A. M. (1992). Extension of the stochastic mixing model to cumulonimbus clouds. *Journal of Atmospheric Sciences*, 49(21):1968–1983.

Rayner, N., Parker, D. E., Horton, E., Folland, C. K., Alexander, L. V., Rowell, D., Kent, E. C., and Kaplan, A. (2003). Global analyses of sea surface temperature, sea ice, and night marine air temperature since the late nineteenth century. *Journal of Geophysical Research: Atmospheres*, 108(D14).

Reed, R. J. (1965). The present status of the 26-month oscillation. *Bulletin of the American Meteorological Society*, 46(7):374–387.

Reed, R. J., Campbell, W. J., Rasmussen, L. A., and Rogers, D. G. (1961). Evidence of a downward-propagating, annual wind reversal in the equatorial stratosphere. *Journal of Geophysical Research*, 66(3):813–818.

Richter, J. H. and Rasch, P. J. (2008). Effects of convective momentum transport on the atmospheric circulation in the Community Atmosphere Model, version 3. *Journal of Climate*, 21(7):1487–1499.

Richter, J. H., Sassi, F., and Garcia, R. R. (2010). Toward a physically based gravity wave source parameterization in a general circulation model. *Journal of the Atmospheric Sciences*, 67(1):136–156.

Rienecker, M. M., Suarez, M., Todling, R., Bacmeister, J., Takacs, L., Liu, H., Gu, W., Sienkiewicz, M., Koster, R., Gelaro, R., et al. (2008). The GEOS-5 Data Assimilation System: Documentation of Versions 5.0. 1, 5.1. 0, and 5.2. 0.

Rienecker, M. M., Suarez, M. J., Gelaro, R., Todling, R., Bacmeister, J., Liu, E., Bosilovich, M. G., Schubert, S. D., Takacs, L., Kim, G.-K., Bloom, S., Chen, J., Collins, D., Conaty, A., da Silva, A., Gu, W., Joiner, J., Koster, R. D., Lucchesi, R., Molod, A., Owens, T., Pawson, S., Pegion, P., Redder, C. R., Reichle, R., Robertson, F. R., Ruddick, A. G., Sienkiewicz, M., and Woollen, J. (15 Jul. 2011). MERRA: NASA's Modern-Era Retrospective Analysis for Research and Applications. *Journal of Climate*, 24(14):3624 – 3648.

Rind, D., Suozzo, R., Balachandran, N., and Prather, M. (1990). Climate change and the middle atmosphere. Part i: The doubled CO_2 climate. *Journal of Atmospheric Sciences*, 47(4):475–494.

Roble, R. G. (1995). Energetics of the mesosphere and thermosphere. *The Upper Mesosphere and Lower Thermosphere: A Review of Experiment and Theory, Geophys. Monogr. Ser*, 87:1–21.

Rodgers, C. D. (2000). *Inverse methods for atmospheric sounding: theory and practice*, volume 2. World scientific.

Rosenlof, K. H. (1995). Seasonal cycle of the residual mean meridional circulation in the stratosphere. *Journal of Geophysical Research: Atmospheres*, 100(D3):5173–5191.

Rosenlof, K. H. and Holton, J. R. (1993). Estimates of the stratospheric residual circulation using the downward control principle. *Journal of Geophysical Research: Atmospheres*, 98(D6):10465–10479.

Rossby, C.-G. (1939). Relation between variations in the intensity of the zonal circulation of the atmosphere and the displacements of the semipermanent centers of action. *J. mar. Res.*, 2:38–55.

Rubin, M. B. (2001). The history of ozone. The Schönbein period, 1839–1868. *Bull. Hist. Chem*, 26(1):40–56.

Rutt, I. C., Hagdorn, M., Hulton, N. R. J., and Payne, A. J. (2009). The Glimmer community ice sheet model. *Journal of Geophysical Research: Earth Surface*, 114(F2).

Saha, S., Moorthi, S., Pan, H.-L., Wu, X., Wang, J., Nadiga, S., Tripp, P., Kistler, R., Woollen, J., Behringer, D., et al. (2010). The NCEP climate forecast system reanalysis. *Bulletin of the American Meteorological Society*, 91(8):1015–1058.

Sander, S., Golden, D., Kurylo, M., Moortgat, G., Wine, P., Ravishankara, A., Kolb, C., Molina, M., Finlayson-Pitts, B., Huie, R., et al. (2006). Chemical kinetics and photochemical data for use in atmospheric studies evaluation number 15. Technical report, Pasadena, CA: Jet Propulsion Laboratory, National Aeronautics and Space ̆2026.

Santer, B. D., Wehner, M. F., Wigley, T., Sausen, R., Meehl, G., Taylor, K., Ammann, C., Arblaster, J., Washington, W., Boyle, J., et al. (2003). Contributions of anthropogenic and natural forcing to recent tropopause height changes. *science*, 301(5632):479–483.

Santer, B. D., Wigley, T. M. L., Boyle, J. S., Gaffen, D. J., Hnilo, J. J., Nychka, D., Parker, D. E., and Taylor, K. E. (2000). Statistical significance of trends and trend differences in layer-average atmospheric temperature time series. *Journal of Geophysical Research: Atmospheres*, 105(D6):7337–7356.

Sato, K., Kinoshita, T., Matsushita, Y., and Kohma, M. (2021). A new three-dimensional residual flow theory and its application to Brewer–Dobson circulation in the middle and upper stratosphere. *Journal of the Atmospheric Sciences*.

Sawyer, J. (1965). The dynamical problems of the lower stratosphere. *Quarterly Journal of the Royal Meteorological Society*, 91(390):407–416.

Scaife, A. and James, I. (2000). Response of the stratosphere to interannual variability of tropospheric planetary waves. *Quarterly Journal of the Royal Meteorological Society*, 126(562):275–297.

Schneider, M., Demoulin, P., Sussmann, R., and Notholt, J. (2013). Fourier transform infrared spectrometry. In *Monitoring Atmospheric Water Vapour*, pages 95–111. Springer.

Schoeberl, M. R., Douglass, A. R., Hilsenrath, E., Bhartia, P. K., Beer, R., Waters, J. W., Gunson, M. R., Froidevaux, L., Gille, J. C., Barnett, J. J., et al. (2006). Overview of the EOS Aura mission. *IEEE Transactions on GEOScience and Remote Sensing*, 44(5):1066–1074.

Scinocca, J. and McFarlane, N. (2000). The parametrization of drag induced by stratified flow over anisotropic orography. *Quarterly Journal of the Royal Meteorological Society*, 126(568):2353–2393.

Scinocca, J. F. (2003). An accurate spectral nonorographic gravity wave drag parameterization for general circulation models. *Journal of the atmospheric sciences*, 60(4):667–682.

Segers, A., van Velthoven, P., Bregman, B., and Krol, M. (2002). On the computation of mass fluxes for eulerian transport models from spectral meteorological fields. In *International Conference on Computational Science*, pages 767–776. Springer.

Seviour, W. J., Butchart, N., and Hardiman, S. C. (2012). The Brewer–Dobson circulation inferred from ERA-Interim. *Quarterly Journal of the Royal Meteorological Society*, 138(665):878–888.

Shangguan, M., Wang, W., and Jin, S. (2019). Variability of temperature and ozone in the upper troposphere and lower stratosphere from multi-satellite observations and reanalysis data. *Atmospheric Chemistry and Physics*, 19(10):6659–6679.

Sheese, P., Boone, C., and Walker, K. (2015). Detecting physically unrealistic outliers in ACE-FTS atmospheric measurements. *Atmospheric Measurement Techniques*, 8(2):741–750.

Sheese, P. E., Walker, K. A., Boone, C. D., Bernath, P. F., Froidevaux, L., Funke, B., Raspollini, P., and von Clarmann, T. (2017). ACE-FTS ozone, water vapour, nitrous oxide, nitric acid, and carbon monoxide profile comparisons with MIPAS and MLS. *Journal of Quantitative Spectroscopy and Radiative Transfer*, 186:63–80.

Shepherd, T. G. (2003). Large-scale atmospheric dynamics for atmospheric chemists. *Chemical reviews*, 103(12):4509–4532.

Shepherd, T. G. (2007). Transport in the middle atmosphere. *Journal of the Meteorological Society of Japan. Ser. II*, 85:165–191.

Shepherd, T. G., Koshyk, J. N., and Ngan, K. (2000). On the nature of large-scale mixing in the stratosphere and mesosphere. *Journal of Geophysical Research: Atmospheres*, 105(D10):12433–12446.

Shepherd, T. G. and McLandress, C. (2011). A robust mechanism for strengthening of the Brewer–Dobson circulation in response to climate change: Critical-layer control of subtropical wave breaking. *Journal of the Atmospheric Sciences*, 68(4):784–797.

Sheppard, P. (1963). Atmospheric tracers and the study of the general circulation of the atmosphere. *Reports on progress in physics*, 26(1):213.

Shi, X., Liu, X., and Zhang, K. (2014). Effects of preexisting ice crystals on cirrus clouds and comparison between different ice nucleation parameterizations with the Community Atmosphere Model (CAM5). *Atmospheric Chemistry & Physics Discussions*, 14(12).

Sigmond, M. and Shepherd, T. G. (2014). Compensation between resolved wave driving and parameterized orographic gravity wave driving of the Brewer–Dobson circulation and its response to climate change. *Journal of climate*, 27(14):5601–5610.

Simmons, A., Soci, C., Nicolas, J., Bell, B., Berrisford, P., Dragani, R., Flemming, J., Haimberger, L., Healy, S., Hersbach, H., et al. (2020). *Global stratospheric temperature bias and other stratospheric aspects of ERA5 and ERA5. 1.* European Centre for Medium Range Weather Forecasts.

Simmons, A. J., Poli, P., Dee, D. P., Berrisford, P., Hersbach, H., Kobayashi, S., and Peubey, C. (2014). Estimating low-frequency variability and trends in atmospheric temperature using ERA-Interim. *Quarterly Journal of the Royal Meteorological Society*, 140(679):329–353.

Simpson, I. R., Hitchcock, P., Shepherd, T. G., and Scinocca, J. F. (2011). Stratospheric variability and tropospheric annular-mode timescales. *Geophysical Research Letters*, 38(20).

Skachko, S., Errera, Q., Ménard, R., Christophe, Y., and Chabrillat, S. (2014). Comparison of the ensemble kalman filter and 4D-Var assimilation methods using a stratospheric tracer transport model. *GEOScientific Model Development*, 7(4):1451–1465.

Skachko, S., Ménard, R., Errera, Q., Christophe, Y., and Chabrillat, S. (2016). EnKF and 4D-Var data assimilation with chemical transport model BASCOE (version 05.06). *GEOScientific Model Development*, 9(8):2893–2908.

Slingo, J. (1987). The development and verification of a cloud prediction scheme for the ECMWF model. *Quarterly Journal of the Royal Meteorological Society*, 113(477):899–927.

Smale, D., Sherlock, V., Griffith, D. W. T., Moss, R., Brailsford, G., Nichol, S., and Kotkamp, M. (2019). A decade of CH_4, CO and N_2 in situ measurements at Lauder, New Zealand: assessing the long-term performance of a Fourier transform infrared trace gas and isotope analyser. *Atmospheric Measurement Techniques*, 12(1):637–673.

Smith, R., Jones, P., Briegleb, B., Bryan, F., Danabasoglu, G., Dennis, J., Dukowicz, J., Eden, C., Fox-Kemper, B., Gent, P., et al. (2010). The parallel ocean program (POP) reference manual ocean component of the community climate system model (CCSM) and community earth system model (CESM). *LAUR-01853*, 141:1–140.

Solomon, S. (1999). Stratospheric ozone depletion: A review of concepts and history. *Reviews of Geophysics*, 37(3):275–316.

Solomon, S., Garcia, R. R., Rowland, F. S., and Wuebbles, D. J. (1986). On the depletion of Antarctic ozone. *Nature*, 321(6072):755–758.

Solomon, S., Ivy, D. J., Kinnison, D., Mills, M. J., Neely, R. R., and Schmidt, A. (2016). Emergence of healing in the Antarctic ozone layer. *Science*, 353(6296):269–274.

Solomon, S., Kinnison, D., Bandoro, J., and Garcia, R. (2015). Simulation of polar ozone depletion: An update. *Journal of Geophysical Research: Atmospheres*, 120(15):7958–7974.

Steele, H., Hamill, P., McCormick, M., and Swissler, T. (1983). The formation of polar stratospheric clouds. *Journal of Atmospheric Sciences*, 40(8):2055–2068.

Stiller, G., Clarmann, T. v., Haenel, F., Funke, B., Glatthor, N., Grabowski, U., Kellmann, S., Kiefer, M., Linden, A., Lossow, S., et al. (2012). Observed temporal evolution of global mean age of stratospheric air for the 2002 to 2010 period. *Atmospheric Chemistry and Physics*, 12(7):3311–3331.

Stiller, G. P., Fierli, F., Ploeger, F., Cagnazzo, C., Funke, B., Haenel, F. J., Reddmann, T., Riese, M., and Clarmann, T. v. (2017). Shift of subtropical transport barriers explains observed hemispheric asymmetry of decadal trends of age of air. *Atmospheric Chemistry and Physics*, 17(18):11177–11192.

Stocker, T. F., Qin, D., Plattner, G.-K., and co authors (2013). Climate Change 2013. The Physical Science Basis. Working Group I Contribution to the Fifth Assessment Report of the Intergovernmental Panel on Climate Change - Abstract for decision-makers.

Stolarski, R. S., Douglass, A. R., and Strahan, S. E. (2018). Using satellite measurements of N_2O to remove dynamical variability from hcl measurements. *Atmospheric Chemistry and Physics*, 18(8):5691–5697.

Stolarski, R. S., Krueger, A. J., Schoeberl, M. R., McPeters, R. D., Newman, P. A., and Alpert, J. (1986). Nimbus 7 satellite measurements of the springtime Antarctic ozone decrease. *Nature*, 322(6082):808–811.

Strahan, S., Oman, L., Douglass, A., and Coy, L. (2015). Modulation of antarctic vortex composition by the quasi-biennial oscillation. *Geophysical Research Letters*, 42(10):4216–4223.

Strahan, S. E., Smale, D., Douglass, A. R., Blumenstock, T., Hannigan, J. W., Hase, F., Jones, N. B., Mahieu, E., Notholt, J., Oman, L. D., et al. (2020). Observed hemispheric asymmetry in stratospheric transport trends from 1994 to 2018. *Geophysical Research Letters*, 47(17):e2020GL088567.

Sundqvist, H. (1988). Parameterization of condensation and associated clouds in models for weather prediction and general circulation simulation. In *Physically-based modelling and simulation of climate and climatic change*, pages 433–461. Springer.

Syakila, A. and Kroeze, C. (2011). The global nitrous oxide budget revisited. *Greenhouse gas measurement and management*, 1(1):17–26.

Talagrand, O. (2010). Variational assimilation. In *Data assimilation*, pages 41–67. Springer.

Teisserenc de Bort, L. (1902). Variations de la temperature de l'air libre dans la zone comprise entre 8 km et 13 km d'altitude. *Compt. Rend. Seances Acad. Sci. Paris*, 134:987–989.

Tian, H., Xu, R., Canadell, J. G., Thompson, R. L., Winiwarter, W., Suntharalingam, P., Davidson, E. A., Ciais, P., Jackson, R. B., Janssens-Maenhout, G., Prather, M. J., Regnier, P., Pan, N., Pan, S., Peters, G. P., Shi, H., Tubiello, F. N., Zaehle, S., Zhou, F., Arneth, A., Battaglia, G., Berthet, S., Bopp, L., Bouwman, A. F., Buitenhuis, E. T., Chang, J., Chipperfield, M. P., Dangal, S. R. S., Dlugokencky, E., Elkins, J. W., Eyre, B. D., Fu, B., Hall, B., Ito, A., Joos, F., Krummel, P. B., Landolfi, A., Laruelle, G. G., Lauerwald, R., Li, W., Lienert, S., Maavara, T., MacLeod, M., Millet, D. B., Olin, S., Patra, P. K., Prinn, R. G., Raymond, P. A., Ruiz, D. J., van der Werf, G. R., Vuichard, N., Wang, J., Weiss, R. F., Wells, K. C., Wilson, C., Yang, J., and Yao, Y. (2020). A comprehensive quantification of global nitrous oxide sources and sinks. *Nature*, 586(7828):248?256.

Tilmes, S., Hodzic, A., Emmons, L., Mills, M., Gettelman, A., Kinnison, D., Park, M., Lamarque, J.-F., Vitt, F., Shrivastava, M., et al. (2019). Climate forcing and trends of organic aerosols in the Community Earth System Model (CESM2). *Journal of Advances in Modeling Earth Systems*, 11(12):4323–4351.

Toohey, M. and von Clarmann, T. (2013). Climatologies from satellite measurements: the impact of orbital sampling on the standard error of the mean. *Atmospheric Measurement Techniques*, 6(4):937–948.

Toon, O. B., Hamill, P., Turco, R. P., and Pinto, J. (1986). Condensation of HNO_3 and HCl in the winter polar stratospheres. *Geophysical Research Letters*, 13(12):1284–1287.

Tritscher, I., Pitts, M. C., Poole, L. R., Alexander, S. P., Cairo, F., Chipperfield, M. P., Groo, J.-U., Hpfner, M., Lambert, A., Luo, B., Molleker, S., Orr, A., Salawitch, R., Snels, M., Spang, R., Woiwode, W., and Peter, T. (2021). Polar Stratospheric Clouds: Satellite Observations, Processes, and Role in Ozone Depletion. *Reviews of Geophysics*, 59(2):e2020RG000702. e2020RG000702 2020RG000702.

Tuckett, R. (2019). Greenhouse gases. In *Encyclopedia of Analytical Science*, pages 362–372. Elsevier.

United Nations Framework Convention on Climate Change (UNFCCC), U. (2009). Kyoto protocol reference manual on accounting of emissions and assigned amount. Technical report, eSocialSciences.

van der Leun, J. C., Tang, X., and Tevini, M. (1998). Environmental effects of ozone depletion: 1998 assessment.

Van Marle, M. J., Kloster, S., Magi, B. I., Marlon, J. R., Daniau, A.-L., Field, R. D., Arneth, A., Forrest, M., Hantson, S., Kehrwald, N. M., et al. (2017). Historic global biomass burning emissions for CMIP6 (BB4CMIP) based on merging satellite observations with proxies and fire models (1750–2015). *GEOScientific Model Development*, 10(9):3329–3357.

Velders, G. J., Andersen, S. O., Daniel, J. S., Fahey, D. W., and McFarland, M. (2007). The importance of the Montreal Protocol in protecting climate. *Proceedings of the National Academy of Sciences*, 104(12):4814–4819.

Vigouroux, C., Blumenstock, T., Coffey, M., Errera, Q., García, O., Jones, N. B., Hannigan, J. W., Hase, F., Liley, B., Mahieu, E., Mellqvist, J., Notholt, J., Palm, M., Persson, G., Schneider, M., Servais, C., Smale, D., Thölix, L., and De Mazière, M. (2015). Trends of ozone total columns and vertical distribution from FTIR observations at eight NDACC stations around the globe. *Atmospheric Chemistry and Physics*, 15(6):2915–2933.

Vincent, D. (1968). Mean meridional circulations in the Northern Hemisphere lower stratosphere during 1964 and 1965. *Quarterly Journal of the Royal Meteorological Society*, 94(401):333–349.

Viscardy, S., Errera, Q., Christophe, Y., Chabrillat, S., and Lambert, J.-C. (2010). Evaluation of ozone analyses from UARS MLS assimilation by BASCOE between 1992 and 1997. *IEEE Journal of Selected Topics in Applied Earth Observations and Remote Sensing*, 3(2):190–202.

Wang, Y., Liu, X., Hoose, C., and Wang, B. (2014). Different contact angle distributions for heterogeneous ice nucleation in the Community Atmospheric Model version 5. *Atmospheric Chemistry and Physics*, 14(19):10411–10430.

Waters, J. W., Froidevaux, L., Harwood, R. S., Jarnot, R. F., Pickett, H. M., Read, W. G., Siegel, P. H., Cofield, R. E., Filipiak, M. J., Flower, D. A., et al. (2006). The earth observing system microwave limb sounder (EOS MLS) on the Aura satellite. *IEEE transactions on GEOScience and remote sensing*, 44(5):1075–1092.

Waugh, D. and Hall, T. (2002). Age of stratospheric air: Theory, observations, and models. *Reviews of Geophysics*, 40(4):1–1.

Waugh, D. W. and Polvani, L. M. (2010). Stratospheric polar vortices.

Waugh, D. W. and Randel, W. J. (1999). Climatology of Arctic and Antarctic polar vortices using elliptical diagnostics. *Journal of the Atmospheric Sciences*, 56(11):1594–1613.

Webb, W. L., Giraytys, J., Tolefson, H. B., Forsberg, R. C., Vick, R. I., Daniel, O. H., and Tucker, L. R. (1966). Meteorological Rocket Network probing of the stratosphere and lower mesosphere. *Bulletin of the American Meteorological Society*, 47(10):788 – 799.

Wegner, T., Kinnison, D. E., Garcia, R. R., and Solomon, S. (2013). Simulation of polar stratospheric clouds in the specified dynamics version of the whole atmosphere community climate model. *Journal of Geophysical Research: Atmospheres*, 118(10):4991–5002.

Wilka, C., Solomon, S., Kinnison, D., and Tarasick, D. (2021). An Arctic ozone hole in 2020 if not for the Montreal Protocol. *Atmospheric Chemistry and Physics*, 21(20):15771–15781.

WMO (2018). *Scientific assessment of ozone depletion: 2018. Global Ozone Research and Monitoring Project–Report No. 58*. Geneva, Switzerland.

Wofsy, S. C., McElroy, M. B., and Yung, Y. L. (1975). The chemistry of atmospheric bromine. *Geophysical Research Letters*, 2(6):215–218.

Wolter, K. and Timlin, M. S. (2011). El Niño/Southern Oscillation behaviour since 1871 as diagnosed in an extended multivariate ENSO index (MEI. ext). *International Journal of Climatology*, 31(7):1074–1087.

Yamazaki, Y., Matthias, V., Miyoshi, Y., Stolle, C., Siddiqui, T., Kervalishvili, G., Latovika, J., Kozubek, M., Ward, W., Themens, D. R., Kristoffersen, S., and Alken, P. (2020). September 2019 Antarctic Sudden Stratospheric Warming: Quasi-6-Day Wave Burst and Ionospheric Effects. *Geophysical Research Letters*, 47(1):e2019GL086577. e2019GL086577 10.1029/2019GL086577.

Zander, R., Mahieu, E., Demoulin, P., Duchatelet, P., Roland, G., Servais, C., Mazire, M. D., Reimann, S., and Rinsland, C. (2008). Our changing atmosphere: Evidence based on long-term infrared solar observations at the Jungfraujoch since 1950. *Science of The Total Environment*, 391(2):184–195. Research at Jungfraujoch - Contributions to the International conference in celebration of the 75th anniversary of the High Altitude Research Station Jungfraujoch at Interlaken, Switzerland (11-13 September, 2006).

Zhang, G. J. and McFarlane, N. A. (1995). Sensitivity of climate simulations to the parameterization of cumulus convection in the Canadian Climate Centre general circulation model. *Atmosphere-ocean*, 33(3):407–446.

Zhang, M., Lin, W., Bretherton, C. S., Hack, J. J., and Rasch, P. J. (2003). A modified formulation of fractional stratiform condensation rate in the NCAR Community Atmospheric Model (CAM2). *Journal of Geophysical Research: Atmospheres*, 108(D1):ACL–10.

Zhou, M., Langerock, B., Wells, K. C., Millet, D. B., Vigouroux, C., Sha, M. K., Hermans, C., Metzger, J.-M., Kivi, R., Heikkinen, P., et al. (2019). An intercomparison of total column-averaged nitrous oxide between ground-based FTIR TCCON and NDACC measurements at seven sites and comparisons with the GEOS-Chem model. *Atmospheric Measurement Techniques*, 12(2):1393–1408.

Zhou, T., Geller, M. A., and Lin, W. (2012). An observational study on the latitudes where wave forcing drives Brewer–Dobson upwelling. *Journal of the atmospheric sciences*, 69(6):1916–1935.